Helicity of the Solar Magnetic Field

A THESIS

Submitted for the award of Ph. D. Degree of

MOHANLAL SUKHADIA UNIVERSITY

in the

Faculty of Science

by

Sanjiv Kumar Tiwari

Under the Supervision of

Dr. P. Venkatakrishnan

Senior Professor, Physical Research Laboratory &

Head, Udaipur Solar Observatory, Udaipur

DEPARTMENT OF PHYSICS

FACULTY OF SCIENCE

MOHANLAL SUKHADIA UNIVERSITY

UDAIPUR

2009

DECLARATION

I hereby declare that the work incorporated in the present thesis entitled **"Helicity of the Solar Magnetic Field"** is my own work and is original. This work (in part or in full) has not been submitted to any University for the award of a Degree or a Diploma.

Date: 16 November 2009 Sanjiv Kumar Tiwari

CERTIFICATE

I feel great pleasure in certifying that the thesis entitled **"Helicity of the Solar Magnetic Field"** embodies a record of the results of investigations carried out by **Mr. Sanjiv Kumar Tiwari** under my supervision.

I am satisfied with the analysis of data, interpretation of results and conclusions drawn.

He has completed the residential requirement as per rules.

I recommend the submission of the thesis.

Dr. P. Venkatakrishnan
Senior Professor
Physical Research Laboratory &
Head, Udaipur Solar Observatory,
Dewali, Badi Road,
Udaipur - 313 001, INDIA.
(Supervisor)

Date: November 16, 2009

To my family members

Acknowledgements

It is a great pleasure to acknowledge my thesis supervisor Prof. P. Venkatakrishnan for his valuable guidance in carrying out this work. He, throughout my Ph. D. period, encouraged me to always "raise the bar". I got more greed to learn after each discussion with him. I am grateful to him for giving me an opportunity to work with him, I could perhaps learn nowhere else what I learnt here with him.

I thank Prof. J. N. Goswami, the Director, Physical Research Laboratory, for providing me all the necessary facilities to carry out my thesis work.

I would like to thank Prof. Kandaswami Subramanian for providing me an opportunity to visit IUCAA and learn many basics of magnetic helicity with him. This visit really raised my spirit to work on the magnetic helicity.

I thank Professor E. N. Parker for very instructive comments on many works at various stages of my thesis. Discussions with him on: the physical meaning of force-free parameter α, the interpretation of currents in the astrophysical plasmas, have been particularly useful.

I am glad to acknowledge Dr. K. Sankarasubramanian for his quick response all the time whenever required. I thank him for providing me ASP and DLSP data used in my thesis. National Solar Observatory is operated by the association of Universities for research in astronomy (AURA) Inc. under cooperative agreement with the National Science Foundation.

I thank Prof. Vinod Krishan for giving me an opportunity to attend and speak in the KT-1 meeting at Kodaikanal. I was enlightened by fruitful scientific discussions in this workshop. I could get an opportunity to discuss with Prof. A. R. Choudhury, Prof. Jagdev Singh and other scientists in various meetings and

schools at Kodaikanal in 2006-2007. I thank Prof. Jagdev Singh for providing me digitized Hα data.

I thank Prof. Rob Rutten who made me to learn the Latex properly while making Evershed proceeding paper. I also thank him for helping me by providing some latex files while writing my thesis.

Thanks to Prof. Ashok Ambastha, Prof. Nandita Srivastava, and Dr. Shibu K. Mathew for their help whenever required at various stages of my thesis work.

I would like to express my gratitude to Dr. Sanjay Gosain, Dr. Brajesh Kumar, Dr. Bhuwan Joshi and Mr. Raja Bayanna for their help and encouragement at various stages of my thesis.

I am thankful to Sanjayji, Vinayji, Jayant, Anand, Raja, Vema and Ram for stimulating scientific discussions and their help and company at USO.

I thank the administrative staff Mr. Raju Koshy, Mr. Rakesh Jaroli, Mr. Pinakin and Mr. Shankarlal Paliwal for providing me all the facilities required, at USO. I also thank the administrative and other staff at PRL, Ahmedabad for their prompt help whenever required.

I thank Mr. Sudhir Kumar Gupta, Mr. Naresh Jain, late Mr. B. L. Paneri, Mr. Mukesh, Mr. Ramachandra Carpenter, Mr. Laxmilal Suthar, Mr. Dalchand Purohit, and Mr. Jagadish Singh Chouhan for their help at various stages and providing me the friendly environment at USO.

The help of library staff Sanjukta, Anie, Hariram and Hushna is acknowledged. I thank Jayant, Sneha, Alkesh, Manish, Sunil, Aditya, Kuldeep and all my friends at PRL main campus, for always creating friendly atmosphere at USO and PRL during various stages of my thesis period.

I acknowledge Hinode Team for making such an excellent telescope. A huge portion of my thesis is based on the data sets obtained from the Solar Optical

Telescope/Spectro-Polarimeter (SOT/SP) aboard Hinode. Hinode is a Japanese mission developed and launched by ISAS/JAXA, collaborating with NAOJ as a domestic partner, NASA and STFC (UK) as international partners. Scientific operation of the Hinode mission is conducted by the Hinode science team organized at ISAS/JAXA. This team mainly consists of scientists from institutes in the partner countries. Support for the post-launch operation is provided by JAXA and NAOJ (Japan), STFC (U.K.), NASA (U.S.A.), ESA, and NSC (Norway).

A few data sets used from GONG telescope is also acknowledged.

I would like to thank the Physics Department and the Ph. D. section of Mohanlal Sukhadia University for their kind co-operation throughout my thesis.

I remember the homely environment provided by Prof. P. Venkatakrishnan and his family, Prof. Ashok Ambastha and his family, Dr. Brajesh Kumar and his family, Dr. Sanjay Gosain and his family, Dr. Bhuwan Joshi and his family, Mr. Raja Bayanna and his family, Dr. V. S. Pandey and his family, Mr. Ram A. Maurya and his family, Mr. Sudhir Gupta and his family, Mr. Rakesh Jaroli and his family, all the other members of USO and their family members. I thank all of them.

Finally, I thank all the members of my family, to whom this thesis is dedicated. Their encouragement and support have been very helpful in finishing the thesis. I hope they will continue their encouragement and support in the same way in future too.

In the last, I thank all the persons who have, directly or indirectly, helped me during my Ph. D. Thesis.

Sanjiv Kumar Tiwari

Contents

List of Figures

List of Tables

Abstract

Magnetic helicity is a physical quantity that measures the degree of linkages and twistedness in the field lines. It is given by a volume integral over the scalar product of magnetic field **B** and its vector potential **A**. Direct computation of magnetic helicity in the solar atmosphere is not possible due to two reasons. First, we do not have the observations at different heights in the solar atmosphere to compute the volume integral. Second, the vector potential **A** is non-unique owing to gauge variance. Many researchers incorrectly inferred twist, a component of magnetic helicity, from the force-free parameter α. We clarified the physical meaning of α and its relation with the magnetic helicity. Also, a direct method is proposed for the computation of global α values of sunspots. An analytical bipole was generated to study the effect of polarimetric noise on the estimation of various magnetic parameters. We find that the effect of polarimetric noise, present in the recent vector magnetograms e.g., from *Hinode* (Solar Optical Telescope/Spectro-Polarimeter (SOT/SP)), on the magnetic parameters like α and magnetic energy, is negligible.

We examined the fine structures of local current and α in the sunspots. Local α patches of opposite signs are present in the umbra of each sunspot. The amplitude of the spatial variation of local α in the umbra is typically of the order of the global α of the sunspot. We find that the local α and current are distributed as alternately positive and negative filaments in the penumbra. The amplitude of azimuthal variation of the local α in the penumbra is approximately an order of magnitude larger than that in the umbra. The contributions of the local positive and negative currents and α in the penumbra cancel each other giving almost no contribution for their global values for whole sunspot.

We have introduced the concept of signed shear angle (SSA) for sunspots and

establish its importance for non force-free fields. The spatially averaged SSA (SASSA) gives the actual twist present in a sunspot irrespective of the force-free nature and the shape of the sunspot. We find that the sign of global α is well correlated with the SASSA of the sunspots but the magnitudes are not.

We find that there is no net current in the sunspots, although there is significant twist present in the photospheric magnetic field of the sunspots. The existence of a global twist for a sunspot even in the absence of a net current is consistent with the fibril-bundle structure of the sunspot magnetic fields. We also discovered the curly interlocking combed structure in the azimuthal component of sunspot magnetic field.

We studied the SASSA of sunspots to predict the flare activity of the associated active regions. We studied the evolution of vector magnetic fields using a large number of vector magnetograms of both, an eruptive and a non-eruptive sunspot. We arrive at a critical threshold value of the SASSA for each class of X-ray flare associated with these two sunspots. Thus, the SASSA holds promise to be very useful in predicting the probability of the occurrence of solar flares.

A good correlation is found between the sign of helicity in the sunspots at the photosphere and the chirality of the associated chromospheric and coronal features. This study will be very useful as a constraint while modeling the chromospheric and coronal features.

We find that a large number of sunspots observed in the declining phase of the solar cycle 23 follow the reverse hemispheric helicity rule. Most of the sunspots observed in the beginning of new solar cycle 24 follow the conventional hemispheric helicity rule. This indicates a long term behaviour of the helicity patterns in the solar atmosphere. However, this needs to be confirmed with the data sets spanning large number of years.

Chapter 1

Introduction

The Sun, our nearest star, provides energy directly or indirectly, to each and every living being on the Earth. It has been worshipped by our ancestors due to both fear and faith. The Sun is an unique plasma laboratory for us. The other stars can not be observed as closely as the Sun. The laboratory plasma has certain limitations, therefore studying Sun provides us the best opportunity to understand the origin, and nature of astrophysical plasma.

The observations of other heavenly bodies and the Sun started with the time of Galileo's invention of the telescope in 1608. Various structures on the Sun, including sunspots, were observed and reported. The rotation of the Sun with a period of about 27 days was discovered by him in 1611 by tracking the sunspots.

About 250 years after the discovery of sunspots, Richard Carrington found in 1861, that the Sun was not rotating as a solid body. He observed that the Sun was rotating faster at equatorial regions in comparison to polar regions. This phenomenon is known as differential rotation of the Sun.

The observations of the solar atmosphere show various structures e.g., sunspots,

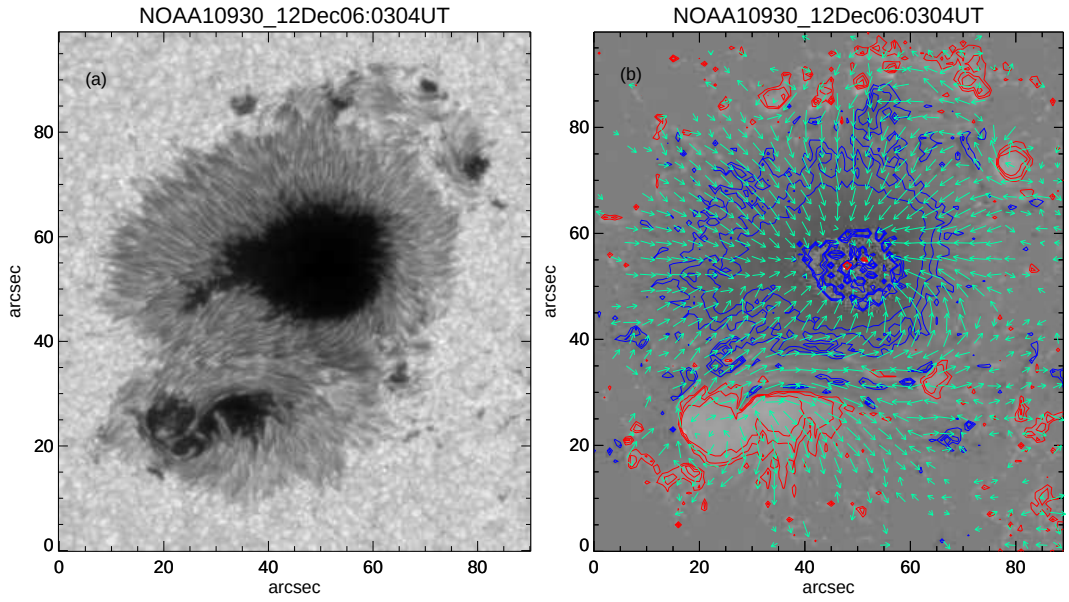

Figure 1.1: (a): An example of sunspot continuum image observed by Hinode. (b): The same sunspot as (a) with photospheric transverse vectors over-plotted on the vertical component of sunspot magnetic field. Blue and red contours represent the negative and positive polarity with contour levels of ±2000, ±1500 and ±1000 G.

filaments, prominences, plages, surges, sigmoids etc. All these structures are controlled by the magnetic field of the Sun. In the corona, the magnetic forces are much larger than the other forces like gravity or gradient of plasma pressure. Here, the magnetic field is forced to adopt a configuration where the gradient of magnetic pressure cancels the magnetic tension to maintain equilibrium. Such configurations are called force-free configurations. The field lines are frozen in the fluid due to high conductivity of plasma.

An example of a sunspot observed in the continuum is shown in Figure 1.1(a). The corresponding transverse vectors of the magnetic field are also shown in Figure 1.1(b) overlaid with the contours of vertical components of magnetic field. The images of filaments and sigmoids observed at chromospheric and coronal heights

respectively in Hα and X-ray wavelengths can be seen in figures in Chapters 7 and 8.

1.1 The Solar Magnetic Field

The Sun possesses both small scale and large scale magnetic fields. The solar magnetic field plays a major role in all the manifestations of solar activity. In fact, it is the magnetic field which allows the storage of energy for the Sun to power the activity and eruptions. In the words of Parker,

> If it were not for its variable magnetic field, the Sun would have been a rather uninteresting star.

The magnetic field on the surface of the Sun can be measured using magnetograms obtained from instruments known as magnetographs. These instruments work mainly on the principle of Zeeman effect, although the Hanle effect has also been employed in recent times to measure the weak and also the turbulent component of the magnetic field.

The measurement of magnetic fields on the surface of the Sun is relatively easier due to presence of ionized iron lines with high Lande g-factor. Also, the inversion theories are well developed for the photospheric atmosphere. In other heights such as the chromosphere and the corona, the complexity of the field lines can be seen delineated in the intensity observations. However, efforts are made to measure the magnetic fields at different heights. We focus on the surface-magnetism of the Sun in the major portion of the present work.

The solar magnetic field is spread on the Sun non-uniformly. Most of the places on the surface of the Sun, i.e., on the photosphere, contain small amounts of the observed magnetic flux density and are known as quiet Sun regions. The

sunspots, on the other hand, bear strong magnetic fields. The sunspots are dark spots on the surface of the Sun where the magnetic field inhibits the convective transport of energy from below.

It is well known that the sunspots follow an approximately 11 year cycle, known as the sunspot cycle. They emerge at a higher latitude in the beginning of any new solar cycle and migrate towards equator as the cycle progresses. By looking at this kind of pattern for 11 years, a butterfly diagram can be constructed. A. H. Joy found that the tilt of bipolar spots decreases as they emerge closer to equator and this behaviour of sunspots is named after him as Joy's law (Hale et al., 1919). Hale and Nicholson (1925) observed that the leading sunspots in a hemisphere have one polarity with opposite polarity of the leading sunspots in the another hemisphere. The vice versa is true for the following polarity. This behaviour was found to reverse with each sunspot cycle. This is known as Hale-Nicholson Law or Hale's polarity law.

The history of the discovery of solar magnetic field goes to early 19^{th} century since the time of G. E. Hale. Hale (1908a) had an intuition of the magnetic nature of the spots after observing sunspot whirls. He applied the newly discovered Zeeman effect (Zeeman, 1897) to sunspots and observed Zeeman splitting of sunspot spectra (Hale, 1908b). Since then, the study of solar magnetic field has been a topic of intensive research. Now it is well known that solar magnetic field causes all the solar phenomenon like sunspots, filaments, prominences, solar flares, coronal mass ejections (CMEs), solar winds etc. Topological changes in the solar magnetic field are supposed to drive all these events. Helicity is a measure of the topological complexity of the magnetic field. The helical structures are observed in the photospheric, chromospheric and also in the corona. An example of twisted sunspot in photosphere is shown in Figure 1.1. The helicity is

supposed to be transported from the solar interior to the corona and then to the interplanetary space. So the study of helicity in the magnetic fields of the Sun is very important. It may be used as an observational tool for understanding the fundamental processes like solar dynamo. The measurement of the distribution and evolution of helicity within active regions allows us to make models for the coronal activities like CMEs and flares. Thus the study of helicity in the solar features is important for both understanding the solar dynamo processes as well as for the space weather.

1.2 The Definition of Helicity

Helicity is a physical quantity that measures the degree of linkage and twistedness in the field. Helicity of any solenoidal (divergence-free) vector field is the integrated scalar product of the field and its vector potential. In general, for a field with vector potential X, the helicity is given as

$$H = \int \mathbf{X} \cdot \nabla \times \mathbf{X} \, dV. \tag{1.1}$$

Similarly the magnetic helicity is a measure of the degree of linkages and twistedness in the magnetic field lines (Moffatt, 1978) and is given by a volume integral over the scalar product of magnetic field B and its vector potential A.

$$H = \int \mathbf{A} \cdot \mathbf{B} \, dV \tag{1.2}$$

The term magnetic helicity was introduced by Elsasser (1956) and many of its important characteristics were studied by Woltjer (1958).

The handedness associated with the field is defined by a term chirality. Helicity is closely related to chirality. If the twist observed on the surface is clockwise, the chirality is negative and the field bears dextral chirality. The sunspot twist

direction is decided by the curvature of sunspot whirls (Martin, 1998; Tiwari et al., 2009b). If the twist is counterclockwise (when we go from sunspot center towards outside), the chirality is sinistral and sign of helicity is positive. The reverse is true for the dextral chirality.

A mathematician Câlugâreanu (1959) proposed a formula (detailed proof was given by White (1969)) to calculate the total helicity of a field line and it is the sum of helicity due to twist in the field and helicity due to writhe in the field.

$$H = (T_w + W_r)\phi^2 \tag{1.3}$$

Self helicity of a field line is the total twist and writhe present in a field line. 'Twist' is the extent to which a flux tube twists around one of its edges. 'Writhe' is the extent to which the axis of flux tube wraps and coils around itself.

Self helicity is given by $N\phi^2$ where N is the number of linkages i.e., twist and writhe in the field line and ϕ is the flux density of the field. Mutual helicity is the number of crossing of field lines with each other, and it is given by $2N\phi^2$, where N is the total number of linkages among the field lines. For example, a closed system containing two field lines interlinked once with zero self helicity bears total helicity of $2\phi^2$.

Twist component can be computed from the spatially averaged signed shear angle (SASSA) by utilizing the photospheric vector magnetograms. Many researchers have used force-free parameter α which gives the degree of twist per unit axial length under certain restrictive conditions. The writhe component of helicity can only be estimated from the chromospheric and the coronal intensity observations.

1.2.1 The Textbook Origin of the Magnetic Helicity

The origin of magnetic helicity goes back to Karl Friedrich Gauss, the great mathematician of the 19^{th} century. He discovered a formula for the linking number of two curves, known as Gauss linking formula. His motivation for this work was to track the paths of asteroids and comets (Berger, 1999).

For a random small scale magnetic field $\mathbf{b}$(x,t), the magnetic helicity can be defined in terms of field as the linkage of its flux using Gauss's linking formula (Moffatt, 1969; Berger and Field, 1984; Subramanian and Brandenburg, 2006):

$$h_G = \frac{1}{4\pi} \int \int \mathbf{b}(\mathbf{x}) \cdot [\mathbf{b}(\mathbf{y}) \times \frac{\mathbf{x}-\mathbf{y}}{|\mathbf{x}-\mathbf{y}|^{\mathbf{3}}}] \; d^3x \; d^3y \tag{1.4}$$

Let us define an auxiliary field as

$$\mathbf{a}(\mathbf{x}) = \frac{1}{4\pi} \int \mathbf{b}(\mathbf{y}) \times \frac{\mathbf{x}-\mathbf{y}}{|\mathbf{x}-\mathbf{y}|^{\mathbf{3}}} \; d^3y \tag{1.5}$$

with $\nabla \times \mathbf{a} = \mathbf{b}$ and $\nabla \cdot \mathbf{a} = 0$. Then we can write Equation 1.4 as,

$$h_G = \int \mathbf{a} \cdot \mathbf{b} \; d^3x. \tag{1.6}$$

This is the origin of textbook definition of the magnetic helicity. The vector potential is coulomb gauge and any other gauge can be applied only for a closed volume.

1.2.2 Some Characteristics of Magnetic Helicity

1.2.2.1 Conservation of Magnetic Helicity

Magnetic helicity is conserved unless the topology changes (Woltjer, 1958). 'Topology' is a branch of mathematics which deals with different transformations, preserving certain connectivities. Topology of the field lines will change only if the reconnection takes place (Choudhuri, 1998).

Thus, for an ideal fluid, the helicity will be fully conserved. Also, if the magnetic helicity is constant, a magnetic configuration satisfying the linear force-free condition ($\nabla \times \mathbf{B} = \alpha \mathbf{B}$) makes the magnetic energy minimum (Woltjer, 1958).

Taylor (1974) proposed that for a low beta plasma (ratio of plasma pressure to magnetic pressure), the magnetic helicity is conserved during the relaxation, while the magnetic energy becomes minimum. The energy dissipation rate ($\int -\eta B^2 dV$) is high in comparison to magnetic helicity dissipation rate ($-2 \int \eta \, \mathbf{J} \cdot \mathbf{B}$ dV). Thus, for highly turbulent plasma (R_m large and η small), the magnetic energy is rapidly dissipated while the helicity changes a little. This is known as Taylor's relaxation theorem.

Also, the magnetic field should be on smaller characteristic scale than the vector potential for the conservation of helicity.

1.2.2.2 Gauge Invariance in a Closed Volume

If we use a vector potential **A'** ($= \mathbf{A} + \nabla\phi$) in Equation 1.2 in place of **A**, we will have

$$\begin{aligned} H' &= \int \mathbf{A} \cdot \mathbf{B} \, dV + \int \nabla \cdot \phi \, \mathbf{B} \, dV \\ &= H + \int \phi \, \mathbf{B} \cdot \mathbf{dS} \qquad (from\ Gauss\ divergence\ theorem) \\ &= H \qquad\qquad\qquad\qquad (iff \quad \int \phi \, \mathbf{B} \cdot \mathbf{dS}\ vanishes). \end{aligned}$$

Thus the vector potential **A** is Gauge invariant only when field is constrained in a closed volume.

1.2.2.3 Magnetic Helicity of Open Fields

As in the case of the Sun, the normal components of magnetic fields exist. For such open fields, Berger and Field (1984) defined a relative magnetic helicity

which is calculated by subtracting the helicity of a reference potential field $\mathbf{B}_p$ from the helicity of the actual field $\mathbf{B}$ which comes out to be

$$H_r = \int (\mathbf{A} + \mathbf{A_p}) \cdot (\mathbf{B} - \mathbf{B_p})\, dV \tag{1.7}$$

This formula can not really give the magnetic helicity due to limited magnetic field observations available only at a few heights in the solar atmosphere.

1.3 Helicity of the Solar Magnetic Field

Helical structures in the solar features like sunspot whirls were reported long back by George E. Hale in 1925 (Hale, 1925, 1927). He found that about 80% of the sunspot whirls were counterclockwise in the northern hemisphere and clockwise in the southern hemisphere. Later, in 1941 this result was confirmed by Richardson (1941) by extending the investigation over four solar cycles. This hemispheric pattern was found to be independent of the solar cycle. Since the 90's, the subject has been rejuvenated and this hemispheric behaviour independent of sunspot cycle is claimed to be observed for many of the solar features such as the active regions (Seehafer, 1990; Pevtsov et al., 1995; Longcope et al., 1998; Abramenko et al., 1996; Bao and Zhang, 1998; Hagino and Sakurai, 2005; Nandy, 2006), the filaments (Martin et al., 1994; Pevtsov et al., 2003; Bernasconi et al., 2005), the coronal loops (Rust and Kumar, 1996; Pevtsov and Longcope, 2001), the interplanetary magnetic clouds (IMCs) (Rust, 1994), the coronal X-ray arcades (Martin and McAllister, 1996) and the network magnetic fields (Pevtsov et al., 2001; Pevtsov and Longcope, 2007) etc. The computation of magnetic helicity is not possible directly from Equation 1.2 due to two major problems as stated in the beginning. One is that magnetic helicity is a volume integral and observation available is at a certain layer only. Second problem is that the vector potential

A is not unique, thereby preventing the calculation of a unique value for the magnetic helicity from the Equation 1.2. Seehafer (1990) pointed out that the helicity of magnetic field can best be characterized by the force-free parameter α, also known as the helicity parameter or twist parameter. The force-free condition (Chandrasekhar, 1961; Parker, 1979) is given as,

$$\nabla \times \mathbf{B} = \alpha \mathbf{B} \tag{1.8}$$

Alpha is a measure of degree of twist per unit axial length under restrictive conditions. This is a local parameter which can vary across the field but is constant along the field lines.

1.3.1 Measurement of Solar Magnetic Field and Magnetic Helicity

It is well known that the reliable measurements of vector magnetic fields are needed to study various important parameters like electric currents in the active regions, magnetic energy dissipation during flares, field geometry of sunspots, magnetic twist etc.

The vector magnetic field is estimated from the observations of polarized line profiles. The polarization state is completely specified by the Stokes parameters I, Q, U and V. Here I represents the total intensity (polarized + unpolarized), Q and U the linear polarization and V represents the circular polarization. First, the observed Stokes profiles I, Q, U and V are inverted to get the magnetic parameters such as field strength, field inclination and the azimuth angle etc. The input in the inversions is Stokes profiles and a model file which includes guess values for the atmospheric parameters B, θ, ϕ, Doppler velocity (0, here in Milne-Eddington atmosphere), Source function, Damping constant, Slope of the source function,

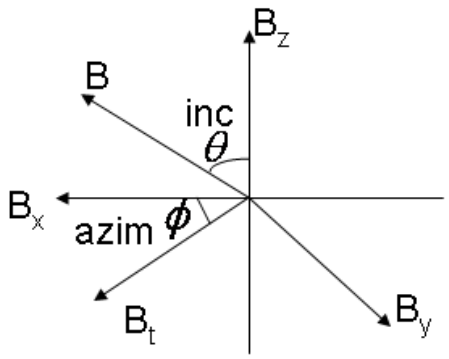

Figure 1.2: A cartoon representation of the geometry of the orientation of fields. The inclination, transverse field, vertical field, resultant field strength and azimuth are shown.

Doppler width, Ratio of center to continuum intensity etc. Outputs are the fitted parameters B, θ, ϕ and the other parameters e.g., Source function, Damping constant, Doppler width etc. After combining the above parameters, we obtain all the three components of magnetic field. The inversion codes used for the polarimetric inversion process are based on the Unno-Rachkowsky (Unno, 1956; Rachkowsky, 1967) inversion under the assumption of a Milne-Eddington atmosphere (Landolfi and Landi Degl'Innocenti, 1982; Skumanich and Lites, 1987). The azimuth determination has inherent 180° ambiguity due to insensitivity of Zeeman effect to a 180° flip in the azimuth. Various methods can be applied to remove the azimuthal ambiguity, however none guarantees for full resolution. We remove this azimuthal ambiguity by using acute angle method.

These parameters are then combined from the following relations to get the vector field components B_x, B_y and B_z:

$$B_x = B\sin(\theta)\cos(\phi) \tag{1.9}$$

$$B_y = B\sin(\theta)\sin(\phi) \tag{1.10}$$

$$B_z = B\cos(\theta) \tag{1.11}$$

The field geometry is shown in Figure 1.2. We can easily derive these equations from the diagram shown in Figure 1.2.

As discussed above, the computation of magnetic helicity is not possible directly due to it being a volume integral and non-uniqueness of vector potential **A**. The global twist component can be calculated from the spatially averaged value of signed shear angle (SASSA). The details of this parameter are given in Section 4.3.

The other measures such as global alpha parameters seem not to be correct due to non force-free nature of sunspots (Metcalf et al., 1995; Socas-Navarro, 2005) and the absence of net current in sunspots (Venkatakrishnan and Tiwari, 2009).

1.4 Motivation and Outline of the Thesis

The plan of the present thesis is given in the flow chart shown in Figure 1.3. It gives a glimpse of the thesis.

Most of the data sets used in my thesis are obtained from Solar Optical Telescope/Spectro-Polarimeter (SOT/SP) aboard space mission Hinode. However, I have also used vector magnetograms from other telescopes such as Advanced Spectro-Polarimeter (ASP), Diffraction Limited Spectro-Polarimeter (DLSP), Solar Vector Magnetograph (SVM) and Vector Spectro-Magnetograph (VSM-Synoptic Optical Long-term Investigations of the Sun (SOLIS)). The Hα images observed from the telescopes at USO, BBSO and coronal intensity images taken from Hinode X-Ray Telescope (XRT) are also used in some portions of the thesis. All these instruments are described briefly in Chapter 2.

In Chapter 3, we have verified the methodology used in the thesis. The phys-

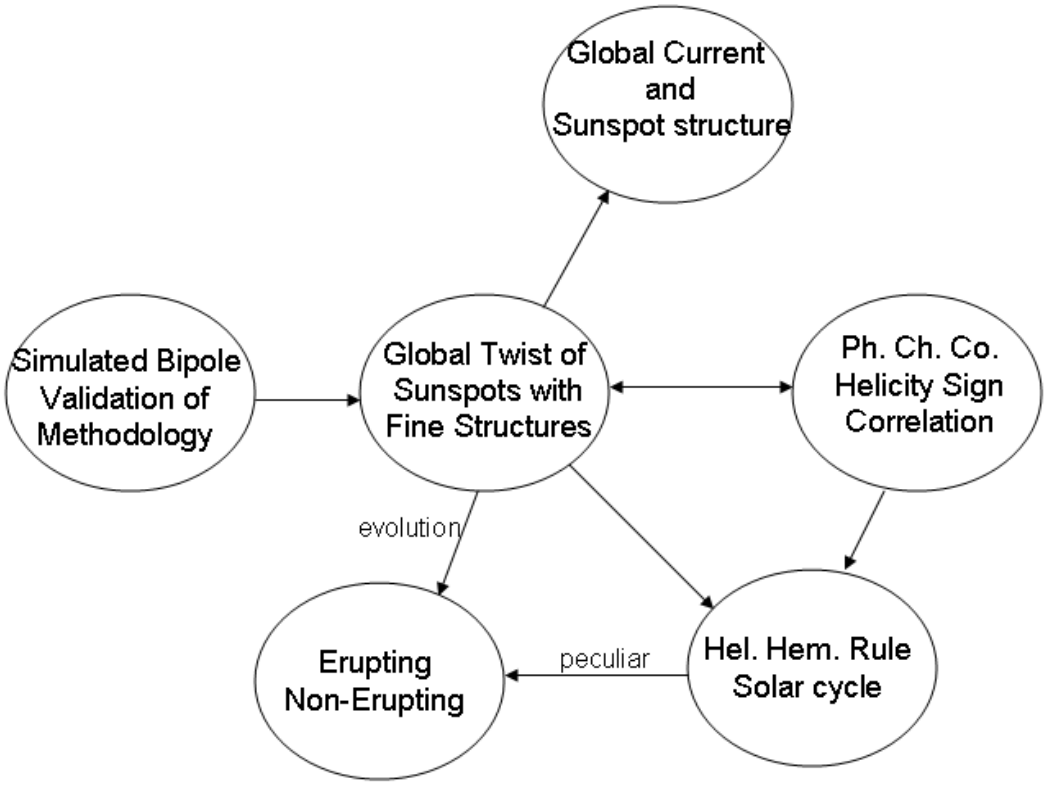

Figure 1.3: Flow chart of the plan of the work. First, an analytical bipole is generated to validate all the methodology used in the study. Then, the global twist of sunspots and their fine structure is studied. The absence of net current in presence of global twist is verified as a supplement of the earlier study. The evolution of sunspot vector magnetic field is studied to find a clue for forecasting flares by finding the difference between erupting/non-erupting active regions. The sign of helicity at different heights in the solar atmosphere is examined in the next study. Then, the relation of the behaviour of sunspots in old and new solar cycle is studied.

ical meaning of force-free parameter α has been explained. The relationship between magnetic helicity and α has been clarified. The effect of polarimetric noise on the estimation of magnetic parameters such as field strength (B), inclination (θ) azimuth (ϕ) and thereafter vector field components B_x, B_y and B_z are studied. The accuracy in the measurement of the parameters α and magnetic energy (E_m) calculated from the recent vector field data has been simulated. All these issues are clarified in Chapter 3. For this, an analytical bipole is simulated with known magnetic parameters.

In Chapter 4, we find out the fine structures in sunspots in terms of vertical current and alpha. The contribution of umbral and penumbral twist to the global twist is determined. We have proposed signed shear angle (SSA) as a new method for computation of twist of sunspots irrespective of force-free nature of the sunspots.

In association with the study in Chapter 4, we continued our study of twist and current in the sunspots. We find very interesting result that no net current exists in a sunspot even in presence of a significant global twist. This result is consistent with the fibril bundle nature of the sunspot. We present this result in Chapter 5. Also, 'curly interlocking combed structure' of sunspot field was discovered. And it is shown in the same chapter that the spatially averaged SSA (SASSA) gives the twist irrespective of shape of the sunspots.

The evolution of vector fields of the sunspot is studied in Chapter 6. We have analyzed a series of data sets of NOAA AR 10930 as an eruptive and NOAA AR 10961 as a non-eruptive example of sunspots. We find critical thresholds of SASSA for different classes of X-ray flares. The results are very interesting and important, and are presented in Chapter 6.

Chapter 7 illustrates the association of sign of helicity in connected features at

different heights in the solar atmosphere. Data sets of chromospheric and coronal heights are also used in this study. This study gives a constraint for modeling the chromospheric and coronal structures/features.

In Chapter 8, we try to find the relation, if any, between the behaviour of active regions (ARs) of old and recently begun new solar cycle. Although, not many sunspots have emerged in the 24^{th} solar cycle till now, we have used the available data sets. Most of the sunspots in new cycle are observed and used in this study.

The discussion and conclusions are given in Chapter 9. The results are summarized in this chapter. Many questions arose during the above work. We discuss on the future scope of the associated study in the last section of this last chapter.

Chapter 2

Brief Description of the Instruments

2.1 Introduction

I have used different data sets obtained at different solar atmospheric heights in the thesis. These data are obtained from different telescopes working all over the world. Although, the chromospheric and coronal intensity data obtained at certain wavelengths at these heights are used in some part of the thesis, the major portion of the thesis work is based on the photospheric vector magnetograms. Most of the sunspot vector magnetograms studied in the thesis, are obtained from Solar Optical Telescope/Spectro-Polarimeter (SOT/SP) aboard *Hinode* which is a space based telescope and was launched on September 23, 2006. However, some of the vector magnetograms are observed from Advanced Stokes Polarimeter (ASP), Diffraction Limited Spectro-Polarimeter (DLSP) of Dunn Solar Telescope (DST), Solar vector Magnetograph at Udaipur Solar Observatory (SVM-USO)

and the Vector Spectro-Magnetograph (VSM) at Synoptic Optical Long-term Investigations of the Sun (SOLIS).

The chromospheric Hα data sets have been obtained from various telescopes operational at various places. Most of the Hα data sets are obtained from Big Bear Solar Observatory (BBSO) and Udaipur Solar Observatory. The BBSO images are available at the following link: `ftp://ftp.bbso.njit.edu/pub/archive/` A few data sets are UBF Hα images from DST. The Hα images can be seen in figures in the Chapters 7 and 8.

Coronal X-ray intensity images are taken from X-Ray Telescope (XRT) aboard Hinode, and Extreme Ultraviolet images are taken from Extreme UV Imaging Telescope (EIT) on-board SOHO.

The details of all the above mentioned instruments are given in the following Sections of this Chapter.

2.2 Instruments Used for Photospheric Observations

As mentioned in the Introduction, we have used the vector magnetograms obtained from the space based instrument SOT/SP (Tsuneta et al., 2008; Shimizu et al., 2008; Suematsu et al., 2008; Ichimoto et al., 2008) aboard Hinode Kosugi et al. (2007), and also ground based instruments such as ASP (Elmore et al., 1992) /DLSP (Sankarasubramanian et al., 2004, 2006) of DST , SVM (Gosain et al., 2004, 2006) of USO and VSM (Jones et al., 2002) of SOLIS (Keller et al., 2003). We will describe the above instruments in detail in this Section.

Table 2.1: Spectro-polarimeter (SP) specifications

Field of view along slit	164" (north-south direction)
Spatial scan range	164"
Slit width	0.16"
Spectral coverage	630.08nm - 630.32nm
Spectral resolution/sampling	30mÅ/ 21.5mÅ
Measurement of polarization	Stokes I,Q,U,V simultaneously with dual beams (orthogonal linear component)
Polarization signal to noise	10^3 (with normal mapping)

2.2.1 Solar Optical Telescope/Spectral-Polarimeter: SOT/SP

Solar Optical Telescope (SOT) on-board Hinode(Solar-B) is the largest aperture, most advanced solar telescope flown in space till date. The SOT consists of the main 50 cm aperture telescope (Optical Telescope Assembly, OTA) and focal plane package (FPP). The combined SOT system is optimized for accurate measurement of the vector magnetic field in the photosphere.

The Spectral-polarimeter (SP) obtains line profiles of two magnetically sensitive Fe lines at 630.15 and 630.25 nm and nearby continuum, using a 0.16"×164" slit. Spectra are exposed and read out continuously 16 times per rotation of the polarization modulator, and the raw spectra are added and subtracted onboard in real time to demodulate, generating Stokes IQUV spectral images. Two spectra are simultaneously taken in orthogonal linear polarizations. When combined in data analysis after downlink, spurious polarization due to any residual image jitter or solar evolution is greatly reduced. The slit can move to map a finite area, up to the full 320" wide FOV.

The SOT/SP specifications are given in Table 2.1.

The SP is flexible in mapping observing regions, allowing one to perform suitable observations depending on science objectives (Table 2.2). The SP only has a few modes of operation: Normal Map, Fast Map, Dynamics, and Deep Magnetogram.

The Normal or Slow Map mode produces polarimetric accuracy of 0.1% with the spatial sampling of 0.16"×0.16". It takes 83 min to scan a 160" wide area which is enough to cover a moderate-sized active region. The cadence becomes faster (50 sec for mapping of 1.6" wide area) if the scanning size is reduced. This would be useful for studying dynamics of small magnetic features. The Fast Map mode of observation can provide 30-min cadence for the 160" wide scanning with polarimetric accuracy of 0.1%. But the resolution reduces to 0.32". The Dynamics mode of observation provides higher cadence (18 sec for 1.6" wide area) with 0.16" resolution, although at lower polarimetric accuracy. In Deep Magnetogram mode, photons may be accumulated over many rotations of the polarization modulator, as long as the data doesn't overflow the summing registers. This allows one to achieve a very high polarization accuracy in very quiet regions, at the expense of time resolution.

We have used most of the maps observed in fast mode i.e., with polarimetric accuracy 0.1% and sampling 0.32"/pixel. However, a few sets of normal mode are also used in a portion of the study.

The SOT is designed and developed by the international collaboration between National Astronomical Observatory of Japan (NAOJ), Lockeed Martin Advanced Technology Center (LM), Mitsubishi Electric Corporation (MELCO), NCAR High Altitude Observatory (HAO), NASA MSFC, and JAXA. The OTA was built, tested and calibrated at the Advanced Technology Center of the NAOJ with Mitsubishi Electric Corporation.

Table 2.2: Typical mapping mode examples for the SP

Normal map	
Time per position	4.8 sec (3 rotations of waveplate)
FOV along slit	164”
Sampling along slit	0.16”
Slit-scan sampling	0.16”
Polarimetric S/N	10^3
Data size	918k pixels in 4.8 sec (191k pixel/s)
Time for map area	50sec for 1.6” wide; 83min for 160” wide
Fast map	
Time per position	3.2 sec (one rotation for 1st slit position and another rotation for 2nd slit position)
FOV along slit	164”
Sampling along slit	0.32”
Slit-scan sampling	0.32”
Polarimetric S/N	10^3
Data size	459k pixels in 3.6 sec (127k pixel/s)
Time for map area	18sec for 1.6” wide; 30min for 160” wide
Dynamics	
Time per position	1.6 sec (one rotation of waveplate)
FOV along slit	32”
Sampling along slit	0.16”
Slit-scan sampling	0.16”
Polarimetric S/N	580
Data size	179k pixels in 1.6 sec (120k pixel/s)
Time for map area	18sec for 1.6” wide
Deep magnetogram	
Time per position	many rotations (up to 8 rotations)
FOV along slit	164”
Sampling along slit	0.16”
Slit-scan sampling	0.16”
Polarimetric S/N	$> 10^3$

2.2.2 Advanced Spectro-Polarimeter and Diffraction Limited Spectro-Polarimeter: ASP/DLSP

Both the instruments are on the Dunn Solar Telescope (DST).

2.2.2.1 Dunn Solar Telescope: DST

The DST is the largest of the solar research instruments atop Sacramento Peak. Approximately 67 meters (220 feet) of this telescope lie out of sight, buried beneath the surface of the mountain peak. Sunlight enters the tower through a 76-centimeter (30 inch) window located 41 meters (136 feet) above the ground. By placing the window so high up, observer avoids distortion of the solar image from local air turbulence near the ground. There, a pair of movable 1.1-meter (44-inch) mirrors direct the sunlight down to the 1.2-meter (48-inch) diameter tube that runs vertically down the center of the observing room floor. The sunlight is reflected from the concave 1.6-meter (64-inch) main mirror of the telescope and then back up to the observing room, producing a 51-centimeter (20-inch) diameter image of the Sun for detailed studies.

The telescope's entire optical system - from the top of the Tower to the base of its underground portion - plus the 12 meter (40 foot) diameter observing room floor, is suspended near the top of the Tower by a mercury-float bearing. The bearing, in turn, is hung on three bolts, each only 76 millimeters (3 inches) in diameter.

2.2.2.2 Advanced Stokes Polarimeter: ASP

The Advanced Stokes Polarimeter (ASP) instrument is a joint project between the National Solar Observatory (NSO) and the High Altitude Observatory (HAO). The aim of this project is to obtain quantitative measurements of the vector mag-

netic field in the photosphere and low chromosphere (as high into the atmosphere as the diagnostics will allow), with spatial resolution that will allow meaningful interpretation of solar features such a sunspots, pores, and active region structures.

For a proper analysis to get improved results, we require: (1) high angular resolution to resolve the fine-scale structure of solar features; (2) spectrally resolved line profiles to take advantage of the inherent polarization induced by the Zeeman effect in solar line profiles and to resolve changes in the polarization profiles due to the strength and orientation of the field and the thermal structure of the solar atmosphere; (3) simultaneous measurements of two nearby lines of a multiplet having differing sensitivity to the Zeeman effect in order to tightly constrain the field measurement; and (4) a sensitivity to polarization adequate to interpret the magnetic field of active regions, which is known to be concentrated into slender flux tubes of high field strength at the photospheric level. These requirements have been discussed in Lites and Skumanich (1989) and Elmore et al. (1992)

This telescope employs two flat mirrors in an alt-azimuth turret atop a 40 m tower to direct the solar beam vertically downward through a vacuum chamber to the primary mirror located 55 m below ground level. The 152 cm dia. f/72 primary forms a solar image just above ground level with an image scale of 266 microns/arcsecond. There is a 76.2 cm dia., 4 cm thick fused silica entrance window at the front of the turret and a 20 cm dia. exit window at ground level. The telescope is evacuated to eliminate internal turbulence and thereby minimize time-variable distortion of the solar image due to "seeing" within the telescope itself. A mount has been added to the turret which may hold either a large linear or circular sheet polarizer in front of the entrance window for calibration of the polarization properties of the DST. This mount also allows the large polarizers

to be remotely and precisely rotated during calibration measurements.

The polarimetric accuracy of ASP is 0.1%. It takes 15 minutes to one hour for a full map of active regions depending on their sizes. The sampling of ASP is approximately 0.3 arcsec/pixel. More details are available in Elmore et al. (1992); Lites and Skumanich (1989).

2.2.2.3 Diffraction-Limited Spectro-Polarimeter: DLSP

The Diffraction-Limited Spectro-Polarimeter (DLSP) is again built in collaboration with the HAO and NSO. It is operated at the NSO (Dunn Solar Telescope) and is an innovative and contemporary grating polarimeter specifically designed to meet the high requirements in solar spectro-polarimetry. With the excellent imaging properties of the instrument and the efficient performance of the high-order adaptive optics system, a spatial resolution of 0.4 arcsec can be achieved. Near synchronous G-Band and Ca II K imaging provides valuable photospheric and low chromospheric information. In order to simplify observations, calibrations and data analysis, the DLSP is limited to one wavelength range in the visible covering the FeI 630.15 nm and FeI 630.25 nm lines. This unique setup, together with the latest modifications related to instrument control and data acquisition implemented to improve its performance, allow for a very quick setup time of about 15 min only. This is the first step towards the realization of queue observing, an observing mode imagined for the Advanced Technology Solar Telescope (ATST). The DLSP is a Facility Research Instrument permanently installed at Port 2 of the DST.

The DLSP is a dual beam grating polarimeter designed to provide a flexible image scale. The spectrograph is in an auto collimated configuration (Littrow mount) with an off-axis parabola (P). The dispersive element is a 79 grooves/mm

Echelle grating (G) working in high order (36^{th} order). The aperture slit (S) has a width of 12 micron. The detector (CCD) is a high speed, backside illuminated split-frame transfer sensor (652 x 494 pixel) manufactured by PixelVision. The DLSP uses two ferro-electric liquid crystals upfront right after the exit port to modulate the light beam. A polarizing beam splitter (PBS) right in front of the detector acts as an analyzer. All optical components are mounted to a base plate. The whole spectrograph is moved to scan a solar active region.

The DLSP has two operation modes: high and low resolution mode. In high resolution, the diffraction limit of the DST @630.2 nm is critically sampled with 0.09 arcsec/pixel covering 59 arcsec along the slit. In low resolution, the spatial sampling is 0.25 arcsec/pixel allowing for a larger FOV of 163 arcsec. In the spectral direction the instrument samples the solar spectrum from 630 nm to 630.4 nm with 2.1 pm per pixel. The smallest step size is matched to the spatial sampling along the slit. Typically, at each slit position, 16 images of 30 ms exposure time each are accumulated for each of the four modulation states leading to a total integration time of 2 s. A map of the full FOV (660 steps) is accomplished in 55 min (5 s per slit position).

The DLSP is permanently installed at port 2 of the DST and is equipped with its own high-order adaptive optics system. The instrument has a very compact design which allows to add additional devices next to it on the same optical table. Typically, observing runs with the DLSP are accompanied by the tunable Universal Birefringent Filter (UBF) or a simple Lyot filter. Furthermore, the upfront setup includes two context channels, one for chromospheric observations in the Ca II K 393.4 nm line and one for photospheric observations in the G-Band at 430.5 nm.

More detailed information about DLSP can be found in Sankarasubramanian

et al. (2003, 2004, 2006).

2.2.3 Solar Vector Magnetograph (SVM-USO)

Two vector magnetograms studied in the thesis are taken from Solar Vector Magnetograph (SVM) at Udaipur Solar Observatory (USO). This magnetograph become operational at USO-island in 2007, January. SVM is basically an instrument which makes two-dimensional spatial maps of solar active regions in the Zeeman induced polarized light of the solar spectral lines. SVM has the following main components: a Schmidt-Cassegrain telescope, rotating wave-plate polarimeter, tunable narrow-band Fabry-Perot filter, calcite analyzer (Savart plate) and a cooled CCD camera. The primary imaging is done by using a Celestron C-8 (TM) Schmidt-Cassegrain telescope of 8 inch aperture. The focal length of the telescope is 2032 mm and the resulting output beam is a f/10 beam. The telescope has a pre-filter in front with a 15nm pass-band centered at 630nm wavelength. A circular aperture of 2 arc-min diameter selects the field of view (FOV) at the prime focus. This FOV is then modulated by the rotating waveplates of the polarimeter. The modulated beam is now collimated by a 180mm focal length lens. This modulated and collimated beam now enters the Fabry-Perot etalon and order sorting pre-filter. Now the re-imaging lens makes the image on the CCD camera. Just before the CCD camera a combination of two crossed calcite beam-displacing crystals is placed for the analysis of polarization. So we get two orthogonal polarized images of the selected FOV onto the CCD camera. The vector magnetograms of the two active regions NOAA 10935 and NOAA 10941 are shown in the Figure 7.2.

The schematic of the instrument is given in Figure 2.1. The details about the instrument can be found elsewhere (Gosain et al., 2004, 2006). The instrument

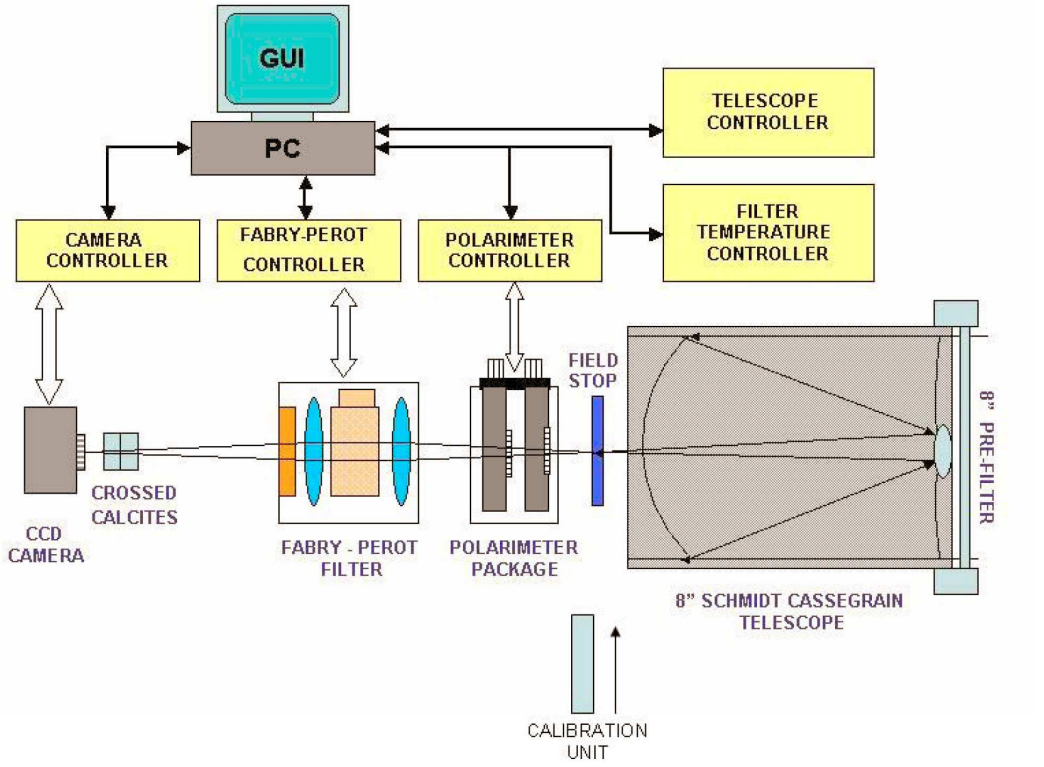

Figure 2.1: The schematic diagram of the Solar Vector Magnetograph (SVM) operational at Udaipur Solar Observatory (USO).

is basically a tunable Fabry-Perot based imaging magnetograph which uses quarter wave-plates as polarization modulator and crossed calcites (Savart plate) as dual beam analyzer. The simultaneous measurements of orthogonal polarization components reduce the seeing induced spurious polarization signals. The straight and symmetric telescope design is used to avoid instrumental polarization to a great extent. The polarized profiles with single camera exposure can be obtained with rms noise level of $< 0.5\%$ in the continuum. The complete Stokes profile with 21 samples across the Fe I 6302.5 Å line can be performed in less than a minute with polarization sensitivity of $< 0.5\%$ of continuum.

In order to facilitate the data analysis and visualization of the calibrated data

in a user-friendly and less time-consuming way, we have developed two graphical user interfaces (GUIs). The first one is developed for performing interactive Stokes inversion of the observed profiles using a Milne-Eddington inversion scheme. While another GUI is developed for visualizing the magnetic field parameters retrieved by Stokes inversion. The details of both the GUI are discussed below and can be found in Gosain et al. (2008).

First GUI is developed for interactively inverting the Stokes profiles over the observed region (see Figure 2.2) under Milne-Eddington atmosphere assumptions (Socas-Navarro, 2001). However, the complete inversion of the observed region is highly time consuming, taking about an hour for a single data set. A hybrid approach is being developed where weak field approximation (WFA) (Jefferies and Mickey, 1991), is used for those pixels where the polarization signals are below a particular threshold. This threshold corresponds to the limit up to which WFA is valid. The threshold value is determined using synthetic Stokes profiles generated by MELANIE. Whereas for pixels above this threshold, Stokes inversion is used to retrieve magnetic field. This approach shall save lot of computational time since WFA is generally valid for major portion of the observed area.

In order to visualize the vector magnetograms, the second GUI has been developed (see Figure 2.3). The inverted data can be visualized in the form of arrows showing transverse field strength and direction while contours showing line-of-sight magnetic field. The quick-look feature is also available for retrieving magnetic field vector from polarized images in the line wing after determining suitable calibration constants. Further, the heliographic transformation of the vector magnetograms observed away from disk center can be performed interactively. The potential field can be calculated and displayed interactively. Also, the 180° ambiguity resolution can be performed using acute angle method. The

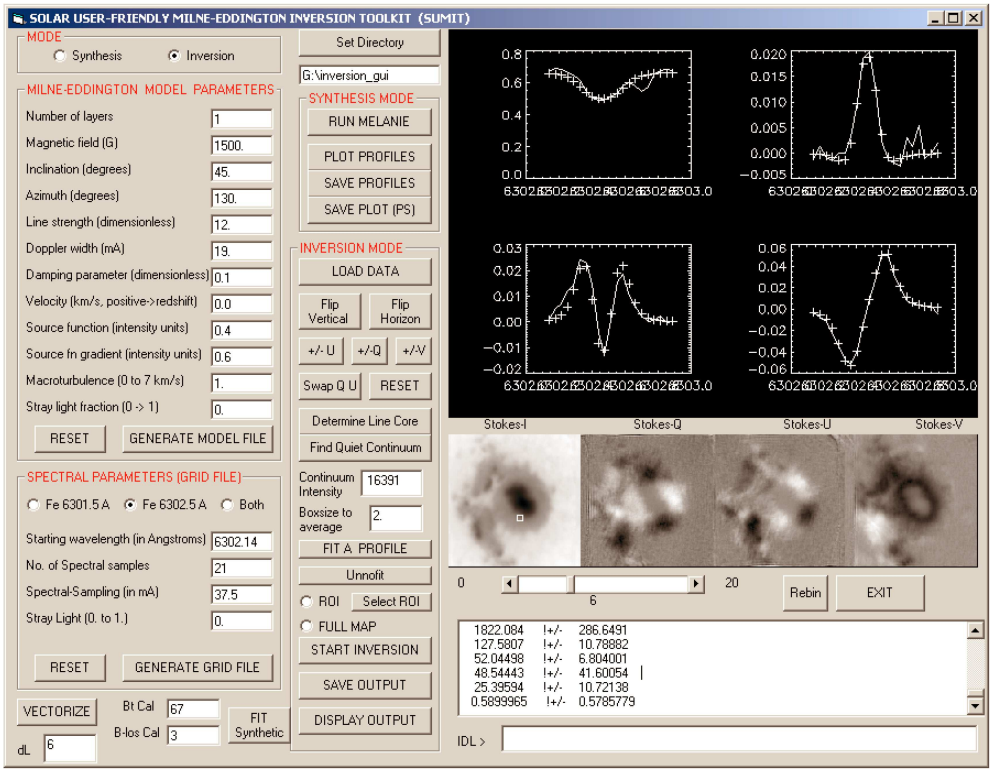

Figure 2.2: A Graphical User Interface (GUI) for the Milne-Eddington Inversion of SVM Stokes profiles.

interface also provides utilities for calculation of L0, B0 and position angle for a given data and time. Also, one can load full disk images of the sun and determine the L and B coordinates of active regions interactively by clicking at them.

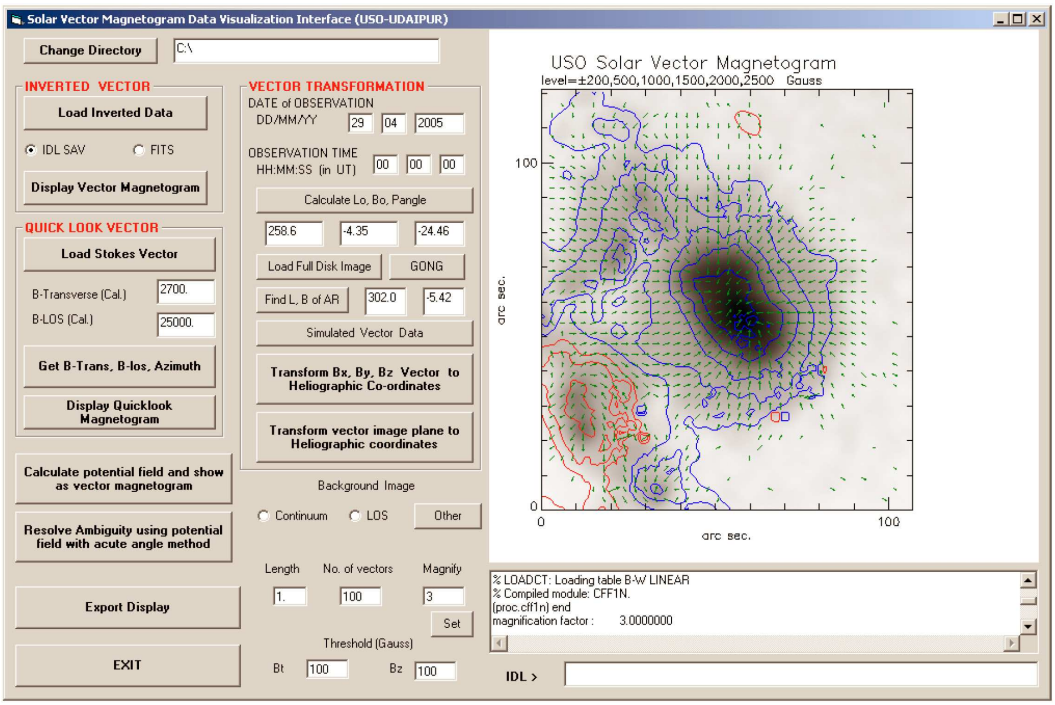

Figure 2.3: A Graphical User Interface for visualizing and transforming the inverted vector field data.

2.2.4 Vector Spectro-Magnetograph (VSM-SOLIS)

Some of the vector magnetograms obtained from Vector Spectro-magnetograph (VSM)/Synoptic Optical Long-term Investigations of the Sun (SOLIS) have been used for the study in Chapter 8. The Milne-Eddington inverted data has been kept online at: `http://solis.nso.edu/vsm/data_summary/DataSumm3.php?stime=1059717600&etime=0&obsmode[]=6302v&display=1&flares=&sobsmode=1&meonly`.

The details of the instrument are as follows:

The VSM takes high-quality magnetic field observations in the photosphere by recording the Zeeman-induced polarization of spectral lines. The VSM operates in four different observing modes at three different wavelengths. The four observing modes are:

1. Stokes I, Q, U, and V profiles in the FeI 630.15 nm and 630.25 nm lines
2. Stokes I and V profiles in the FeI 630.15 nm and 630.25 nm lines
3. Stokes I and V profiles in the CaII 854.2 nm line
4. Stokes I in the HeI 1083.0 nm line and the near-by SiI line

To measure vector magnetic fields outside sunspots in the visible part of the spectrum, it is indispensable to observe at least two spectral lines with different Lande g factors. The FeI 630.15 and 630.25 nm lines were chosen because they are the most appropriate lines to measure vector magnetic fields in quiet as well as active regions. Other often used lines such as the FeI lines around 525.0 nm are hampered by molecular blends in sunspots. Furthermore, the Advanced Stokes Polarimeter (ASP), an instrument discussed above, delivers precise vector field measurements, has used the FeI lines at 630.2 nm, and the analysis tools have already been developed for this line pair.

An initial transmission budget for the complete optical system indicated that a 50-cm aperture telescope with a 10% obstruction is sufficient to achieve the required polarization sensitivity. Therefore, the aperture was fixed at effectively 50 cm. To match the CCD pixel size of 16 m per pixel (=1 arcsec) an f/6.6 is required.

The specifications of the telescope are given in Table 2.3.

The telescope does not need to be diffraction limited. It is a 50-cm quasi Ritchey-Chrtien with a two-lens field corrector to provide adequate image quality over the whole field of view, minimal geometric distortion, equal image size for

Table 2.3: Specifications of VSM/SOLIS

Parameter	Specification	Comment Angular
Element	1.00 by 1.00 arcsec	
coverage	2048 by 2048 arcsec	Slightly larger than full disk
format	2048 by 1	Proposal specified 2000 by 1
geometric accuracy	better than 0.5 arcsec rms	After re-mapping
instrumental mtf	measurable to $\pm$ 0.01	
total mtf	$<$ 0.1 at frequencies $>$ Nyquist	
motion in RA	0.25 degrees	Added for flat fielding
Temporal		
scan rate	0.05-5.0 s/arcsec	to provide fast or accurate B_z
timing accuracy	better than 1 s	
knowledge of start & end of integration at each slit-pos	better than 1ms	For comparison with other data and accurate remapping
frequency	$<$ 20 minutes for full disk $<$ 2 minutes for active region	For accurate polarimetry
full-disk longitudinal with reduced sensitivity	$<$ 2 minutes	To provide fast magnetograms with VSM
Spectral		
spectral lines	630.15,630.25,854.20,1083nm,	Selected suitable spectral lines
spectral resolution	200,000	
wavelength range	630.15-0.05 to 630.25+0.05nm 854.2 $\pm$ 0.1 to 1083.0 $\pm$ 0.5nm	Were unable to design efficient instrument over full range of 600 to 1600 nm
spectral lines	at least two simultaneously	
Polarimetry		
Type	630.2 nm: I,Q,U,V 854.2 nm: I,V 1083.0 nm: I	Analysis of vector polarimetry in 854.2 nm not clear, wider spectral range in 1083.0nm for polarimetry
sensitivity	0.0002 per pixel in 0.5 s	
relative accuracy	0.001	
Miscellaneous		
image motion stabilization	at about 100 Hz	To improve spatial resolution

all wavelengths, and a telecentric beam to minimize field of view effects in the polarization modulators.

In the case of the 630.2-nm wavelength calibration, the polarizer and the wave plate are rotated with respect to each other and with respect to the entrance slit while data are recorded at each rotational position.

2.3 Instruments Used for Chromospheric Observations

As mentioned in the Introduction, the chromospheric Hα data sets also have been obtained from various telescopes operational at various places. Most of the Hα data sets are obtained from Big Bear Solar Observatory (BBSO) and Udaipur Solar Observatory. The processed BBSO images are available at the following link: `ftp://ftp.bbso.njit.edu/pub/archive/`. A few data sets are UBF Hα images taken from DST.

A brief description of these instruments are given below:

2.3.0.1 Big Bear Solar Observatory: BBSO

The Big Bear Solar Observatory (BBSO) is located in Big Bear Lake, California high in the San Bernardino Mountains. The mountain lake is characterized by sustained atmospheric stability, which is essential for any dedicated telescopes and instruments. BBSO is operated by the New Jersey Institute of Technology (NJIT). Their principal telescope is the 1.6 m clear aperture, off-axis telescope. Under a separate dome two full-disk telescopes - one for Hα and one for earthshine are being operated. The Center for Solar-Terrestrial Research (CSTR) at NJIT studies a range of phenomena from the Sun to the terrestrial atmosphere.

Table 2.4: Telescope description of BBSO/Hα

Telescope Description	
Location:	Ash Dome
Telescope Aperture:	10 cm
Filter Bandpass:	Zeiss Lyot Filter 0.025 nm
Tunable Filter Range:	+/- 0.30 nm
Camera:	JAI PULNIX TM4200GE Camera
Detector:	Kodak KAI 4021, 2048 x 2048 pixel
Dynamic Range:	12 bit

The telescope description is given in Table 2.4.

2.3.0.2 Spar Hα Telescope at USO

The Udaipur Solar Observatory is situated on an island in the middle of the Lake Fatehsagar (Location: 240 35.1' : 730 42.8'). The large water body surrounding the telescopes decreases the amount of heating of the surface layers. This decreases the turbulence in the air mass and thereby improves the image quality and seeing. The main objective of obtaining the high spatial and temporal resolution observations of solar photospheric and chromospheric activity is to understand the various dynamic phenomena occurring on the surface of the Sun.

A 12-foot solar spar with 15-cm aperture telescope is being used for observing small high resolution chromospheric structures with the help of a narrow passband Halle-birefringent filter centered at 6563 Å Hα spectral line.

We have used high resolution Hα images taken from Udaipur Solar Observatory (USO) from Spar Telescope. The Spar Telescope uses 1392×1024 ccd with the pixel resolution of 0.395 arcsec and the SVM has 1024×1024 ccd with pixel

resolution of 0.98 arcsec. The Spar Telescope has f/15 doublet lens with focal length of 2.25 meters and objective 0.15 meters. It uses a Hα Halle lyot type filter with FWHM of 500 mÅ operating at the wavelength of 6563 Å. The telescope utilizes a 1392×1024 CCD with the pixel size of 6.45 μm. The pixel resolution of the CCD is 0.395 arc-sec and the field of view it covers is 9 arc-min × 7 arc-min. The Hα images of the active regions NOAA 10930, NOAA 10935 and NOAA 10941, as examples, are shown in the Figure 7.3.

2.3.0.3 Universal Birefringent Filter (UBF-DST)

The Universal Birefringent Filter (UBF) is a Lyot type filter with rotating crystal elements using quarter wave plates and linear polarizers to tune. The filter is a very flexible instrument to use. The UBF can be used as a primary or secondary instrument on the Port 4 optical bench or a secondary limited range tunable filter on the Port 2 additional science bench. The following information relates to the UBF in its standard configuration.

The specified tunable range of the UBF is from 4000 to 7000 Angstroms. The suggested operating range of the UBF is 4900 to 6700 Angstroms.

Field of View:

Port 4 primary/secondary science bench: 169 x 169 arcsec for intensity or velocity mode. Port 2 secondary science bench: 180 x 180 arcsec for intensity or velocity mode. Port 2 UBF wavelength range is limited to 4500 - 6000 Angstrom. Modes of UBF Operation Intensity Mode: direct imaging with wavelength scanning (direct filtergrams). Magnetic Field Mode: imaging of opposite circular polarizations (Zeeman Splitting). Velocity Mode: imaging of red and blue shifted transmission profiles (Doppler Effect).

Magnetic Field Mode:

a. Magnetic Field Mode - Simultaneous Imaging:

To study magnetic fields, the filter is tuned to the wing of a Fraunhofer line which exhibits a strong Zeeman splitting. A Wollaston prism positioned in front of the UBF forms two images in opposite circular polarization. It is essential that these two images be generated before the filter since the filter itself destroys the polarization properties of the incident image caused by the Zeeman effect. If the Zeeman splitting is zero, the difference in intensity between the two images will be zero. If the Zeeman splitting is not equal to zero there will be an intensity difference. This difference is proportional to the Zeeman splitting and therefore to the magnetic field strength.

b. Magnetic Field Mode - synchronized Non-simultaneous Imaging:

This magnetic field mode is the application most commonly used at the DST. A Wollaston prism is not used in this process. Images of opposite circular polarization are registered in a timed sequence with the average lapse time between the exposure end of the first state and the exposure beginning of the second state being approximately 1500 milliseconds. This mode utilizes a linear polarizer positioned directly in front of the UBF and a (quarter) wave plate positioned upstream of the polarizer. Image "sets" consist of sequential exposures taken at two quarter wave plate positions (+/-45.0 of the entrance polarizer axis).

2.4 Instruments used for Coronal Observations

The coronal intensity images are also used in two Chapters (7 and 8) of the Thesis. The X-ray images are taken from X-ray Telescope (XRT: Golub et al. (2007); Kano et al. (2008)) aboard Hindoe (Kosugi et al., 2007). The coronal images in other wavelengths are taken from Extreme Ultra-Violet Imaging Telescope (EIT:

Table 2.5: As-built XRT performance parameters

Parameter	Requirement	As-built
Optical design	Single mirror pair	Generalized asphere
Wavelength range	$6 - 60$ Å	Bare zerodur
Entrance diameter	341.7 ± 0.1 mm	341.7 mm
Focal length	2708 ± 2 mm	2707.5 mm
Focus knowledge	$\pm$ 0.050 mm	$\pm$ 1.4 mm
Field of view	35 arcmin	Optimized over 15 arcmin
Encircled energy	68% at 0.5 keV	68% at 0.56 keV
diameter	1.57 arcsec	2.3 arcsec
Effective area	1.0 cm^2	1.9 cm^2

Delaboudinière et al. (1995); Defise et al. (1995)) aboard SOHO (Bonnet and Felici, 1997). A brief information of these instruments are give below:

2.4.1 X-Ray Telescope (XRT-Hinode)

The X-ray Telescope (XRT) aboard Hinode is the highest resolution solar X-ray Telescope that has been ever flown till date. The scientific objectives of the XRT are: 1. to understand the trigger mechanism of CMEs, 2. relation of CMEs to magnetic field structures, 3. dynamics of fine structures, 4. to infer the cause of coronal heating (whether is due to loop-loop interaction?), 5. to understand flare energetics, 6. photospheric-coronal coupling etc.

The XRT utilizes both entrance aperture pre-filters and focal plane analysis filters. The visible-light-blocking requirement for the XRT is 10-12, which translates into a requirement for the pre-filter and analysis filters of 10-6 each.

As-built XRT performance parameters are given in Table 2.5.

More details of XRT instrumentation are available in Golub et al. (2007).

2.4.2 Extreme Ultraviolet Imaging Telescope (EIT-SOHO)

The Extreme Ultraviolet Imaging Telescope (EIT) is operating on-board the Solar and Heliospheric Observatory (SOHO) spacecraft since January 1996. EIT provides EUV intensity images of corona in four narrow channels: 171 (Fe IX and Fe X), 195 (Fe XII), 284 and 304 Å.

At the focal plane of the telescope, a 1024 x 1024 pixel CCD detects the solar radiation. This detector was specially processed for EUV sensitivity enhancement. Each collecting element has a 2.6 x 2.6 arcsec viewing angle over the solar corona observed from the SOHO spacecraft. The instrument underwent a ground-based calibration program that provided a complete calibration of the system (Defise et al., 1995), in order to fulfill all the scientific objectives of the instrument. Since the first months of operations, that started in early 1996, the instrument has been operating nominally.

The Extreme Ultraviolet Imaging Telescope (EIT) provides the best images of the coronal layers of the Sun. Such pictures are obtained regularly in the four bands covered by EIT which span temperatures ranging from 80 000 IS to 2 million K. They allow a continuous observation and the most detailed view of the coronal magnetic field structures.

We are thankful to the scientific teams of all the above instruments and wish to acknowledge their support for providing the data for the present study.

Chapter 3

Effect of Polarimetric Noise on the Estimation of Twist and Magnetic Energy of Force-Free Fields

3.1 Introduction

In this chapter, we estimate the error in the calculation of field strength, inclination and azimuth and thereafter in the calculation of the vector field components B_x, B_y and B_z. Then we estimate the error in the determination of global α parameter due to noise in polarimetric profiles constructed from the analytical vector field data. We have also estimated the error in the calculation of magnetic energy derived using virial theorem, due to polarimetric noise.

The physical meaning of the force free parameter α has been clarified in Sec-

tion 3.2. The relation of α to magnetic helicity has been explained in Section 3.3. We then discuss a direct method for calculation of a single global α for an active region in Section 3.4. An analytical bipole has been generated for this study, so that all the input magnetic parameters are known and the methodology can be validated. We describe the method of simulating an analytical bipole field in the Section 3.5. Section 3.6 contains the analysis and the results. Error estimation in global α is given in section 3.7. In section 3.8, we discuss the process of estimating the error in the virial magnetic energy. Section 3.9 deals with discussion and conclusions.

As described in Chapter 1, the magnetic helicity H_m is given by a volume integral over the scalar product of the magnetic field **B** and its vector potential **A** (Elsasser, 1956).

$$H_m = \int_V \mathbf{A} \cdot \mathbf{B} \, dV \tag{3.1}$$

with $\mathbf{B} = \nabla \times \mathbf{A}$.

It is well known that the vector potential **A** is not unique, thereby preventing the calculation of a unique value for the magnetic helicity from the Equation 3.1. Seehafer (1990) pointed out that the helicity of magnetic field can best be characterized by the force-free parameter α, also known as the helicity parameter or twist parameter. The force-free condition (Chandrasekhar, 1961; Parker, 1979) is given as,

$$\nabla \times \mathbf{B} = \alpha \mathbf{B} \tag{3.2}$$

Alpha is a measure of degree of twist per unit axial length (see Section 3.2). This is a local parameter which can vary across the field but is constant along the field lines. The physical meaning of α will be explained in the next section.

Researchers have claimed to have determined the sign of magnetic helicity on the photosphere by calculating alpha, e.g. α_{best} (Pevtsov et al., 1995), averaged

alpha e.g. $< \alpha_z > = < J_z/B_z >$ (Pevtsov et al., 1994) with current density $J_z = (\nabla \times B)_z$. Some authors have used current helicity density $H_c = B_z \cdot J_z$ and α_{av} (Bao and Zhang, 1998; Hagino and Sakurai, 2004, 2005). A good correlation was found between α_{best} and $\langle \alpha_z \rangle$ by Burnette et al. (2004) and Leka et al. (1996). But the sign of magnetic helicity cannot be inferred from the force-free parameter α under all conditions as we have described in Section 3.3.

It is well known that the reliable measurements of vector magnetic fields are needed to study various important parameters like electric currents in the active regions, magnetic energy dissipation during flares, field geometry of sunspots, magnetic twist etc. The study of error propagation from polarization measurements to the calculation of vector field parameters is very important (Lites and Skumanich, 1985; Klimchuk et al., 1992). Klimchuk et al. (1992) have studied the effects of realistic errors e.g., due to random polarization noise, crosstalk between different polarization signals, systematic polarization bias and seeing induced crosstalk etc. on known magnetic fields. They derived analytical expressions for how these errors produce errors in the estimation of magnetic energy (calculated from virial theorem). However, they simulated these effects for magnetographs which sample polarization at few fixed wavelength positions in line wings. It is well known that such observations lead to systematic under-estimation of field strength and also suffer from magneto-optical effects (West and Hagyard, 1983). Whereas in our analysis, we simulate the effect of polarimetric noise on field parameters as deduced by full Stokes inversion. The details are discussed in the section 3.8.

Pevtsov et al. (1995) found large variations in the global α values from repeated observations of the same active regions. It is important to model the measurement uncertainties before looking for physical explanations for such a

scatter.

In a study by Hagyard and Pevtsov (1999), the noise levels in the observed fields were analyzed, but a quantitative relationship between the uncertainties in fields and the uncertainties in global α value were not established. They could only determine the extent to which the incremental introduction of noise affects the observed value of α. However, for the proper tracking of error propagation, we need to start with ideal data devoid of noise and with known values of α and magnetic energy. We follow the latter approach in our present analysis.

Here, we estimate the accuracy in the calculation of the α parameter and the magnetic energy due to different noise levels in the spectro-polarimetric profiles. Modern instruments measure the full Stokes polarization parameters within the line profile. Basically there are two types of spectro-polarimeters : (i) Spectrograph based e.g., Advanced Stokes Polarimeter (ASP : Elmore et al. (1992)), Zurich Imaging Polarimeter (ZIMPOL : Keller et al. (1992); Povel (1995); Stenflo (1996); Stenflo and Keller (1997)), THEMIS-MTR (Arnaud et al. (1998)), SOLIS - Vector Spectro-Magnetograph (VSM : Jones et al. (2002); Keller et al. (2003)), Polarimetric Littrow Spectrograph (POLIS : Schmidt et al. (2003)), Diffraction Limited Spectro-polarimeter (DLSP : Sankarasubramanian et al. (2004, 2006)), Hinode (SOT/SP : Tsuneta et al. (2008)), etc. and (ii) Filter-based e.g., Imaging Vector Magnetograph (IVM) at Mees Solar Observatory, Hawaii (Mickey et al., 1996), Solar Vector Magnetograph at Udaipur Solar Observatory (SVM-USO)(Gosain et al., 2004, 2006) etc.

Earlier magnetographs like Crimea (Stepanov and Severny, 1962), MSFC (Hagyard et al., 1982), HSP (Mickey, 1985), OAO (Makita et al., 1985), HSOS (Ai and Hu, 1986), Potsdam vector magnetograph (Staude et al., 1991), SFT (Sakurai et al., 1995) etc. were mostly based on polarization measurements at

a few wavelength positions in the line wings and hence subject to Zeeman saturation effects as well as magneto-optical effects like Faraday rotation (West and Hagyard, 1983; Hagyard et al., 2000).

The magnetic field vector deduced from Stokes profiles by modern techniques are almost free from such effects (Skumanich and Lites, 1987; S'anchez Almeida, 1998; Socas-Navarro, 2001).

3.2 Physical Meaning of Force-Free Parameter α

Taking surface integral on both sides of Equation 3.2, we get

$$\begin{aligned} \alpha \int \mathbf{dS} \cdot \mathbf{B} &= \int \mathbf{dS} \cdot \nabla \times \mathbf{B} \\ &= \oint \mathbf{dl} \cdot \mathbf{B} \quad (from\ Stokes\ theorem) \end{aligned} \tag{3.3}$$

$$or,$$

$$\alpha = \frac{\oint \mathbf{dl} \cdot \mathbf{B}}{\Phi} \tag{3.4}$$

where $\Phi = \int \mathbf{dS} \cdot \mathbf{B}$ is the magnetic flux.

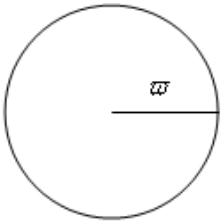

Figure 3.1: A cross-section of cylindrical flux tube with ϖ as its radius.

In the cylindrical coordinate we can write Equation 3.3 as

$$\alpha = \frac{2\pi\varpi B_\phi}{\pi\varpi^2 B_z}$$

$$= \frac{2B_\phi}{\varpi B_z} \tag{3.5}$$

where z and ϖ are axial and radial distances from origin, respectively The equation of field lines in cylindrical coordinates is given as :

$$\frac{B_z}{dz} = \frac{B_\phi}{\varpi d\phi} \tag{3.6}$$

or,

$$\frac{B_\phi}{B_z} = \frac{\varpi d\phi}{dz} \tag{3.7}$$

Using Equations 3.5 & 3.7, we get

$$\alpha = 2\,\frac{d\phi}{dz} \tag{3.8}$$

From Equation 3.8, it is clear that the α gives twice the degree of twist per unit axial length. If we take one complete rotation of flux tube i.e., $\phi = 2\pi$, and loop length $\lambda \approx 10^9$ meters, then

$$\alpha = \frac{2 \times 2\pi}{\lambda} \tag{3.9}$$

comes out of the order of approximately 10^{-8} per meter.

3.3 Correlation Between Sign of Magnetic Helicity and that of α

Equation 3.2 can be written as

$$\begin{aligned} \nabla \times \mathbf{B} &= \alpha(\nabla \times \mathbf{A}) \\ &= \nabla \times (\alpha \mathbf{A}) \end{aligned} \tag{3.10}$$

giving vector potential in terms of scalar potential ϕ as

$$\mathbf{A} = \mathbf{B}\alpha^{-\mathbf{1}} + \nabla\phi \tag{3.11}$$

which is valid only for constant α.

Using this relation in Equation 3.1, we get magnetic helicity as

$$\begin{aligned} H_m &= \int (\mathbf{B}\alpha^{-1} + \nabla\phi) \cdot \mathbf{B}\ dV \\ &= \int B^2\alpha^{-1} dV + \int (\mathbf{B}\cdot\nabla)\phi\ dV \end{aligned} \tag{3.12}$$

We know the following vector identity

$$\nabla \cdot (\phi\mathbf{B}) = \phi(\nabla\cdot\mathbf{B}) + (\mathbf{B}\cdot\nabla)\phi \tag{3.13}$$

where 1^{st} term in right hand side (RHS) is zero. Second term in the right hand side of Equation 3.12 can be written as,

$$\begin{aligned} \int (\mathbf{B}\cdot\nabla)\phi\ dV &= \int \nabla\cdot(\phi\mathbf{B})\ dV \\ &= \int (\phi\ \mathbf{B})\cdot\mathbf{n}\ dS \end{aligned} \tag{3.14}$$

(from Gauss Divergence Theorem) which is equal to zero for a closed volume where magnetic field does not cross the volume boundary ($\mathbf{n}\cdot\mathbf{B} = \mathbf{0}$) provided that ϕ remains finite on the surface. Therefore, we get magnetic helicity in terms of α as

$$H_m = \int B^2\alpha^{-1}\ dV \tag{3.15}$$

which shows that the force free parameter α has the same sign as that of the magnetic helicity. However, if $\mathbf{n}\cdot\mathbf{B} \neq \mathbf{0}$, then the contribution of the second term in Equation 3.12 remains unspecified since ϕ can be any arbitrary scalar function. Thus it is not correct to use α to determine the sign of magnetic helicity for the half space above the photosphere since $\mathbf{n}\cdot\mathbf{B} \neq \mathbf{0}$ at the photosphere.

3.4 A Direct Method for Calculation of Global α

Taking the z-component of magnetic field, from the force-free field Equation 3.2, α can be written as,

$$\alpha = \frac{(\nabla \times \mathbf{B})_\mathbf{z}}{B_z} \tag{3.16}$$

For a least squares minimization, we should have

$$\begin{aligned} \sum(\alpha - \alpha_g)^2 &= minimum \\ or, \qquad \alpha_g &= (1/N)\sum \alpha \end{aligned} \tag{3.17}$$

where α is the local value at each pixel, α_g is the global value of α for the complete active region and N is total number of pixels.
Since Equation 3.17 will lead to singularities at the neutral lines where B_z approaches 0, therefore the next moment of minimization,

$$\sum(\alpha - \alpha_g)^2 B_z^2 = minimum \tag{3.18}$$

should be used. From Equation 3.18, we have

$$\frac{\partial}{\partial \alpha_g}(\sum(\alpha - \alpha_g)^2 B_z^2) = 0 \tag{3.19}$$

which leads to the following result,

$$\alpha_g = \frac{\sum(\frac{\partial B_y}{\partial x} - \frac{\partial B_x}{\partial y})B_z}{\sum B_z^2} \tag{3.20}$$

This formula gives a single global value of α in a sunspot and is the same as $\alpha_{av}^{(2)}$ of Hagino and Sakurai (2004). We prefer this direct way of obtaining global α which is different from the method discussed in Pevtsov et al. (1995) for determining α_{best}. The main advantages are: (1). the singularities at neutral line are

automatically avoided in our method by using the second moment of minimization and (2). the computation of constant α force-free fields for different test values of α is not required. Hagino and Sakurai (2004) used a different parameter $\alpha_{av}^{(1)}$ to avoid the effect of Faraday rotation in sunspot umbrae. However, modern inversion techniques using complete Stokes profiles are free of this problem.

It must be noted that one can generate different values of α_g using higher moments of minimization, e.g., by weighting J_z with B_z^n, with n=3, 5, 7, ... etc. The higher moments will be more sensitive to spatial variation of B_z. Such large and complex variation of B_z is found generally in flare productive active regions (Ambastha et al., 1993; Wang et al., 1996; Hagyard et al., 1999). Thus we can try to use higher order α_g as a global index for predicting the flare productivity in active regions.

Finally, to compute α_g we need all the three components of magnetic field which is obtained from the measurements of vector magnetograms. Here we use the analytically generated bipole, as discussed in the following section, with known values of all the magnetic parameters to investigate the effect of polarimetric noise.

3.5 Generation of Theoretical Bipole

We use the analytic, non-potential force-free fields of the form derived by Low (1982). These fields describe an isolated bipolar magnetic region which is obtained by introducing currents into a potential field structure. This potential field is produced by an infinite straight line current running along the intersection of the planes y = 0 and z = -a, where negative sign denotes planes below the photosphere

z = 0. At the photosphere (z = 0), the field has the following form :

$$B_x = -\frac{B_0 a}{r}\cos\phi(r) \tag{3.21}$$

$$B_y = \frac{B_0 axy}{r(y^2+a^2)}\cos\phi(r) - \frac{B_0 a^2}{(y^2+a^2)}\sin\phi(r) \tag{3.22}$$

$$B_z = \frac{B_0 a^2 x}{r(y^2+a^2)}\cos\phi(r) - \frac{B_0 ay}{(y^2+a^2)}\sin\phi(r) \tag{3.23}$$

where B_0 is the magnitude of the field at origin and $r^2 = x^2 + y^2 + a^2$. The function $\phi(r)$ is a free generating function related to the force-free parameter α (see Equation 3.2) by

$$\alpha = -\frac{d\phi}{dr} \tag{3.24}$$

which determines the current structure and hence the amount and location of shear present in the region. By choosing $\phi(r) = constant = \pi/2$ we can obtain a simple potential (current-free, $\alpha = 0$) field produced by the infinite line current lying outside the domain. Steeper gradient of $\phi(r)$ results in a more sheared (non-potential) field.

In Equation 3.24, the sign on the right hand side is taken positive in the paper by Low (1982) which is a typing mistake (confirmed by B. C. Low, 2008, private communication). We mention this here to avoid carrying forward of this typo as was done in Wilkinson et al. (1989).

A grid of 100 x 100 pixels was selected for calculating the field components. The magnitude of field strength at the origin has been taken as 1000G and the value of 'a' is taken as 15 pixels (below the photosphere, z = 0).

The simulated field components with corresponding contours are shown in the Figure 3.2.

Here we use the following function (e.g., Wilkinson et al., 1989) for the generation of the field components (B_x, B_y, B_z):

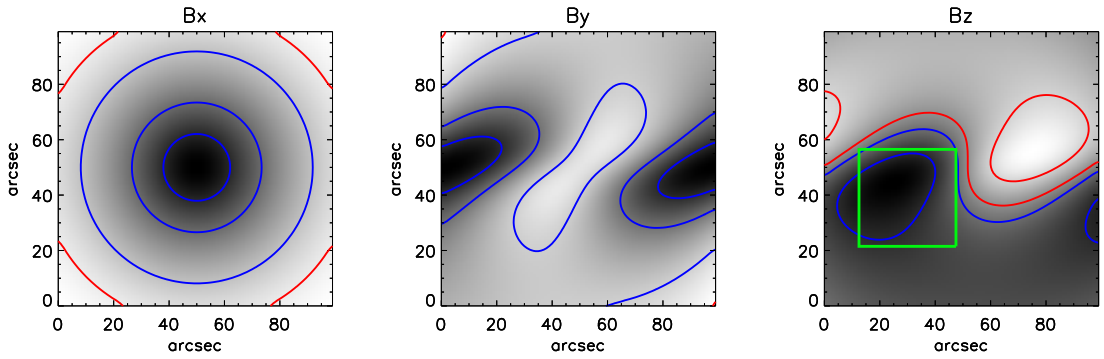

Figure 3.2: Contours of the field components overlaid on their gray-scale images. The contour levels are 100, 500 and 800 G of magnetic fields. The red and blue contours denote the 'positive' and 'negative' polarities, respectively. The green box in B_z shows the area which is selected for the calculation of global α. For details see the text.

$$\phi(r) = \frac{\pi}{2}\frac{r-a}{2a}, \quad r \leq 3a \tag{3.25}$$

$$= \frac{\pi}{2}, \quad r > 3a \tag{3.26}$$

Results for the fields generated by different $\phi(r)$ are quantitatively similar. In this way we generate a set of vector fields with known values of α.

Most of the time one of the bipoles of a sunspot observed on the Sun is compact (leading) and the other (following) is comparatively diffuse. Observations of the compact pole gives half of the total flux of the sunspot and is mostly used for the analysis. One can derive the twist present in the sunspot using one compact pole of the bipolar sunspot for constant α. Thus we have selected a single polarity of the analytical bipole as shown in Figure 3.2 to calculate the twist.

Fine structure in real sunspots is difficult to model. Our present analysis applies to the large scale patterns of the magnetic field regardless of fine structure. However, we address the fine structures in real sunspots in the next Chapter.

All the following Sections in this Chapter discuss the analysis and results obtained.

3.6 Profile Generation from the Analytical Data and Inversion

Using the analytical bipole method (Low, 1982), the non-potential force-free field components B_x, B_y & B_z in a plane have been generated and are given as in Equations 3.21, 3.22 & 3.23. We have shown B_x, B_y, & B_z maps (generated on a grid of 100 x 100 pixels) in Figure 3.2. From these components, we have derived magnetic field strength (B), inclination (γ) and azimuth (ξ : free from 180^o ambiguity). In order to simulate the effect of typical polarimetric noise in actual solar observations on magnetic field measurements, and to study the error in the calculation of α and magnetic energy, we have generated the synthetic Stokes profiles for each B, γ and ξ in a grid of 100 x 100 pixels, using the He-Line Information Extractor "HELIX" code (Lagg et al., 2004). This code is a Stokes inversion code based on fitting the observed Stokes profiles with synthetic ones obtained by Unno-Rachkovsky solutions (Unno, 1956; Rachkowsky, 1967) to the polarized radiative transfer equations (RTE) under the assumption of Milne-Eddington (ME) atmosphere (Landolfi and Landi Degl'Innocenti, 1982) and local thermodynamical equilibrium (LTE). However, one can also use this code for generating synthetic Stokes profiles for an input model atmosphere. The synthetic profiles are functions of magnetic field strength (B), inclination (γ), azimuth (ξ), line of sight velocity (v_{Los}), Doppler width (v_{Dopp}), damping constant (Γ), ratio of the center to continuum opacity (η_0), slope of the source function (S_{grad}) and the source function (S_0) at $\tau = 0$. The filling factor is taken as unity. In

our profile synthesis only magnetic field parameters B, γ, ξ are varied while other model parameters are kept same for all pixels. The typical values of other thermodynamical parameters are given in Table 3.1.

Table 3.1: Model parameters for generating synthetic profile

Model Parameter	Value
Doppler velocity, v_{Los} (ms^{-1})	0
Doppler width, v_{Dopp} (mÅ)	20
Ratio of center to continuum opacity, η_o	20
Source function, S_o	0.001
Slope of the source function, S_{grad}	1.0
Damping constant, Γ	1.4

We use the same parameters for all pixels. Further, all the physical parameters at each pixel are taken to be constant in the line forming region. However, one must remember that real solar observations have often Stokes V area asymmetries (Solanki, 1989; Khomenko et al., 2005) as a result of vertical magnetic and velocity field gradients present in the line forming region. This has not been taken into account in our simulations.

A set of Stokes profiles with 0.5% and 2.0% noise for a pixel is shown in Figure 3.3.

The wavelength grid used for generating synthetic spectral profiles is same as that of *Hinode* (SOT/SP) data, which are as follows: start wavelength of 6300.89 Å, spectral sampling 21.5 mÅ/pixel, and 112 spectral samples. We add normally distributed random noise of different levels in the synthetic Stokes profiles. Typical noise levels in Stokes profiles obtained by Hinode (SOT/SP) normal mode scan are of the order of 10^{-3} of the continuum intensity, I_c (Ichimoto et al., 2008). We add random noise of 0.5 % of the continuum intensity I_c to the polarimetric

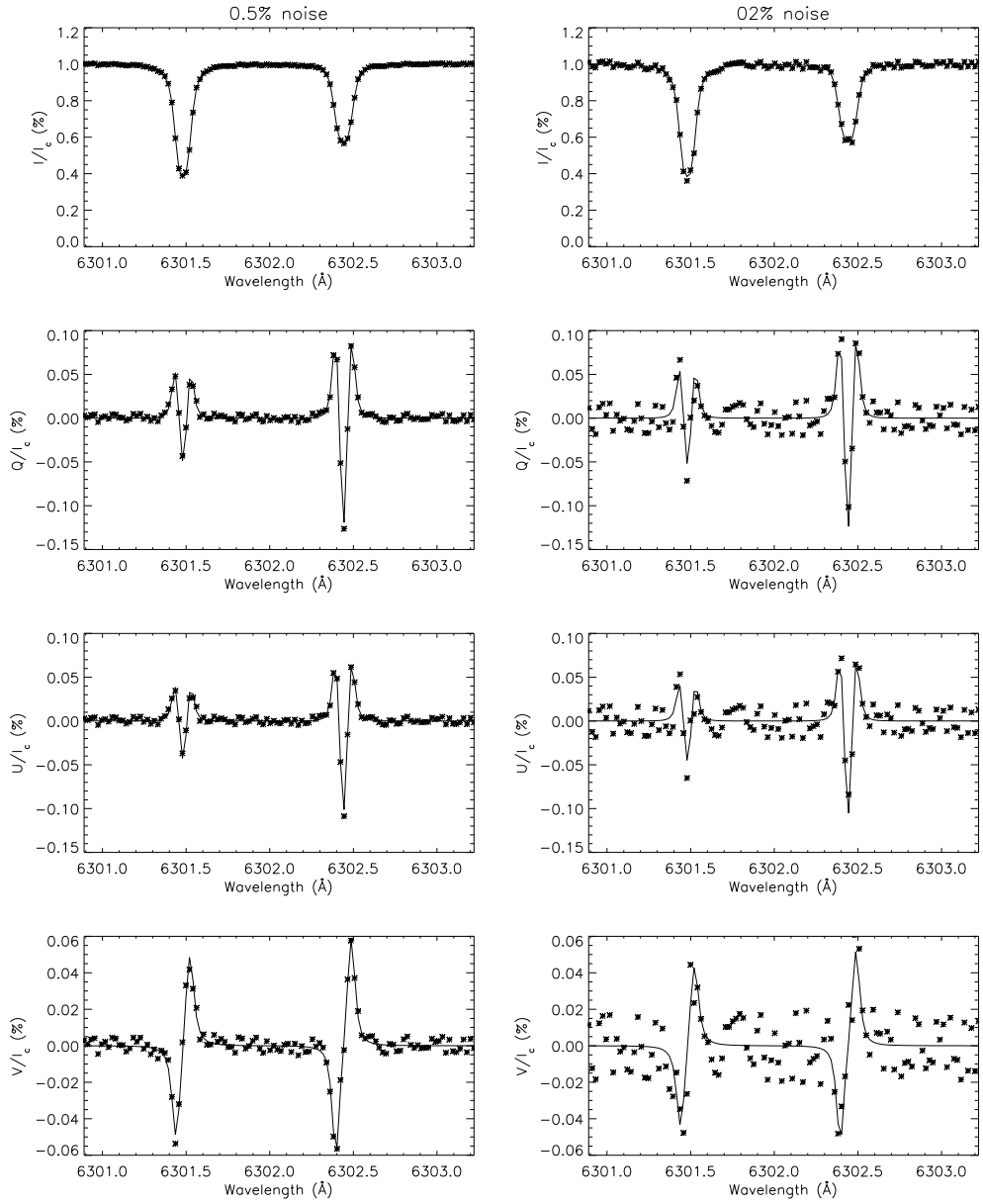

Figure 3.3: Example of Stokes profiles with 0.5% (left column) and 2.0% (right column) noise along with the fitted profiles. The input parameters for the associated pixel are as follows : field strength= 861 G, inclination=101°, azimuth=19°. The corresponding output parameters are 850 G, 101°, 19° for 0.5% noise and 874 G, 99°, 19° for 2.0% noise.

profiles. In addition, we also study the effect of adding a noise of 2.0% level to Stokes profiles as a worst case scenario. We add 100 realizations of the noise of the orders mentioned above to each pixel and invert the corresponding 100 noisy profiles using the "HELIX" code.

The guess parameters to initialize the inversion are generated by perturbing known values of B, γ and ξ by 10%. Thus after inverting 100 times we get 100 sets of B, γ & ξ maps for the input B, γ & ξ values from bipole data. In this way we estimate the spread in the derived field values for various field strengths, inclinations etc. First, the inversion is done without adding any noise in the profiles to check the accuracy of inversion process. We get the results retrieved in this process which are very similar to that of the initial analytical ones. The scatter plot of input field strength, inclination, azimuth against the corresponding retrieved strength, inclination, azimuth after noise addition and inversion is shown in Figure 3.4 (upper panel). Typical B_x, B_y & B_z maps with different noise levels are shown in the lower panel. As the noise increases B_x, B_y & B_z maps become more grainy.

From the plots shown in Figure 3.4, we can see that the error in the field strength for a given noise level decreases for strong fields. This is similar to the results of Venkatakrishnan and Gary (1989). As the noise increases in the profiles, error in deriving the field strength increases. We find that the error in the field strength determination is $\sim$ 15% for 0.5% noise and $\sim$ 25% for 2% noise in the profiles. Inclination shows more noise near 0° & 180° than at $\sim$ 90°. The error is less even for large noisy profiles for the inclination angles between $\sim$ 50°-130°. The reason for this may be understood in the following way. Linear polarization is weaker near 0 and 180° inclinations and is therefore more affected by the noise. The azimuth determination has inherent 180°ambiguity due to insensitivity of

Zeeman effect to orientation of transverse fields. Thus in order to compare the input and output azimuths we resolve this ambiguity in ξ_{out} by comparing it with ξ_{in} i.e., the value of ξ_{out} which makes acute angle with ξ_{in} has been taken as correct. We can see azimuth values after resolving the ambiguity in this way show good correlation with input azimuth values. Some scatter is due to the points where ambiguity was not resolved due to 90° difference in ξ_{in} and ξ_{out}.

First, the α_g was calculated from the vector field components derived from the noise free profiles to verify the method of calculating global alpha and also the inversion process. We have used the single polarity to calculate global alpha present in sunspot as discussed in Section 3.5. We retrieved the same value of α_g as calculated using the initial analytical field components.

From the Figure 3.5, we can see that the effect of noise on the field components is not much for the case of 0.5% noise but as the noise in the profiles is increased to 2.0%, the field components, specially transverse fields, show more uncertainty. The vertical field is comparatively less affected with noise. The scatter plot in Figure 3.5 shows that the inversion gives good correlation to the actual field values. The points with large scatter are due to poor "signal to noise" ratio in the simulated profiles. The mean percentage error in the further discussions is given in terms of weighted average of error.

3.7 Estimation of the Error in the Calculation of Global Alpha (α_g)

We calculate the percentage error in global alpha each time after getting the inverted results, for both the cases when 0.5% and 2.0% (of I_c) noise is added in the profiles, by the following relation:

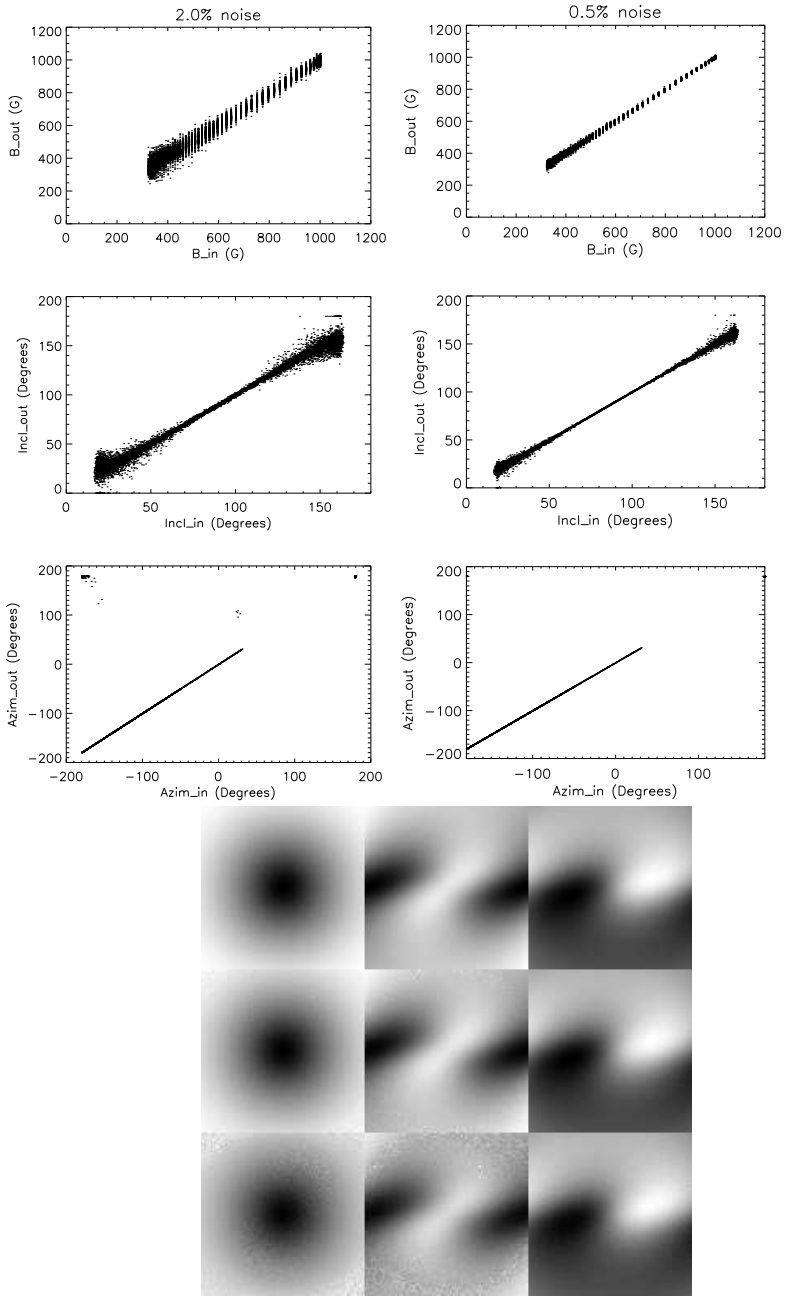

Figure 3.4: Scatter plot (upper panel) between the field strength, inclination and azimuth before and after the inversion with 0.5% (1^{st} column) and 2.0% (2^{nd} column) noises in the profiles. The lower panel shows the images of vector fields B_x, B_y & B_z before (1^{st} row) and after inversion with 0.5% (2^{nd} row) and 2% (3^{rd} row) noise in the profiles.

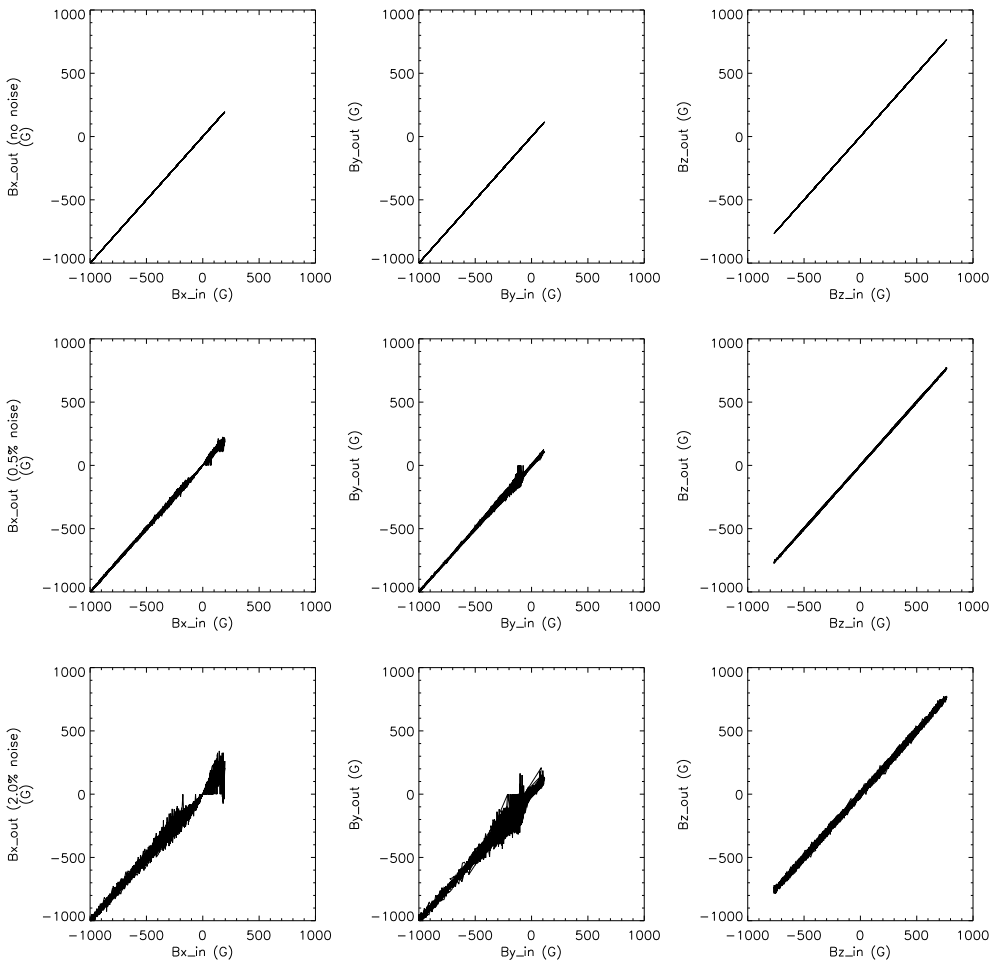

Figure 3.5: Scatter plot between B_x, B_y & B_z before and after inversion without noise (1^{st} row) and with noise added in the profiles: 2^{nd} row with 0.5% noise and 3^{rd} row with 2.0% noise (of I_c) in the polarimetric profiles.

$$\frac{\triangle \alpha_g}{\alpha_g}(\%) = \frac{\alpha_g^* - \alpha_g}{\alpha_g} \times 100 \tag{3.27}$$

where α_g^* is calculated global alpha and α_g is the analytical global alpha.

The histogram of the results obtained is shown in Figure 3.6.

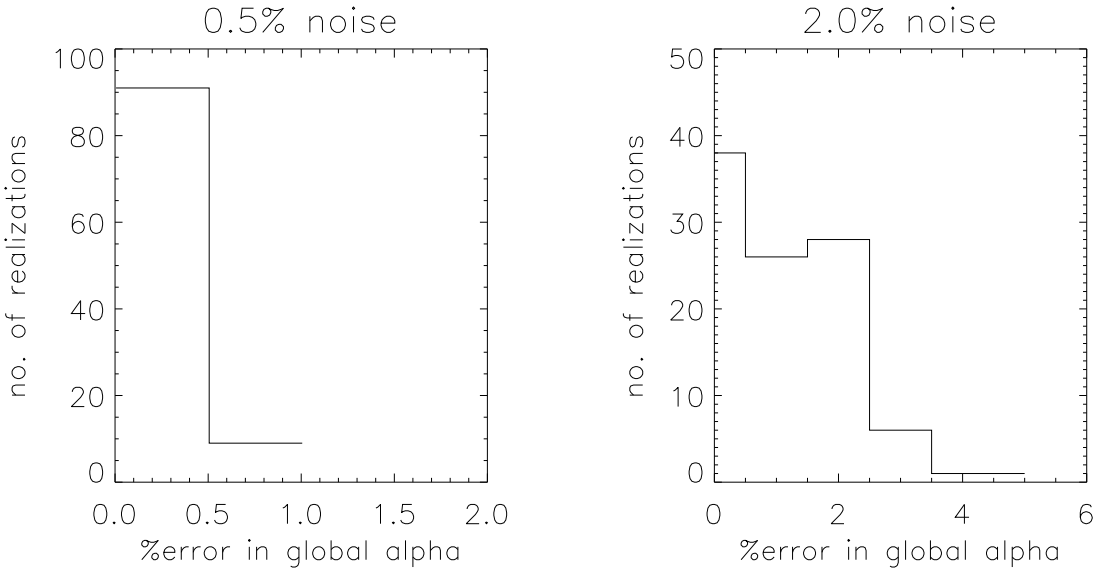

Figure 3.6: Histogram of the percentage error in the calculation of α_g with 0.5% and 2.0% noise (of I_c) in polarimetric profiles, respectively.

First, we inverted the profiles without adding any noise and calculated α_g from retrieved results to compare it with the 'true' α_g calculated from the analytically generated vector field components. We get less than 0.002% difference in the both α_g values.

For the case of 0.5% noise in polarimetric profiles we get a mean error of 0.3% in the calculation of α_g and error is never more than 1%. Thus the calculation of α_g is almost free from the effect of noise in this case. Hence, by using data from *Hinode* (SOT/SP), one can derive the accurate value of twist present in a sunspot.

If 2.0% noise is present in the polarization, then maximum $\sim$ 5% error is obtained. Weighted average shows only 1% error. Thus the estimation of alpha is not influenced very much even from the data obtained with old and ground based magnetographs. In any event it is unlikely that a realistic error will be large enough to create a change in the sign of α_g.

3.8 Estimation of the Error in the Calculation of Magnetic Energy ($\mathbf{E}_m$)

The magnetic energy has been calculated using virial theorem. One form of the general virial theorem (Chandrasekhar, 1961) states that for a force-free magnetic field, the magnetic energy contained in a volume V is given by a surface integral over the boundary surface S,

$$\int \frac{1}{8\pi} B^2 dV = \frac{1}{4\pi} \int [\frac{1}{2} B^2 \mathbf{r} - (\mathbf{B} \cdot \mathbf{r})\mathbf{B}] \cdot \hat{\mathbf{n}} \;\; dS \tag{3.28}$$

where $\mathbf{r}$ is the position vector relative to an arbitrary origin, and $\hat{n}$ is the normal vector at surface. Let us adopt Cartesian coordinates, taking as z=0 plane for photosphere. This assumption is reasonable because the size of sunspots are very small compared to the radius of the Sun. If we make the further reasonable assumption that the magnetic field strength decreases with distance more rapidly than $r^{-3/2}$ whereas a point dipole field falls off as r^{-3}, then the Equation 3.28 can be simplified to Molodensky (1974)

$$\int \frac{1}{8\pi} B^2 \; dxdydz = \frac{1}{4\pi} \int (xB_x + yB_y) B_z \; dxdy \tag{3.29}$$

where x and y are the horizontal spatial coordinates. B_x, B_y & B_z are the vector magnetic field components. This Equation 3.29 is referred as the "magnetic virial theorem".

Thus magnetic energy of an active region can be calculated simply by substituting the derived vector field components into the surface integral of Equation 3.29 (Low, 1982, 1985, 1989). Magnetic field should be solenoidal and force-free as is the case for our analytical field. So the energy integral is independent of choice of the origin.

If all the above conditions are satisfied then the remaining source of uncertainty in the magnetic energy estimation is the errors in the vector field measurements themselves. So, before the virial theorem can be meaningfully applied to the Sun, it is necessary first to understand how the errors in the vector field measurements produce errors in the calculated magnetic energies.

Earlier, the efforts were made to estimate the errors (Gary et al., 1987; Klimchuk et al., 1992) for magnetographs like Marshall Space Flight Center (MSFC) magnetograph. Gary et al. (1987) constructed a potential field from MSFC data and computed its virial magnetic energy. Then, they modified the vector field components by introducing random errors in B_x, B_y and B_z and recomputed the energy. They found the two energies differ by 11%. Klimchuk et al. (1992) approached the problem differently. They introduced errors in the polarization measurements from which the field is derived instead of introducing errors to magnetic fields directly. In this way they were able to approximate reality, more closely and were able to include certain type of errors such as crosstalk which were beyond the scope of the treatment by Gary et al. (1987). They found that the energy uncertainties are likely to exceed 20% for the observations made with the vector magnetographs present at that time (e.g., MSFC).

Here, our approach is very similar to that of Klimchuk et al. (1992) except that we consider full Stokes profile measurements to derive the magnetic fields like in the most of the recent vector magnetographs e.g., *Hinode* (SOT/SP), SVM-

USO etc. as mentioned earlier. We begin with an analytical field, determine polarization signal as explained in earlier parts, introduce the random noise of certain known levels (0.5% & 2.0% of I_c) in the polarization profiles, infer an 'observed' magnetic field after doing the inversion of the noisy profiles, compute an 'observed' magnetic energy from the 'observed' field and then compare this energy with the energy of the 'true' magnetic field. The percentage error is calculated from the following expression:

$$\frac{\triangle E_m}{E_m}(\%) = \frac{E_m^* - E_m}{E_m} \times 100 \tag{3.30}$$

where E_m^* is 'observed' energy and E_m is 'true' energy. All the above processes have been described in detail in Section 3.6.

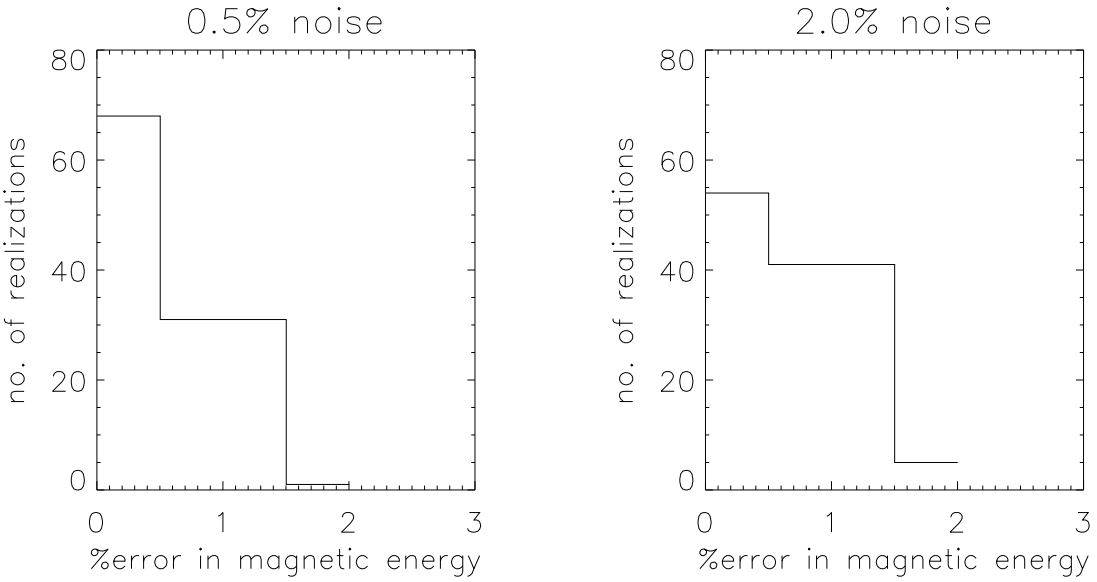

Figure 3.7: Histogram of the percentage error in the calculation of magnetic energy when 0.5% and 2.0% noise (of I_c) is present in polarimetric profiles, respectively.

Figure 3.7 shows the uncertainty estimated in the calculation of magnetic energy in two cases when error in the polarimetric profiles is 0.5% and 2.0% of

I_c. Needless to say, we first checked the procedure by calculating the magnetic energy from the vector fields derived from inverted results with no noise in the profiles. We found the same energy as calculated from the initial analytical fields.

We can see that the magnetic energy can be calculated with a very good accuracy when less noise is present in the polarization as is observed in the modern telescopes like *Hinode* (SOT/SP) for which very small (of the order of 10^{-3} of I_c) noise is expected in profiles. We find that a mean of 0.5% and maximum up to 2% error is possible in the calculation of magnetic energy with such data. So, the magnetic energy calculated from the Hinode data will be very accurate provided the force-free field condition is satisfied.

The error in the determination of magnetic energy increases for larger levels of noise. In the case of high noise in profiles (e.g. 2.0% of I_c) the energy estimation is very much vulnerable to the inaccuracies of the field values. We replaced the inverted value of the field parameters with the analytical value wherever the inverted values deviated by more than 50% of the 'true' values. We then get the result shown in the right panel. We can see that the error is very small even in this case. The mean value of error is $\sim 0.7\%$.

3.8.1 Estimate of Energy Release in Different Classes of X-ray Flares

With the simplifying assumption that all classes of soft X-ray flares have a typical duration of 16 min (Drake, 1971), we can see that the energy released in the different classes of flares will be proportional to their peak power. Since X-class flares typically release radiant energy of the order of 10^{32} ergs (Emslie et al., 2005), therefore M-class, C-class, B-class and A-class flares will release radiant energy of the order of respectively 10^{31}, 10^{30}, 10^{29} and 10^{28} ergs. These estimates

will have to be modified for individual events depending upon the duration of the event.

3.9 Discussion and Conclusions

We have discussed the direct method of estimating α_g from vector magnetograms using the 2^{nd} moment of minimization. The higher order moments also hold promise for generating an index for predicting the flare productivity in active regions.

The global value of α of an active region can be measured with a very good accuracy by calculating α_g. Accurate value of α can be obtained even if one polarity of a bipole is observed.

The magnetic energy calculation is very accurate as seen from our results. Very less error (approximately 0.5%) is seen in magnetic energy with 0.5% noise in the profiles. Thus we conclude that the magnetic energy can be estimated with very good accuracy using the data obtained from modern telescopes like *Hinode* (SOT/SP). This gives us the means to look for magnetic energy changes released in weak C-class flares which release radiant energy of the order of 10^{30} ergs (see Section 3.8.1), thereby improving the statistics.

These energy estimates are however subject to the condition that the photospheric magnetic field is force-free, a condition which is not always met with. We must then obtain the energy estimates using vector magnetograms observed at higher atmospheric layers where the magnetic field is force-free (Metcalf et al., 1995).

The 180° azimuthal ambiguity (AA) is another source of error for determining parameters like α_g and magnetic free energy in real sunspot observations. The

smaller the polarimetric noise, the smaller is the uncertainty in azimuth determination, thereby allowing us to extend the range of the acute angle method used in our analysis. On the other hand it is difficult to predict the level of uncertainty produced by AA. Influence of AA is felt more at highly sheared regions which will anyway deviate from the global alpha value. Thus, avoiding such pixels will improve determination of α_g. Magnetic energy calculation at such pixels could be done by comparing energy estimates obtained by 'flipping' the azimuths and choosing the mean of the smallest and the largest estimate of the energy. Here we assume that half the number of pixels have the true azimuth. This is the best one can do for a problem that really has no theoretical solution allowed by the Zeeman effect (but see also, Metcalf et al. (2006) and references therein). Observational techniques such as use of chromospheric chirality (López Ariste et al., 2006; Martin et al., 2008; Tiwari et al., 2008) or use of magnetograms observed from different viewing angles could perhaps resolve the AA .

Patches of both signs of alpha can be present in a single sunspot (Pevtsov et al., 1994; Hagino and Sakurai, 2004). In those cases the physical meaning of α_g becomes unclear. Efforts are needed to understand the origin of such complex variation of α in a sunspot. Real sunspots show filamentary structures. If this structure is accompanied by local variations of α, then does the global α result from correlations in the local α values? Or, are the small scale variations due to a turbulent cascade from the large scale features? The answers to these questions are beyond the scope of our present study. Modeling sunspots with such complex fine structures is a great challenge. However, we address the question of fine structure of twists in real sunspots observed from *HINODE* (SOT/SP), in the next Chapter.

For the present, we demonstrate that the global alpha of an active region can

be accurately measured without ambiguity in its sign. Furthermore, the high accuracy of magnetic energy estimation that can be obtained using data from modern instruments will improve the probability for detecting the flare related changes in the magnetic energy of active regions. The azimuth determination is also very accurate as seen by the Monte Carlo simulations, and is independent of the formal uncertainties of the inversion process.

Chapter 4

Global Twist of Sunspot Magnetic Fields Obtained from High-Resolution Vector Magnetograms

4.1 Introduction

After simulating the measurement uncertainties of the field parameters using an analytical bipole model in the last chapter, we proceed to study the vector magnetic fields of the real sunspots in this chapter.

As stated in the earlier Chapter 1, the twist patterns in the sunspots and associated features have been observed for a long time (Hale, 1925, 1927; Richardson, 1941) with a hemispheric preference of their chirality, which is independent of solar cycle. Since the 90's, the subject has been intensively revisited and the similar

behaviour of hemispheric patterns for various solar features have been reported by many researchers (Pevtsov and Longcope, 2001; Hagino and Sakurai, 2004; Bernasconi et al., 2005; Nandy, 2006; Pevtsov and Longcope, 2007, and references therein). However, this hemispheric behaviour needs further investigation due to some inconsistencies reported for different phases of a solar cycle and also for data sets obtained from different magnetographs (Hagino and Sakurai, 2005; Pevtsov et al., 2008).

For a force-free field, the global twist per unit axial length is given by the force-free parameter α (see Section 3.2 for details). Some recent studies (Tiwari et al., 2008, 2009b,c) (see also Chapter 7) have shown that the global α of an active region bears the same sign as its associated features/structures observed at chromospheric and coronal heights. The chromospheric and coronal sign of twist is inferred from the topological chirality sign of the observed features. This leads us to believe that some finite amount of the photospheric global twist exists on the scale of sunspots. However, the structures in the sunspot fields revealed by modern vector magnetographs with high spatial and spectral resolution compels us to make a careful revaluation of global α and its physical meaning.

Since the photospheric field is not force-free (Metcalf et al., 1995; Socas-Navarro, 2005), we need an alternative measure of the twist other than α. We introduce the concept of signed shear angle (SSA) for sunspot magnetic fields in this Chapter and show how the sign of the spatially averaged SSA (SASSA) is directly related to the sign of global α, irrespective of the force-free nature of the sunspot fields.

The presence of oppositely directed current densities in a single unipolar sunspot was first shown by Severnyi (1965). For a detailed investigation of local α distribution in three sunspots using 46 vector magnetograms, see Pevtsov et al.

(1994). Recently, Su et al. (2009) reported an interesting pattern of fine structures in the α distribution within one active region (AR) using Hinode data with higher resolution. We present a comprehensive study of 43 sunspots with high resolution and establish the negligible contribution of such fine structures to the global twist. For this purpose we will rely on J_z and α values.

The helicity hemispheric rule or more precisely twist hemispheric rule is claimed to be established by many researchers (Seehafer, 1990; Pevtsov et al., 1995; Abramenko et al., 1996; Bao and Zhang, 1998; Longcope et al., 1998; Hagino and Sakurai, 2005; Nandy, 2006) and has recently been a matter of some debate (Hagino and Sakurai, 2005; Pevtsov et al., 2008). A model developed by Choudhuri et al. (2004) predicts deviation from the twist hemispheric rule in the beginning of the solar cycle. However, some observers claim this deviation from the hemispheric rule may be present in different phases of different solar cycles (Pevtsov et al., 2008). We have studied forty three AR's (as shown in Table 4.1) mostly observed during the declining phase of the solar cycle 23. All but five follow the reverse twist hemispheric rule, while 5 regions follow the conventional rule.

In the following section (Section 4.2), we discuss the data sets used. We define the signed shear angle (SSA) in Section 4.3. Section 4.4 describes the analysis and results obtained. Finally in Section 4.5 we present our conclusions for this chapter.

4.2 The Data Sets Used

We have used the vector magnetograms obtained from the Solar Optical Telescope/ Spectro-polarimeter (SOT/SP: Tsuneta et al. (2008); Shimizu et al. (2008);

Suematsu et al. (2008); Ichimoto et al. (2008)) onboard Hinode Kosugi et al. (2007) and the Advanced Stokes Polarimeter (ASP; Elmore et al. (1992)) as well as the Diffraction Limited Spectro-polarimeter (DLSP; Sankarasubramanian et al. (2004, 2006)) of the Dunn Solar Telescope (DST). Standard and well-established calibration procedure was adopted for ASP/DLSP data. The procedure for obtaining the vector fields from the ASP/DLSP data are described elsewhere (Elmore et al., 1992; Sankarasubramanian et al., 2004, 2006).

The *Hinode* (SOT/SP) data have been calibrated by the standard "sp_prep" routine available in the Solar-Soft packages. The prepared polarization spectra have been inverted to obtain vector magnetic field components using an Unno-Rachkowsky (Unno, 1956; Rachkowsky, 1967) inversion under the assumption of Milne-Eddington (ME) atmosphere (Landolfi and Landi Degl'Innocenti, 1982; Skumanich and Lites, 1987). We have used the inversion code "Strokesfit.pro" which has been kindly, made available by late Prof. T. R. Metcalf as a part of Solar-Soft package. We have used the newest version of this code which returns true field strengths along with the filling factor. The 180° azimuthal ambiguity in the data sets are removed by using acute angle method (Harvey, 1969; Sakurai et al., 1985; Cuperman et al., 1992). All the data sets used, have high spatial sampling. For example ASP $\sim$ 0.3 arcsec/pix, DLSP $\sim$ 0.1 arcsec/pixel and *Hinode* (SOT/SP) $\sim$ 0.3 arcsec/pixel. However, a few observations are seeing limited to about an arcsec.

To minimize noise, pixels having transverse (B_t) and longitudinal magnetic field (B_z) greater than a certain level are only analyzed. A quiet Sun region is selected for each sunspot and 1σ deviation in the three vector field components B_x, B_y and B_z are evaluated separately. The resultant deviations in B_x and B_y is then taken as the 1σ noise level for transverse field components while deviations in

B_z is taken as 1σ for noise level of line of sight component of magnetic field. Only those pixels where longitudinal and transverse fields are simultaneously greater than twice the above mentioned noise levels are analyzed.

The data sets with their observation details are given in Table 4.1. The data sets observed from August 2001 to April 2005 are obtained with the ASP and those observed from June 2005 to December 2005 are from the DLSP. Two vector magnetograms observed on 09 January 2007 and 06 February 2007 from Solar Vector Magnetograph at Udaipur Solar Observatory (SVM-USO: Gosain et al. (2004, 2006)) and reported in Tiwari et al. (2008), have also been included to improve the statistics. All the other data sets obtained since November 2006 onwards are taken from *Hinode* (SOT/SP).

4.3 Twist Irrespective of Force-Free Nature: Introduction of Signed Shear Angle (SSA)

Hagyard et al. (1984) introduced the shear angle $\Delta\Phi = \Phi_{obs} - \Phi_{pot}$, where Φ_{obs} and Φ_{pot} are the azimuthal angles of observed and potential fields respectively. The amplitude of this angle was studied at the polarity inversion lines to investigate the flare related changes (Venkatakrishnan et al., 1988, 1989; Hagyard et al., 1990; Ambastha et al., 1993; Hagyard et al., 1999). To emphasize the sign of shear angle we wish to introduce the signed shear angle (SSA) for the sunspots as follows : We choose an initial reference azimuth for a current-free field (obtained from the observed line of sight field). Then we move to the observed field azimuth from the reference azimuth through an acute angle. If this rotation is counter-clockwise, then we assign a positive sign for the SSA. A negative sign is given for clockwise rotation. This sign convention will be consistent with the sense of azimuthal field

Table 4.1: List of the active regions studied. The global α value, the spatially averaged signed shear angle (SASSA) and other details of the sunspots are given:

AR No. (NOAA)	Date of Observation	Global Alpha (α_g:/meter)	Shear Angle (SASSA: deg)	Position	Hemispheric Helicity Rule
10972	07 Oct 2007	-2.331×10^{-8}	-1.085	S05W20(t)	No
10971	29 Sep 2007	3.053×10^{-8}	3.214	N03W07	No
10970	05 Sep 2007	-2.001×10^{-8}	-0.308	S07W58(t)	No
10969	29 Aug 2007	-3.424×10^{-8}	-4.488	S05W33(t)	No
10966	09 Aug 2007	-2.539×10^{-8}	-3.595	S06E07	No
10963(−)	12 Jul 2007	-2.459×10^{-8}	-4.636	S06E14(t)	No
10963(+)	12 Jul 2007	-3.440×10^{-8}	-4.495	S06E14(t)	No
10961	02 Jul 2007	-5.119×10^{-8}	-4.973	S10W16(t)	No
10960	07 Jun 2007	3.027×10^{-8}	4.486	S07W03	Yes
10956(−)	18 May 2007	9.642×10^{-8}	11.595	N02E07	No
10956(+)	18 May 2007	6.458×10^{-8}	5.352	N02E07	No
10955	13 May 2007	-6.737×10^{-8}	-1.887	S09W35(t)	No
10953	29 Apr 2007	-6.673×10^{-9}	-3.071	S10E22(t)	No
10944	03 Mar 2007	-2.084×10^{-8}	-4.635	S05W30(t)	No
10941	06 Feb 2007	-2.745×10^{-8}	-3.069	S07W36(t)	No
10940	01 Feb 2007	-1.948×10^{-8}	-4.726	S04W05	No
10939(−)	23 Jan 2007	-3.033×10^{-8}	-5.105	S04W57(t)	No
10939(+)	23 Jan 2007	-8.289×10^{-9}	-0.869	S04W57(t)	No
10935	09 Jan 2007	-2.412×10^{-8}	-3.414	S07W30(t)	No
10933	05 Jan 2007	-1.119×10^{-9}	-2.423	S04W01	No
10930(−)	12 Dec 2006	-3.519×10^{-8}	-6.676	S05W21(t)	No
10930(+)	12 Dec 2006	-1.624×10^{-7}	-18.067	S05W21(t)	No
10926	03 Dec 2006	-7.049×10^{-9}	-1.538	S09W32(t)	No
10923	16 Nov 2006	1.090×10^{-9}	0.785	S05W30(t)	Yes
10921	06 Nov 2006	-3.318×10^{-7}	-14.054	S08W38(t)	No
10841	28 Dec 2005	1.114×10^{-7}	9.383	N12E20(t)	No
10838	22 Dec 2005	2.294×10^{-7}	14.757	N17E20(t)	No
10808(−)	13 Sep 2005	1.017×10^{-7}	8.015	S11E17(t)	Yes
10808(+)	13 Sep 2005	1.225×10^{-7}	1.020	S11E17(t)	Yes
10804	26 Aug 2005	-4.977×10^{-8}	-5.237	N11W02	Yes
10803	26 Aug 2005	2.559×10^{-7}	6.151	N12E53(t)	No
10800	26 Aug 2005	1.331×10^{-7}	3.967	N17W49(t)	No
10782	02 Jul 2005	-3.626×10^{-7}	-10.230	S17W18(t)	No
10781	04 Jul 2005	1.027×10^{-7}	7.786	N13W03	No
10780	24 Jun 2005	-6.357×10^{-8}	-0.806	S08W28(t)	No
10752	17 Apr 2005	9.960×10^{-8}	8.365	N02W00	No
10330	09 Apr 2003	3.988×10^{-8}	11.031	N07W04	No
09601	03 Sep 2001	1.367×10^{-8}	2.178	N14W06(t)	No
09596	30 Aug 2001	2.125×10^{-7}	9.297	N21E15(t)	No
09591(−)	30 Aug 2001	-2.359×10^{-7}	-6.111	S18W36(t)	No
09591(+)	30 Aug 2001	-1.839×10^{-7}	-2.226	S18W36(t)	No
09590	26 Aug 2001	-3.148×10^{-7}	-2.069	S29W01(t)	No
09585	24 Aug 2001	5.310×10^{-8}	1.730	N14W30(t)	No

(t) : *transformed*

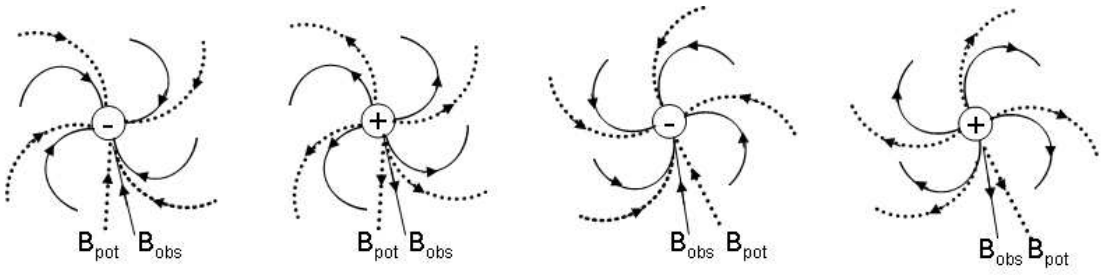

Figure 4.1: Cartoon diagrams of circular unipolar spots with positive and negative chirality are shown with the directions of observed transverse field (B_{obs}) and potential transverse field (B_{pot}). Solid and dashed lines represent the observed and potential fields respectively. In this cartoon, B_{obs} is tangential to the solid curved lines, while B_{pot} is tangential to the dashed curved lines which have lesser curvature than the solid lines. First two cases bear positive chirality and later two bear negative chirality. Plus and minus sign in the central circular region represents the positive and negative polarity respectively. For details see the text.

produced by a vertical current. This sign convention is also consistent with the sense of chirality.

4.3.1 Relation Between the Sign of SSA and the Sense of Chirality

The definition of the signed shear angle (SSA) is introduced as above.

Figure 4.1 shows four structures, first two having positive chirality and the next two having negative chirality. The sign of B_{pot} and B_{obs} point inward for negative B_z and outward for positive B_z. The rotation from B_{pot} to B_{obs} through an acute angle is counter clockwise for the cases of positive chirality and clockwise for negative chirality. This is consistent with positive and negative SSA respectively, by definition. Thus, the sign of SSA will bear the same sign of the

chirality.

The potential field has been computed using the method of Sakurai (1989). Spatial average of the SSA (SASSA) obtained for a whole sunspot is taken as the global value of SSA for that sunspot.

4.4 The Data Analysis and Results

We have used the following formula to compute the local α values

$$\alpha = \frac{(\nabla \times \mathbf{B})_\mathbf{z}}{B_z}. \tag{4.1}$$

The global α value of the active regions is estimated from the following formula as described in Tiwari et al. (2009a)

$$\alpha_g = \frac{\sum(\frac{\partial B_y}{\partial x} - \frac{\partial B_x}{\partial y})B_z}{\sum B_z^2}. \tag{4.2}$$

This estimate was shown to be not seriously affected by the polarimetric noise (Tiwari et al., 2009a). Moreover, since α_g is weighted by strong field values (Hagino and Sakurai, 2004) and not affected by singularities at polarity inversion lines (Tiwari et al., 2009a), this parameter is more accurate than a simple average of local α.

The force-free parameter α involves three dimensions since it basically represents the rate of change of rotation per unit axial length. The SSA is the rotational deviation of the projection of the field onto the photosphere from that of a reference current-free field. The α parameter is a gradient of angle per unit length while SSA is just an angle. We therefore cannot expect a strong correlation between the amplitudes of both the quantities, the SSA and the α parameter. But we do find a good correlation between their signs as evident from Table 4.1.

Signed shear angle (SSA) provides the sign of twist irrespective of whether the photospheric magnetic field is force-free or not. Table 4.1 shows that the sign of α_g is same as the sign of spatially averaged signed shear angle (SASSA). Thus, we conclude that even if the photosphere is non force-free, the sign of global α will empirically give the sign of SASSA and therefore the sign of global twist (chirality) of the sunspots.

To avoid any kind of projection effect we have transformed the data sets to disk center (Venkatakrishnan and Gary, 1989) if the observed sunspot is more than 10 degrees away from the disk center. In some active regions both the polarities are compact enough to be studied separately. We have treated each pole of those active regions as an individual sunspot and this is denoted in the Table 4.1 after the NOAA no. of sunspots by plus or minus sign.

Two examples of the local α distribution for the data sets obtained from *Hinode* (SOT/SP) are shown in Figure 4.2. The positive/negative contours are shown in red/blue colors. The local α patches are seen in the umbra and filamentary distribution of α is observed in the penumbral region. We find that the inclination angles oscillate between $\sim$ 30-80 degrees when we go along azimuthal direction. This is consistent with the interlocking-comb penumbral structure (Ichimoto et al., 2007) of the penumbral magnetic fields. The vertical current J_z has two components, viz. $-\frac{1}{r}\frac{\partial B_r}{\partial \phi}$ and $\frac{1}{r}\frac{\partial (rB_\phi)}{\partial r}$. If we approximate the observed transverse field (B_t) to be mostly radial ($\mathrm{B}_t \sim B_r$) then we can interpret the azimuthal variation of J_z to result from the term $-\frac{1}{r}\frac{\partial B_r}{\partial \phi}$. This term is not expected to contribute to global twist. However $\frac{1}{r}\frac{\partial (rB_\phi)}{\partial r}$ could be an important contributor to the global twist. A detailed investigation of this interesting possibility is deferred to another investigation. For the present, we obtain positive and negative values of current side by side in the penumbra. Because the α parameter depends

on the current, this oscillation across the penumbral filaments is expected for the α values too.

The distribution of vertical current and local α in the penumbra show higher values than that in the umbral regions. An arc and a straight line, selected respectively in the penumbra and umbra of AR NOAA 10933 have been over plotted as shown in the upper panel of Figure 4.2. The corresponding values of vertical current and α along the arc and the line are shown in the Figure 4.3(a) and Figure 4.3(b) respectively. We can see that both the positive and negative vertical current as well as α are equally distributed in the penumbra along the azimuthal direction. This gives a negligible contribution to the global current and global α values thereby indicating that the contribution of $-\frac{1}{r}\frac{\partial B_r}{\partial \phi}$ is indeed small. We have selected an arc rather than the complete circle because many times sunspots are not circular and therefore selecting a proper penumbral region is not possible for a full circle. Similar arcs have been selected in the other sunspots and all the time it is seen that both the positive and the negative vertical current as well as α are distributed equally in the penumbra giving negligible contribution to their global values. While current and α variations are correlated for positive B_z, they will be anti correlated for negative B_z.

Figure 4.3(b) shows a typical profile of spatial variations of current and α across the umbra (along the line) in the AR NOAA 10933 shown in the upper panel of Figure 4.2. We see that the amplitude of variation of α in the umbra is smaller than that in the penumbra by approximately an order of the magnitude and is of the same order as that of the global α value of the whole sunspot. The amplitude of current density variations is not very much smaller than that in the penumbra but are less balanced out than in the penumbra.

In the lower panel of Figure 4.2, an arc like structure (partial ring) with

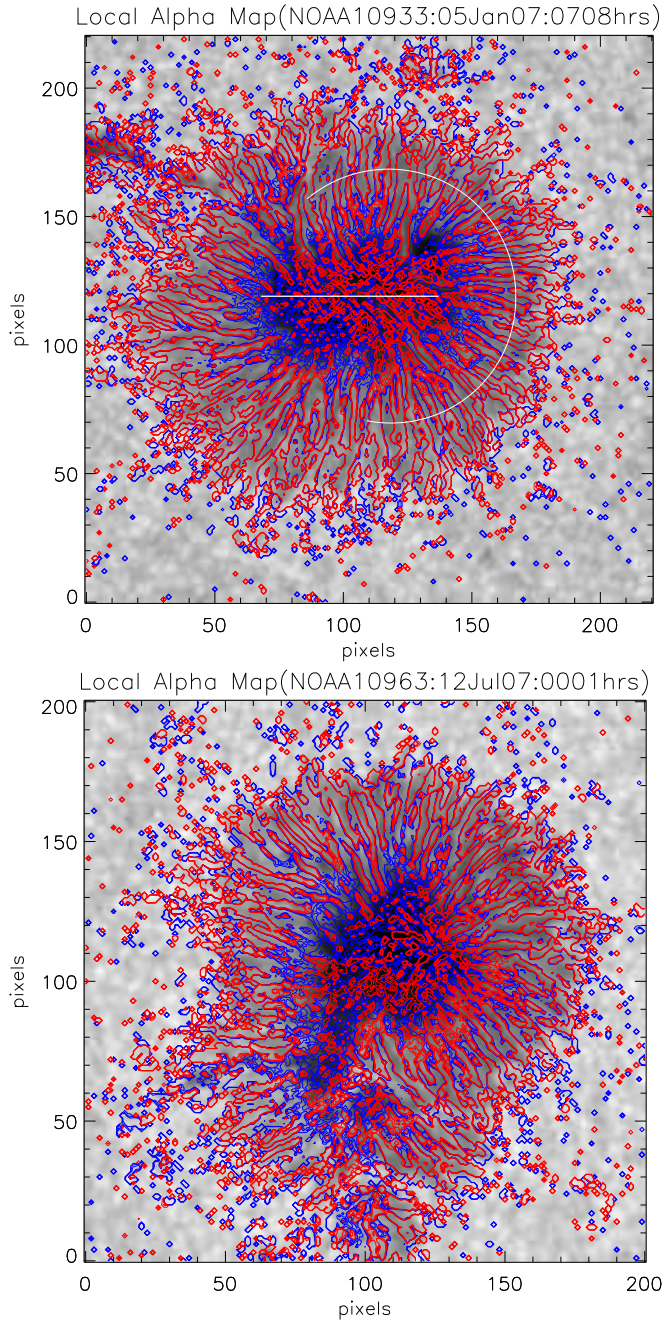

Figure 4.2: Two examples of local α distribution observed in Hinode (SOT/SP) data. The background is the continuum image. The red and blue contours represent positive and negative values of α respectively. The contour levels are $\pm 1 \times 10^{-8} m^{-1}$, $\pm 5 \times 10^{-8} m^{-1}$, and $\pm 10 \times 10^{-8} m^{-1}$. The values of vertical current and α along the arc shown in the penumbra of the image in the upper panel, is plotted in Figure 4.3(a) and those along the straight line in the umbra are plotted in Figure 4.3(b).

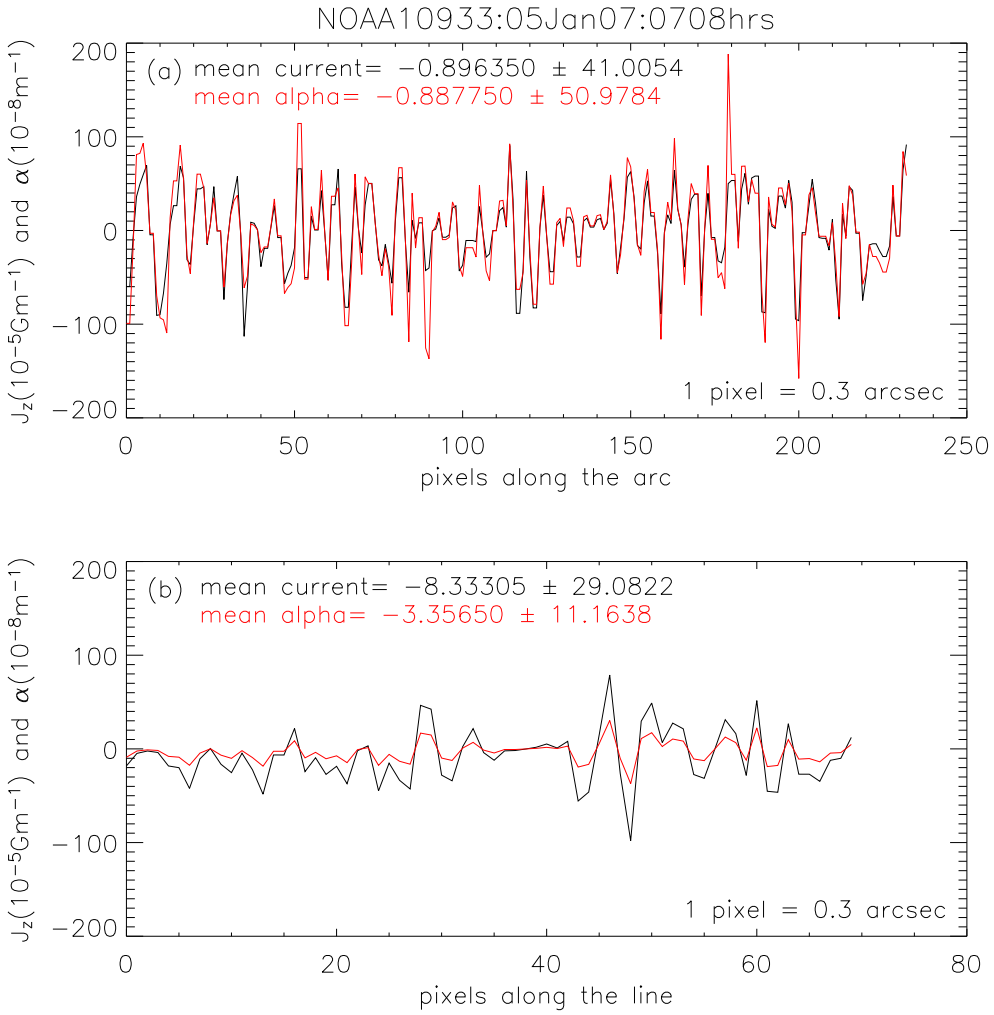

Figure 4.3: Plots of vertical current and α values along (a) the arc and (b) the straight line shown in the penumbra and umbra of AR NOAA 10933 (upper panel of Figure 4.2) respectively. Black and red colors represent the current and α values respectively. The mean values of both the vertical current and the α values with their 1σ standard deviations in the arc and the line are printed on the plots in their respective colors.

bunch of red contours (positive α) can be observed. This is opposite to that of the dominant negative global α of the sunspot. Such partial rings with opposite sign of the global value are observed in 10 of the sunspots from our sample. In the rest of the sunspots, mixed current and α are present in the umbra with one dominant sign and no such specific structures are seen at the umbral-penumbral boundaries.

A few sunspots in our data sets studied are small and have no penumbra. Some ASP data doesn't show fine structures in penumbra due to lack of spatial resolution. We have included these active regions in our study to look at the hemispheric behaviour of the global twist.

Most of the data sets we studied are observed during the declining minimum phase of the solar cycle 23. All except five of the sunspots observed follow the reverse twist hemispheric rule, while five follow the conventional twist hemispheric rule. The detailed discussion about this interesting result is deferred to Chapter 8.

4.5 Discussion and Conclusions

We have introduced the concept of SSA for sunspots and further find that the SASSA and the global α value of sunspots have the same sign. Thus, α gives the same sign as the SSA and therefore the same sign of the photospheric chirality of the sunspots, irrespective of the force-freeness of the sunspot fields. As can be observed from the Table 4.1, the magnitudes of SASSA and α_g are not well correlated. This lack of correlation could be due to a variety of reasons: (a) departure from the force-free nature (b) even for the force-free fields, α is the gradient of twist variation whereas SASSA is purely an angle. The missing link is

the scale length of variation of twist. The magnitude of SASSA, therefore, holds promise for characterizing global twist of the sunspot magnetic fields, irrespective of its force-free nature.

Patches of vertical current and α with opposite signs are present in the umbra of each sunspot studied. One sign of α dominates in the umbra which is also seen to be the sign of the global α of the sunspot. Similarly, the magnitude of the global α is of the same order as the amplitude of variation of the local α in the umbra.

The filamentary structures of vertical current density and local α are observed in the penumbra of the sunspots and are, as discussed above, due to oscillatory behaviour in the inclination values and therefore gradients of the transverse field in the azimuthal direction. We find that the contributions of both positive and negative values of vertical current density and α to their global values cancel each other in the penumbra of the sunspot. Thus the penumbral fine structures provide a negligible contribution to the global α and current values of sunspots. The spatial variation of curl $\mathbf{B}$ (and thus current density) depicts the local variation of the Lorentz force and thus the local variation of the external forces exerted by the plasma on the field. The amplitude of α variation is approximately an order of magnitude smaller in the umbral regions than that in the penumbral regions and is of the order of the global α of the whole sunspot.

Partial rings with opposite signs to that of dominant sign of umbral α are observed at the umbral-penumbral boundaries in 10 out of the 43 sunspots studied. However even in these few cases, the rings are never complete in any sunspot. Su et al. (2009) have connected the ring-like structure to the draping of poloidal field around the toroidal field as suggested by Chatterjee et al. (2006).

Most of the AR's observed do not follow the twist hemispheric rule. This

issue of hemispheric rule needs to be reinvestigated over a longer period as well as with improved data and is discussed in detail in Chapter 8.

Some researchers have tried to predict flare activity from local distribution of α as well as global α values of sunspots (Nandy (2008); Hahn et al. (2005) and references therein). Nandy (2008) concluded from a study of AR 6982 that the global twist present in a sunspot does not influence the flaring activity. It is rather, governed by the spatial distribution and evolution of twisted sub-structures present in the sunspot. This conclusion indeed needs more study. We have addressed, in Chapter 6, the question of relation between flaring activity and the role of global twist present in a large number of vector magnetograms of two sunspots.

For the present, we demonstrate that the sign of the SASSA provides the sign of the photospheric chirality irrespective of its force-free nature. The sign of the global α of a sunspot is determined by the dominant sign of umbral α values without much contribution from the penumbral α values.

Chapter 5

Absence of Photospheric Net Currents in Presence of Significant Global Twist of Sunspots

5.1 Introduction

In continuation of the study of the fine structures in the sunspots presented in the last chapter, we present the analysis of 14 high-resolution vector magnetograms and the results for the net electric currents along with their global twist values in this Chapter.

As discussed in the earlier chapters, we know that the sunspots have shown evidence for twist even from the time of Hale (1925, 1927) who postulated the hemispheric rule for the chirality of chromospheric whirls. This was later con-

firmed with a larger data set by Richardson (1941). Evidence for photospheric chirality was noticed even in early continuum images of sunspots, obtained with exceptional image quality. Later, global twist was inferred from the non-vanishing averages of the force-free parameter using photospheric vector magnetograms (Pevtsov et al. (1994); Hagino and Sakurai (2004); Nandy (2006) and references therein). The non-force-free nature of photospheric magnetic field in the sunspots, prompted Tiwari et al. (2009b) to propose the spatially averaged signed shear angle (SASSA) as a more robust measure of the global twist of the sunspot magnetic field. This method has been described in Section 4.3.

Although, the sign of the SASSA matches well with the sign of the global α parameter, the magnitudes are not correlated. The physical significance of a globally averaged α parameter rests heavily on the existence of a net current in the photospheric sunspot magnetic field. One way of arriving at a global α is by taking the ratio of net vertical current to the total flux (integral method). This value was found to agree with the values obtained by other methods (Hagino and Sakurai, 2004).

The global twist and net current is expected to be well correlated for a monolithic sunspot magnetic field, by Ampere's Law. However, the existence of a net current is ruled out theoretically for fibril bundles as well as for monolithic fields with azimuthal field decreasing faster than $1/\varpi$, where ϖ is the radial distance from the spot center (Parker, 1996). On the other hand, Melrose (1992, 1995) believes that there must be a current in the lower reaches of the solar atmosphere due to the magnetic coupling between the photosphere and the corona. Several attempts to resolve this problem using vector magnetograms have not been very conclusive so far (Wilkinson et al., 1992; Leka et al., 1996; Wheatland, 2000). The poor resolution of the earlier vector magnetogram data perhaps did not al-

low them to reach an ultimate conclusion. Although, Wheatland (2000) made an effort for the same using significant number (21) of vector magnetograms, it seems lack of high resolution did not allow him the clear results. He got net currents present in some cases and absent in some. However, he concluded in favour of presence of net current in the monopoles of sunspots depending on the majority of such cases in his data sets.

A resolution of this problem can be used to disentangle the relation between global twist and the global α parameter. Also, the resolution is needed to evaluate the so called hemispheric helicity rule seen in the global α parameter calculated from photospheric vector magnetograms (Pevtsov et al., 1994, 1995; Hagino and Sakurai, 2004; Nandy, 2006). The availability of high resolution vector magnetograms from *Hinode* (SOT/SP), gives us the best opportunity so far to address this problem. The effect of polarimetric noise is expected to be negligible in the estimation of magnetic parameters (Tiwari et al., 2009a) from these data.

In the next Section, we obtain an expression for the net current using a generalization of the expression obtained by Parker (1996). We then proceed to measure this current from several vector magnetograms of nearly circular sunspots. We finally discuss the results and present our conclusions.

5.2 Expression For Net Current

We consider a long straight flux bundle surrounded by a region of "field free" plasma following Parker (1996). The words "field free" is used in an approximate fashion meaning that there is no large scale coherent and unipolar background magnetic field surrounding the flux bundle. Also, we include the case where the bundle can be replaced by a monolithic field. Parker (1996) assumed azimuthal

symmetry as well as zero radial component B_r, of the magnetic field. For realistic sunspot fields, we have already seen the ubiquitous fine structure of the radial magnetic field. Hence, we need to relax both these assumptions.

The vertical component of the electric current density consists of two terms, viz. $-\frac{1}{\mu_0 r}\frac{\partial B_r}{\partial \psi}$ and $\frac{1}{\mu_0 r}\frac{\partial (rB_\psi)}{\partial r}$. We will call the first term as the "pleat current density", j_p and the second term as the "twist current density", j_t. The total current I_z within a distance ϖ from the center is then given by

$$I_z(\varpi) = \int_0^{2\pi} d\psi \int_0^{\varpi} r dr (j_p + j_t) \tag{5.1}$$

The ψ integral over j_p vanishes, while the second term yields

$$I_z(\varpi) = \frac{\varpi}{\mu_0} \int_0^{2\pi} d\psi B_\psi(\varpi, \psi) \tag{5.2}$$

which gives the net currents within a circular region of radius ϖ.

5.3 The Data Sets and Analysis

We have analyzed the vector magnetograms obtained from Solar Optical Telescope/ Spectro-polarimeter (SOT/SP: Tsuneta et al. (2008); Shimizu et al. (2008); Suematsu et al. (2008); Ichimoto et al. (2008)) onboard Hinode (Kosugi et al., 2007). The calibration of data sets have been performed using the standard "sp_prep" routine available in the Solar-Soft package. The prepared polarization spectra have the been inverted to obtain vector magnetic field components using an Unno-Rachkowsky (Unno, 1956; Rachkowsky, 1967) inversion under the assumption of Milne-Eddington (ME) atmosphere (Landolfi and Landi Degl'Innocenti, 1982; Skumanich and Lites, 1987). We have used the inversion code "Strokesfit.pro" which has been kindly, made available by late Prof. T. R. Metcalf as a part of Solar-Soft package. We have used the newest version of this code which returns

true field strengths along with the filling factor. The azimuth determination has inherent 180°ambiguity due to insensitivity of Zeeman effect to a 180° flip in the azimuth. Numerous techniques have been developed and applied to resolve this problem, but not even one guarantee for the complete resolution of it. The 180° azimuthal ambiguity in our data sets are removed by using acute angle method (Harvey, 1969; Sakurai et al., 1985; Cuperman et al., 1992). For regions with modest magnetic shear this method is more than adequate to resolve the ambiguity. It is only in places of high magnetic shear that the ambiguity becomes almost impossible to resolve. Fortunately all the active regions studied here were indeed devoid of very high magnetic shear.

Like in earlier chapter, the noise filtering is done in the data sets used in this work. In order to minimize the noise, pixels with transverse (B_t) and longitudinal magnetic field (B_z) greater than a certain level are only analyzed. This threshold value is determined as follows: A quiet Sun region is selected for each sunspot and the 1σ standard deviation in the three vector field components B_x, B_y and B_z are evaluated separately. The resultant standard deviations of B_x and B_y is then taken as the 1σ noise level for transverse field components. Likewise the standard deviation of B_z is taken as the 1σ noise level for the line of sight magnetic field component.

Only those pixels where longitudinal and transverse fields are simultaneously greater than twice the above mentioned noise levels are analyzed. The data sets with their observation details are given in Table 5.1. We have treated each polarity of a bipolar active region as an individual sunspot whenever both the polarities are observed and compact enough to be studied.

The results of the inversions yield the 3 magnetic parameters, viz. the field strength B, the inclination to the line of sight γ, and the azimuth ϕ. These

parameters are used to obtain the 3 components of magnetic field in Cartesian geometry as

$$B_z = B\cos\gamma \tag{5.3}$$

$$B_y = B\sin\gamma\sin\phi \tag{5.4}$$

$$B_x = B\sin\gamma\cos\phi \tag{5.5}$$

These equations have already been described in Chapter 1.

This vector field is then transformed to heliographic coordinates (Venkatakrishnan and Gary, 1989) for the spots observed at viewing angle more than 10°. The transverse vector is then expressed in cylindrical geometry as

$$B_r = \frac{1}{r}(xB_x + yB_y) \tag{5.6}$$

$$B_\psi = \frac{1}{r}(-yB_x + xB_y) \tag{5.7}$$

The azimuthal field B_ψ is then used in Equation 5.2 for obtaining the value for the total vertical current within a radius ϖ.

We have computed "twist angle" for all the sunspots using B_ψ and B_r as follows:

$$Twist\ \ angle = tan^{-1}(B_\psi/B_r) \tag{5.8}$$

The value of twist angle for each sunspot has been given in Table 5.1.

The error in "twist" measurement is simply the error in azimuth measurement. We can calculate the azimuth under weak field approximation from $\tan 2\psi = U/Q$. Now, we can estimate the error in ψ as equal to percentage error in linear polarization measurements. Thus a 1% error in polarimetry means the error in ψ is equal to 0.01 radians or 0.57 degrees. We have verified using Monte-Carlo simulations (Gosain et al., 2009, in preparation) that the error in ψ is consistent with the value estimated from the weak field approximation.

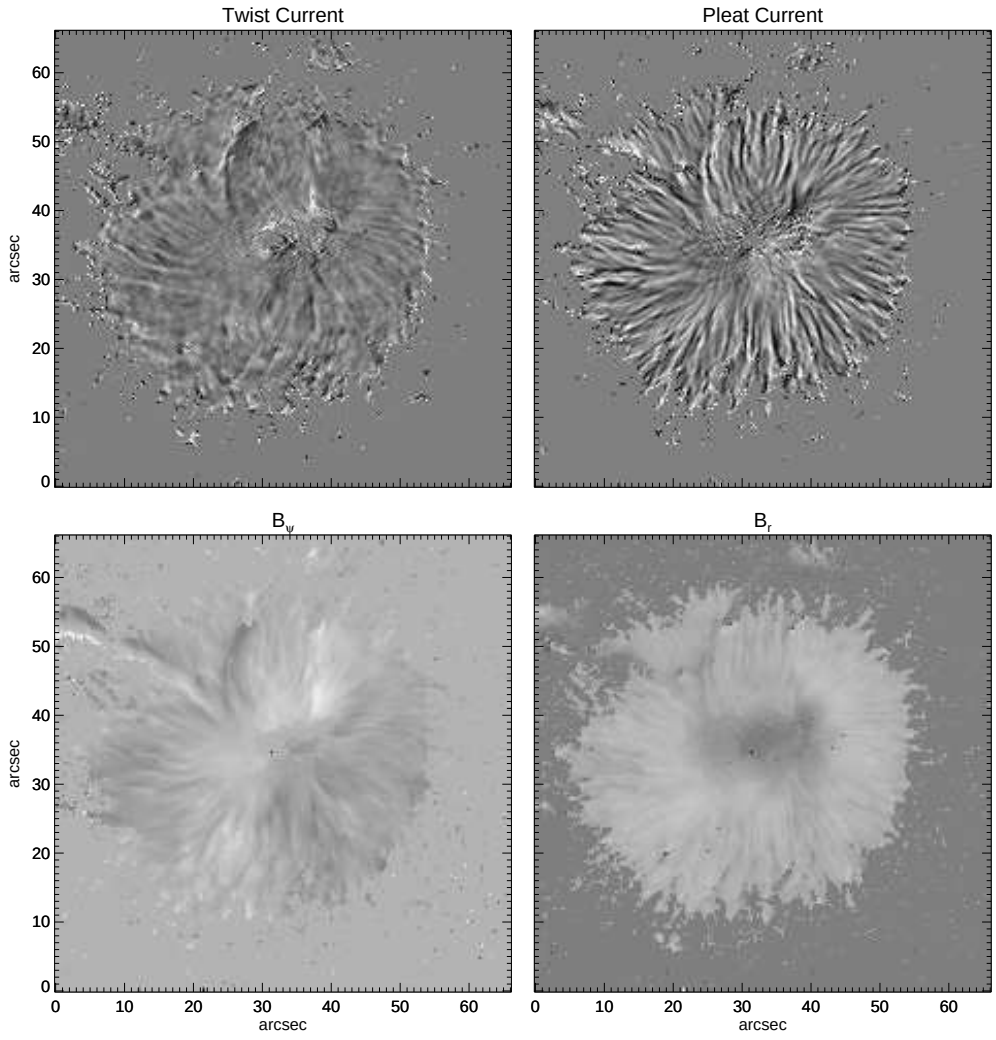

Figure 5.1: Examples of the two components of the vertical electric current density namely the "twist" and the "pleat" current densities (j_t and j_p) observed in NOAA AR 10933 are shown in the upper panel. The lower panel shows the azimuthal and radial component of the magnetic field (B_ψ and B_r).

Table 5.1: List of the active regions studied. The power index δ: the slope of decrease of B_ψ value, the twist angle, the spatially averaged signed shear angle (SASSA) and other details of the sunspots are given:

AR No. (NOAA)	Date of Observation	Slope δ	Shear Angle (SASSA: deg)	Twist Angle (deg)	Position	Hemisph. Hel. Rule
10969	29 Aug 2007	7.514	-4.488	-4.009	S05W33(t)	No
10966	07 Aug 2007	4.349	-5.120	-7.028	S06E20(t)	No
10963(−)	12 Jul 2007	4.366	-5.123	$41.873^\sharp$	S06E14(t)	No
10963(+)	12 Jul 2007	4.210	-4.495	-5.112	S06E14(t)	No
10961	02 Jul 2007	4.976	-4.973	$29.451^\sharp$	S10W16(t)	No
10960	07 Jun 2007	3.267	3.182	$-24.012^\sharp$	S07W03	Yes
10953	29 Apr 2007	8.249	-3.382	$7.200^\sharp$	S10E22(t)	No
10944	03 Mar 2007	2.407	-4.635	-5.130	S05W30(t)	No
10940	01 Feb 2007	2.281	-4.726	-7.950	S04W05	No
10933	05 Jan 2007	9.584	-3.103	-2.689	S04W01	No
10930(−)	12 Dec 2006	0.203	-6.676	$34.001^\sharp$	S05W21(t)	No
10930(+)	12 Dec 2006	1.864	-18.067	-20.124	S05W21(t)	No
10926	03 Dec 2006	2.750	-1.538	$6.001^\sharp$	S09W32(t)	No
10923	10 Nov 2006	3.175	0.785	$-9.010^\sharp$	S05W30(t)	Yes

(t) : *transformed*

$\sharp$ *: twist angle for irregular sunspots does not fit to a cylindrical assumption and therefore gives incorrect values.*

We can see in the Table 5.1 that the twist angle for regular sunspots match well with the SASSA as expected whereas they do not match for irregular sunspots.

It can also be observed from the Table 5.1 that only 2 out of 14 sunspots follow the hemispheric helicity rule, while the remaining 12 sunspots follow the reverse hemispheric helicity rule.

5.4 The Results

Figure 5.1 shows an example of the maps of twist current, pleat current, B_ψ and B_r for a sunspot NOAA AR 10933 which is nearly circular. Figure 5.2(a) shows plots of B_ψ and B_r along with the different concentric circles around spot center. In Figure 5.2(b), the spatial variation of both B_ψ and B_r are clearly seen. This variation is corresponding to a typical circle selected in the penumbra. The B_r variation in the penumbra is a manifestation of the interlocking combed structure (Ichimoto et al., 2007; Tiwari et al., 2009a). The B_ψ variation in the penumbra shows that not only is there an interlocking combed structure, but these structures are curled as well. In other words, we may describe the penumbral field as possessing a "curly interlocking combed" structure. Mathew et al. (2003) also mention the deviation of the vector field azimuths from a radial direction in the magnetic field of a sunspot belonging to NOAA AR 8706, using the infra-red FeI line pair at 1.56 micron, but did not emphasize their result perhaps due to a single case.

The azimuthal averages $< B_r >$ and $< B_\psi >$ were obtained at different values of ϖ. Figure 5.2(c) shows the plots of $< B_r >$ and $< B_\psi >$ as a function of ϖ. The circles corresponding to the selected radii are shown in the upper panel of the same figure. The azimuth-averaged $< B_r >$ drops rapidly to a very low value

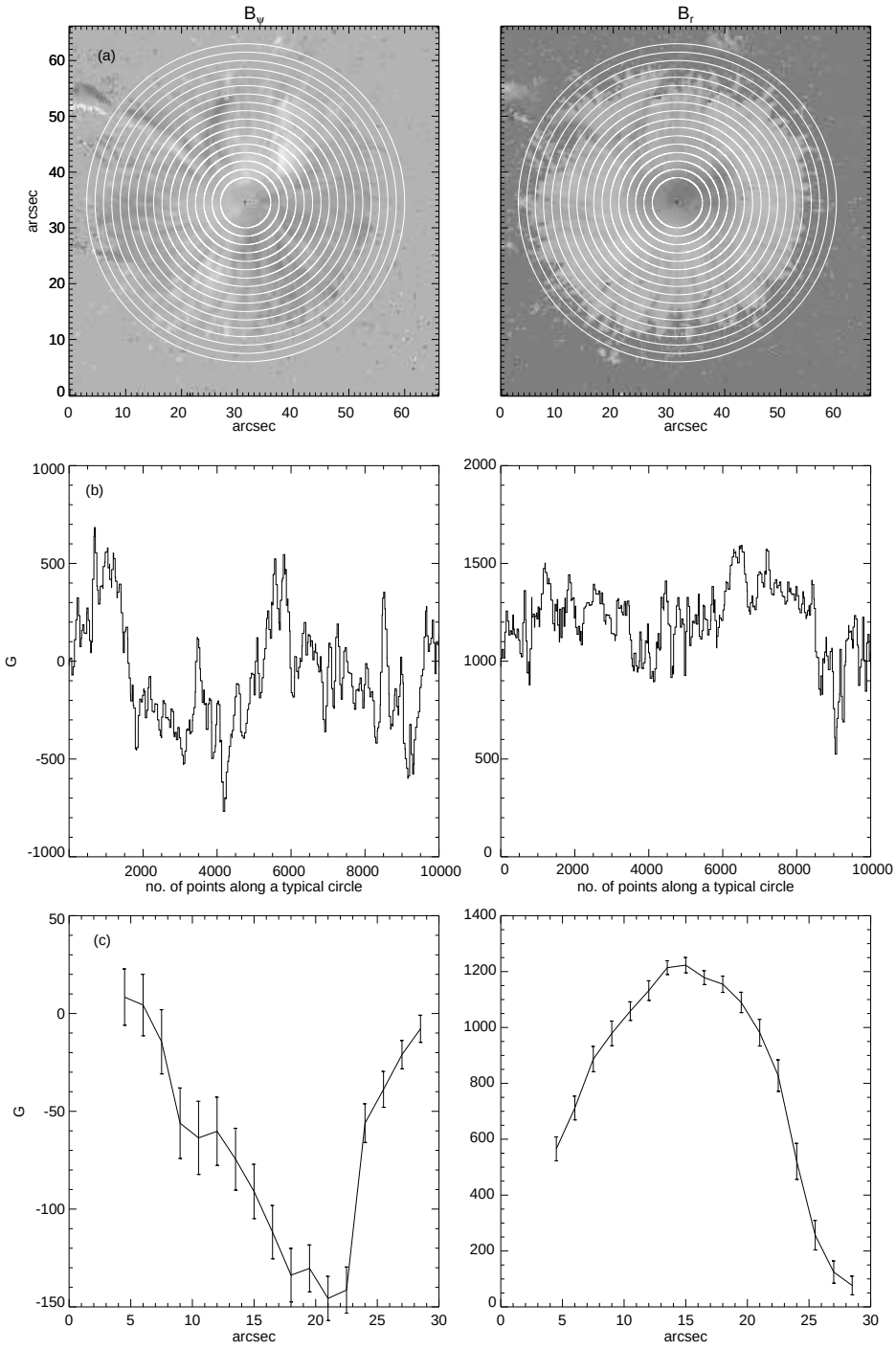

Figure 5.2: (a): The same image as the lower panel of Figure 5.1 but with concentric circles over plotted on them. (b): Plots of B_ψ and B_r along the periphery of a typical circle (45^{th} pixel away from center) selected in the sunspot. (c): The mean B_ψ and the mean B_r with $\frac{1}{16}$ and $\frac{1}{8}$ of their variations respectively along radial direction for different values of ϖ have been plotted.

at the edge of the sunspot. This is a clear evidence for the existence of a canopy where the field lines lift up above the line forming region. It must be remembered however, that this feature of the B_r variation would be difficult to observe in a complex active region because of the multiplicity of the canopies. Figure 5.3 shows the plot of $\log < B_\psi >$ as a function of $\log \varpi$. The slope δ of the declining portion of this plot is 9.584, which shows that field varies faster than $1/\varpi$. This can be construed as evidence for the neutralization of the global current. The δ for other sunspots have also been computed and are given in Table 5.1.

Figure 5.5 shows the net current within a radius ϖ as a function of ϖ. As expected from the trend in Figure 5.3, the net current shows evidence for a rapid decline after reaching a maximum. Similar trends were seen in other sunspots. Table 5.1 shows the summary of results for all the sunspots analyzed. Along with the power law index δ of B_ψ decrease, we have also shown the average deviation of the azimuth from the radial direction ("twist angle"), as well as the SASSA. The average deviation of the azimuth is well correlated with the SASSA for nearly circular sunspots, but is not correlated with SASSA for more irregularly shaped sunspots. Thus, SASSA is a more general measure of the global twist of sunspots, irrespective of their shape.

Negative polarity of complex NOAA AR 10930 does not show fall of net current so rapidly as in other sunspots tabulated in the Table 1. Due to the close proximity of the opposite polarity spots the field lines could have been bent in such a manner that the canopy forms below the line forming region. Alternately, the plurality of the canopies could also lead to a slower decline of the $< B_\psi >$ as a function of ϖ starting from the center of the sunspot.

Infrared line observations could perhaps resolve this problem as posed by the observations such as of AR 10930.

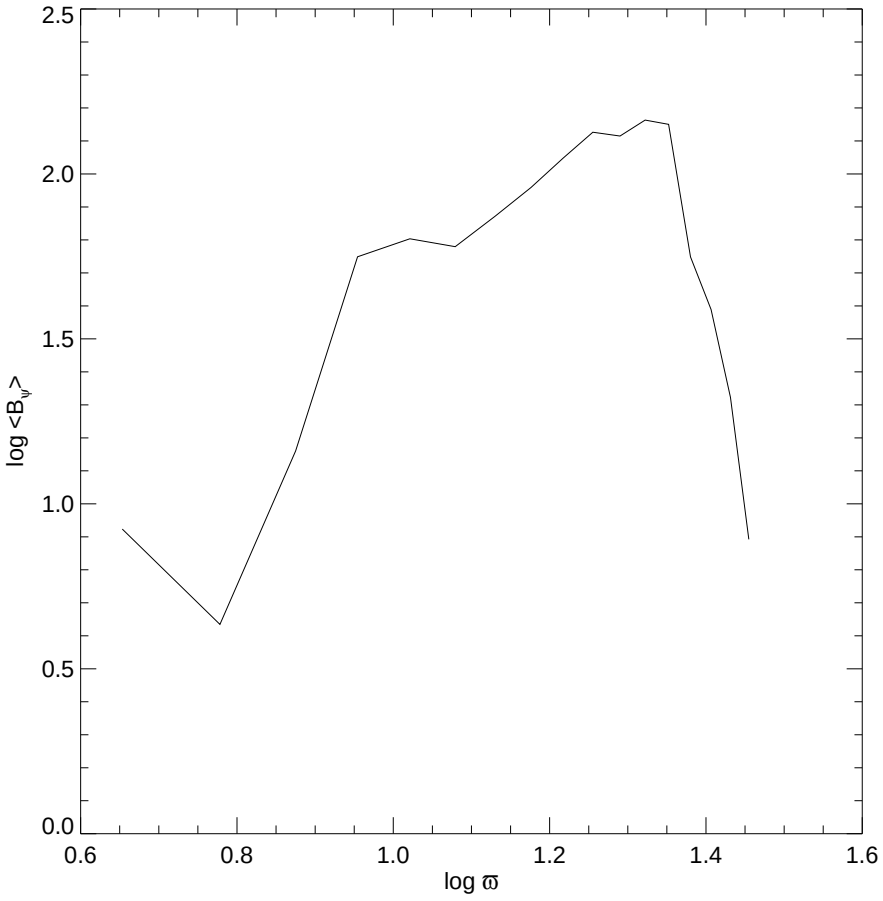

Figure 5.3: Variation of log $< B_\psi >$ with log ϖ. The slope of the declining portion of the plot has been calculated as a simple power law index δ for each sunspot and has been given in Table 5.1.

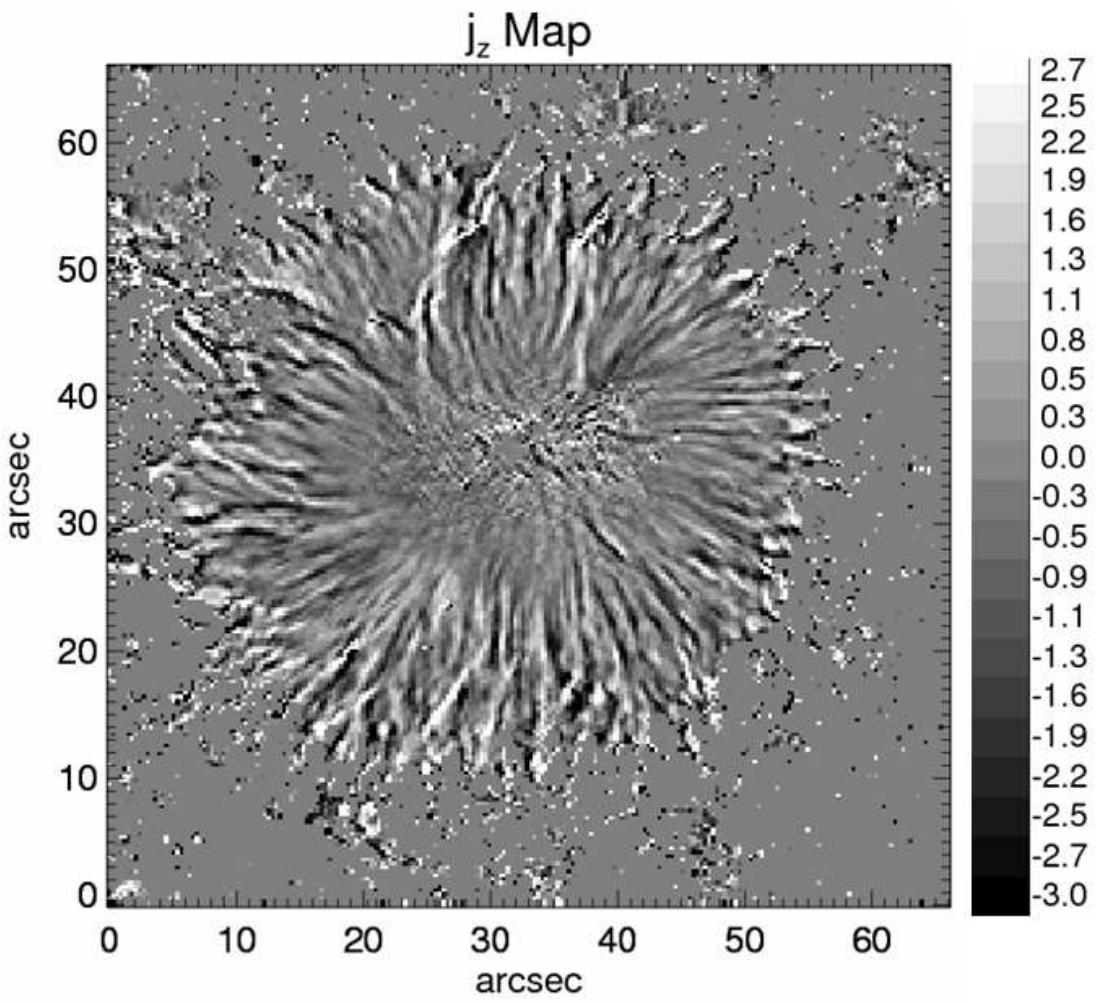

Figure 5.4: The map of vertical current density j_z for NOAA AR 10933 is shown with intensity scale. The values are expressed in Giga Amperes per square meter (GA/m^2) We can see that it is difficult to infer an opposite current in inner and outer portions of the sunspot respectively.

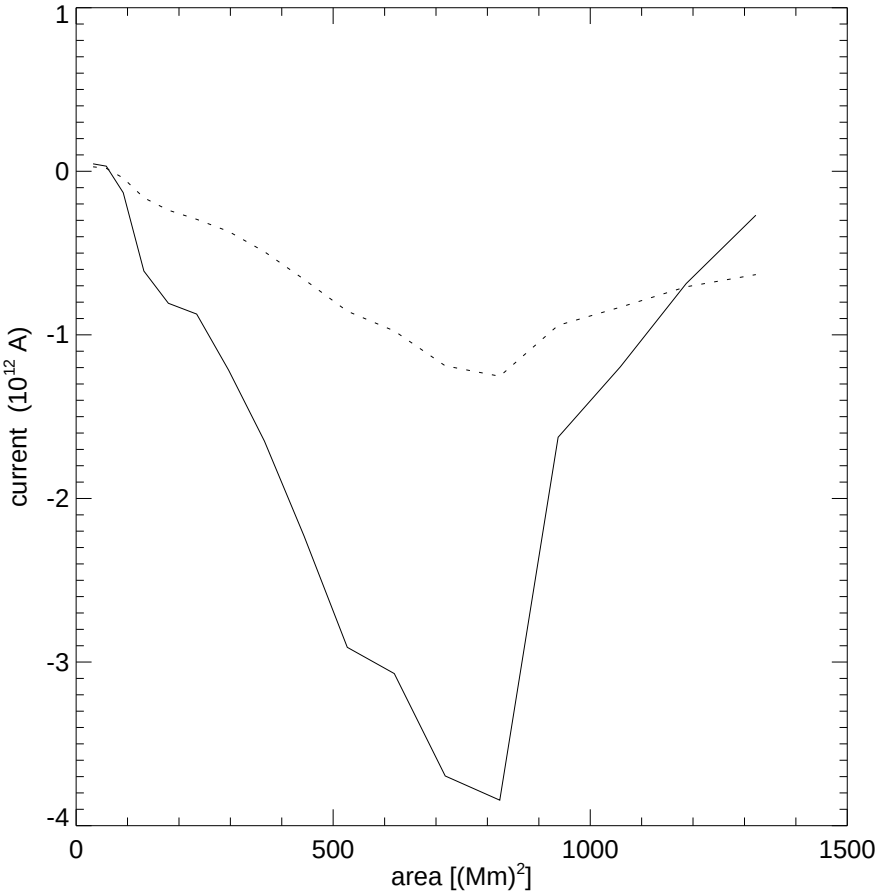

Figure 5.5: The net current variation with increasing area has been shown. The solid line shows the results of the calculations from the Equation 5.2. Also shown, by a dashed line, is the results from the derivative method. We can see the net current reduces very fast after a peak and almost vanishes for complete sunspot. On the other hand the net current computed from the derivative method shows a shallow behaviour.

It is worth mentioning that the different observational results obtained earlier (Wilkinson et al., 1992; Leka et al., 1996; Wheatland, 2000) could be due to the different spectral lines used for the measurements, since it is now very much evident from SIR inversions of sunspot data, that there could be large depth variation of the magnetic parameters even within the line forming region (Louis et al., 2009).

5.5 Discussion and Conclusions

It is well known for astrophysical plasmas, that the plasma distorts the magnetic field and the curl of this distorted field produces a current by Ampere's law (Parker, 1979). Parker's (1996) expectation of net zero current in a sunspot was chiefly motivated by the concept of a fibril structure for the sunspot field. However, he also did not rule out the possibility of vanishing net current for a monolithic field where the azimuthal component of the vector field in a cylindrical geometry declines faster than $1/\varpi$. While it is difficult to detect fibrils using the Zeeman effect, notwithstanding the superior resolution of SOT on *Hinode*, the stability and accuracy of the measurements have allowed us to detect the faster than $1/\varpi$ decline of the azimuthal component of the magnetic field, which in turn can be construed as evidence for the confinement of the sunspot field by the external plasma. The resulting pattern of curl $\mathbf{B}$ appears as a sharp decline in the net current at the sunspot boundary.

If this lack of net current turns out to be a general feature of sunspot magnetic fields in the photosphere, then measurement of helicity from a global average of the force-free parameter becomes suspect. On the other hand, sunspots are evidently twisted at photospheric levels, as seen from the non-vanishing average

twist angle as well as the SASSA (Table 5.1). Although the existence of a global twist in the absence of a net current is possible for a monolithic sunspot field (Baty, 2000; Archontis et al., 2004; Fan and Gibson, 2004; Aulanier et al., 2005), a fibril model of the sunspot field can accommodate a global twist even without a net current (Parker, 1996) A sunspot, made up of a bundle of magnetically isolated current free fibrils, can be given an overall torsion without inducing a global current.

The spatial pattern of current in a sunspot is really a manifestation of the deformation of the magnetic field (viz., $\nabla \times \mathbf{B}$) by the forces applied by the plasma. The Lorentz force exerted by the field on the plasma produces an equal and opposite force by the plasma, thereby confining the field. Thus our analysis actually shows the pattern of the forces exerted by the plasma on the field. The sharp decline of the azimuthal field with radial distance thus shows the confinement of the sunspot magnetic field by the radial gradient of the plasma pressure.

Theoretical understanding of the penumbral fine structure has improved considerably in recent times (Thomas et al., 2002; Weiss et al., 2004). The onset of a convective instability for magnetic field inclination exceeding a critical value was proposed by Tildesley (2003) and Hurlburt et al. (2002). A bifurcation in the onset (Rucklidge et al., 1995) could explain other features like hysteresis in the appearance of penumbra as a function of sunspot size. Numerical simulation of magneto-convection also steadily improved (Heinemann et al., 2007; Rempel et al., 2009b), culminating in very realistic production of penumbral field structure (Rempel et al., 2009a). It is possible, owing to the random and stochastic nature of convective structures, that no net twist in the simulated spot field would be produced by convection for negligible Coriolis force. If so, it would be very interesting to simulate magneto-convection in a twisted sunspot field. In this

case, would the resulting fine structure mimic the observed "curly interlocking combed" structure of the penumbral magnetic field? If not, we must look elsewhere for explaining the "curly interlocking combed" structure. A twisted fibril bundle would then be a solution. Recent examples of filamentary penumbral structures based on such cluster models (Solanki and Montavon, 1993; Spruit and Scharmer, 2006; Scharmer and Spruit, 2006) have also been proposed.

Melrose (1992, 1995) asserts that there is always a net longitudinal current with important physical consequences. He believes that there must be a magnetic coupling between the coronal current to photospheric current as included in a solar flare model given by Gold and Hoyle (1960). Melrose (1995) suggests a simple way of including such coupling and that is through a time-dependent inductance or a mutual inductance in a circuit model (E-j paradigm). He argues that the magnetic field $\mathbf{B}$ and fluid velocity $\mathbf{v}$ (B-v paradigm) are incomplete for the proper formulation of large-scale dynamics of the solar magnetic field. And this should be supplemented by the considerations on the electric current $\mathbf{j}$. He describes his ideas of the solar flares dynamics completely in terms of electric currents and circuits (E-j paradigm). Parker (1996) argues that, the E-j paradigm may be true only for microphysics of the fluid where local production of plasma turbulence and anomalous resistivity, electric double layers, or particle acceleration at restricted sites within the magnetic fields, are possible, and can not be true for the large-scale dynamics of the fluid and magnetic field as is the case in the Sun. Parker (1996) believes that the dynamics of the fluid and field is completely determined by the initial conditions and the boundary conditions on $\mathbf{B}$ and $\mathbf{v}$ and not on $\mathbf{E}$ and $\mathbf{j}$. The initial conditions of $\mathbf{B}$ and $\mathbf{v}$ specify the dynamical problem to be treated e.g., a flare in the corona.

However, Parker agrees that there can be a real and net longitudinal current

in the photosphere, only insofar as the magnetic field is not in a fibril state. Also, a net longitudinal current would be inferred for a non-fibril (monolithic) mono-polar magnetic region for which the encircling transverse magnetic field $\mathbf{B}_\perp$ declined outward as $1/\varpi$. A faster decline, as is seen in our analysis, indicate no net current. So, from our results viz., no net current in the monopole of sunspot fields and decline of $\mathbf{B}_\perp$ faster than $1/\varpi$, we can not conclude whether the sunspots are in the fibril state or in the monolithic state.

Parker (1996) also mentions the possibility of global currents in the corona, continuing down to the height where the first splicing takes place. In other words, the individual magnetic fibrils on the lower reaches of the solar atmosphere expand above the photosphere to fill all the available space and thus, the field does not remain in the fibril state in the corona but merges in forming a tissue of contiguous flux bundles with a net current in the corona (Parker, 1981a,b, 1983a,b, 1994). The net longitudinal current remains zero, and the overall torsion of the magnetic field involves the currents within each flux bundle and also, it involves the equal and opposite currents present in the boundaries between the contiguous flux bundles (Parker, 1979, Pp.172). The total longitudinal current falls to zero in the lower reaches where the field first cleaves. But the current is conserved. Then, what happened to the longitudinal current flowing along the continuous field at coronal heights? Parker (1996) answers this question as follows: The splitting of a monolithic field into fibrils is not a force-free operation. There are currents flowing perpendicular to the field on the surface of the each fibril. The external fluid pressure confines the fibrils by pushing them inwards. Plasma pressure decreases with height and thus the external pressure reduces, thereby merging the fibril bundles into a monolithic field. It would therefore be interesting to look for the net currents at higher reaches of the solar atmosphere.

This is very important because several theories of flares (Melrose, 1995) and CME triggers (Forbes and Isenberg, 1991; Kliem and Török, 2006) rely heavily on the existence of net currents in the corona above the sunspots.

Future large ground based telescopes equipped with adaptive optics and multi spectral line capabilities would go a long way in addressing these issues. In the meantime, direct measurement of the global twist of sunspots using parameters like the SASSA should serve as proxies for estimating the net currents of active regions in the corona. The SASSA will also be a better parameter to base a fresh look at the hemispheric rule in photospheric chirality.

Chapter 6

Evolution of Active Region Vector Magnetic Fields: *Hinode* (SOT/SP) Observations

6.1 Introduction

Observing and monitoring the evolution of the vector magnetic field of an active region by studying various magnetic parameters e.g. twist, can help us in predicting the solar eruptions on the Sun. Here, we study some of such parameters which appear to be extremely useful to predict the eruptions on the Sun.

Magnetic shear at the polarity inversion lines have been studied for the purpose of predicting flares by many researchers (e.g., Hagyard et al., 1984, 1990; Ambastha et al., 1993; Hagyard et al., 1999). The magnetic energy computation also has been made by these and many other researchers. But understanding and predicting flares have not been yet possible. We make here an effort to decide

a critical threshold of magnetic twist by studying two parameters. These parameters are: (1) spatially averaged signed shear angle (SASSA), which gives the global twist present in a sunspot irrespective of force-free nature and shape of the sunspot (Tiwari et al., 2009b); (2) force-free parameter α, which gives the degree of twist per unit axial length (Tiwari et al., 2009a) under force-free assumption.

We have studied the evolution of these parameters in time series vector magnetograms of one highly eruptive and another quiet sunspot. These parameters are evaluated in many vector magnetograms of an active region (AR) NOAA 10930. The AR 10930 was highly eruptive and is the most active sunspot observed by Hinode. Three major X-class flares of X6.5, X3.4 and X1.5 were observed by Hinode (SOT/SP) on 06, 13 and 14 December 2006 respectively. Many C and B class flares were also associated with the same sunspot, as is shown in Table 6.1.

Various aspects of the AR 10930 have already been studied such as flux emergence (Zhang et al., 2007; Kubo et al., 2007), sunspot rotation (Su et al., 2008) evolution of magnetic field (Su et al., 2007; Moon et al., 2007; Wang et al., 2008a; Schrijver et al., 2008; Guo et al., 2008), Hα flare ribbons (Isobe et al., 2007), umbral dots (Bharti et al., 2007), intermittency in the photosphere (Abramenko et al., 2008), radio burst events (Yan et al., 2007; Wang et al., 2008b), coronal mass ejections (Liu et al., 2008), magnetic helicity evolution (Magara and Tsuneta, 2008), filament eruption (Williams et al., 2009), helicity sign at different heights in the solar atmosphere (Tiwari et al., 2008, 2009c), penumbral flows (Tan et al., 2009), its relation to extreme ultraviolet (EUV) emissions (Harra et al., 2009), temporal development of α-distribution (Magara, 2009), coherent lateral motion of penumbral filaments (Gosain et al., 2009) etc.

We have also studied the evolution AR NOAA 10961 which is a non-eruptive sunspot observed by SOT. Our purpose of this study is to find the difference

between the evolution of erupting and non-erupting active regions (ARs). Is it possible to decide a critical threshold of twist for different classes of X-ray flares.

In the following section (Section 6.2), we discuss the magnetic parameters: the SSA and the force-free parameter α, very briefly. In Section 6.3, we describe the data sets used. Section 6.4 describes the analysis and results obtained. Finally in Section 6.5 we present our conclusions.

6.2 A Brief Description of the Parameters Studied: the SSA and the α

6.2.1 The SSA

Signed shear angle (SSA) represents the angular deviation of observed transverse vectors from the potential transverse vectors with positive or negative sign. The spatially averaged value of SSA (SASSA) is taken to infer the global twist of the whole sunspot. This parameter gives the actual twist present in the sunspots irrespective of the force-free nature (Tiwari et al., 2009b) and shape of sunspots (Venkatakrishnan and Tiwari, 2009). For more details, we refer the readers to follow the above two references and Chapters 4 and 5 of this thesis.

6.2.2 The α Parameter

The spatially averaged or global value of force-free parameter α has been used to infer the twist as well as the sign of magnetic helicity for a long time. Both the two inferences are physically incorrect (Tiwari et al., 2009a). The α parameter actually gives the degree of twist per unit axial length (see Appendix A of Tiwari

et al. (2009a)). The photosphere is not really force-free (Metcalf et al., 1995) and net current in a sunspot does not exist (Venkatakrishnan and Tiwari, 2009), thereby preventing us to believe on the existence of a global α.

On the other hand, the global alpha (α_g) values of sunspots bear the same sign as the global twist of sunspots (Tiwari et al., 2009b). However the magnitudes are not correlated. The α_g gives the axial gradient of twist of sunspots under force-free condition. Why does the azimuthal twist correlate with the axial gradient of twist in sign? This question is still unanswered. We therefore, considered the α parameter too in our present study.

6.3 The Data Sets Used

We have used the series of vector magnetograms of an eruptive AR NOAA 10930 and a non-eruptive AR NOAA 10961 obtained from the Solar Optical Telescope/Spectro-polarimeter (SOT/SP: Tsuneta et al. (2008); Suematsu et al. (2008); Ichimoto et al. (2008)) onboard *Hinode* (Kosugi et al., 2007).

The *Hinode* (SOT/SP) data have been calibrated by the standard "SP_PREP" routine developed by B. Lites and available in the Solar-Soft package. The prepared polarization spectra have been inverted to obtain vector magnetic field components using an Unno-Rachkowsky (Unno, 1956; Rachkowsky, 1967) inversion under the assumption of Milne-Eddington (ME) atmosphere (Landolfi and Landi Degl'Innocenti, 1982; Skumanich and Lites, 1987). We use the "STOKESFIT" inversion code developed by T. R. Metcalf and available in the Solar-Soft package. The latest version of the inversion code is used which returns the true field strengths along with the filling factor.

There is an inherent 180° ambiguity in the azimuth determination due to

insensitivity of Zeeman effect to a 180° flip in the azimuth. Numerous techniques have been developed and applied to resolve this problem, still complete resolution is not possible. The chromospheric and coronal structures are also proposed to complement the other methods. The 180° azimuthal ambiguity in our data sets have been removed by using acute angle method (Harvey, 1969; Sakurai et al., 1985; Cuperman et al., 1992). All the data sets used, have high spatial sampling with ~ 0.3 arcsec/pixel. A few observations are observed in "Normal mode" of SOT with a spatial sampling of ~ 0.16 arcsec/pixel.

The noise in the data has been minimized in the following way: the pixels having transverse (B_t) and longitudinal magnetic field (B_z) values greater than a certain level are only analyzed. To decide this critical threshold, a quiet Sun region is selected for each sunspot and 1σ deviation in the three vector field components B_x, B_y and B_z are evaluated separately. The resultant deviation in B_x and B_y is then taken as 1σ noise level for transverse field components while the deviation in B_z is taken as the 1σ noise level for the line of sight field. Only those pixels with longitudinal and transverse fields simultaneously greater than twice the above mentioned noise levels are analyzed.

We have also used the GOES X-Ray plots to infer the position of different flares during 8-15 December 2006. The data sets with their observation details are given in Table 6.1. The flares related with sunspots at different times are given in this table. The dotted lines in Figures 6.8 and 6.9 show the times of these flares along with the values of SASSA, and global α. The results in detail are given in the following section.

Table 6.1: List of the X-Ray flares associated with the active regions studied: NOAA 10930 and NOAA 10961.

AR NOAA 10930			AR NOAA 10961
Date & Time(UT)	X-Class Flares	Date & Time(UT)	X-Class Flares
06 Dec 2006: 1845	X6.5	27 Jun 2007: 1800	B9
07 Dec 2006: 1910	M2	28 Jun 2007: 1715	B3
08 Dec 2006: 0435	B6	29 Jun 2007: 2010	B9
08 Dec 2006: 2020	B3	30 Jun 2007: 0135	A4
09 Dec 2006: 1055	C1	30 Jun 2007: 1925	A2
09 Dec 2006: 1915	B2	01 Jul 2007: 0825	B2
10 Dec 2006: 0730	B5	01 Jul 2007: 2150	B1
10 Dec 2006: 1715	B1	02 Jul 2007: 0345	A0
11 Dec 2006: 0815	C2	02 Jul 2007: 2245	A0
11 Dec 2006: 1745	B1	03 Jul 2007: 0025	A0
12 Dec 2006: 2245	B6	03 Jul 2007: 1910	A0
13 Dec 2006: 0240	X3.4	04 Jul 2007: 1330	A7
13 Dec 2006: 1825	C1	04 Jul 2007: 2005	A1
14 Dec 2006: 2215	X1.5	05 Jul 2007: 0515	A2
15 Dec 2006: 0000	C2	05 Jul 2007: 2245	A0
16 Dec 2006: 0910	B8	06 Jul 2007: 0340	A1
16 Dec 2006: 2025	B3	06 Jul 2007: 2245	A0
17 Dec 2006: 1710	C2		

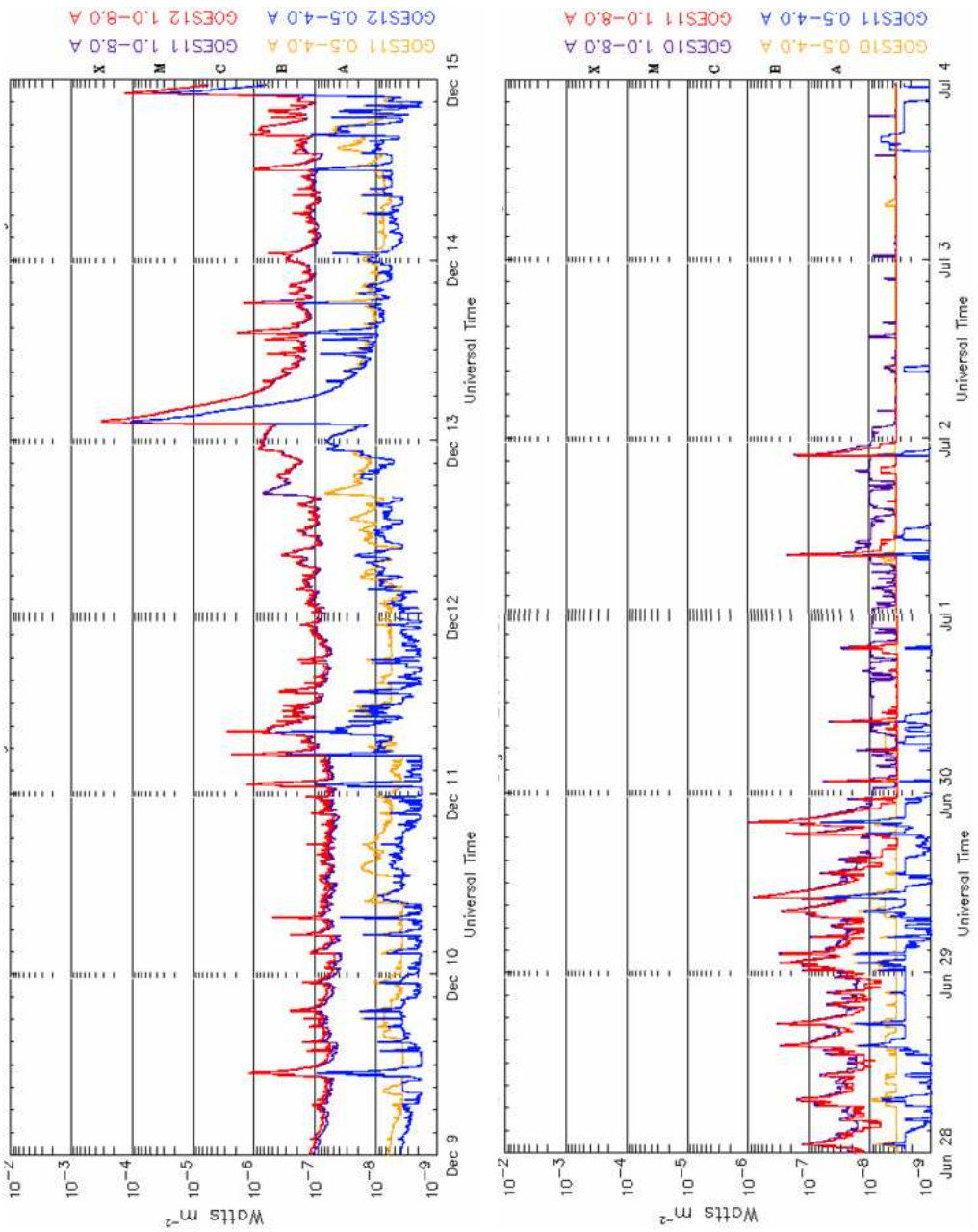

Figure 6.1: Plots of the time variation of the X-ray flux from the GOES 12 satellite. Upper panel: The data ranges from 09 December 2006 to 15 December 2006. Wavelengths are given on the plots itself. Lower panel: The X-ray plots of June 28, 2007 to July 4, 2007 are shown. We can see that the activity was more in NOAA AR 10930 and it was less in NOAA AR 10961. Only a few (mostly A and B class) small flares occurred in NOAA AR 10961 whereas NOAA AR 10930 was very active. Many C-class flares were occurring and two X-class flares can be observed in the upper panel. The details are also given in Table 6.1.

6.4 Data Analysis and Results

The Figure 6.1 shows GOES X-Ray plots of different X-class flares observed for many days during the passage of AR NOAA 10930 and NOAA 10961. We can see that the activity in NOAA 10930 increases with time. The reverse behaviour can be observed for NOAA 10961.

A large number (34) of vector magnetograms of NOAA AR 10930 have been analyzed. Also, 28 vector magnetograms of NOAA AR 10961 are analyzed to study the evolution of these sunspot magnetic fields. The continuum images of some of these sunspots NOAA 10930 and NOAA 10961 are shown in the Figures 6.2 and 6.5 respectively. It can be seen that the small and positive polarity of NOAA AR 10930 gets high twist with time and get diffused and separated from the big opposite polarity spot with time. Similarly, a small portion of the NOAA AR 10961 goes away and gets diffused with time. But unlike to the case of NOAA AR 10930, this small region is of the same polarity.

Corresponding transverse vectors and contours of vertical fields for both the sunspots NOAA AR 10930 and NOAA AR 10961 are shown in Figures 6.3 and 6.6 respectively. From the figures, it can be noticed that the vectors in the big and negative spot in NOAA AR 10930 do not evolve much, but the small positive spot show significant evolution of transverse vectors. They show small twist in the beginning and increase with time. Afterwards, the vectors show patchy and less twisted behaviour with diffused parts of this spot. The evolution of transverse vectors can be also observed in NOAA AR 10961. In this case vectors are twisted in the beginning and show decrease of twist with time. Only a few sunspots in the beginning show a relative small twist. Also, the evolution of local α in these two sunspots is shown in Figures 6.4 and 6.7.

Figure 6.8 shows the plots of global values of the SSA, and the alpha in NOAA

AR 10930. The dotted lines show the time and class of flares. The lines with big dashes represent X-class X-ray flares and the lines with smaller dashes represent C and B class flares respectively. From the plot of SASSA, it is very clear that any X-class flare happened only when the SASSA was greater than -8 degrees. If the SASSA is greater than -4 degree, only then C-class flares took place. If SASSA is less than -4 degrees, only B-class flares happened. Similar plots for the quiet sunspot NOAA AR 10961 is shown in Figure 6.9. Here the big dashes show B-class flares positions and smaller dashed lines show A-class flares. No other flares happened in this sunspot. We can see that the SASSA in this case also indicate the similar behaviour. When the SASSA is greater than -2.5 degrees, B-class flare happened. Only small A-class flares happened when SASSA is less than -2 degrees. The exact time and class of flares can be seen in Table 6.1.

The lower panels of the Figures 6.8 and 6.9 show the evolution of global alpha (α_g) in the both sunspots with time. We can see that the α_g shows similar patterns as SASSA with time, but the magnitudes does not show a proper difference between the flaring and non-flaring sunspots. Thus, we should depend on the SASSA for studying the evolution of twist in sunspot magnetic fields.

6.5 Discussion and Conclusions

From the upper panels the Figures 6.8 and 6.9, it is very clear that a critical threshold of the SASSA can be given for each class of X-ray flare. Global α behaves in similar way but the magnitudes do not show a significant difference between the erupting and non-erupting cases. Thus, we conclude that the SASSA can be used to predict the flare activity. Although, more investigations are required, the present study seems to promise for providing a better understanding

of sunspot eruption leading to flares, CMEs and other associated events.

Once the routinely observed vector magnetograms are available, by calculating the SASSA in series of vector magnetograms, a critical threshold for different X-class flares can be established. This will provide the inputs to space weather models.

Other parameters such as, magnetic energy and tension forces can also be studied to provide a supplement for the SASSA. All these quantities, once studied together, in a large number of cases will certainly provide a good prediction of sunspot eruptivity.

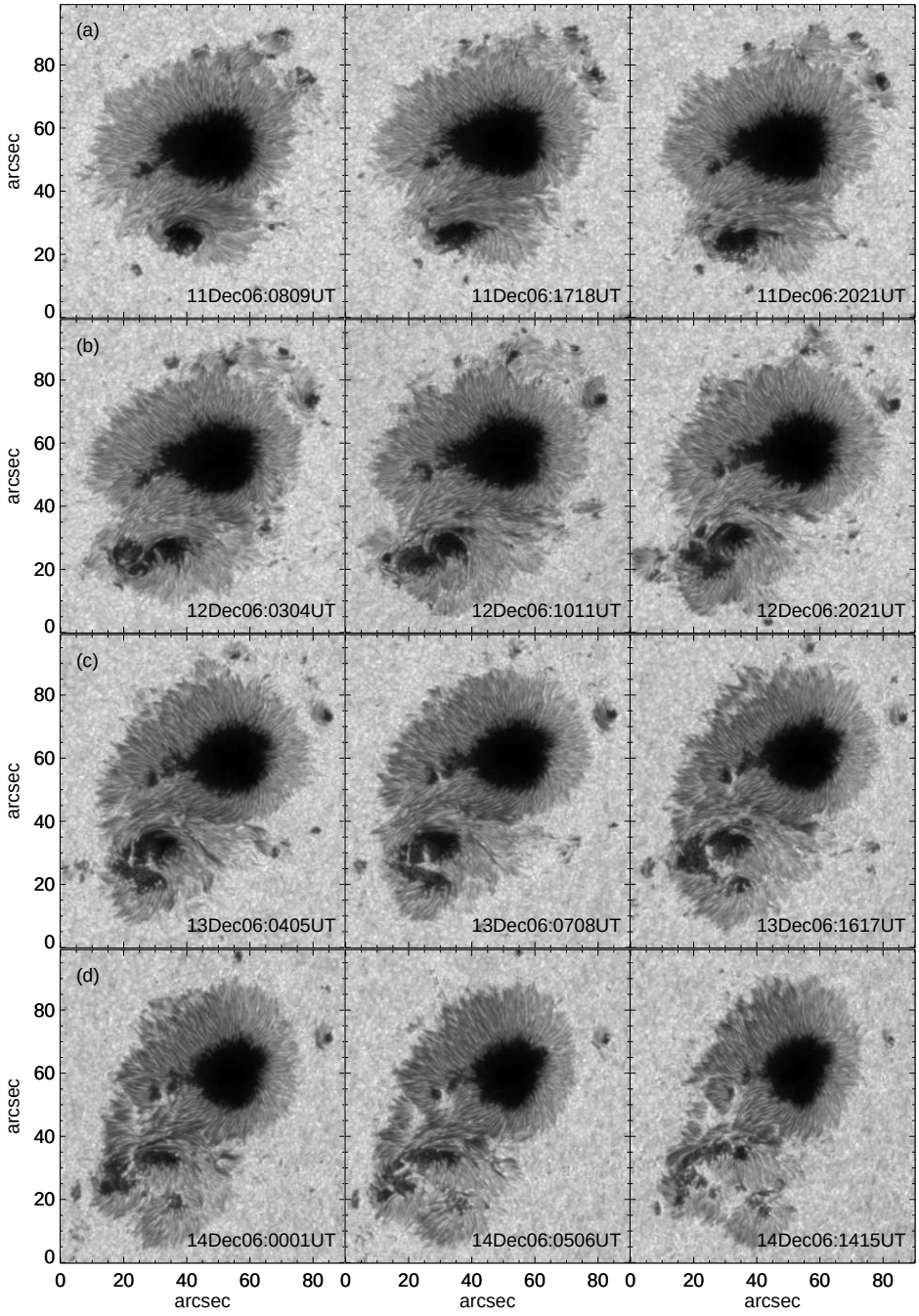

Figure 6.2: Plots of time series of continuum images of NOAA AR 10930. Three images per day are shown for four days. We can see that the evolution of the rotating positive pole is faster causing the eruption and afterwards becomes weak and diffused.

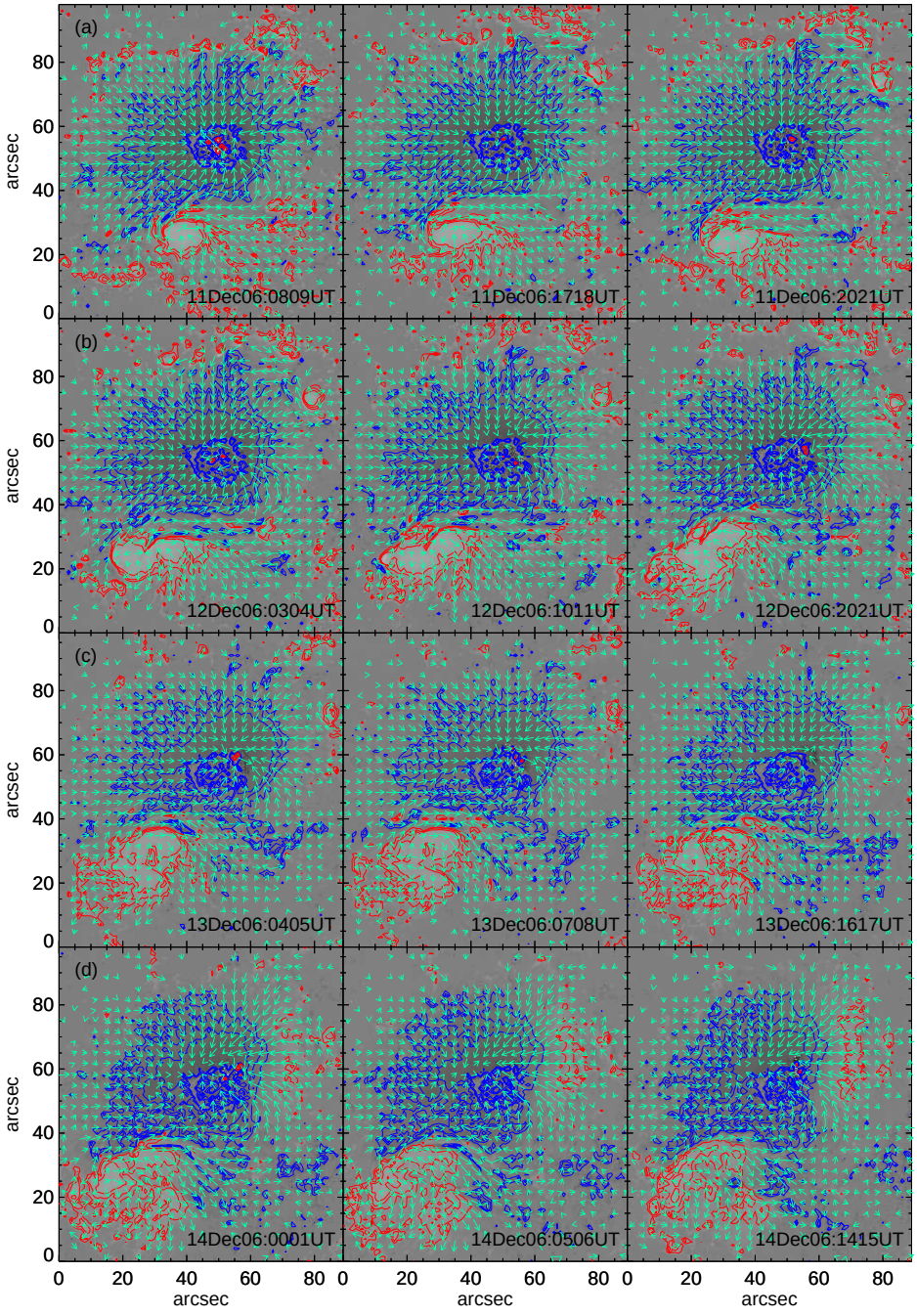

Figure 6.3: Plots of time series of transverse vectors of NOAA AR 10930. The vertical field is taken as background. The blue and red contours denote negative and positive polarities respectively. The contour levels are: $\pm 1000, \pm 1500, \pm 2000$. Three images per day are shown for four days. We can see that the evolution of the rotating positive pole is faster and causes the eruption.

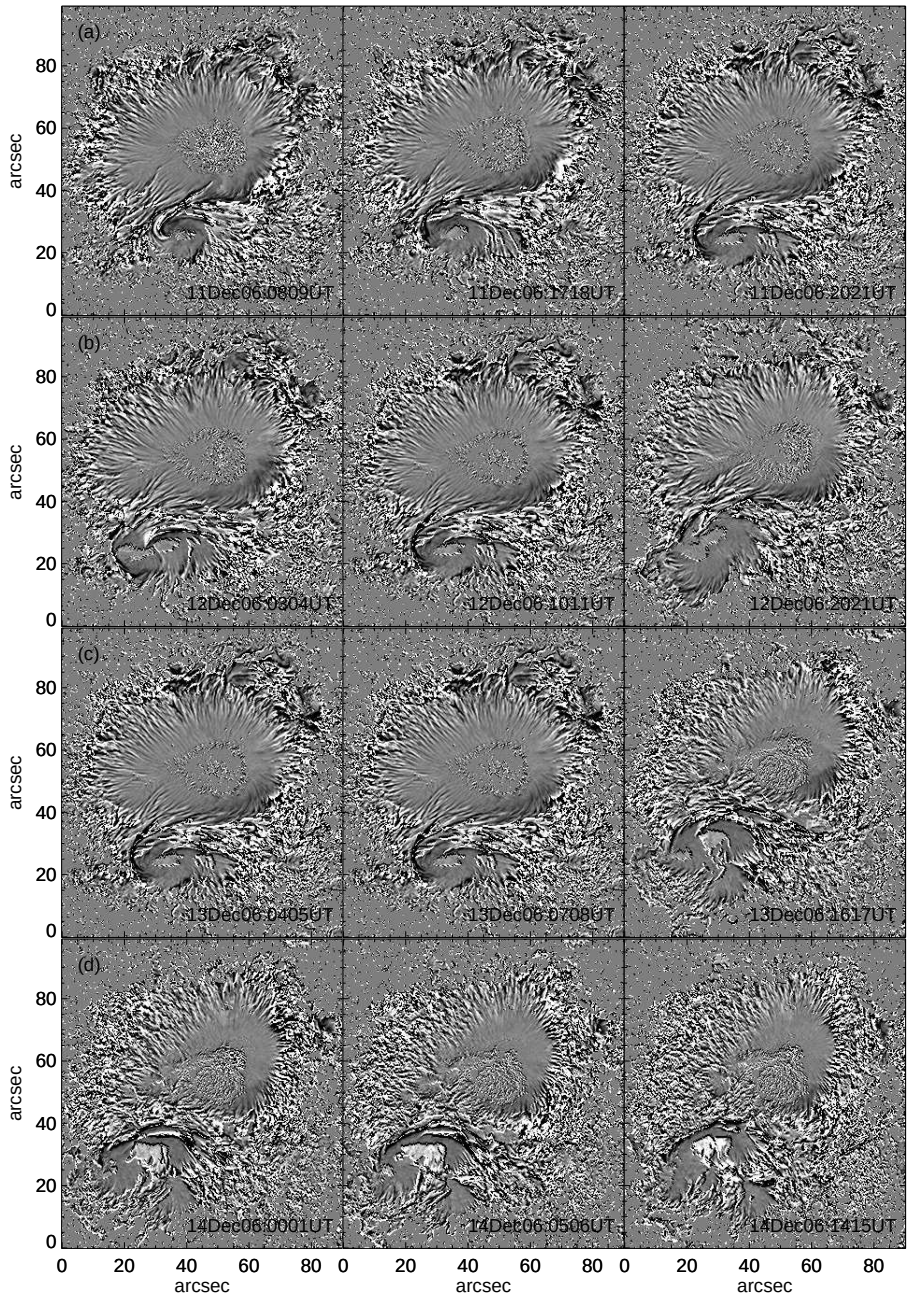

Figure 6.4: Plots of time series of local α maps of NOAA AR 10930. Three images per day are shown for four days. We can see that the evolution of the rotating positive pole is faster and causes the eruption.

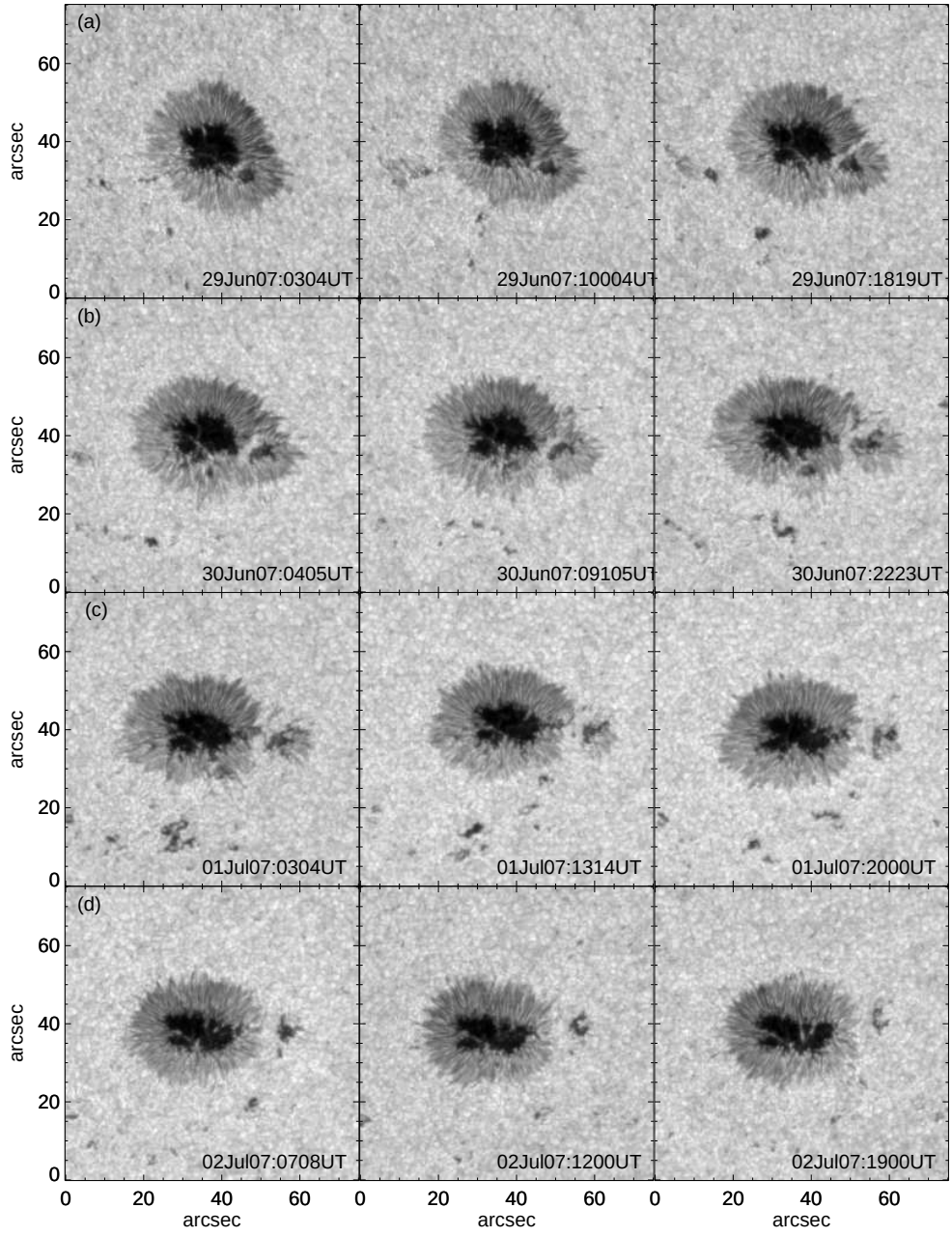

Figure 6.5: Plots of time series of continuum images of NOAA AR 10961. Three images per day are shown for four days. We can see that a small portion of the same polarity gets separated and goes away with the sunspot. The sunspot becomes more relaxed with time.

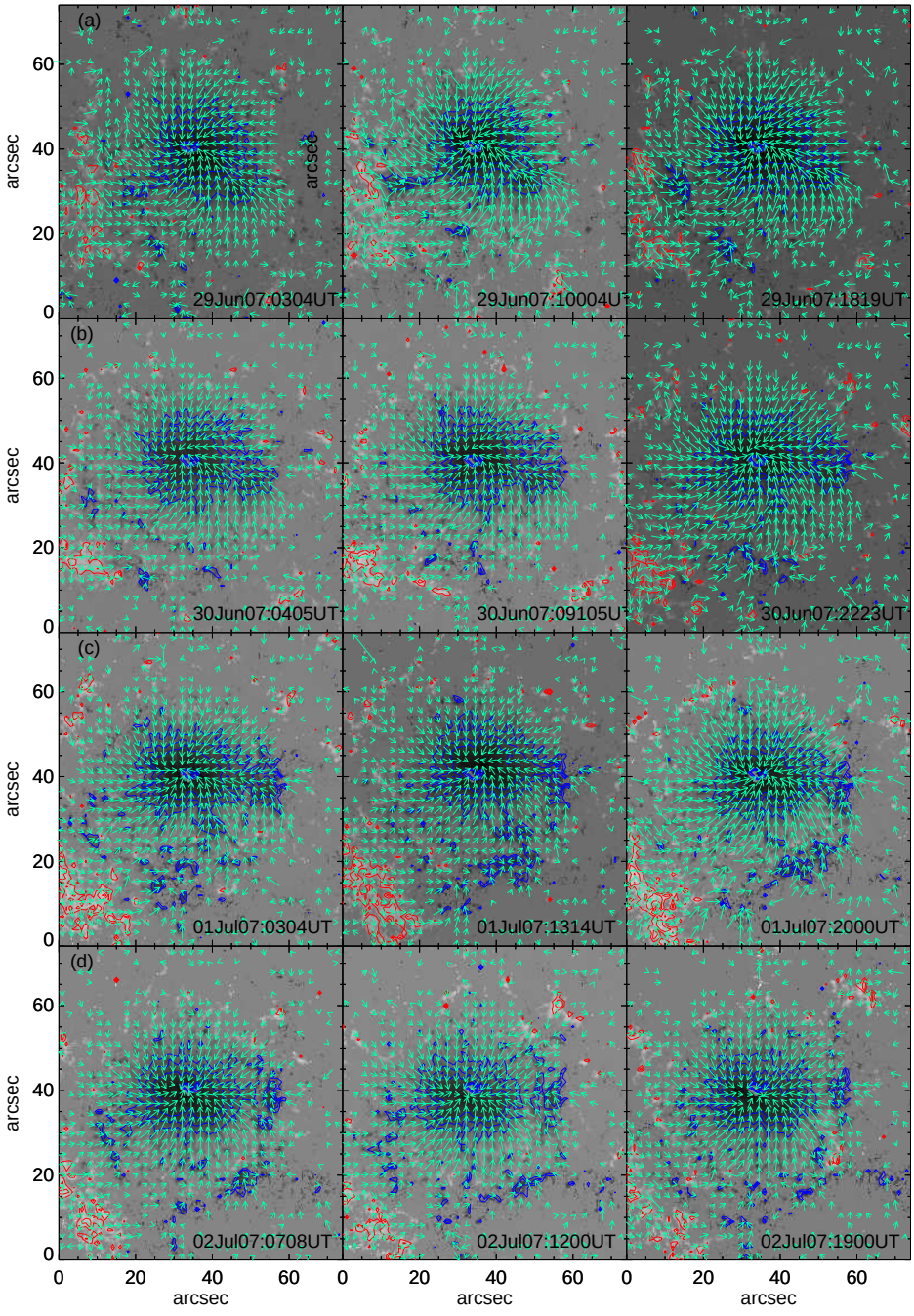

Figure 6.6: Plots of time series of transverse vectors of NOAA AR 10961. The vertical field is taken as background. The blue and red contours show negative and positive polarities respectively. The contour levels are: $\pm 1000, \pm 1500, \pm 2000$. Three images per day are shown for four days. We can see that a small portion of the same polarity gets separated and goes away with the sunspot. The sunspot becomes more relaxed with time.

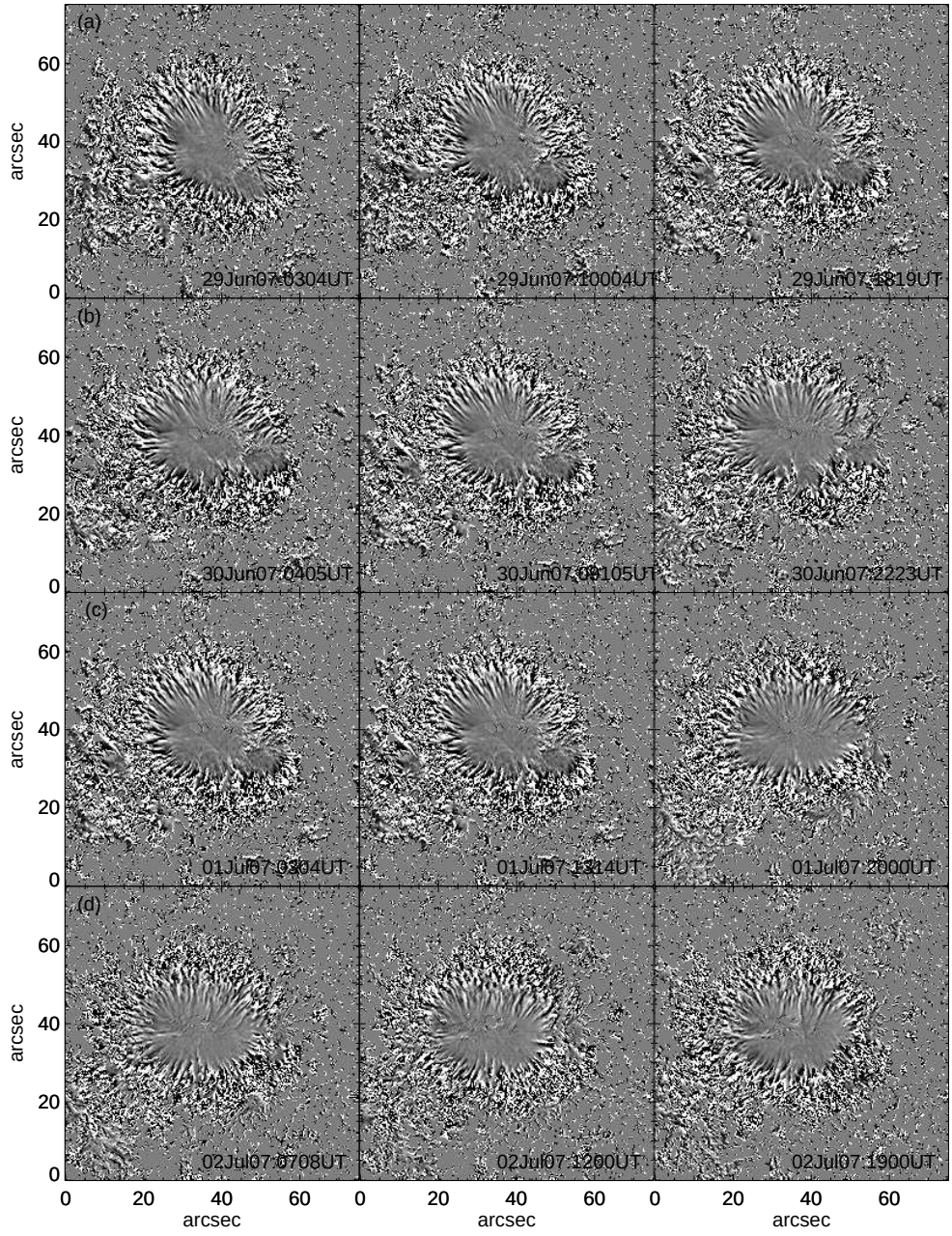

Figure 6.7: Plots of time series of local alpha maps of NOAA AR 10961. Three images per day are shown for four days. We can see that a small portion of the same polarity gets separated and goes away with the sunspot. The sunspot becomes more relaxed with time.

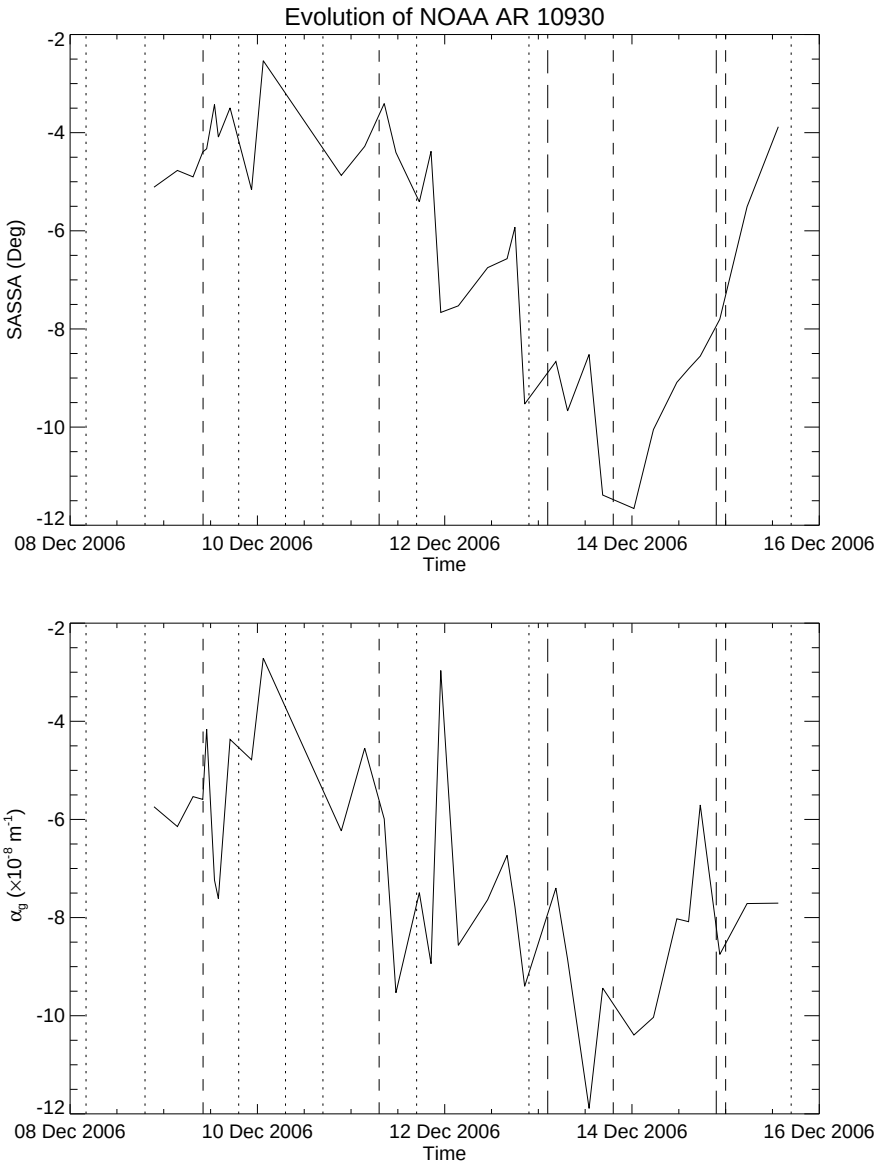

Figure 6.8: The time variation plots of spatially averaged SSA (SASSA), and global α for AR NOAA 10930. Dotted lines represent the time of different flares as given in Table 6.1. We can see that a lower boundary for SASSA and α_g can be decided for X-class and other flares. See text for details.

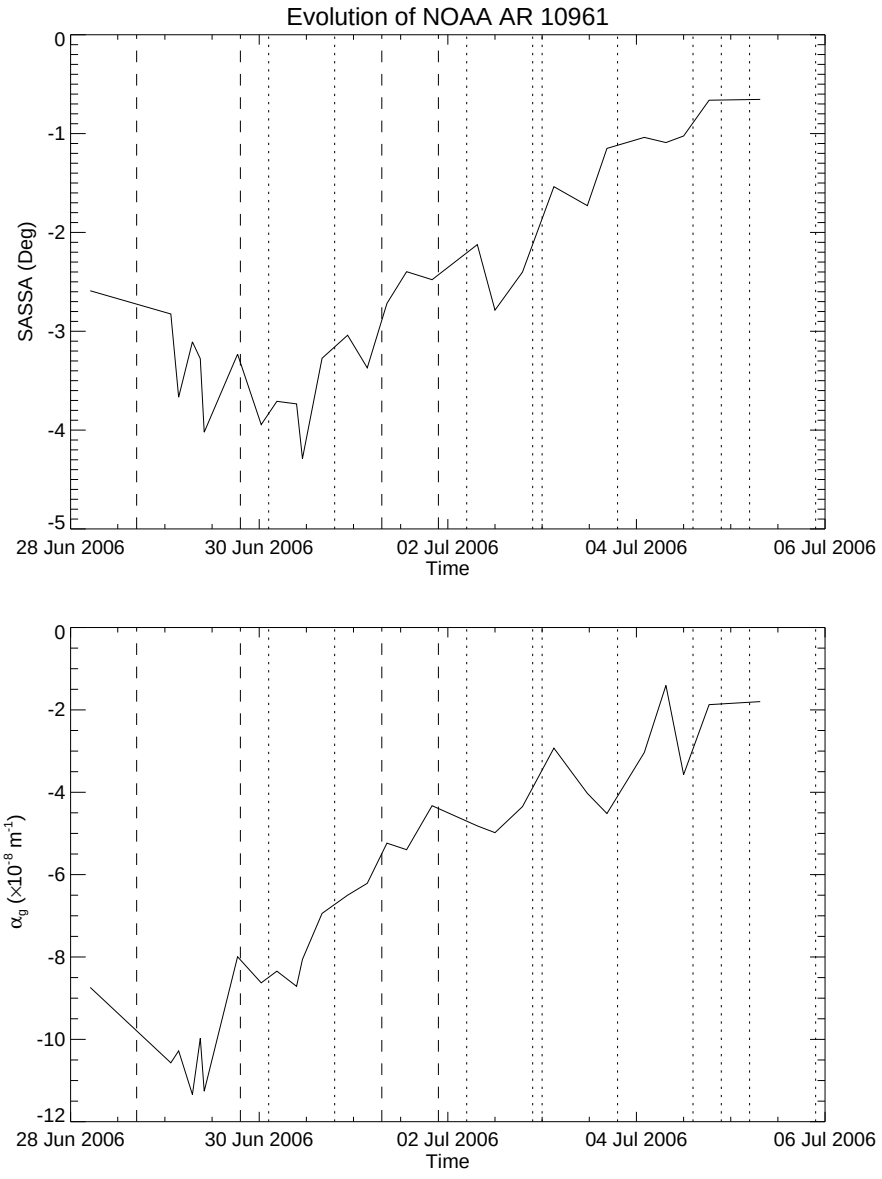

Figure 6.9: The time variation plots of SASSA, and global α_g for AR NOAA 10961. Dotted lines represent the time of different flares as given in Table 6.1. We can see that a lower boundary for SASSA and α_g can be decided for X-class and other flares. See text for details.

Chapter 7

Sign of Helicity at Different Heights in the Solar Atmosphere

7.1 Introduction

In this Chapter, we investigate the relation between the sign of twist and therefore helicity and chirality of solar features observed at different heights in the solar atmosphere.

As discussed in earlier chapters, the magnetic fields exhibit chirality and is observed in most of the solar features like filament channels, filaments, sunspots, coronal loops, coronal X-Ray arcades and interplanetary magnetic clouds (IMCs) (Seehafer (1990); Pevtsov et al. (1995); Martin (1998) and the references therein). First of all G.E. Hale in 1925 (Hale, 1925, 1927) observed vortices in Hα around sunspots and he called these features as 'sunspot whirls'. He postulated a hemispheric rule for the chirality of chromospheric whirls. This was later confirmed with a larger data set by Richardson (1941). It was reported by many researchers

later that negative/positive helicity dominates in the northern/southern hemisphere. For active regions the hemispheric helicity rule holds in the photosphere, see Hagino and Sakurai (2005) and references therein. Similarly for the chromospheric and coronal helicity rules, see Bernasconi et al. (2005) and references therein, and Pevtsov et al. (2001) and references therein. The topology of chromospheric and coronal features decide the sign of the associated helicity. Chirality is the term used for the sign of the helicity in these features. Thus, helicity is a physical attribute of chirality. The chirality of active region features shows correspondence with the sign of the helicity in the associated lower/upper atmospheric features. For example, the chirality of X-ray features with S (inverse-S) shapes are associated with sinistral (dextral) filaments (Martin, 2003; Rust, 2003). Chae (2000) reported for a few cases that active filaments showing dextral/sinistral chirality are related with negative/positive magnetic helicity. Pevtsov et al. (2001) demonstrated correspondence between photospheric and coronal chirality for a few active regions. However, this needs to be confirmed. We have reported similar helicity signs at photospheric, chromospheric, and coronal heights for a few active regions (Tiwari et al., 2008). Recently, Chandra et al. (2009) also reported similar sign of helicity for a NOAA AR 10365 at three different heights in the solar atmosphere. Lim and Chae (2009) studied the sign of intermediate filament chirality and found strong correlation with the sign of AR magnetic helicity. The filaments which are formed between or around active regions, are called intermediate filaments. They inferred the sign of magnetic helicity of AR's from the chirality of coronal intensity images giving the reference as following: Canfield et al. (2007) which is incorrect. (Burnette et al., 2004) found that the twists of active regions at photosphere and corona were similar (strongly correlated). This behaviour was in accordance with the modeling of Longcope and Welsch (2000).

But one must remember that the results of Burnette et al. (2004) do not show 100% correlation of photospheric and coronal twists of AR's.

We compute twist of AR directly to get the sign of magnetic helicity at photosphere and infer the sign of magnetic helicity at associated chromospheric and coronal features by identifying the chirality in the associated intensity images.

The chirality of the Hα filament can be directly recognized by looking at the filament barbs (see Figure 7.1 of this Chapter for a cartoon diagram of the filament). If the orientation of the barbs is clockwise when we go from filament axis to barbs through an acute angle, the chirality of the filament is known to be dextral and if it is counterclockwise, the chirality is sinistral. Martin et al. (2008) show that the chirality of the solar features can be used for resolving 180 degree azimuthal ambiguity in the solar vector magnetic field. It is believed that there is one-to-one correspondence between the filament chirality and the magnetic helicity sign. A right-handed twist and a clockwise rotation of the loops, when viewed from the above implies positive helicity or chirality and vice-versa.

Comparison between magnetic helicity signs at different heights in the solar atmosphere may be a useful tool to predict solar eruptions leading to interplanetary events. Also, it may help to constrain modeling chromospheric and coronal features taking the photosphere as boundary condition. However, the data required to do this are not directly available and are often non-conclusive, sometimes due to poor resolution and sometimes due to equal distribution of positive and negative chirality in magnetic features. Vector magnetic fields are not available as routinely as is necessary to derive photospheric twist values. Chromospheric Hα images may be available most of the time by combining data from different telescopes, but are not always conclusive due to lack of angular resolution as well as due to presence of both kind of whirls showing positive and negative chirality. As

we know now that both kind of twist are present in the sunspots (Tiwari et al., 2009a) but there exists a global twist and that is our main target to study for the sign of magnetic helicity. Analysis of coronal loop observations is required to determine coronal helicity signs, but these are also not available routinely. Above all, it is hard to find data taken simultaneously at different heights in the solar atmosphere. In this work we combine photospheric chromospheric and coronal data from multiple solar observatories and telescopes. They were often not taken at precisely the same time. We therefore assume that the sign of the magnetic helicity does not change within a few hours.

7.2 The Sign of Magnetic Helicity at Photosphere

The sign of helicity in the photosphere is usually found from the force-free parameter α, e.g., $\alpha_{\rm best}$ (Pevtsov et al., 1995), averaged α, e.g., $< \alpha_z > = < \mathbf{J_z}/\mathbf{B_z} >$ (Pevtsov et al., 1994) with current density $\mathbf{J_z} = \nabla \times \mathbf{B_z}$, where $\mathbf{B_z}$ is the vertical component of the magnetic field. Some authors have used the current helicity density $H_c = \mathbf{B_z} \cdot \mathbf{J_z}$ (Bao and Zhang, 1998; Hagino and Sakurai, 2005). A good correlation was found between $\alpha_{\rm best}$ and $\langle \alpha_z \rangle$ by Burnette et al. (2004) and Leka et al. (1996). The force-free parameter α has the same sign as the magnetic helicity (Pevtsov et al., 2008) but not in all conditions (Tiwari et al., 2009a). Also, the current helicity (which is not a conserved quantity like magnetic helicity) has the same sign as that of the magnetic helicity (Seehafer, 1990; Hagyard and Pevtsov, 1999; Pevtsov, 2008; Sokoloff et al., 2008). Theoretically, saying that the sign of α has the same sign as magnetic helicity is not correct (see Section 3.3). At the same time, we find that α_g bears same sign as twist computed from the

spatially averaged signed shear angle (SASSA) as discussed in earlier chapters. Because twist is a component of magnetic helicity and supposed to bear the sign of magnetic helicity, SASSA bears the same sign as the magnetic helicity. Thus any out of the two: α_g and SASSA, can be used to infer the sign of magnetic helicity on the photosphere. However, SASSA is better measure of twist helicity, irrespective of force-free nature and shape of sunspots, and thus a better quantity to infer the sign of magnetic helicity.

It is worth mentioning at the same time that there are other ways used for inference of sign of chirality on the photosphere using line of sight field (Luoni et al., 2004; López Fuentes et al., 2000; Démoulin and Pariat, 2009). However using neutral lines for inferring the sign of magnetic helicity seems to be ambiguous (Lim and Chae, 2009) and we do not use these methods for getting the sign of magnetic helicity.

In this study, we use the sign of the spatially averaged SSA (SASSA) as the sign of magnetic helicity, which gives the global twist present in the active region.

7.3 The Chromospheric Sign of Magnetic Helicity

Numerical measurement of the sign of the chromospheric and coronal magnetic helicity is not possible due to non-availability of vector magnetic field observations at these heights. However, the twist present in the morphological intensity features have been reported already since a long time ago (Hale, 1925; Richardson, 1941) to tend to follow the hemispheric helicity rule, independent of the solar cycle. Later, many researchers studied the chirality of different chromospheric features such as filaments, fibrils, filament channels etc. (Martin et al.,

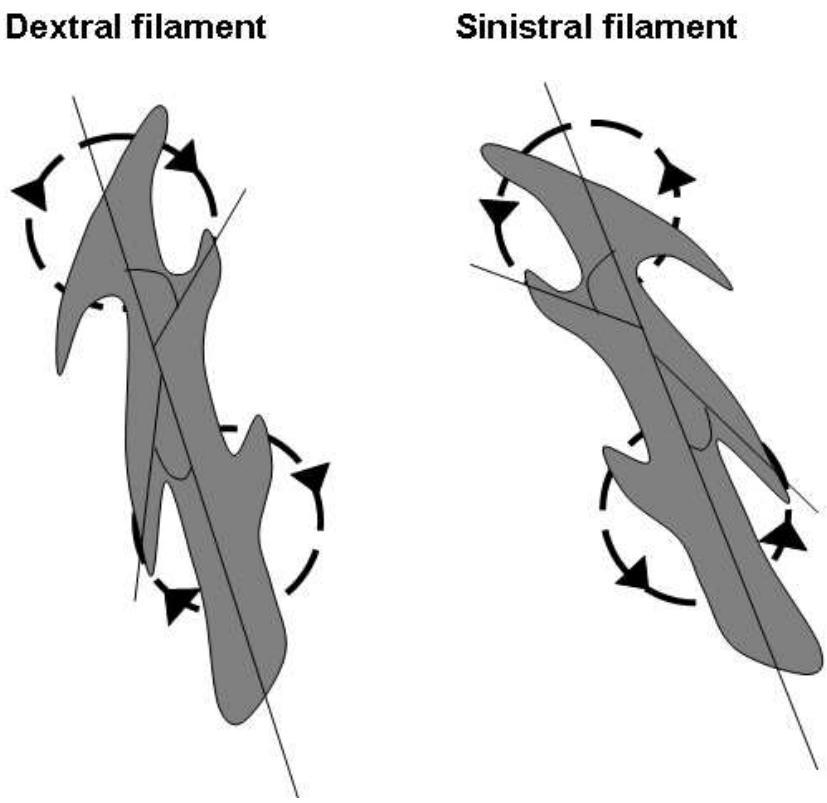

Figure 7.1: A cartoon image of filaments showing dextral and sinistral chirality. If we move from filament axis towards barb through an acute angle and the orientation is clockwise, then the filament is dextral and reverse is true for the sinistral filament.

1994; Martin, 1998; Aulanier et al., 1998; Martin, 2003; Démoulin and Pariat, 2009). The sign of chirality of chromospheric features can be easily drawn by looking at the them. For a pictorial presentation of many of these features, see Martin (1998). We have shown a cartoon diagram to identify dextral and sinistral filaments in Figure 7.1.

If we go from filament axis through an acute angle towards the barbs and the resulting rotation is counterclockwise, then the chirality is called sinistral and helicity is positive. Reverse is true for the dextral chirality. Similarly, the chirality of sunspot whirls can be defined. If the rotation is counterclockwise while going towards penumbral region from umbral region along the whirls, then the chirality is sinistral and vice versa (see Figure 4.1 for a cartoon diagram of sunspot whirls). In the cases where both kind of whirls are present, we take the sign of chirality as the sign of dominant sense of chirality according to Balasubramaniam et al. (2004). As we know both kind of twists are present on the photospheric sunspots and also chromospheric features show both kind of chirality in a single feature, the only way to get a global sense of twist is taking the dominant sign of helicity.

We use the chirality of these chromospheric features, mostly sunspot whirls and filament-barbs observed in Hα to derive its association with the photospheric sign of magnetic helicity.

7.4 The Coronal Sign of Magnetic Helicity

In the X-ray images, we usually see S, inverse-S, C and J shaped structures. The sign of magnetic helicity has been inferred from these structures by many researchers (Pevtsov et al., 1996; Rust and Kumar, 1996; Canfield et al., 1999;

Martin, 2003; Luoni et al., 2007) etc and references therein. The patterns in X-rays are normally S or inverse-S, which correspond to positive and negative chirality respectively. In the case when S or inverse-S is not visible (developed) one can distinguish the sign of chirality by looking at the partial S or inverse-S shapes. These shapes actually then appear as C or J shaped structures. Similarly for EUV images, we can identify the chirality of features by looking at their shapes.

We use such structures in X-ray images or EUV intensity images to infer the sign of magnetic helicity in the corona.

7.5 The Data Sets Used

Most of the data sets have been compiled from different solar observatories and telescopes due to the unavailability of all required data from the same place. The vector magnetic field data were obtained from the Advanced Stokes Polarimeter (ASP: Elmore et al. (1992)), the Diffraction Limited Spectro-polarimeter (DLSP: (Sankarasubramanian et al., 2004, 2006)) both at the DST, Solar Optical Telescope/Spectro-polarimeter (SOT/SP: Tsuneta et al. (2008); Shimizu et al. (2008); Suematsu et al. (2008); Ichimoto et al. (2008)) onboard Hinode (Kosugi et al., 2007) and a few from Solar Vector Magnetograph (SVM: Gosain et al. (2004, 2006)) at Udaipur Solar Observatory (USO).

Near-simultaneous Hα images from the Universal Bi-refringent Filter (UBF) at the DST are used whenever obtained along with the ASP and DLSP. These Hα images are registered first from the continuum images of DLSP data by manual method and then with automatic registration for sub-pixel accuracy.

For the vector field observations which do not have corresponding UBF data,

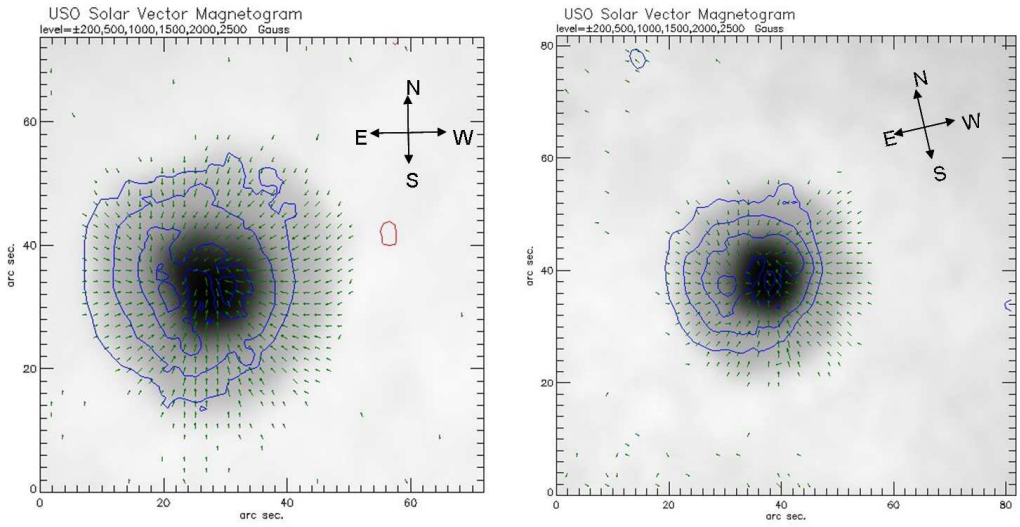

Figure 7.2: Solar vector magnetograms of NOAA AR 10935 and 10941 observed on 09 January 2007 and 06 February 2007 respectively. These data are taken from Solar Vector Magnetoraph (SVM) at Udaipur Solar Observatory (USO).

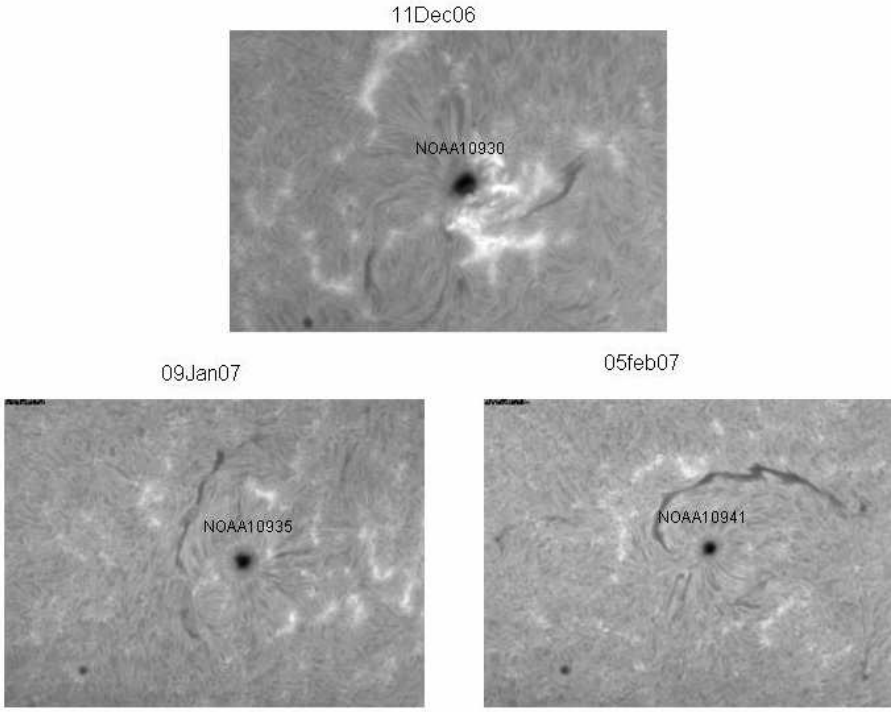

Figure 7.3: Hα images taken from Udaipur Solar Observatory (USO).

Hα images from Udaipur Solar Observatory (USO) and Big Bear Solar Observatory (BBSO) were used. We made sure that in these cases the Hα images were collected within less than a day. Standard and well-established processing was done to derive vector fields. The procedure is described in the references given above. Detailed analysis of SOT/SP data aboard Hinode is described in Chapter 4.

X-ray images for this purpose are taken from *Hinode* (XRT) and EUV images are taken from the Extreme Ultraviolet Imaging Telescope (EIT) on-board Solar and Heliospheric Observatory (SOHO). The registration of coronal images is done by taking near simultaneous full disk images at photospheric and chromospheric heights.

7.6 Results and Discussion

Table 7.1 shows that the sign of helicity at the photospheric level and the chirality in associated features at chromospheric and coronal heights are well correlated. Figure 7.4 (a) and (b) clearly show that the Hα whirls follow the transverse magnetic field vectors measured at photospheric heights. These vector data are taken from DLSP and Hα are UBF images. One more example is shown in Figure 7.5. In Figure 7.5, the background image is the Hα image taken from Spar telescope at USO and transverse vectors are derived from the vector magnetograms taken from Solar Vector Magnetograph at USO as shown in Figure 7.2. Figure 7.3 show the corresponding Hα images taken from Spar telescope at USO. The positive/negative helicity derived from the global twist in this sunspot from the photospheric vector data is directly associated with the sinistral/dextral chirality derived from the chromospheric Hα data. Also, the associated coronal data show

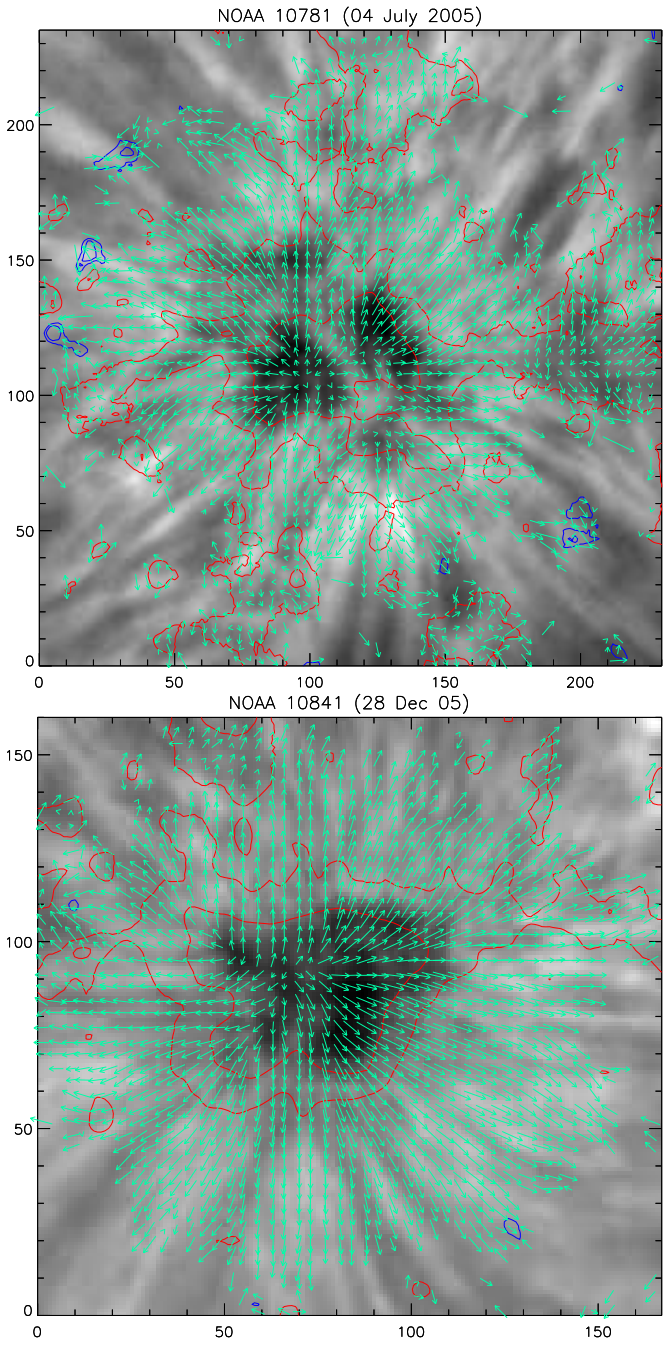

Figure 7.4: Two examples of the chromospheric sunspots (UBF images), with the photospheric transverse vectors (using DLSP data) of the same field of view over-plotted on them. The axis divisions are pixel numbers. The contours and vectors show longitudinal and transverse magnetic fields, respectively.

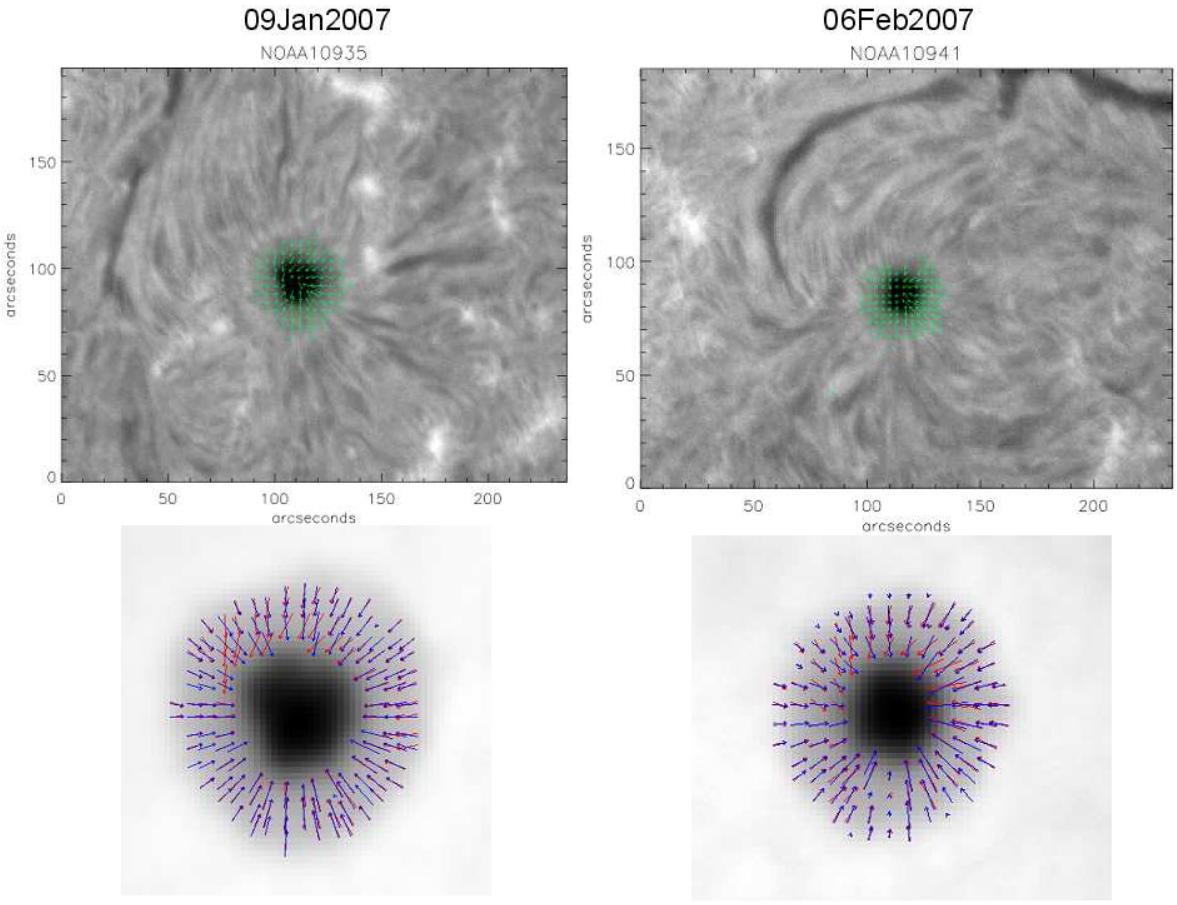

Figure 7.5: The plots of the vector magnetic fields of the sunspots overplotted upon the respective Hα images. In the lower part of the image, blue arrows show the radial direction and the red arrows show the actual vector field direction. We can see the shear of the field. The transverse vectors are obtained from the SVM at USO and the Hα images are taken from the Spar telescope at USO.

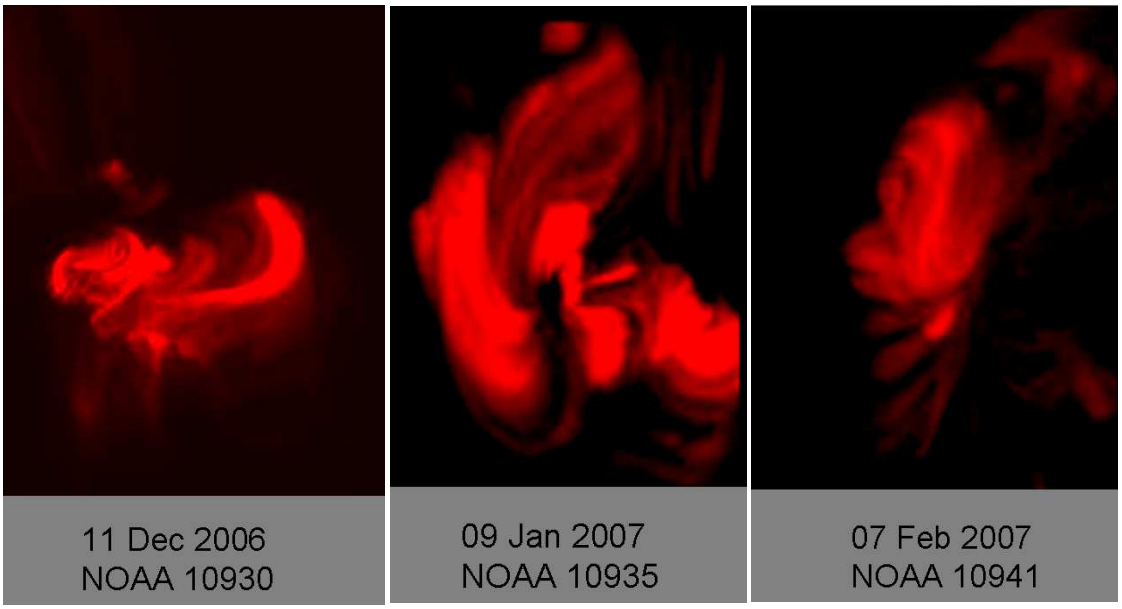

Figure 7.6: XRT (Hinode) data reverse-S sigmoid showing the dextral chirality in comparison with that of photospheric and chromospheric data. All the three panels show the negative helicity sign.

Table 7.1: List of the active regions studied. The sign of helicity at different heights and other details of the sunspots are given:

AR No. (NOAA)	Date of Observation	Photospheric Chirality	Chromospheric Chirality	Coronal Chirality	Position (Photospheric AR)
10972	07 Oct 2007	Negative	NR	NR	S05W20(t)
10971	29 Sep 2007	Positive	Positive	Positive	N03W07
10970	05 Sep 2007	Negative	Negative	Negative	S07W58(t)
10969	29 Aug 2007	Negative	Negative	Negative	S05W33(t)
10966	09 Aug 2007	Negative	Negative	Negative	S06E07
10963(−)	12 Jul 2007	Negative	Negative	Negative	S06E14(t)
10963(+)	12 Jul 2007	Negative	Negative	Negative	S06E14(t)
10961	02 Jul 2007	Negative	Negative	NA	S10W16(t)
10960	07 Jun 2007	Positive	NR	both	S07W03
10956(−)	18 May 2007	Positive	Positive	Positive	N02E07
10956(+)	18 May 2007	Positive	Positive	Positive	N02E07
10955	13 May 2007	Negative	NR	Positive	S09W35(t)
10953	29 Apr 2007	Negative	Positive(dom)	Negative(dom)	S10E22(t)
10944	03 Mar 2007	Negative	Negative	NA	S05W30(t)
10941	06 Feb 2007	Negative	Negative	Negative	S07W36(t)
10940	01 Feb 2007	Negative	Negative	Negative	S04W05
10939(−)	23 Jan 2007	Negative	Negative	Negative	S04W57(t)
10939(+)	23 Jan 2007	Negative	Negative	Negative	S04W57(t)
10935	09 Jan 2007	Negative	Negative	Negative	S07W30(t)
10933	05 Jan 2007	Negative	Negative	Negative	S04W01
10930(−)	12 Dec 2006	Negative	Negative (dom)	Negative	S05W21(t)
10930(+)	12 Dec 2006	Negative	Negative	Negative	S05W21(t)
10926	03 Dec 2006	Negative	Negative	NA	S09W32(t)
10923	16 Nov 2006	Positive	Positive	Positive(dom)	S05W30(t)
10921	06 Nov 2006	Negative	NR	Negative(dom)	S08W38(t)
10841	28 Dec 2005	Positive	Positive(dom)	Positive	N12E20(t)
10838	22 Dec 2005	Positive	Positive	NR	N17E20(t)
10808(−)	13 Sep 2005	Positive	Positive(dom)	NA	S11E17(t)
10808(+)	13 Sep 2005	Positive	Positive(dom)	NA	S11E17(t)
10804	26 Aug 2005	Negative	both	both	N11W02
10803	26 Aug 2005	Positive	Positive(both)	both	N12E53(t)
10800	26 Aug 2005	Positive	Positive(both)	both	N17W49(t)
10782	02 Jul 2005	Negative	Negative(both)	NA	S17W18(t)
10781	04 Jul 2005	Positive	Positive(dom)	NA	N13W03
10780	24 Jun 2005	Negative	Negative	NA	S08W28(t)
10752	17 Apr 2005	Positive	Positive	Positive	N02W00
10330	09 Apr 2003	Positive	Positive(dom)	Positive	N07W04
09601	03 Sep 2001	Positive	NR(both)	Negative	N14W06(t)
09596	30 Aug 2001	Positive	Positive	Positive	N21E15(t)
09591(−)	30 Aug 2001	Negative	NR	Negative	S18W36(t)
09591(+)	30 Aug 2001	Negative	NR	Negative	S18W36(t)
09590	26 Aug 2001	Negative	Negative	Negative	S23W01(t)
09585	24 Aug 2001	Positive	Positive	Positive	N14W30(t)

(t) : *transformed*

dom: dominant sense (both present)

both: both equally present

NR: Not Recognigible

NA: Not Available

similar pattern of chirality as shown in Figure 7.6.

In this analysis, we thus conclude that the sign of helicity (positive/negative) derived from global twist present in sunspots in the photosphere has one-to-one correspondence with the (sinistral/dextral) sense of chirality observed in the associated chromospheric and coronal data. We mostly use the chirality of chromospheric whirls to derive the chromospheric helicity sign. It is known (Martin, 1998, 2003) that filaments, filament channels, etc., have the same sense of chirality as the whirls above the associated active regions. The chirality of filaments associated with an active region can therefore be used to determine the chromospheric sense of chirality when high resolution Hα data are not available. For coronal intensities, the S, inverse-S, C or J shapes are used for inferring the sign of magnetic helicity.

Lim and Chae (2009) also found similar results for intermediate filaments. They concluded that the sign of intermediate filament chirality is strongly correlated with the sign of AR magnetic helicity. They used coronal features to infer the AR helicity while we use photospheric vector magnetograms to get the twist values of AR and therefore inferred the sign of magnetic helicity. We have used many of their features to find the chromospheric chirality and related directly its sign with the sign of twist helicity in the associated photospheric AR. This study is very useful as a constraint to model the chromospheric and coronal features.

Tian et al. (2001) found that the active regions having abnormal helicity are more eruptive. Is it that the AR's with changed sign of helicity with height are more eruptive? This is needed to be investigated which will help in space weather predictions.

The sign of magnetic helicity at different heights in the solar atmosphere is expected to be the same if no forces are able to distort them in the solar

atmosphere. There might be the forces acting on them but may be too weak to change the sign of helicity. But the same time we find a few exceptional cases where the sign of helicity is found not matching at the three levels. Do those cases indicate a change in helicity due to external forces? Is it that the plasma β transition phase is playing a role as suspected by Parker (1979)? The answers to these questions are beyond the present study but we will try to answer these questions in further investigations.

Chapter 8

Relation with Solar Cycle

8.1 Introduction

In this Chapter, we report on the helicity sign of the first few active regions (AR's) which emerged in the beginning of 24^{th} solar cycle. We compare the behaviour of magnetic helicity sign of AR's observed in the beginning of new solar cycle with some AR's observed in the declining phase of 23^{rd} solar cycle. These sunspots of earlier cycle are studied in the Chapters 4, 5 and 7.

Hale (1908b) looked at sunspot whirls and suspected the magnetic nature of spots. He applied the newly discovered Zeeman effect (Zeeman, 1897) and observed Zeeman splitting of sunspot spectra in 1908 (Hale, 1908a). Evershed wanted to detect the azimuthal flow of plasma along the whirls but instead discovered the radial flow of the plasma in 1909 (Evershed, 1909) at the newly established Kodaikanal observatory. Hale continued his sunspot measurements and discovered the 22 year sunspot cycle as well as the polarity law (Hale and Nicholson, 1925), confirming the global nature of the sunspot fields which required

a global dynamo.

Hale also found in 1925 (Hale, 1925), that about 80% sunspot whirls had counterclockwise orientation in the northern hemisphere and clockwise in the southern hemisphere using Hα data over three solar cycles, however only a small number of sunspots (51) were studied. He found that this behaviour was independent of the solar cycle. Richardson (1941) reinvestigated the same for the data extending over four solar cycles and concluded the similar result. He studied 141 sunspots, which again was not a big number over four solar cycles.

The subject is being intensively revisited since the 90s, and many researchers have found the same result in photospheric (Seehafer, 1990; Pevtsov et al., 1995; Bao and Zhang, 1998; Nandy, 2006) and chromospheric (Rust, 1994; Martin et al., 1993) data. This behaviour is known as "helicity hemispheric rule" as has been described several times in earlier chapters. Rust and Kumar (1996), using Yohkoh (SXT) data found that about 70% of coronal loops (sigmoids) in northern hemisphere had inverse-S shape (negative chirality) and S-shape (positive chirality) in the southern hemisphere. Tian et al. (2001) found a relationship between tilt and twist in active region magnetic fields. A negative correlation was found for 60% of their data and these active regions had "normal" chirality i.e., left/right handed twist accompanied by right/left handed writhe. One third of their data had "abnormal" chirality i.e., same sign for tilt and twist and these were all eruptive regions. Zhang (2006) found that active regions with weaker magnetic fields follow the helicity hemispheric rule while stronger fields do not. This preferential behaviour was never found very strong and recently has been a matter of debate (Bao et al., 2000; Hagino and Sakurai, 2005; Pevtsov et al., 2008). As can be seen in the Chapter 4, we (Tiwari et al., 2009b) find that most of the active regions observed during the declining phase of cycle 23 do not follow the hemispheric

helicity rule. In this chapter, we make an effort to relate this behaviour of active regions observed in decay phase of 23^{rd} solar cycle with the active regions that emerged in the beginning of the 24^{th} solar cycle till date.

As stated many times in earlier chapters, a quantitative measure of the chiral properties of these magnetic structures is the magnetic helicity (Moffatt, 1978; Berger and Field, 1984; Brown et al., 1999). The origin of chirality and magnetic helicity is still a matter of debate. Helicity might be generated by the twisting of magnetic flux tubes in the convection zone where dynamo action amplifies the fields prior to their appearance at the surface (Seehafer, 1990; Seehafer et al., 2003; Berger and Ruzmaikin, 2000). Some researchers claim that the flux tubes are originally untwisted and acquires helicity in a shallow region below the photosphere due to the shearing of the photospheric foot points of magnetic loops caused by differential motion (DeVore, 2000; Longcope et al., 1998).

There are some kinematic dynamo theories (Choudhuri et al., 2004) that predict deviations from helicity hemispheric rule at the beginning of each solar cycle. Bao et al. (2000) found the reverse sign of rule for active regions during the beginning of solar cycle 23 whereas Pevtsov et al. (2001) found no change in the hemispheric helicity rule for the same period and this matter remains unresolved. At the same time, there are few recent studies, as discussed in Chapter 4, which suspect the hemispheric helicity rule (Pevtsov et al., 2008; Hagino and Sakurai, 2005). We find in Chapter 4 as told above, that the most of the AR's observed in the declining phase of 23^{rd} solar cycle do not follow this rule. Does it mean the AR's follow reverse hemispheric helicity rule during this phase? Does the helicity rule have a long period?

Greater accuracy in the measurements will be required to settle this issue since the earlier measurements had errors up to a hundred percent (Pevtsov et al.,

1994). Similarly, the error bars in the results presented by Zhang (2006) are also very large.

Further, the variation of helicity parameter α on different scales arise from the presence of vorticity on different scales. This could produce a range of α within the same active region as reported recently by Tiwari et al. (2009b) and Su et al. (2009) and described in Chapter 4.

The long awaited 24^{th} solar cycle began in the first week of January 2008 when NOAA AR 10981 was observed. We can see in Figure 8.1 that the leading/following polarity of NOAA AR 10981 is opposite to that of the old solar cycle's (23^{rd}) sunspots. Also, it appears at a latitude N 30 and tilt angle with respect to equator is high (~ 30) in accordance with Joy's law (Hale et al., 1919). Thus it has all the characteristics of a new solar cycle's active region. The field strength is weak as usually observed in the beginning of any other solar cycle. Till the date, 18 active regions of the new solar cycle with all the above characteristics have been observed. We have inferred the chirality signs of all these active regions using chromospheric and coronal data. Also, we have computed global twist (using SASSA) of a few AR's depending on the availability of the vector magnetograms. We then, compare the behaviour of these AR's with that of old solar cycle's active regions.

There are two main motivations of this study: 1. to compare the behaviour of AR's observed in the declining phase of 23^{rd} and beginning of 24^{th} solar cycles. 2. To verify some dynamo theories which talk about the behaviour of AR helicity emerging in the beginning and declining phases of solar cycles.

As is well known that this solar cycle is behaving peculiarly and very few active regions could be observed since January 2008 when the cycle began. One interesting thing can be observed that the sunspots emerging with time seems to

decline towards equator as happens in normal cycles with time and a butterfly diagram can be constructed. However, this conclusion does not seem strong enough until we get some more sunspots.

In the Section 8.2, we discuss the data sets used and the analysis process, filtering and registrations etc. Then we give the results in Section 8.3. Finally the discussion and conclusions are given in Section 8.4.

8.2 The Data Used and its Analysis

We use the line of sight magnetograms data taken from GONG (Global Oscillation Network Group) instrument at Udaipur for observing the polarity of the active region (e.g., Figure 8.1). Please note that the negative (black)/positive (white) is leading/following polarity in the northern hemisphere which is just opposite to that in the 23^{rd} solar cycle. Also its emergence at 30 degrees latitude is as expected for the beginning of a solar cycle. Tilt angle is in accordance with the Joy's law (Hale et al., 1919). All other active regions observed are in accordance with the above criteria.

The chromospheric Hα data are used from BBSO (full disk) and USO (high resolution, small field of view (fov)). Full disk Hα images from BBSO are used to confirm the filament structures as sometimes the filaments are small and weak. This is done by looking at the neutral line, by overlaying the contours of full disk longitudinal magnetograms after rebinning and registering them properly. Figures 8.2 and 8.4 are such two examples.

Figures 8.3 and 8.5 show two examples of high-resolution Hα images taken from the Spar telescope at Udaipur Solar Observatory. As described in Chapter 2, the Spar telescope uses a Hα Halle lyot type filter with FWHM of 500 mÅ

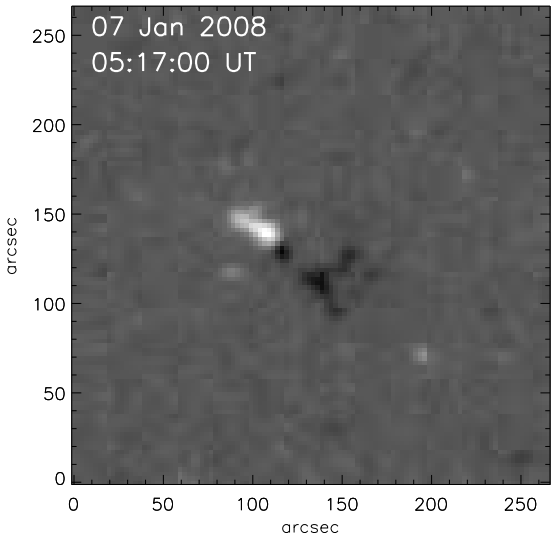

Figure 8.1: GONG magnetogram (UD) of NOAA AR 10981 : Observed in the northern hemisphere, this is the first sunspot observed in the 24^{th} solar cycle. We can see the polarity of leader and follower is in accordance with sunspots expected to emerge in the northern hemisphere in 24^{th} solar cycle i.e., negative polarity as leader and positive polarity as follower which is opposite to that of 23^{rd} solar cycle, following the Hale's polarity law. Also the latitude is N 30° and is in accordance with Sporer's law for butterfly diagram.

operating at the wavelength of 6563 Å. The telescope utilizes a 1392 × 1024 CCD with the pixel size of 6.45 m. The pixel resolution of the CCD is 0.395 arc-sec and the field of view it covers is 9 arc-min × 7 arc-min. Both the figures (Figures 8.3 and 8.5) show the selected region (2'×1.8') out of the full images (9'×7') taken from our Hα telescope.

For enhancing the barbs structures, we have taken the square root of logarithm of the observed image and then used wiener filter

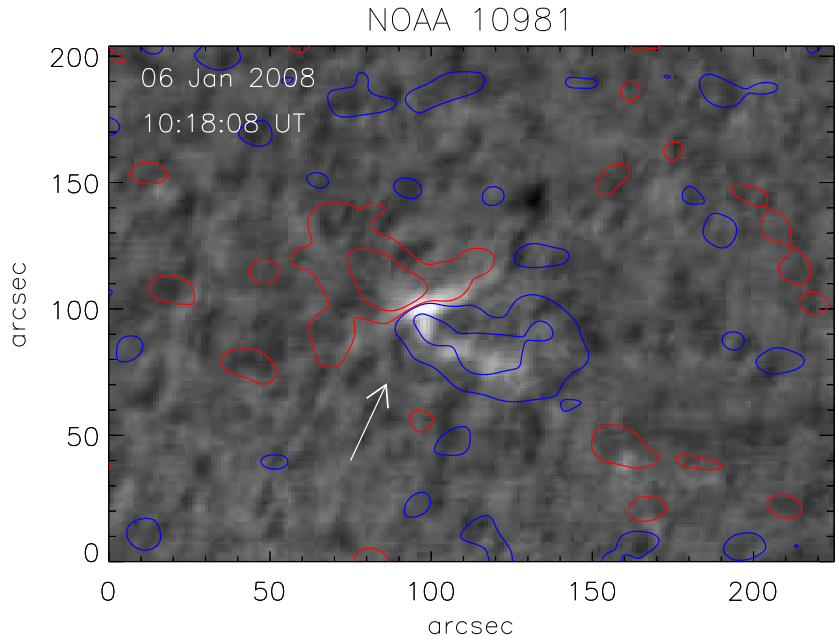

Figure 8.2: Contours of magnetogram (GONG - 06 January 2008 : 1014UT) on the corresponding Hα image (BBSO - 06 January 2008 : 1018UT) showing the neutral line. The arrow shows the position of the neutral line where the barb was developed later which we observed from USO-Spar telescope and is shown in Figure 8.3. Even in this Hα image, we can identify the chirality of the filament as dextral, by looking at the upper portion of the filament. But later, in 17-18 hours the lower part of the filament was developed as shown in Figure 8.3.

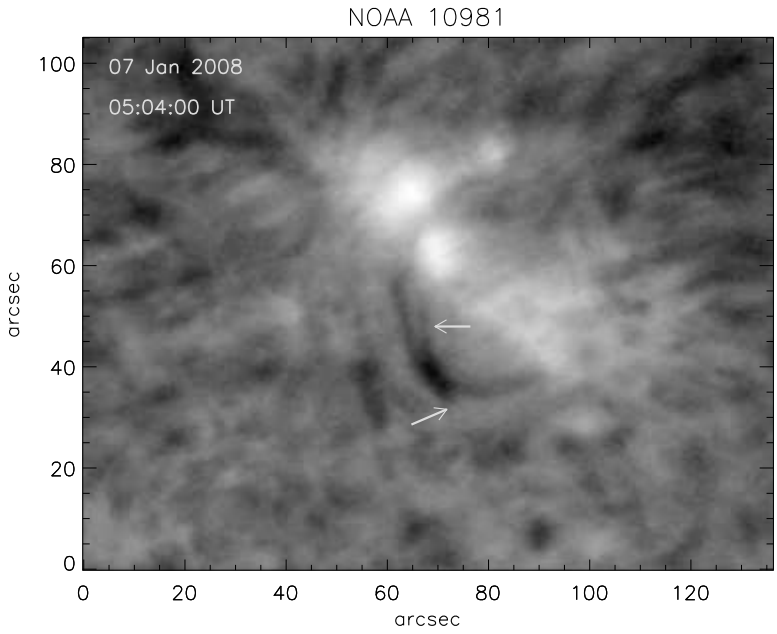

Figure 8.3: USO Hα image of NOAA AR 10981, the first AR observed in solar cycle 24, lower part of filament showing dextral chirality. Arrows indicate the positions of the barbs. Since the beginning of the filament, it shows dextral chirality in some or other portion of the filament.

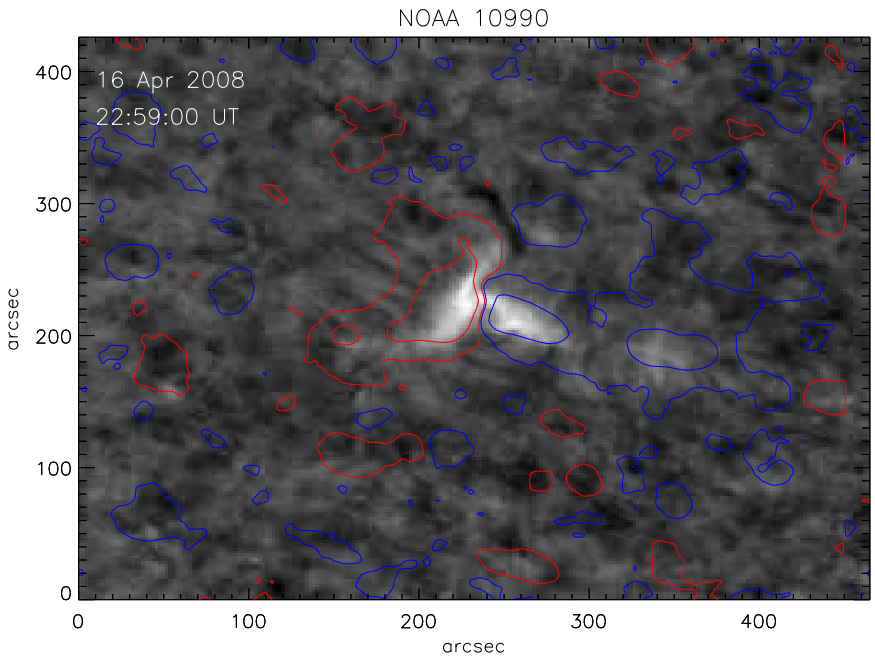

Figure 8.4: Another example: Contours of magnetogram (GONG - 16 April 2008 : 2254UT) overlaid on corresponding Hα image (BBSO - 16 April 2008 : 2259UT) showing the neutral line. The high-resolution Hα image of the same filament observed from USO is shown in Figure 8.5.

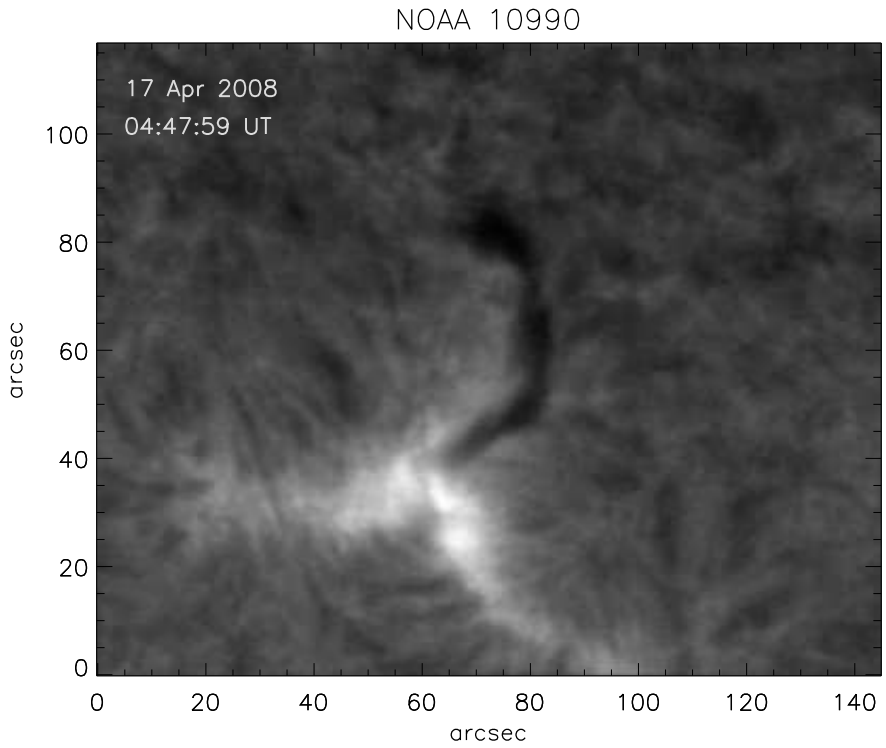

Figure 8.5: USO Hα image for NOAA AR 10990 on 17 April 2008, clearly showing the dextral chirality in the filament which means as the negative sign of magnetic helicity.

$$F(u,v) = \frac{|P(u,v)|^2}{|P(u,v)|^2 + N^2} \tag{8.1}$$

where,

$$P(u,v) = \exp(-0.008 \times \sqrt{(u^2 + v^2)}) \tag{8.2}$$

is the point spread function in the fourier domain. N is the noise with value 9.40924. u and v are the spatial frequencies.

The chirality of a filament can be identified by looking at the filament-associated barbs (see Figure 7.1). Viewing from any side of a filament, the barbs are right bearing for dextral chirality and left bearing for sinistral chirality (Martin et al., 1993; Martin, 1998). Also, we find that if one goes from the axis of the filament towards barb's axis through an acute angle, then the direction of angular change is clockwise for a dextral filament and counterclockwise for a sinistral filament.

We see (two examples, Figures 8.3 and 8.5) that the barbs associated with the filament are oriented clockwise when we move from filament axis towards axis of barb through acute angle and therefore the filaments are dextral. The arrows in Figure 8.3 indicate the position of the barbs. We observed this filament from 0504UT to 1100UT but the barbs were identifiable only for a brief period. It disappeared in few hours but we were able to observe some of the images in which the barbs could be identified. The whirls associated with the active region also showed the clockwise orientation (when we go towards penumbra from inside umbra) showing dextral chirality and thus negative helicity. The filament shown in Figure 8.5 was on disk for a long time and barbs were clearly visible showing the dextral chirality of the filament.

Figures 8.2 and 8.4 are the corresponding images of BBSO Hα with contours of longitudinal magnetograms obtained from GONG. These small portions are taken after rebinning and registering both the full disk images in each case. Registration

is done using full disk magnetograms of Hα and GONG magnetograms to get the neutral lines and identifying the filament whether they are exactly at neutral line. For this the contour of line of sight magnetic field is drawn on the Hα images and can be seen in Figures 8.2 and 8.4.

The chirality of coronal features is identified by looking at X-ray and EUV images as described in Chapter 7. The chirality of all active regions studied can be found in Table 8.1. Also, for a few cases whenever vector magnetograms were available, we have computed the photospheric twist of AR's. For this we have computed SASSA as described in Chapter 4. The vector magnetograms are taken from Synoptic Optical Long-term Investigations of the Sun (SOLIS) and is available online at: `http://solis.nso.edu/vsm/data_summary/DataSumm3.php?stime=1059717600&etime=0&obsmode[]=6302v&display=1&flares=&sobsmode=1&meonly`

The processed and inverted data is available at this place. The inversion is done under Milne-Eddington assumption and therefore the field parameters are assumed constant in the line forming region. The observation is done in Fe-I line 6302 Å. All of the VSM data are corrected for the 180° azimuthal ambiguity using the Non-Potential Field Calculation (NPFC) method developed by Georgoulis (2005).

The results are given in next section.

8.3 Results

Eighteen active regions which emerged in the beginning of 24^{th} solar cycle till the date, have been collected and the sign of their magnetic helicity is studied. We can see from Table 8.1 that out of 18, only two are not following the hemispheric

Table 8.1: List of the active regions studied. The chirality of features and global twist value (SASSA whenever vector field available) and other details of the sunspots are given:

AR No. (NOAA)	Date of Observation	Twist(Phot.) (SASSA:deg)	Chrom. Chirality	Coronal Chirality	Position (AR Phot.)	Hemisph. Hel. Rule
11025	02 Sep 2009	NA	Dextral	Dextral	N17E04	Yes
11024	04 Jul 2009	1.290	Sinistral	NR	S25E02	Yes
11020	10 Jun 2009	1.965	NR	Sinistral	N24W19	No
11019	03 Jun 2009	2.506	Sinistral	Sinistral	N28E02	No
11018	24 May 2009	0.590	Sinistral	Sinistral	S06E07	Yes
11017	15 May 2009	−0.698	NR	NR	N18E03	Yes
11013	25 Feb 2009	NA	Dextral	Dextral	N26E06	Yes
11010	12 Jan 2009	NA	Dextral	NR	N18E05	Yes
11008	12 Nov 2008	NA	Dextral	Dextral	N33W09	Yes
11007	01 Nov 2008	NA	Dextral	Dextral	N34E04	Yes
11005	15 Oct 2008	NA	Dextral	Dextral	N27W02	Yes
11003	06 Oct 2008	NA	Sinistral	NA	S23E15	Yes
11002	23 Sep 2008	NA	Dextral	Dextral	N25W27	Yes
11000	21 Jul 2008	NA	Sinistral	Sinistral	S12W05	Yes
10998	14 Jun 2008	NA	Sinistral	Sinistral	S10E12	Yes
10993	06 May 2008	NA	Sinistral	Sinistral	S31E14	Yes
10990	16 Apr 2008	NA	Dextral	Dextral	N27E05	Yes
10981	07 Jan 2008	NA	Dextral	Dextral	N27W04	Yes

NR: Not Recognigible

NA: Not Available

helicity rule. Other 16 AR's are following this rule, i.e., the AR's observed in northern hemisphere are bearing dextral chirality and those observed in southern hemisphere are bearing sinistral chirality.

We have used the chirality sign at the three heights (i.e., photospheric, chromospheric and coronal) in the solar atmosphere to infer the sign of magnetic helicity. The reason is that we do not have a continuous observation at a given level in the solar atmosphere. We know that the sign of helicity at different heights in the solar environment are correlated (see Chapter 7), thus identifying the chirality sign at any of the three heights is enough to infer the sign of magnetic helicity of the active region.

We can see in Table 4.1 that the 38 active regions out of 43 follow the reverse hemispheric helicity rule. Most of these active regions were observed in the declining phase of the solar cycle 23. The earlier belief that the hemispheric helicity rule is independent of the solar cycle therefore needs to be revaluated. Does this behaviour depend on the different phases of a solar cycle? Or, does it vary even on a larger scale which is larger than that of the solar cycle?

The kinematic dynamo theories assume the monolithic structure of sunspots and introduce convection to get the behaviour of emerging sunspots. Such a dynamo theory (Choudhuri et al., 2004) predicts that the active regions emerging in the beginning of a solar cycle do not follow the hemispheric helicity rule while they should follow the rule during the declining phase of the cycle. Unfortunately, our observations do not support this model. It seems that a deeper understanding of the dynamo mechanism is required to settle this issue and understand the real nature of sunspot configurations.

One such suggestion, which of course is difficult due to complexity in solving high order non linear equations for convection, is to use fibril bundle nature of

sunspots. We find that the real sunspots might not be actually monolithic but could be in the form of fibril bundles. The details can be found in Chapter 5.

8.4 Discussion and Conclusions

We observed the first few active regions of solar cycle 24 and identified the chirality of the filaments and sigmoids associated with these active regions. In a few cases when vector magnetograms were available, the photospheric chirality are also inferred from the calculation of SASSA.

We can see from Table 8.1 that most of these AR's do follow the hemispheric helicity rule. All these AR's are observed in the beginning of 24^{th} solar cycle. Now, if we see at the Table 1 of Chapter 4, only 5 out of 43 follow this behaviour. Others follow opposite rule. Most of those AR's are observed in the declining phase of 23^{rd} solar cycle. This behaviour shows that understanding hemispheric rule requires more and careful study. It seems, then, either there is no such hemispheric rule in reality, or, the rule changes on a long time scale. This behaviour may change with different phases of a solar cycle and also with different solar cycles. This needs very serious evaluation for understanding the dynamo behaviour.

As mentioned earlier, according to some dynamo theories the active regions emerging in the beginning of the solar cycle should have helicities opposite in sign to helicity hemispheric rule. On the other hand none of the hemispheric rules are followed without exceptions. Here in our cases, we find exactly opposite behaviour than expected by some kinematic dynamo theories.

As we have mentioned earlier, the helicity can be produced both from the dynamo processes and from the helical turbulence in the convection zone. The

stochastic component of the dynamo process will produce a distribution of field strength for the active regions. Weaker fields, which are influenced by the coriolis force, are more likely to follow the helicity hemispheric rule. Same applies for the strong but force free fields. Most of the strong fields will not be affected by the coriolis force. Thus, for active regions with strong, non-force-free magnetic field configuration, compliance with or deviation from helicity hemispheric rule will be dictated by dynamo related processes.

Alternately, as suggested by Zhang (2006), the weaker fields could represent the mean field dynamo, helicity of which is known to follow the helicity hemispheric rule, while the stronger fields represent the fluctuating part of the dynamo and helicity of these active regions is expected to disobey the hemispheric rule. Clearly there is need for more accurate measurements and better understanding of the dynamo as well as the sunspot configuration.

Chapter 9

Summary, Conclusions and Future Scope

9.1 Discussion and Conclusions

The present thesis clarifies many very important issues related to magnetic helicity of solar magnetic field. We, first justify the measurements of vector magnetic fields from recent instruments e.g., *Hinode* (SOT/SP). This is done by simulating an analytical bipole. The input magnetic parameters are known in such a bipole and desired level of the polarimetric noise can be added. Thus, this is the best way to estimate the effect of polarimetric noise on the derivation of vector fields from the observations. We find that the modern telescopes give high quality data and the vector fields and associated quantities like twist and magnetic energy can accurately be measured with very small or negligible errors. The inversion techniques are also verified using theoretical bipole. Chapter 3 includes all the above study.

The data sets used in the study of present thesis are taken from various telescopes. The brief description of all those instruments is given in Chapter 2.

We also elucidate the physical meaning of force-free parameter which gives the gradient of twist in axial direction. We recollect the relation of magnetic helicity with the force-free parameter. It is found that α bears the sign of magnetic helicity only if all the field lines are closed within a volume which is not the case on the Sun. All the above points are described in detail in Chapter 3. We have also given a direct method for computation of global alpha (α_g) in the same chapter. However, the physical meaning of α_g became suspect after getting no net current in sunspots as seen in Chapter 5.

The above simulation of analytical bipole did not consider fine structures in the bipole. Whereas in real sunspots, the fine structures have been observed from high resolution images and magnetograms. The distribution of local α and current in sunspots are studied next. It is found that the amplitudes of α and current are greater in penumbra by approximately an order magnitude. And these values cancel each other giving no contribution to their global values. The umbral values of current and α were found to be of the order of the global values of sunspots, which is an order smaller than the values observed in sunspot penumbra. This work is described in Chapter 4.

The photosphere is not actually force-free and therefore the measurement of α is worth suspecting. We have introduced a new method signed shear angle (SSA) to measure the twist present in sunspots irrespective of the force-free nature of sunspot magnetic fields. Spatially averaged signed shear angle (SASSA) is also found to be independent of shape of the sunspots. Thus, the SASSA is the best measure of global twist of sunspots.

The interesting result of absence of net currents in sunspots observed from

high-resolution data obtained from *Hinode* (SOT/SP) is reported in Chapter 5. We find that the net current increases with circular area as we go from umbra to mid penumbra and then starts falling rapidly. This result is exciting and difficult to interpret whether the sunspot is made of fibrils as Parker believes. We could derive twist and pleat currents and have shown in Figure 5.1. Also, "curly interlocking combed structure" has been discovered in the azimuthal component of the magnetic field.

We have then studied the evolution of NOAA AR 10930 which is the most eruptive sunspot observed from *Hinode* (SOT/SP) till date. An interesting result is obtained that a critical twist decides the class of X-ray flares. If twist is found more than -8 deg, then X-class X-ray flares are possible. Similarly for other flare classes the lower twist is observed. The result is very much supported by a quiet sunspot NOAA AR 10961 studied for comparison.

We find a good correlation between the the sign of magnetic helicity observed at different heights in the solar atmosphere. The photospheric, chromospheric and coronal data are used to verify this result. In most of the cases out of a large number of samples, it is found that the sign of chirality is similar at all the heights in the solar atmosphere. This is very important to be used as a boundary condition while modeling the chromospheric and coronal structures. Also, the majority of active regions observed during the declining phase of solar cycle 23, are following the inverse hemispheric helicity rule, while majority of those observed in the beginning of cycle 24 are following the conventional hemispheric helicity rule. This needs more study to confirm whether there is a hemispheric rule and, if yes, what is its period? Is it longer than solar magnetic cycles time scale?

There are some kinematic dynamo theories which expect that the sunspots emerging in the beginning of solar cycle do not follow the hemispheric helicity

rule whereas they follow during end phase of a sunspot cycle. We wished to compare the behaviour of the sunspots merging in the beginning and end of solar cycles. We could observe some sunspots emerging in the beginning of the solar cycle 24. A good sample of sunspots observed in the declining phase of the solar cycle 23 was also collected from ASP/DLSP and Hinode. It is found that the sunspots actually do not behave in the expected manner. We, after getting no net current in sunspots with significant global twists present in them, suspect that the problem may be solved if we solve the MHD equations assuming that the sunspots are made of fibril bundles.

Finally, the whole thesis can be summarized in few sentences as follows:

> The magnetic field parameters can be derived very accurately using the recent data available (e.g., from *Hinode* (SOT/SP)) and advanced inversion codes. The SASSA is the best measure of the global magnetic twist, one component of the magnetic helicity, irrespective of the force-free nature and the shape of the sunspots. The force-free parameter α, which gives gradient of twist in axial direction, is not a good measure of global twist due to non force-free nature of sunspot magnetic field and also due to absence of net currents in the sunspots. The sunspots with significant twist and no net currents show consistency with the fibril bundle nature of the sunspots. The magnetic helicity sign of sunspots studied has good correlation with the sign of chirality of associated features observed at chromospheric and coronal heights. The majority of the sunspots studied in the declining phase of solar cycle 23 follow a reverse hemispheric rule, whereas most of the ARs emerged in the beginning of solar cycle 24 are found to follow the conventional hemispheric helicity rule. This result indicates

that revisiting the hemispheric helicity rule using data sets of several years is required. The study of evolution of SASSA of sunspots showed threshold values for different classes of X-ray flares. This is an important discovery which was being sought after for many decades.

9.2 Future Work Projection

9.2.1 Using SASSA for Flare-Prediction

The SSA can be used for predicting eruptivity of sunspots. A one case study of evolution of SASSA in NOAA AR 10930, indicates the importance of SASSA, as described in Chapter 6. We need to study a large number of sunspot vector magnetograms to decide a critical threshold of twist in general for predicting the eruptivity of sunspots. Many other parameters such as magnetic energy and tension force can be complemented with the SASSA for this purpose. The details about magnetic energy computation can be found in Section 3.6. The computation of tension force can be done as follows:

9.2.1.1 Using the Tension Force

In any plasma with magnetic field **B** and plasma pressure p, the equation for magneto-hydrostatic equilibrium is given by,

$$(\nabla \times \mathbf{B}) \times \mathbf{B}/4\pi - \nabla p + \rho g = 0 \tag{9.1}$$

where ρ is the plasma density and g is the acceleration due to gravity. The first term in Equation 9.1 is the Lorentz force, second term is the force due to plasma pressure and the last term is the force on the plasma due to gravity. We can split

up the Lorentz force (say F) in two terms as,

$$\mathbf{F} = \frac{(\mathbf{B} \cdot \nabla)\mathbf{B}}{4\pi} - \frac{\nabla(\mathbf{B} \cdot \mathbf{B})}{8\pi} \tag{9.2}$$

The first term in this equation is the tension force (say T). The second term represents the force due to magnetic pressure. The tension term can be simplified to,

$$\mathbf{T} = \frac{1}{4\pi}[B_x \frac{\partial B_z}{\partial x} + B_y \frac{\partial B_z}{\partial y} - B_z(\frac{\partial B_x}{\partial x} + \frac{\partial B_y}{\partial y})] \tag{9.3}$$

where, the last component is drawn from the condition,

$$\nabla \cdot \mathbf{B} = 0 \tag{9.4}$$

In a force-free condition, tension force balances the magnetic pressure gradient or magnetic force. In that condition the Equation 9.1 reduces to hydrostatic equilibrium

$$\nabla p = \rho g \tag{9.5}$$

where the plasma pressure scale height will be independent of the scale height of the magnetic field. Whereas, in a tension-free fields, the magneto-hydrostatic equilibrium becomes,

$$\partial/\partial z(B^2/8\pi + p) = \rho g. \tag{9.6}$$

The field in this condition can not be force-free. In the case when tension is non-zero, the pressure scale height depend on the scale height of the magnetic field.

High magnetic shear shows low magnetic tension, thereby indicating towards flare initiation (Venkatakrishnan, 1990b).

For greater details, kindly see Venkatakrishnan (1990a,b); Venkatakrishnan et al. (1993). We will compute the tension force using Equation 9.3 and infer it in terms of solar gravitational acceleration ($g_{\odot}$)

9.2.1.2 Using Higher Moments of α

As suggested in Chapter 3, the higher order components of α_g which weigh more for higher magnetic field values, may also help in predicting the eruptivity of sunspots.

9.2.2 Understanding Sunspot Structure

Understanding the sunspot structure is a great challenge. We have found some important results and is given in details in Chapter 5. It certainly requires more study to confirm the fibril bundle nature of sunspots. Also, the partial rings observed in some sunspots seem telling something important. The behaviour of sunspots with such rings is important to study.

9.2.3 Currents at Higher Reaches

The net currents in sunspots are found to vanish at photosphere. Hinode (SOT/SP) data have been used for this purpose and is explained in the Chapter 5. The currents seem to exist in the corona as inferred from the sigmoidal loop structures. This is a challenging question to understand how the currents are produced in the corona. We wish to study the net currents at different heights in the solar atmosphere above the photosphere. We require observations of vector fields at those heights in the solar atmosphere.

9.2.4 Revisiting Hemispheric Helicity Rule

Revisiting hemispheric helicity rule using the parameter SASSA is required to understand the behaviour of sunspot helicity. Whether there is a long term

variation in the behaviour of sunspot helicity. Or, there is no hemispheric helicity rule and the behaviour of sunspots in both the hemispheres is random. Also, by studying more sunspots of new solar cycle 24, as done for few sunspots in Chapter 8, the constraint to some dynamo theories can be provided.

Bibliography

Abramenko, V., Yurchyshyn, V., and Wang, H. (2008). Intermittency in the Photosphere and Corona above an Active Region. *ApJ*, 681:1669–1676.

Abramenko, V. I., Wang, T., and Yurchishin, V. B. (1996). Analysis of Electric Current Helicity in Active Regions on the Basis of Vector Magnetograms. *Solar Phys.*, 168:75–89.

Ai, G.-X. and Hu, Y.-F. (1986). Propose for a solar magnetic field telescope and its working theorem. *Publications of the Beijing Astronomical Observatory*, 8:1–10.

Ambastha, A., Hagyard, M. J., and West, E. A. (1993). Evolutionary and flare-associated magnetic shear variations observed in a complex, flare-productive active region. *Solar Phys.*, 148:277–299.

Archontis, V., Moreno-Insertis, F., Galsgaard, K., Hood, A., and O'Shea, E. (2004). Emergence of magnetic flux from the convection zone into the corona. *A&A*, 426:1047–1063.

Arnaud, J., Mein, P., and Rayrole, J. (1998). The Solar Telescope THEMIS. In Priest, E. R., Moreno-Insertis, F., and Harris, R. A., editors, *Crossroads for European Solar and Heliospheric Physics. Recent Achievements and Future Mission Possibilities*, volume 417 of *ESA Special Publication*, page 213.

Aulanier, G., Démoulin, P., and Grappin, R. (2005). Equilibrium and observational properties of line-tied twisted flux tubes. *A&A*, 430:1067–1087.

Aulanier, G., Demoulin, P., van Driel-Gesztelyi, L., Mein, P., and Deforest, C. (1998). 3-D magnetic configurations supporting prominences. II. The lateral feet as a perturbation of a twisted flux-tube. *A&A*, 335:309–322.

Balasubramaniam, K. S., Pevtsov, A., and Rogers, J. (2004). Statistical Properties of Superpenumbral Whorls around Sunspots. *ApJ*, 608:1148–1155.

Bao, S. and Zhang, H. (1998). Patterns of Current Helicity for the Twenty-second Solar Cycle. *ApJ*, 496:L43–L46.

Bao, S. D., Ai, G. X., and Zhang, H. Q. (2000). The Hemispheric Sign Rule of Current Helicity During the Rising Phase of Cycle 23. *Journal of Astrophysics and Astronomy*, 21:303.

Baty, H. (2000). Magnetic topology during the reconnection process in a kinked coronal loop. *A&A*, 360:345–350.

Berger, M. A. (1999). Magnetic Helicity in Space Physics. In Brown, M. R., Canfield, R. C., and Pevtsov, A. A., editors, *Magnetic Helicity in Space and Laboratory Plasmas*, pages 1–9.

Berger, M. A. and Field, G. B. (1984). The topological properties of magnetic helicity. *Journal of Fluid Mechanics*, 147:133–148.

Berger, M. A. and Ruzmaikin, A. (2000). Rate of helicity production by solar rotation. *Journal of Geophysical Research*, 105:10481–10490.

Bernasconi, P. N., Rust, D. M., and Hakim, D. (2005). Advanced Automated Solar Filament Detection And Characterization Code: Description, Performance, And Results. *Solar Phys.*, 228:97–117.

Bharti, L., Joshi, C., and Jaaffrey, S. N. A. (2007). Observations of Dark Lanes in Umbral Fine Structure from the Hinode Solar Optical Telescope: Evidence for Magnetoconvection. *ApJ*, 669:L57–L60.

Bonnet, R. M. and Felici, F. (1997). Overview of the soho mission. *Advances in Space Research*, 20:2207–2218.

Brown, M. R., Canfield, R. C., and Pevtsov, A. A., editors (1999). *Magnetic Helicity in Space and Laboratory Plasmas*.

Burnette, A. B., Canfield, R. C., and Pevtsov, A. A. (2004). Photospheric and Coronal Currents in Solar Active Regions. *ApJ*, 606:565–570.

Câlugâreanu, G. (1959). L'int'e9gral de Gauss et l'analyse des nuds tridimensionnels. *Rev. Math. Pures Appl.*, 4:5–20.

Canfield, R. C., Hudson, H. S., and McKenzie, D. E. (1999). Sigmoidal morphology and eruptive solar activity. *Geophysics Research Letters*, 26:627–630.

Canfield, R. C., Kazachenko, M. D., Acton, L. W., Mackay, D. H., Son, J., and Freeman, T. L. (2007). Yohkoh SXT Full-Resolution Observations of Sigmoids: Structure, Formation, and Eruption. *ApJ*, 671:L81–L84.

Chae, J. (2000). The Magnetic Helicity Sign of Filament Chirality. *ApJ*, 540:L115–L118.

Chandra, R., Schmieder, B., Aulanier, G., and Malherbe, J. M. (2009). Evidence of Magnetic Helicity in Emerging Flux and Associated Flare. *Solar Phys.*, 258:53–67.

Chandrasekhar, S. (1961). *Chapter-2 : Hydrodynamic and hydromagnetic stability*. International Series of Monographs on Physics, Oxford: Clarendon, 1961.

Chatterjee, P., Choudhuri, A. R., and Petrovay, K. (2006). Development of twist in an emerging magnetic flux tube by poloidal field accretion. *A&A*, 449:781–789.

Choudhuri, A. R. (1998). *The physics of fluids and plasmas : an introduction for astrophysicists* . New York, Cambridge University Press,. QB466.F58 C46 1998.

Choudhuri, A. R., Chatterjee, P., and Nandy, D. (2004). Helicity of Solar Active Regions from a Dynamo Model. *ApJ*, 615:L57–L60.

Cuperman, S., Li, J., and Semel, M. (1992). Magnetic shear-based removal of the 180-deg ambiguity in the observed transverse photospheric magnetic field - Feasibility and limitations. *A&A*, 265:296–307.

Defise, J.-M., Song, X. Y., Delaboudiniere, J.-P., Artzner, G. E., Carabetian, C., Hochedez, J.-F. E., Brunaud, J., Moses, J. D., Catura, R. C., Clette, F., and Maucherat, A. J. (1995). Calibration of the EIT instrument for the SOHO mission. In S. Fineschi, editor, *Society of Photo-Optical Instrumentation Engineers (SPIE) Conference Series*, volume 2517 of *Presented at the Society of Photo-Optical Instrumentation Engineers (SPIE) Conference*, pages 29–39.

Delaboudinière, J.-P., Artzner, G. E., Brunaud, J., Gabriel, A. H., Hochedez, J. F., Millier, F., Song, X. Y., Au, B., Dere, K. P., Howard, R. A., Kreplin, R.,

Michels, D. J., Moses, J. D., Defise, J. M., Jamar, C., Rochus, P., Chauvineau, J. P., Marioge, J. P., Catura, R. C., Lemen, J. R., Shing, L., Stern, R. A., Gurman, J. B., Neupert, W. M., Maucherat, A., Clette, F., Cugnon, P., and van Dessel, E. L. (1995). EIT: Extreme-Ultraviolet Imaging Telescope for the SOHO Mission. *Solar Phys.*, 162:291–312.

Démoulin, P. and Pariat, E. (2009). Modelling and observations of photospheric magnetic helicity. *Advances in Space Research*, 43:1013–1031.

DeVore, C. R. (2000). Magnetic Helicity Generation by Solar Differential Rotation. *ApJ*, 539:944–953.

Drake, J. F. (1971). Characteristics of Soft Solar X-Ray Bursts. *Solar Phys.*, 16:152–185.

Elmore, D. F., Lites, B. W., Tomczyk, S., Skumanich, A. P., Dunn, R. B., Schuenke, J. A., Streander, K. V., Leach, T. W., Chambellan, C. W., and Hull, H. K. (1992). The Advanced Stokes Polarimeter - A new instrument for solar magnetic field research. In Goldstein, D. H. and Chipman, R. A., editors, *Society of Photo-Optical Instrumentation Engineers (SPIE) Conference Series*, volume 1746 of *Society of Photo-Optical Instrumentation Engineers (SPIE) Conference Series*, pages 22–33.

Elsasser, W. M. (1956). Hydromagnetic dynamo theory. *Rev. Mod. Phys.*, 28(2):135–163.

Emslie, A. G., Dennis, B. R., Holman, G. D., and Hudson, H. S. (2005). Refinements to flare energy estimates: A followup to "Energy partition in two solar flare/CME events" by A. G. Emslie et al. *Journal of Geophysical Research (Space Physics)*, 110:11103.

Evershed, J. (1909). Radial movement in sun-spots. *The Observatory*, 32:291–292.

Fan, Y. and Gibson, S. E. (2004). Numerical Simulations of Three-dimensional Coronal Magnetic Fields Resulting from the Emergence of Twisted Magnetic Flux Tubes. *ApJ*, 609:1123–1133.

Forbes, T. G. and Isenberg, P. A. (1991). A catastrophe mechanism for coronal mass ejections. *ApJ*, 373:294–307.

Gary, G. A., Moore, R. L., Hagyard, M. J., and Haisch, B. M. (1987). Nonpotential features observed in the magnetic field of an active region. *ApJ*, 314:782–794.

Georgoulis, M. K. (2005). A New Technique for a Routine Azimuth Disambiguation of Solar Vector Magnetograms. *ApJ*, 629:L69–L72.

Gold, T. and Hoyle, F. (1960). On the origin of solar flares. *MNRAS*, 120:89–105.

Golub, L., Deluca, E., Austin, G., Bookbinder, J., Caldwell, D., Cheimets, P., Cirtain, J., Cosmo, M., Reid, P., Sette, A., Weber, M., Sakao, T., Kano, R., Shibasaki, K., Hara, H., Tsuneta, S., Kumagai, K., Tamura, T., Shimojo, M., McCracken, J., Carpenter, J., Haight, H., Siler, R., Wright, E., Tucker, J., Rutledge, H., Barbera, M., Peres, G., and Varisco, S. (2007). The X-Ray Telescope (XRT) for the Hinode Mission. *Solar Phys.*, 243:63–86.

Gosain, S., Tiwari, S. K., Joshi, J., and Venkatakrishnan, P. (2008). Software for interactively visualizing solar vector magnetograms of udaipur solar observatory. *Journal of Astrophysics and Astronomy*, 29:107–111.

Gosain, S., Venkatakrishnan, P., and Tiwari, S. K. (2009). HINODE Observations of Coherent Lateral Motion of Penumbral Filaments during a X-class Flare. *ApJ*, 706:L240–L245.

Gosain, S., Venkatakrishnan, P., and Venugopalan, K. (2004). Design of Instrument Control Software for Solar Vector Magnetograph at Udaipur Solar Observatory. *Experimental Astronomy*, 18:31–38.

Gosain, S., Venkatakrishnan, P., and Venugopalan, K. (2006). Design and Status of Solar Vector Magnetograph (SVM-I) at Udaipur Solar Observatory. *Journal of Astrophysics and Astronomy*, 27:285–292.

Guo, Y., Ding, M. D., Wiegelmann, T., and Li, H. (2008). 3D Magnetic Field Configuration of the 2006 December 13 Flare Extrapolated with the Optimization Method. *ApJ*, 679:1629–1635.

Hagino, M. and Sakurai, T. (2004). Latitude Variation of Helicity in Solar Active Regions. *PASJ*, 56:831–843.

Hagino, M. and Sakurai, T. (2005). Solar-Cycle Variation of Magnetic Helicity in Active Regions. *PASJ*, 57:481–485.

Hagyard, M. J., Adams, M. L., Smith, J. E., and West, E. A. (2000). Effects of Faraday rotation observed in filter magnetograph data. *Solar Phys.*, 191:309–324.

Hagyard, M. J., Cumings, N. P., West, E. A., and Smith, J. E. (1982). The MSFC Vector Magnetograph. *Solar Phys.*, 80:33–51.

Hagyard, M. J. and Pevtsov, A. A. (1999). Studies of Solar Helicity Using Vector Magnetograms. *Solar Phys.*, 189:25–43.

Hagyard, M. J., Stark, B. A., and Venkatakrishnan, P. (1999). A Search for Vector Magnetic Field Variations Associated with the M-Class Flares of 10 June 1991 IN AR6659. *solphys*, 184:133–147.

Hagyard, M. J., Teuber, D., West, E. A., and Smith, J. B. (1984). A quantitative study relating observed shear in photospheric magnetic fields to repeated flaring. *Solar Phys.*, 91:115–126.

Hagyard, M. J., Venkatakrishnan, P., and Smith, Jr., J. B. (1990). Nonpotential magnetic fields at sites of gamma-ray flares. *ApJS*, 73:159–163.

Hahn, M., Gaard, S., Jibben, P., Canfield, R. C., and Nandy, D. (2005). Spatial Relationship between Twist in Active Region Magnetic Fields and Solar Flares. *ApJ*, 629:1135–1140.

Hale, G. E. (1908a). Solar Vortices. *PASP*, 20:203–220.

Hale, G. E. (1908b). Solar Vortices and the Zeeman Effect. *PASP*, 20:220–224.

Hale, G. E. (1925). Nature of the Hydrogen Vortices Surrounding Sun-spots. *PASP*, 37:268–270.

Hale, G. E. (1927). The fields of force in the atmosphere of the Sun. *Nature*, 119:708–714.

Hale, G. E., Ellerman, F., Nicholson, S. B., and Joy, A. H. (1919). The Magnetic Polarity of Sun-Spots. *ApJ*, 49:153–185.

Hale, G. E. and Nicholson, S. B. (1925). The Law of Sun-Spot Polarity. *ApJ*, 62:270–300.

Harra, L. K., Williams, D. R., Wallace, A. J., Magara, T., Hara, H., Tsuneta, S., Sterling, A. C., and Doschek, G. A. (2009). Coronal Nonthermal Velocity Following Helicity Injection Before an X-Class Flare. *ApJ*, 691:L99–L102.

Harvey, J. W. (1969). *Magnetic Fields Associated with Solar Active-Region Prominences.* PhD thesis, AA(University of Colorado at Boulder.).

Heinemann, T., Nordlund, Å., Scharmer, G. B., and Spruit, H. C. (2007). MHD Simulations of Penumbra Fine Structure. *ApJ*, 669:1390–1394.

Hurlburt, N. E., Alexander, D., and Rucklidge, A. M. (2002). Complete Models of Axisymmetric Sunspots: Magnetoconvection with Coronal Heating. *ApJ*, 577:993–1005.

Ichimoto, K., Lites, B., Elmore, D., Suematsu, Y., Tsuneta, S., Katsukawa, Y., Shimizu, T., Shine, R., Tarbell, T., Title, A., Kiyohara, J., Shinoda, K., Card, G., Lecinski, A., Streander, K., Nakagiri, M., Miyashita, M., Noguchi, M., Hoffmann, C., and Cruz, T. (2008). Polarization Calibration of the Solar Optical Telescope onboard Hinode. *Solar Phys.*, 249:233–261.

Ichimoto, K., Shine, R. A., Lites, B., Kubo, M., Shimizu, T., Suematsu, Y., Tsuneta, S., Katsukawa, Y., Tarbell, T. D., Title, A. M., Nagata, S., Yokoyama, T., and Shimojo, M. (2007). Fine-Scale Structures of the Evershed Effect Observed by the Solar Optical Telescope aboard Hinode. *PASJ*, 59:593–599.

Isobe, H., Kubo, M., Minoshima, T., Ichimoto, K., Katsukawa, Y., Tarbell, T. D., Tsuneta, S., Berger, T. E., Lites, B., Nagata, S., Shimizu, T., Shine, R. A., Suematsu, Y., and Title, A. M. (2007). Flare Ribbons Observed with G-band and FeI 6302Å, Filters of the Solar Optical Telescope on Board Hinode. *PASJ*, 59:807–813.

Jefferies, J. T. and Mickey, D. L. (1991). On the inference of magnetic field vectors from Stokes profiles. *ApJ*, 372:694–702.

Jones, H. P., Harvey, J. W., Henney, C. J., Hill, F., and Keller, C. U. (2002). Data analysis for the SOLIS Vector Spectromagnetograph. In Sawaya-Lacoste, H., editor, *SOLMAG 2002. Proceedings of the Magnetic Coupling of the Solar*

Atmosphere Euroconference, volume 505 of *ESA Special Publication*, pages 15–18.

Kano, R., Sakao, T., Hara, H., Tsuneta, S., Matsuzaki, K., Kumagai, K., Shimojo, M., Minesugi, K., Shibasaki, K., Deluca, E. E., Golub, L., Bookbinder, J., Caldwell, D., Cheimets, P., Cirtain, J., Dennis, E., Kent, T., and Weber, M. (2008). The Hinode X-Ray Telescope (XRT): Camera Design, Performance and Operations. *Solar Phys.*, 249:263–279.

Keller, C. U., Aebersold, F., Egger, U., Povel, H. P., Steiner, P., and Stenflo, J. O. (1992). Z"urich Imaging Stokes Polarimeter - ZIMPOL I. Design review. *LEST Found., Tech. Rep., No. 53,*, 53.

Keller, C. U., Harvey, J. W., and Giampapa, M. S. (2003). SOLIS: an innovative suite of synoptic instruments. In Keil, S. L. and Avakyan, S. V., editors, *Society of Photo-Optical Instrumentation Engineers (SPIE) Conference Series*, volume 4853 of *Presented at the Society of Photo-Optical Instrumentation Engineers (SPIE) Conference*, pages 194–204.

Khomenko, E. V., Shelyag, S., Solanki, S. K., and Vögler, A. (2005). Stokes diagnostics of simulations of magnetoconvection of mixed-polarity quiet-Sun regions. *A&A*, 442:1059–1078.

Kliem, B. and Török, T. (2006). Torus Instability. *Physical Review Letters*, 96(25):255002.

Klimchuk, J. A., Canfield, R. C., and Rhoads, J. E. (1992). The practical application of the magnetic virial theorem. *ApJ*, 385:327–343.

Kosugi, T., Matsuzaki, K., Sakao, T., Shimizu, T., Sone, Y., Tachikawa, S., Hashimoto, T., Minesugi, K., Ohnishi, A., Yamada, T., Tsuneta, S., Hara, H.,

Ichimoto, K., Suematsu, Y., Shimojo, M., Watanabe, T., Shimada, S., Davis, J. M., Hill, L. D., Owens, J. K., Title, A. M., Culhane, J. L., Harra, L. K., Doschek, G. A., and Golub, L. (2007). The Hinode (Solar-B) Mission: An Overview. *Solar Phys.*, 243:3–17.

Kubo, M., Ichimoto, K., Shimizu, T., Tsuneta, S., Suematsu, Y., Katsukawa, Y., Nagata, S., Tarbell, T. D., Shine, R. A., Title, A. M., Frank, Z. A., Lites, B., and Elmore, D. (2007). Formation of Moving Magnetic Features and Penumbral Magnetic Fields with Hinode/SOT. *PASJ*, 59:607–612.

Lagg, A., Woch, J., Krupp, N., and Solanki, S. K. (2004). Retrieval of the full magnetic vector with the He I multiplet at 1083 nm. Maps of an emerging flux region. *A&A*, 414:1109–1120.

Landolfi, M. and Landi Degl'Innocenti, E. (1982). Magneto-optical effects and the determination of vector magnetic fields from Stokes profiles. *Solar Phys.*, 78:355–364.

Leka, K. D., Canfield, R. C., McClymont, A. N., and van Driel-Gesztelyi, L. (1996). Evidence for Current-carrying Emerging Flux. *ApJ*, 462:547.

Lim, E.-K. and Chae, J. (2009). Chirality of Intermediate Filaments and Magnetic Helicity of Active Regions. *ApJ*, 692:104–108.

Lites, B. W. and Skumanich, A. (1985). The inference of vector magnetic fields from polarization measurements with limited spectral resolution. In Hagyard, M. J., editor, *Measurements of Solar Vector Magnetic Fields*, pages 342–367.

Lites, B. W. and Skumanich, A. (1989). The Advanced Stokes Polarimeter. In O. von der Luehe, editor, *High spatial resolution solar observations*, page 389.

Liu, Y., Luhmann, J. G., Müller-Mellin, R., Schroeder, P. C., Wang, L., Lin, R. P., Bale, S. D., Li, Y., Acuña, M. H., and Sauvaud, J. (2008). A Comprehensive View of the 2006 December 13 CME: From the Sun to Interplanetary Space. *ApJ*, 689:563–571.

Longcope, D. W., Fisher, G. H., and Pevtsov, A. A. (1998). Flux-Tube Twist Resulting from Helical Turbulence: The Sigma-Effect. *ApJ*, 507:417–432.

Longcope, D. W. and Welsch, B. T. (2000). A Model for the Emergence of a Twisted Magnetic Flux Tube. *ApJ*, 545:1089–1100.

López Ariste, A., Aulanier, G., Schmieder, B., and Sainz Dalda, A. (2006). First observation of bald patches in a filament channel and at a barb endpoint. *A&A*, 456:725–735.

López Fuentes, M. C., Demoulin, P., Mandrini, C. H., and van Driel-Gesztelyi, L. (2000). The Counterkink Rotation of a Non-Hale Active Region. *ApJ*, 544:540–549.

Louis, R. E., Bellot Rubio, L. R., Mathew, S. K., and Venkatakrishnan, P. (2009). Supersonic Downflows in a Sunspot Light Bridge. *ApJ*, 704:L29–L33.

Low, B. C. (1982). Magnetic field configurations associated with polarity intrusion in a solar active region. I - The force-free fields. *Solar Phys.*, 77:43–61.

Low, B. C. (1985). Modeling solar magnetic structures. *Measurements of Solar Vector Magnetic Fields*, 2374:49–65.

Low, B. C. (1989). Magnetic Free-Energy in the Solar Atmosphere. *Washington DC American Geophysical Union Geophysical Monograph Series*, 54:21.

Luoni, M. L., Mandrini, C. H., Dasso, S., Démoulin, P., and Van Driel-Gesztelyi, L. (2007). From The Photosphere to the Interplanetary Medium: The Magnetic Helicity Sign from Observations. *Boletin de la Asociacion Argentina de Astronomia La Plata Argentina*, 50:43–46.

Luoni, M. L., Mandrini, C. H., Démoulin, P., van Diel-Gesztelyi, L., and Kövári, Z. (2004). Can we determine the magnetic helicity sign of the solar active regions? *Boletin de la Asociacion Argentina de Astronomia La Plata Argentina*, 47:14–17.

Magara, T. (2009). Characteristic Development of Magnetic Shear in a Flare-producing Sunspot Obtained from Vector Magnetic Field Measurements by Hinode. *ApJ*, 702:386–391.

Magara, T. and Tsuneta, S. (2008). Hinode's Observational Result on the Saturation of Magnetic Helicity Injected into the Solar Atmosphere and Its Relation to the Occurrence of a Solar Flare. *PASJ*, 60:1181–1189.

Makita, M., Hamana, S., Nishi, K., Shimizu, M., and Koyano, H. (1985). Observations by the solar vector magnetograph of the Okayama Astrophysical Observatory. *PASJ*, 37:561–573.

Martin, S. F. (1998). Filament Chirality: A Link Between Fine-Scale and Global Patterns (Review). In Webb, D. F., Schmieder, B., and Rust, D. M., editors, *IAU Colloq. 167: New Perspectives on Solar Prominences*, volume 150 of *Astronomical Society of the Pacific Conference Series*, pages 419–429.

Martin, S. F. (2003). Signs of helicity in solar prominences and related features. *Advances in Space Research*, 32:1883–1893.

Martin, S. F., Bilimoria, R., and Tracadas, P. W. (1993). Magnetic Field Configurations Basic to Filament Channels and Filaments. In *Bulletin of the American Astronomical Society*, volume 25 of *Bulletin of the American Astronomical Society*, page 1217.

Martin, S. F., Bilimoria, R., and Tracadas, P. W. (1994). Magnetic field configurations basic to filament channels and filaments. In Rutten, R. J. and Schrijver, C. J., editors, *Solar Surface Magnetism*, page 303.

Martin, S. F., Lin, Y., and Engvold, O. (2008). A Method of Resolving the 180-Degree Ambiguity by Employing the Chirality of Solar Features. *Solar Phys.*, 250:31–51.

Martin, S. F. and McAllister, A. H. (1996). The Skew of X-ray Coronal Loops Overlying H alpha Filaments. In Uchida, Y., Kosugi, T., and Hudson, H. S., editors, *IAU Colloq. 153: Magnetodynamic Phenomena in the Solar Atmosphere - Prototypes of Stellar Magnetic Activity*, page 497.

Mathew, S. K., Lagg, A., Solanki, S. K., Collados, M., Borrero, J. M., Berdyugina, S., Krupp, N., Woch, J., and Frutiger, C. (2003). Three dimensional structure of a regular sunspot from the inversion of IR Stokes profiles. *A&A*, 410:695–710.

Melrose, D. B. (1992). Energy propagation into a flare kernel during a solar fire. *ApJ*, 387:403–413.

Melrose, D. B. (1995). Current Paths in the Corona and Energy Release in Solar Flares. *ApJ*, 451:391–401.

Metcalf, T. R., Jiao, L., McClymont, A. N., Canfield, R. C., and Uitenbroek, H. (1995). Is the solar chromospheric magnetic field force-free? *ApJ*, 439:474–481.

Metcalf, T. R., Leka, K. D., Barnes, G., Lites, B. W., Georgoulis, M. K., Pevtsov, A. A., Balasubramaniam, K. S., Gary, G. A., Jing, J., Li, J., Liu, Y., Wang, H. N., Abramenko, V., Yurchyshyn, V., and Moon, Y.-J. (2006). An Overview of Existing Algorithms for Resolving the 180° Ambiguity in Vector Magnetic Fields: Quantitative Tests with Synthetic Data. *Solar Phys.*, 237:267–296.

Mickey, D. L. (1985). The Haleakala Stokes polarimeter. *Solar Phys.*, 97:223–238.

Mickey, D. L., Canfield, R. C., Labonte, B. J., Leka, K. D., Waterson, M. F., and Weber, H. M. (1996). The Imaging Vector Magnetograph at Haleakala. *Solar Phys.*, 168:229–250.

Moffatt, H. K. (1969). The degree of knottedness of tangled vortex lines. *Journal of Fluid Mechanics*, 35:117–129.

Moffatt, H. K. (1978). *Magnetic field generation in electrically conducting fluids.*

Molodensky, M. M. (1974). Equilibrium and stability of force-free magnetic field. *Solar Phys.*, 39:393–404.

Moon, Y., Kim, Y., Park, Y., Ichimoto, K., Sakurai, T., Chae, J., Cho, K. S., Bong, S., Suematsu, Y., Tsuneta, S., Katsukawa, Y., Shimojo, M., Shimizu, T., Shine, R. A., Tarbell, T. D., Title, A. M., Lites, B., Kubo, M., Nagata, S., and Yokoyama, T. (2007). Hinode SP Vector Magnetogram of AR10930 and Its Cross-Comparison with MDI. *PASJ*, 59:625–630.

Nandy, D. (2006). Magnetic helicity and flux tube dynamics in the solar convection zone: Comparisons between observation and theory. *Journal of Geophysical Research (Space Physics)*, 111:A12S01.

Nandy, D. (2008). Magnetic Helicity, Coronal Heating and Solar Flaring Activity: A Review of the Role of Active Region Twist. In Howe, R., Komm, R. W.,

Balasubramaniam, K. S., and Petrie, G. J. D., editors, *Subsurface and Atmospheric Influences on Solar Activity*, volume 383 of *Astronomical Society of the Pacific Conference Series*, page 201.

Parker, E. N. (1979). *Cosmical magnetic fields: Their origin and their activity*. Oxford, Clarendon Press; New York, Oxford University Press, 1979.

Parker, E. N. (1981a). The Dissipation of Inhomogeneous Magnetic Fields and the Problem of Coronae - Part Two - the Dynamics of Dislocated Flux. *ApJ*, 244:644–652.

Parker, E. N. (1981b). The dissipation of inhomogeneous magnetic fields and the problem of coronae. I - Dislocation and flattening of flux tubes. II - The dynamics of dislocated flux. *ApJ*, 244:631–652.

Parker, E. N. (1983a). Magnetic Neutral Sheets in Evolving Fields - Part Two - Formation of the Solar Corona. *ApJ*, 264:642–647.

Parker, E. N. (1983b). Magnetic neutral sheets in evolving fields. I - General theory. . *ApJ*, 264:635–647.

Parker, E. N. (1994). *Spontaneous current sheets in magnetic fields : with applications to stellar x-rays(New York : Oxford University Press)*.

Parker, E. N. (1996). Inferring Mean Electric Currents in Unresolved Fibril Magnetic Fields. *ApJ*, 471:485–488.

Pevtsov, A. A. (2008). What helicity can tell us about solar magnetic fields. *Journal of Astrophysics and Astronomy*, 29:49–56.

Pevtsov, A. A., Balasubramaniam, K. S., and Rogers, J. W. (2003). Chirality of Chromospheric Filaments. *ApJ*, 595:500–505.

Pevtsov, A. A., Canfield, R. C., and Latushko, S. M. (2001). Hemispheric Helicity Trend for Solar Cycle 23. *ApJ*, 549:L261–L263.

Pevtsov, A. A., Canfield, R. C., and Metcalf, T. R. (1994). Patterns of helicity in solar active regions. *ApJ*, 425:L117–L119.

Pevtsov, A. A., Canfield, R. C., and Metcalf, T. R. (1995). Latitudinal variation of helicity of photospheric magnetic fields. *ApJ*, 440:L109–L112.

Pevtsov, A. A., Canfield, R. C., Sakurai, T., and Hagino, M. (2008). On the Solar Cycle Variation of the Hemispheric Helicity Rule. *ApJ*, 677:719–722.

Pevtsov, A. A., Canfield, R. C., and Zirin, H. (1996). Reconnection and Helicity in a Solar Flare. *ApJ*, 473:533–538.

Pevtsov, A. A. and Longcope, D. W. (2001). Origin of Helicity in the Quiet Sun. In Sigwarth, M., editor, *Advanced Solar Polarimetry – Theory, Observation, and Instrumentation*, volume 236 of *Astronomical Society of the Pacific Conference Series*, page 423.

Pevtsov, A. A. and Longcope, D. W. (2007). Helicity as the Ultimate Test to the Surface Dynamo Problem. In Shibata, K., Nagata, S., and Sakurai, T., editors, *New Solar Physics with Solar-B Mission*, volume 369 of *Astronomical Society of the Pacific Conference Series*, page 99.

Povel, H. (1995). Imaging Stokes polarimetry with piezoelastic modulators and charge-coupled-device image sensors. *Optical Engineering*, 34:1870–1878.

Rachkowsky, D. N. (1967). . *Izv. Krymsk. Astrofiz. Obs.*, 37:56.

Rempel, M., Schüssler, M., Cameron, R. H., and Knölker, M. (2009a). Penumbral Structure and Outflows in Simulated Sunspots. *Science*, 325:171–174.

Rempel, M., Schüssler, M., and Knölker, M. (2009b). Radiative Magnetohydrodynamic Simulation of Sunspot Structure. *ApJ*, 691:640–649.

Richardson, R. S. (1941). The Nature of Solar Hydrogen Vortices. *ApJ*, 93:24–28.

Rucklidge, A. M., Schmidt, H. U., and Weiss, N. O. (1995). The abrupt development of penumbrae in sunspots. *MNRAS*, 273:491–498.

Rust, D. M. (1994). Spawning and shedding helical magnetic fields in the solar atmosphere. *Geophysics Research Letters*, 21:241–244.

Rust, D. M. (2003). The helicial flux rope structure of solar filaments. *Advances in Space Research*, 32:1895–1903.

Rust, D. M. and Kumar, A. (1996). Evidence for Helically Kinked Magnetic Flux Ropes in Solar Eruptions. *ApJ*, 464:L199–L202.

Sakurai, T. (1989). Computational modeling of magnetic fields in solar active regions. *Space Science Reviews*, 51:11–48.

Sakurai, T., Ichimoto, K., Nishino, Y., Shinoda, K., Noguchi, M., Hiei, E., Li, T., He, F., Mao, W., Lu, H., Ai, G., Zhao, Z., Kawakami, S., and Chae, J.-C. (1995). Solar flare telescope at Mitaka. *PASJ*, 47:81–92.

Sakurai, T., Makita, M., and Shibasaki, K. (1985). Observation of magnetic field vector in solar active regions. *MPA Rep., No. 212, p. 312 - 315.*

S'anchez Almeida, J. (1998). The Unresolved Structure of Photospheric Magnetic Fields: Truths, Troubles and Tricks (Invited review). In Alissandrakis, C. E. and Schmieder, B., editors, *Three-Dimensional Structure of Solar Active Regions*, volume 155 of *Astronomical Society of the Pacific Conference Series*, page 54.

Sankarasubramanian, K., Elmore, D. F., Lites, B. W., Sigwarth, M., Rimmele, T. R., Hegwer, S. L., Gregory, S., Streander, K. V., Wilkins, L. M., Richards, K., and Berst, C. (2003). Diffraction limited spectro-polarimeter - Phase I. In S. Fineschi, editor, *Society of Photo-Optical Instrumentation Engineers (SPIE) Conference Series*, volume 4843 of *Presented at the Society of Photo-Optical Instrumentation Engineers (SPIE) Conference*, pages 414–424.

Sankarasubramanian, K., Gullixson, C., Hegwer, S., Rimmele, T. R., Gregory, S., Spence, T., Fletcher, S., Richards, K., Rousset, E., Lites, B., Elmore, D., Streander, K., and Sigwarth, M. (2004). The Diffraction Limited Spectro-Polarimeter: a new instrument for high-resolution solar polarimetry. In Fineschi, S. and Gummin, M. A., editors, *Society of Photo-Optical Instrumentation Engineers (SPIE) Conference Series*, volume 5171, pages 207–218.

Sankarasubramanian, K., Lites, B., Gullixson, C., Elmore, D., Hegwer, S., Streander, K., Rimmele, T., Fletcher, S., Gregory, S., and Sigwarth, M. (2006). The Diffraction Limited Spectro-Polarimeter. In Casini, R. and Lites, B. W., editors, *Astronomical Society of the Pacific Conference Series*, volume 358, page 201.

Scharmer, G. B. and Spruit, H. C. (2006). Magnetostatic penumbra models with field-free gaps. *A&A*, 460:605–615.

Schmidt, W., Beck, C., Kentischer, T., Elmore, D., and Lites, B. (2003). POLIS: A spectropolarimeter for the VTT and for GREGOR. *Astronomische Nachrichten*, 324:300–301.

Schrijver, C. J., De Rosa, M. L., Metcalf, T., Barnes, G., Lites, B., Tarbell, T., McTiernan, J., Valori, G., Wiegelmann, T., Wheatland, M. S., Amari,

T., Aulanier, G., Démoulin, P., Fuhrmann, M., Kusano, K., Régnier, S., and Thalmann, J. K. (2008). Nonlinear Force-free Field Modeling of a Solar Active Region around the Time of a Major Flare and Coronal Mass Ejection. *ApJ*, 675:1637–1644.

Seehafer, N. (1990). Electric current helicity in the solar atmosphere. *Solar Phys.*, 125:219–232.

Seehafer, N., Gellert, M., Kuzanyan, K. M., and Pipin, V. V. (2003). Helicity and the solar dynamo. *Advances in Space Research*, 32:1819–1833.

Severnyi, A. B. (1965). . *Izv. Krymsk. Astrofiz. Obs.*, 33:34.

Shimizu, T., Nagata, S., Tsuneta, S., Tarbell, T., Edwards, C., Shine, R., Hoffmann, C., Thomas, E., Sour, S., Rehse, R., Ito, O., Kashiwagi, Y., Tabata, M., Kodeki, K., Nagase, M., Matsuzaki, K., Kobayashi, K., Ichimoto, K., and Suematsu, Y. (2008). Image Stabilization System for Hinode (Solar-B) Solar Optical Telescope. *Solar Phys.*, 249:221–232.

Skumanich, A. and Lites, B. W. (1987). Stokes profile analysis and vector magnetic fields. I - Inversion of photospheric lines. *ApJ*, 322:473–482.

Socas-Navarro, H. (2001). Stokes Inversion Techniques: Recent Achievements and Future Horizons. In Sigwarth, M., editor, *Advanced Solar Polarimetry – Theory, Observation, and Instrumentation*, volume 236 of *Astronomical Society of the Pacific Conference Series*, page 487.

Socas-Navarro, H. (2005). Are Electric Currents Heating the Magnetic Chromosphere? *ApJ*, 633:L57–L60.

Sokoloff, D., Zhang, H., Kuzanyan, K. M., Obridko, V. N., Tomin, D. N., and Tutubalin, V. N. (2008). Current Helicity and Twist as Two Indicators of the Mirror Asymmetry of Solar Magnetic Fields. *Solar Phys.*, 248:17–28.

Solanki, S. K. (1989). The origin and the diagnostic capabilities of the Stokes V asymmetry observed in solar faculae and the network. *A&A*, 224:225–241.

Solanki, S. K. and Montavon, C. A. P. (1993). Uncombed fields as the source of the broad-band circular polarization of sunspots. *A&A*, 275:283–292.

Spruit, H. C. and Scharmer, G. B. (2006). Fine structure, magnetic field and heating of sunspot penumbrae. *A&A*, 447:343–354.

Staude, J., Hofmann, A., and Bachmann, G. (1991). The Potsdam vector magnetograph: methodical experiences and results. In *11. National Solar Observatory / Sacramento Peak Summer Workshop: Solar polarimetry, p. 49 - 58*, pages 49–58.

Stenflo, J. O. (1996). New window for spectroscopy. *Nature*, 382:588.

Stenflo, J. O. and Keller, C. U. (1997). The second solar spectrum. A new window for diagnostics of the Sun. *A&A*, 321:927–934.

Stepanov, V. E. and Severny, A. B. (1962). . *Izv. Krymsk. Astrofiz. Obs.*, 28:166.

Su, J., Liu, Y., Liu, J., Mao, X., Zhang, H., Li, H., Wang, X., and Xie, W. (2008). Lorentz Force: A Possible Driving Force for Sunspot Rotation. *Solar Phys.*, 252:55–71.

Su, J. T., Sakurai, T., Suematsu, Y., Hagino, M., and Liu, Y. (2009). Local Twist and Current Helicity Distributions of Active Region NOAA 10930. *ApJ*, 697:L103–L107.

Su, Y., Golub, L., van Ballegooijen, A., Deluca, E. E., Reeves, K. K., Sakao, T., Kano, R., Narukage, N., and Shibasaki Kiyoto (2007). Evolution of the Sheared Magnetic Fields of Two X-Class Flares Observed by Hinode/XRT. *PASJ*, 59:785–791.

Subramanian, K. and Brandenburg, A. (2006). Magnetic Helicity Density and Its Flux in Weakly Inhomogeneous Turbulence. *ApJ*, 648:L71–L74.

Suematsu, Y., Tsuneta, S., Ichimoto, K., Shimizu, T., Otsubo, M., Katsukawa, Y., Nakagiri, M., Noguchi, M., Tamura, T., Kato, Y., Hara, H., Kubo, M., Mikami, I., Saito, H., Matsushita, T., Kawaguchi, N., Nakaoji, T., Nagae, K., Shimada, S., Takeyama, N., and Yamamuro, T. (2008). The Solar Optical Telescope of Solar-B (Hinode): The Optical Telescope Assembly. *Solar Phys.*, 249:197–220.

Tan, C., Chen, P. F., Abramenko, V., and Wang, H. (2009). Evolution of Optical Penumbral and Shear Flows Associated with the X3.4 Flare of 2006 December 13. *ApJ*, 690:1820–1828.

Taylor, J. B. (1974). Relaxation of Toroidal Plasma and Generation of Reverse Magnetic Fields. *Physical Review Letters*, 33:1139–1141.

Thomas, J. H., Weiss, N. O., Tobias, S. M., and Brummell, N. H. (2002). Downward pumping of magnetic flux as the cause of filamentary structures in sunspot penumbrae. *Nature*, 420:390–393.

Tian, L., Bao, S., Zhang, H., and Wang, H. (2001). Relationship in sign between tilt and twist in active region magnetic fields. *A&A*, 374:294–300.

Tildesley, M. J. (2003). On the origin of filamentary structure in sunspot penumbrae: linear instabilities. *MNRAS*, 338:497–507.

Tiwari, S. K., Joshi, J., Gosain, S., and Venkatakrishnan, P. (2008). Evolution of Magnetic Helicity in NOAA 10923 Over Three Consecutive Solar Rotations. In Hasan, S. S., Gangadhara, R. T., and Krishan, V., editors, *Turbulence, Dynamos, Accretion Disks, Pulsars and Collective Plasma Processes*, Astrophysics and Space Science Proceedings, pages 329–335.

Tiwari, S. K., Venkatakrishnan, P., Gosain, S., and Joshi, J. (2009a). Effect of Polarimetric Noise on the Estimation of Twist and Magnetic Energy of Force-Free Fields. *ApJ*, 700:199–208.

Tiwari, S. K., Venkatakrishnan, P., and Sankarasubramanian, K. (2009b). Global Twist of Sunspot Magnetic Fields Obtained from High Resolution Vector Magnetograms. *ApJ*, 702:L133–L137.

Tiwari, S. K., Venkatakrishnan, P., and Sankarasubramanian, K. (2009c). Helicity at Photospheric and Chromospheric Heights. *arXiv, (http://adsabs.harvard.edu/abs/2009arXiv0904.4353T)*.

Tsuneta, S., Ichimoto, K., Katsukawa, Y., Nagata, S., Otsubo, M., Shimizu, T., Suematsu, Y., Nakagiri, M., Noguchi, M., Tarbell, T., Title, A., Shine, R., Rosenberg, W., Hoffmann, C., Jurcevich, B., Kushner, G., Levay, M., Lites, B., Elmore, D., Matsushita, T., Kawaguchi, N., Saito, H., Mikami, I., Hill, L. D., and Owens, J. K. (2008). The Solar Optical Telescope for the Hinode Mission: An Overview. *Solar Phys.*, 249:167–196.

Unno, W. (1956). Line Formation of a Normal Zeeman Triplet. *PASJ*, 8:108–125.

Venkatakrishnan, P. (1990a). Implications of Tension-Free Equilibria for Pre-Flare Energy Build UP. In E. R. Priest & V. Krishan, editor, *Basic Plasma Processes on the Sun*, volume 142 of *IAU Symposium*, page 323.

Venkatakrishnan, P. (1990b). Loss of magnetic tension in pre-flare magnetic configurations. *Solar Phys.*, 128:371–376.

Venkatakrishnan, P. and Gary, G. A. (1989). Off disk-center potential field calculations using vector magnetograms. *Solar Phys.*, 120:235–247.

Venkatakrishnan, P., Hagyard, M. J., and Hathaway, D. H. (1988). Elimination of projection effects from vector magnetograms - The pre-flare configuration of active region AR 4474. *Solar Phys.*, 115:125–131.

Venkatakrishnan, P., Hagyard, M. J., and Hathaway, D. H. (1989). Evaluation of magnetic shear in off-disk center active regions. *Solar Phys.*, 122:215–226.

Venkatakrishnan, P., Narayanan, R. S., and Prasad, N. D. N. (1993). Correlation between magnetic shear and magnetic tension in a solar active region. *Solar Phys.*, 144:315–322.

Venkatakrishnan, P. and Tiwari, S. K. (2009). On the Absence of Photospheric Net Currents in Vector Magnetograms of Sunspots Obtained from Hinode (Solar Optical Telescope/Spectro-Polarimeter). *ApJ*, 706:L114–L119.

Wang, H., Jing, J., Tan, C., Wiegelmann, T., and Kubo, M. (2008a). Study of Magnetic Channel Structure in Active Region 10930. *ApJ*, 687:658–667.

Wang, J., Shi, Z., Wang, H., and Lue, Y. (1996). Flares and the Magnetic Nonpotentiality. *ApJ*, 456:861.

Wang, S. J., Yan, Y. H., Liu, Y. Y., Fu, Q. J., Tan, B. L., and Zhang, Y. (2008b). Solar Radio Spikes in 2.6 - 3.8 GHz during the 13 December 2006 Event. *Solar Phys.*, 253:133–141.

Weiss, N. O., Thomas, J. H., Brummell, N. H., and Tobias, S. M. (2004). The Origin of Penumbral Structure in Sunspots: Downward Pumping of Magnetic Flux. *ApJ*, 600:1073–1090.

West, E. A. and Hagyard, M. J. (1983). Interpretation of vector magnetograph data including magneto-optic effects. I - Azimuth angle of the transverse field. *Solar Phys.*, 88:51–64.

Wheatland, M. S. (2000). Are Electric Currents in Solar Active Regions Neutralized? *ApJ*, 532:616–621.

White, J. H. (1969). . *Am. J. Maths*, 91:693.

Wilkinson, L. K., Emslie, A. G., and Gary, G. A. (1992). On neutralized currents in the solar corona. *ApJ*, 392:L39–L42.

Wilkinson, L. K., Emslie, G. A., and Gary, G. A. (1989). The effects of viewing angle on the inference of magnetic shear in preflare active regions. *Solar Phys.*, 119:77–86.

Williams, D. R., Harra, L. K., Brooks, D. H., Imada, S., and Hansteen, V. H. (2009). Evidence from the Extreme-Ultraviolet Imaging Spectrometer for Axial Filament Rotation before a Large Flare. *PASJ*, 61:493.

Woltjer, L. (1958). The Stability of Force-Free Magnetic Fields. *ApJ*, 128:384–391.

Yan, Y., Huang, J., Chen, B., and Sakurai, T. (2007). Diagnostics of Radio Fine Structures around 3 GHz with Hinode Data in the Impulsive Phase of an X3.4/4B Flare Event on 2006 December 13. *PASJ*, 59:815–821.

Zeeman, P. (1897). On the Influence of Magnetism on the Nature of the Light Emitted by a Substance. *ApJ*, 5:332–347.

Zhang, J., Li, L., and Song, Q. (2007). Interaction between a Fast Rotating Sunspot and Ephemeral Regions as the Origin of the Major Solar Event on 2006 December 13. *ApJ*, 662:L35–L38.

Zhang, M. (2006). Helicity Observations of Weak and Strong Fields. *ApJ*, 646:L85–L88.

List of Publications

I. Papers in Journals:

1. *Effect of Polarimetric Noise on the Estimation of Twist and Magnetic Energy of Force-Free Fields*,

- Sanjiv Kumar Tiwari, P. Venkatakrishnan, Sanjay Gosain, and Jayant Joshi, *Astrophysical Journal*, **700**, 199-208 (2009).

2. *Global Twist of Sunspot Magnetic Fields Obtained from High-Resolution Vector Magnetograms*,

- Sanjiv Kumar Tiwari, P. Venkatakrishnan, and K. Sankarasubramanian, *Astrophysical Journal Letters*, **702**, L133-L137 (2009).

3. *On the Absence of Photospheric Net Currents in Vector Magnetograms of Sunspots Obtained From Hinode (Solar Optical Telescope/Spectro-Polarimeter)*,

- P. Venkatakrishnan, and **Sanjiv Kumar Tiwari**,

Astrophysical Journal Letters, **706**, L114-L119 (2009).

4. *HINODE Observations of Coherent Lateral Motion of Penumbral Filaments during a X-class Flare*,

- Sanjay Gosain, P. Venkatakrishnan, and **Sanjiv Kumar Tiwari**,

Astrophysical Journal Letters, **706**, L240-L245 (2009).

II. In Conference Proceedings:

1. *Evolution of Magnetic Helicity in NOAA 10923 Over Three Consecutive Solar Rotations*,

- Sanjiv Kumar Tiwari, Jayant Joshi, Sanjay Gosain, and P. Venkatakrishnan, in *"Turbulence, Dynamos, Accretion Disks, Pulsars and Collective Plasma Processes"*, eds. S. S. Hasan, R. T. Gangadhara and V. Krishan, Astrophysics and Space Science Proceedings, Volume . ISBN 978-1-4020-8867-4, Springer-Verlag,

Heidelberg, Berlin, 329-335 (2008).

2. *Software for Interactively Visualizing Solar Vector Magnetograms of Udaipur Solar Observatory*,

- Sanjay Gosain, **Sanjiv Kumar Tiwari**, Jayant Joshi, and P. Venkatakrishnan, *Journal of Astrophysics and Astronomy*, **29**, 107-111(2008).

3. *Helicity at Photospheric and Chromospheric Heights*,

- Sanjiv Kumar Tiwari, P. Venkatakrishnan, and K. Sankarasubramanian, in *"Magnetic Coupling between the Interior and the Atmosphere of the Sun"*, eds. S. S. Hasan and R. J. Rutten, Astrophysics and Space Science Proceedings, Springer-Verlag, Heidelberg, Berlin, In Press (2009).

The Astrophysical Journal, 700:199–208, 2009 July 20 doi:10.1088/0004-637X/700/1/199

EFFECT OF POLARIMETRIC NOISE ON THE ESTIMATION OF TWIST AND MAGNETIC ENERGY OF FORCE-FREE FIELDS

Sanjiv Kumar Tiwari, P. Venkatakrishnan, Sanjay Gosain, and Jayant Joshi
Udaipur Solar Observatory, Physical Research Laboratory, Dewali, Bari Road, Udaipur-313 001, India; stiwari@prl.res.in, pvk@prl.res.in, sgosain@prl.res.in, jayant@prl.res.in
Received 2009 March 5; accepted 2009 April 29; published 2009 July 1

ABSTRACT

The force-free parameter α, also known as helicity parameter or twist parameter, bears the same sign as the magnetic helicity under some restrictive conditions. The single global value of α for a whole active region gives the degree of twist per unit axial length. We investigate the effect of polarimetric noise on the calculation of global α value and magnetic energy of an analytical bipole. The analytical bipole has been generated using the force-free field approximation with a known value of constant α and magnetic energy. The magnetic parameters obtained from the analytical bipole are used to generate Stokes profiles from the Unno–Rachkovsky solutions for polarized radiative transfer equations. Then we add random noise of the order of 10^{-3} of the continuum intensity (I_c) in these profiles to simulate the real profiles obtained by modern spectropolarimeters such as *Hinode* (SOT/SP), SVM (USO), ASP, DLSP, POLIS, and SOLIS etc. These noisy profiles are then inverted using a Milne–Eddington inversion code to retrieve the magnetic parameters. Hundred realizations of this process of adding random noise and polarimetric inversion is repeated to study the distribution of error in global α and magnetic energy values. The results show that (1) the sign of α is not influenced by polarimetric noise and very accurate values of global twist can be calculated, and (2) accurate estimation of magnetic energy with uncertainty as low as 0.5% is possible under the force-free condition.

Key words: Sun: magnetic fields – Sun: photosphere

Online-only material: color figure

1. INTRODUCTION

Helical structures in the solar features like sunspot whirls were reported long back by George E. Hale in 1925 (Hale 1925, 1927). He found that about 80% of the sunspot whirls were counterclockwise in the northern hemisphere and clockwise in the southern hemisphere. Later, in 1941 the result was confirmed by Richardson (Richardson 1941) by extending the investigation over four solar cycles. This hemispheric pattern was found to be independent of the solar cycle. Since the 90s, the subject has been rejuvenated and this hemispheric behavior independent of sunspot cycle has been observed for many of the solar features such as active regions (Seehafer 1990; Pevtsov et al. 1995; Longcope et al. 1998; Abramenko et al. 1996; Bao & Zhang 1998; Hagino & Sakurai 2005), filaments (Martin et al. 1994; Pevtsov et al. 2003; Bernasconi et al. 2005), coronal loops (Rust & Kumar 1996; Pevtsov & Longcope 2001), interplanetary magnetic clouds (IMCs; Rust 1994), coronal X-ray arcades (Martin & McAllister 1996), and network magnetic fields (Pevtsov et al. 2001; Pevtsov & Longcope 2007) etc.

Helicity is a physical quantity that measures the degree of linkages and twistedness in the field lines (Berger & Field 1984). Magnetic helicity H_m is given by a volume integral over the scalar product of the magnetic field **B** and its vector potential **A** (Elsasser 1956).

$$H_m = \int_V \mathbf{A} \cdot \mathbf{B} dV \tag{1}$$

with $\mathbf{B} = \nabla \times \mathbf{A}$.

It is well known that the vector potential **A** is not unique, thereby preventing the calculation of a unique value for the magnetic helicity from Equation (1). Seehafer (1990) pointed out that the helicity of magnetic field can best be characterized by the force-free parameter α, also known as the helicity parameter or twist parameter. The force-free condition (Chandrasekhar 1961, Chapter 2; Parker 1979) is given as

$$\nabla \times \mathbf{B} = \alpha \mathbf{B}. \tag{2}$$

Alpha is a measure of the degree of twist per unit axial length (see Appendix A for details of physical meaning of alpha). This is a local parameter which can vary across the field but is constant along the field lines.

Researchers have claimed to have determined the sign of magnetic helicity on the photosphere by calculating alpha, e.g., $\alpha_{\rm best}$ (Pevtsov et al. 1995), averaged alpha, e.g., $\langle \alpha_z \rangle = \langle J_z / B_z \rangle$ (Pevtsov et al. 1994) with current density $J_z = (\nabla \times \mathbf{B})_z$. Some authors have used current helicity density $H_c = B_z \cdot J_z$ and α_{av} (Bao & Zhang 1998; Hagino & Sakurai 2004, 2005). A good correlation was found between $\alpha_{\rm best}$ and $\langle \alpha_z \rangle$ by Burnette et al. (2004) and Leka et al. (1996). But the sign of magnetic helicity cannot be inferred from the force-free parameter α under all conditions (see Appendix B).

It is well known that the reliable measurements of vector magnetic fields are needed to study various important parameters such as electric currents in the active regions, magnetic energy dissipation during flares, field geometry of sunspots, magnetic twist etc. The study of error propagation from polarization measurements to vector field parameters is very important (Lites & Skumanich 1985; Klimchuk et al. 1992). Klimchuk et al. (1992) have studied the effects of realistic errors, e.g., due to random polarization noise, cross talk between different polarization signals, systematic polarization bias, and seeing induced cross talk etc. on known magnetic fields. They derived analytical expressions for how these errors produce errors in the estimation of magnetic energy (calculated from virial theorem). However, they simulated these effects for magnetographs which sample polarization at few fixed wavelength positions in line wings. It

is well known that such observations lead to systematic underestimation of field strength and also suffer from magneto-optical effects (West & Hagyard 1983). Whereas in our analysis, we simulate the effect of polarimetric noise on field parameters as deduced by full Stokes inversion. The details are discussed in the Section 6.

Pevtsov et al. (1995) found large variations in the global α values from repeated observations of the same active regions. It is important to model the measurement uncertainties before looking for physical explanations for such a scatter.

In a study by Hagyard & Pevtsov (1999) the noise levels in the observed fields were analyzed, but a quantitative relationship between the uncertainties in fields and the uncertainties in global α value were not established. They could only determine the extent to which the incremental introduction of noise affects the observed value of alpha. However, for the proper tracking of error propagation, we need to start with ideal data devoid of noise and with known values of α and magnetic energy. We follow the latter approach in our present analysis.

Here, we estimate the accuracy in the calculation of the α parameter and the magnetic energy due to different noise levels in the spectropolarimetric profiles. Modern instruments measure the full Stokes polarization parameters within the line profile. Basically there are two types of spectropolarimeters: (1) Spectrograph based, e.g., Advanced Stokes Polarimeter (ASP; Elmore et al. 1992), Zurich Imaging Polarimeter (ZIMPOL; Keller et al. 1992; Povel 1995; Stenflo 1996; Stenflo & Keller 1997), THEMIS-MTR (Arnaud et al. 1998), SOLIS–Vector Spectro-Magnetograph (VSM; Jones et al. 2002; Keller et al. 2003), Polarimetric Littrow Spectrograph (POLIS; Schmidt et al. 2003), Diffraction Limited Spectro-polarimeter (DLSP; Sankarasubramanian et al. 2004, 2006), *Hinode* (SOT/SP; Tsuneta et al. 2008), etc., and (2) Filter-based, e.g., Imaging Vector Magnetograph (IVM) at Mees Solar Observatory, Hawaii (Mickey et al. 1996), Solar Vector Magnetograph at Udaipur Solar Observatory (SVM-USO; Gosain et al. 2004, 2006) etc.

Earlier magnetographs such as Crimea (Stepanov & Severny 1962), MSFC (Hagyard et al. 1982), HSP (Mickey 1985), OAO (Makita et al. 1985), HSOS (Ai & Hu 1986), Potsdam vector magnetograph (Staude et al. 1991), SFT (Sakurai et al. 1995) etc. were mostly based on polarization measurements at a few wavelength positions in the line wings and hence subjected to Zeeman saturation effects as well as magneto-optical effects such as Faraday rotation (West & Hagyard 1983; Hagyard et al. 2000).

The magnetic field vector deduced from Stokes profiles by modern techniques is almost free from such effects (Skumanich & Lites 1987; S'anchez Almeida 1998; Socas-Navarro 2001).

This paper serves three purposes. First, we estimate the error in the calculation of field strength, inclination, and azimuth and thereafter in the calculation of the vector field components B_x, B_y, and B_z. Second, we estimate the error in the determination of global α due to noise in polarimetric profiles constructed from the analytical vector field data. Third, we estimate the error in the calculation of magnetic energy derived using virial theorem, due to polarimetric noise.

In the next section (Section 2) we discuss a direct method for calculation of a single global α for an active region. In Section 3, we describe the method of simulating an analytical bipole field. Section 4 contains the analysis and the results. Error estimation in global α is given in Section 5. In Section 6, we discuss the process of estimating the error in the virial magnetic energy. Section 7 deals with discussion and conclusions.

2. A DIRECT METHOD FOR CALCULATION OF GLOBAL α

Taking the z-component of magnetic field, from the force-free field Equation (2) α can be written as

$$\alpha = \frac{(\nabla \times \mathbf{B})_\mathbf{z}}{B_z}. \tag{3}$$

For a least-squares minimization, we should have

$$\sum(\alpha - \alpha_g)^2 = minimum$$
$$or, \alpha_g = (1/N)\sum \alpha, \tag{4}$$

where α is the local value at each pixel, α_g is the global value of α for the complete active region, and N is total number of pixels. Since Equation (4) will lead to singularities at the neutral lines where B_z approaches 0, therefore the next moment of minimization,

$$\sum(\alpha - \alpha_g)^2 B_z^2 = minimum \tag{5}$$

should be used. From Equation (5) we have

$$\frac{\partial}{\partial \alpha_g}\left(\sum(\alpha - \alpha_g)^2 B_z^2\right) = 0 \tag{6}$$

which leads to the following result,

$$\alpha_g = \frac{\sum\left(\frac{\partial B_y}{\partial x} - \frac{\partial B_x}{\partial y}\right)B_z}{\sum B_z^2}. \tag{7}$$

This formula gives a single global value of α in a sunspot and is the same as $\alpha_{av}^{(2)}$ of Hagino & Sakurai (2004). We prefer this direct way of obtaining global α which is different from the method discussed in Pevtsov et al. (1995) for determining $\alpha_{\rm best}$. The main differences are: (1) the singularities at neutral line are automatically avoided in our method by using the second moment of minimization and (2) the computation of constant α force-free fields for different test values of α is not required. Hagino & Sakurai (2004) used a different parameter $\alpha_{av}^{(1)}$ to avoid the effect of Faraday rotation in sunspot umbrae. However, modern inversion techniques using complete Stokes profiles are free of this problem.

It must be noted that one can generate different values of α_g using higher moments of minimization, e.g., by weighting J_z with B_z^n, with $n = 3, 5, 7,...$ etc. The higher moments will be more sensitive to spatial variation of B_z. Such large and complex variation of B_z is found generally in flare productive active regions (Ambastha et al. 1993; Wang et al. 1996; Hagyard et al. 1999). Thus, we can try to use higher-order α_g as a global index for predicting the flare productivity in active regions.

Finally, to compute α_g we need all the three components of magnetic field which is obtained from the measurements of vector magnetograms. However, here we use the analytically generated bipole, as discussed in the following section, with known values of all the magnetic parameters to investigate the effect of polarimetric noise.

3. GENERATION OF THEORETICAL BIPOLE

We use the analytic, nonpotential force-free fields of the form derived by Low (1982). These fields describe an isolated bipolar

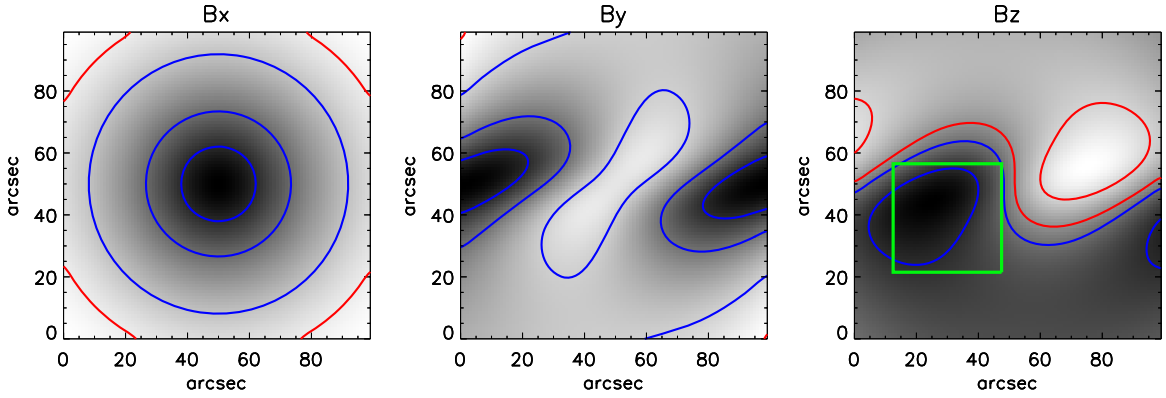

Figure 1. Contours of the field components overlaid on their gray-scale images. The contour levels are 100, 500, and 800 G of magnetic fields. The red and blue contours denote the "positive" and "negative" polarities, respectively. The green box in B_z shows the area which is selected for the calculation of global α. For details see the text.

(A color version of this figure is available in the online journal.)

magnetic region which is obtained by introducing currents into a potential field structure. This potential field is produced by an infinite straight line current running along the intersection of the planes $y = 0$ and $z = -$a, where negative sign denotes planes below the photosphere $z = 0$. At the photosphere ($z = 0$), the field has the following form:

$$B_x = -\frac{B_0 a}{r}\cos\phi(r) \tag{8}$$

$$B_y = \frac{B_0 a x y}{r(y^2+a^2)}\cos\phi(r) - \frac{B_0 a^2}{(y^2+a^2)}\sin\phi(r) \tag{9}$$

$$B_z = \frac{B_0 a^2 x}{r(y^2+a^2)}\cos\phi(r) - \frac{B_0 a y}{(y^2+a^2)}\sin\phi(r), \tag{10}$$

where B_0 is the magnitude of the field at origin and $r^2 = x^2 + y^2 + a^2$. The function $\phi(r)$ is a free generating function related to the force-free parameter α (see Equation (2)) by

$$\alpha = -\frac{d\phi}{dr} \tag{11}$$

which determines the current structure and hence the amount and location of shear present in the region. By choosing $\phi(r) = constant = \pi/2$ we can obtain a simple potential (current-free, $\alpha = 0$) field produced by the infinite line current lying outside the domain. Steeper gradient of $\phi(r)$ results in a more sheared (nonpotential) field.

In Equation (11) the sign on the right hand side is taken positive in the paper by Low (1982) which is a typing mistake (confirmed by B. C. Low 2008, private communication). We mention this here to avoid carrying forward of this typo as was done in Wilkinson et al. (1989).

A grid of 100 × 100 pixels was selected for calculating the field components. The magnitude of field strength at origin has been taken as 1000 G and the value of "a" is taken as 15 pixels (below the photosphere, $z = 0$).

The simulated field components with corresponding contours are shown in the Figure 1.

Here we use the following function (e.g., Wilkinson et al. 1989) for the generation of the field components (B_x, B_y, B_z):

$$\phi(r) = \frac{\pi}{2}\frac{r-a}{2a}, \quad r \leqslant 3a \tag{12}$$

$$= \frac{\pi}{2}, \quad r > 3a. \tag{13}$$

Results for the fields generated by different $\phi(r)$ are quantitatively similar. In this way we generate a set of vector fields with known values of α.

Most of the time one of the bipoles of a sunspot observed on the Sun is compact (leading) and the other (following) is comparatively diffuse. Observations of compact poles give half of the total flux of the sunspot and are mostly used for analysis. One can derive the twist present in the sunspot using one compact pole of the bipolar sunspot for constant α. Thus, we have selected a single polarity of the analytical bipole as shown in Figure 1 to calculate the twist.

The fine structure in real sunspots is difficult to model. Our analysis applies to the large scale patterns of the magnetic field regardless of fine structure. All the following sections discuss the analysis and results obtained.

4. PROFILE GENERATION FROM THE ANALYTICAL DATA AND INVERSION

Using the analytical bipole method (Low 1982) the nonpotential force-free field components B_x, B_y, and B_z in a plane have been generated and are given as in Equations (8), (9), and (10). We have shown B_x, B_y, and B_z maps (generated on a grid of 100 × 100 pixels) in Figure 1. From these components we have derived magnetic field strength (B), inclination (γ), and azimuth (ξ: free from 180° ambiguity). In order to simulate the effect of typical polarimetric noise in actual solar observations on magnetic field measurements and study the error in the calculation of α and magnetic energy, we have generated the synthetic Stokes profiles for each B, γ, and ξ in a grid of 100 × 100 pixels, using the He-Line Information Extractor "HELIX" code (Lagg et al. 2004). This code is a Stokes inversion code based on fitting the observed Stokes profiles with synthetic ones obtained by Unno–Rachkovsky solutions (Unno 1956; Rachkowsky 1967) to the polarized radiative transfer equations (RTE) under the assumption of Milne–Eddington (ME) atmosphere (Landolfi & Landi Degl'Innocenti 1982) and local thermodynamical equilibrium (LTE). However, one can also use this code for generating synthetic Stokes profiles for an input model atmosphere. The synthetic profiles are functions of magnetic field strength (B), inclination (γ), azimuth (ξ), line of sight velocity ($v_{\rm Los}$),

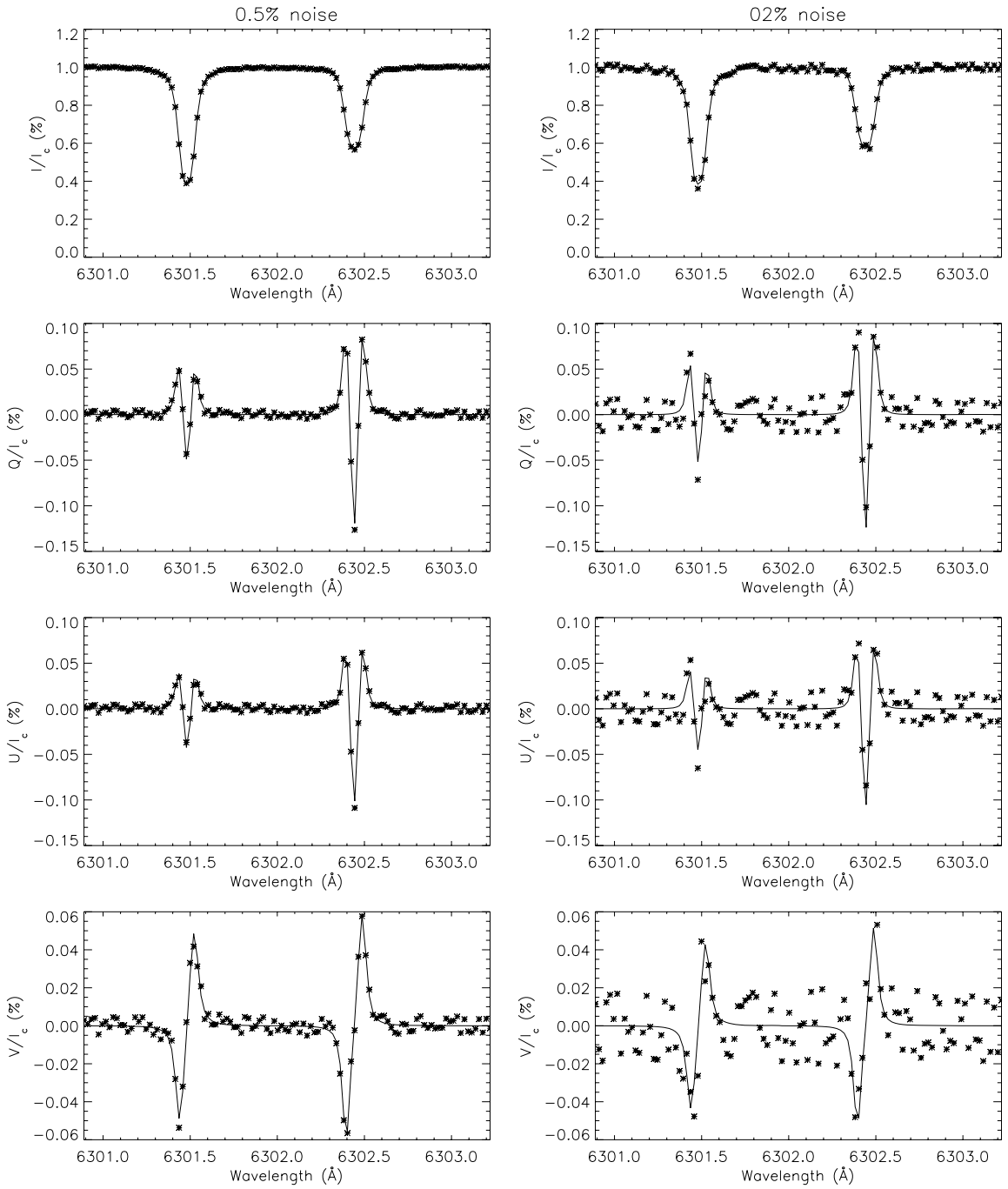

Figure 2. Example of Stokes profiles with 0.5% (left column) and 2.0% (right column) noise along with fitted profiles. The input parameters for the associated pixel are as follows: field strength = 861 G, inclination = 101°, azimuth = 19°. The corresponding output parameters are 850 G, 101°, 19° for 0.5% noise and 874 G, 99°, 19° for 2.0% noise.

Doppler width ($\upsilon_{\rm Dopp}$), damping constant (Γ), ratio of the center to continuum opacity (η_0), slope of the source function ($S_{\rm grad}$), and the source function (S_0) at $\tau = 0$. The filling factor is taken as unity. In our profile synthesis only magnetic field parameters B, γ, and ξ are varied while other model parameters are kept same for all pixels. The typical values of other thermodynamical parameters are given in Table 1. We use the same parameters for all pixels. Further, all the physical parameters at each pixel are taken to be constant in the line forming region. However, one must remember that real solar observations have often Stokes V area asymmetries (Solanki 1989; Khomenko et al. 2005) as a result of vertical magnetic and velocity field gradients present in the line-forming region. This has not been taken into account in our simulations.

A set of Stokes profiles with 0.5% and 2.0% noise for a pixel is shown in Figure 2.

The wavelength grid used for generating synthetic spectral profiles is same as that of *Hinode* (SOT/SP) data which are as follows: start wavelength of 6300.89 Å, spectral sampling 21.5 mÅ pixel^{-1}, and 112 spectral samples. We add normally distributed random noise of different levels in the synthetic Stokes profiles. Typical noise levels in Stokes profiles obtained by *Hinode* (SOT/SP) normal mode scan are of the order of 10^{-3} of the continuum intensity, I_c (Ichimoto et al. 2008). We

Table 1
Model Parameters for Generating Synthetic Profile

Model Parameter	Value
Doppler velocity, $v_{\rm Los}$ ($\rm ms^{-1}$)	0
Doppler width, $v_{\rm Dopp}$ (mÅ)	20
Ratio of center to continuum opacity, η_o	20
Source function, S_o	0.001
Slope of the source function, $S_{\rm grad}$	1.0
Damping constant, Γ	1.4

add random noise of 0.5% of the continuum intensity I_c to the polarimetric profiles. In addition, we also study the effect of adding a noise of 2.0% level to Stokes profiles as a worst case scenario. We add 100 realizations of the noise of the orders mentioned above to each pixel and invert the corresponding 100 noisy profiles using the "HELIX" code.

The guess parameters to initialize the inversion are generated by perturbing known values of B, γ, and ξ by 10%. Thus, after inverting 100 times we get 100 sets of B, γ, and ξ maps for the input B, γ, and ξ values from bipole data. In this way we estimate the spread in the derived field values for various field strengths, inclinations etc. First, the inversion is done without adding any noise in the profiles to check the accuracy of the inversion process. We get the results retrieved in this process which are very similar to those of the initial analytical ones. The scatter plot of input field strength, inclination, azimuth against the corresponding retrieved strength, inclination, azimuth after noise addition and inversion is shown in Figure 3 (upper panel). Typical B_x, B_y, and B_z maps with different noise levels are shown in the lower panel. As the noise increases B_x, B_y, and B_z maps become more grainy.

From the plots shown in Figure 3 we can see that the error in the field strength for a given noise level decreases for strong fields. This is similar to results of Venkatakrishnan & Gary (1989). As the noise increases in the profiles, error in deriving the field strength increases. We find that the error in the field strength determination is ∼15% for 0.5% noise and ∼25% for 2% noise in the profiles. Inclination shows more noise near 0° & 180° than at ∼90°. The error is less even for large noisy profiles for the inclination angles between ∼50°–130°. The reason for this may be understood in the following way. Linear polarization is weaker near 0° and 180° inclinations and is therefore more affected by the noise. The azimuth determination has inherent 180° ambiguity due to insensitivity of Zeeman effect to orientation of transverse fields. Thus in order to compare the input and output azimuths we resolve this ambiguity in $\xi_{\rm out}$ by comparing it with $\xi_{\rm in}$, i.e., the value of $\xi_{\rm out}$ which makes acute angle with $\xi_{\rm in}$ has been taken as correct. We can see azimuth values after resolving the ambiguity in this way show good correlation with input azimuth values. Some scatter is due to the points where ambiguity was not resolved due to 90° difference in $\xi_{\rm in}$ and $\xi_{\rm out}$.

First, the α_g was calculated from the vector field components derived from the noise free profiles to verify the method of calculating global alpha and also the inversion process. We have used the single polarity to calculate global alpha present in sunspot as discussed in Section 3. We retrieved the same value of α_g as calculated using the initial analytical field components. From Figure 4 we can see that the effect of noise on the field components is not much for the case of 0.5% noise but as the noise in the profiles is increased to 2.0%, the field component's specially transverse fields show more uncertainty. The vertical field is comparatively less affected with noise. The scatter plot in Figure 4 shows that the inversion gives good correlation to the actual field values. The points with large scatter are due to poor signal-to-noise ratio in the simulated profiles. The mean percentage error in further discussions is given in terms of weighted average of error.

5. ESTIMATION OF THE ERROR IN THE CALCULATION OF GLOBAL ALPHA (α_g)

We calculate the percentage error in global alpha each time after getting the inverted results, for both the cases when 0.5% and 2.0% (of I_c) noise is added in the profiles, by the following relation:

$$\frac{\triangle\alpha_g}{\alpha_g}(\%) = \frac{\alpha_g^* - \alpha_g}{\alpha_g} \times 100 \qquad (14)$$

where α_g^* is calculated global alpha and α_g is the analytical global alpha.

The histogram of the results obtained is shown in Figure 5.

First, we inverted the profiles without adding any noise and calculated α_g from retrieved results to compare it with the "true" α_g calculated from the analytically generated vector field components. We get less than 0.002% difference in the both α_g values.

For the case of 0.5% noise in polarimetric profiles we get a mean error of 0.3% in the calculation of α_g and error is never more than 1%. Thus, the calculation of α_g is almost free from the effect of noise in this case. Hence, by using data from *Hinode* (SOT/SP), one can derive the accurate value of twist present in a sunspot.

If 2.0% noise is present in the polarization, then maximum ∼5% error is obtained. Weighted average shows only 1% error. Thus, the estimation of alpha is not influenced very much even from the data obtained with old and ground based magnetographs. In any event it is unlikely that a realistic error will be large enough to create a change in the sign of α_g.

6. ESTIMATION OF THE ERROR IN THE CALCULATION OF MAGNETIC ENERGY (E_m)

The magnetic energy has been calculated using virial theorem. One form of the general virial theorem (Chandrasekhar 1961, Chapter 2) states that for a force-free magnetic field, the magnetic energy contained in a volume V is given by a surface integral over the boundary surface S,

$$\int \frac{1}{8\pi} B^2 dV = \frac{1}{4\pi} \int \left[\frac{1}{2} B^2 \mathbf{r} - (\mathbf{B}\cdot\mathbf{r})\mathbf{B}\right] \cdot \hat{\mathbf{n}}\ dS, \qquad (15)$$

where $\mathbf{r}$ is the position vector relative to an arbitrary origin, and n^ is the normal vector at surface. Let us adopt Cartesian coordinates, taking as $z = 0$ plane for photosphere. This assumption is reasonable because the size of sunspots is very small compared to the radius of the Sun. If we make a further reasonable assumption that the magnetic field strength decreases with distance more rapidly than $r^{-3/2}$ whereas a point dipole field falls off as r^{-3}, then the Equation (15) can be simplified to (Molodensky 1974)

$$\int \frac{1}{8\pi} B^2 dx dy dz = \frac{1}{4\pi} \int (x B_x + y B_y) B_z dx dy, \qquad (16)$$

where x and y are the horizontal spatial coordinates. B_x, B_y, and B_z are the vector magnetic field components. This Equation (16) is referred to as the "magnetic virial theorem."

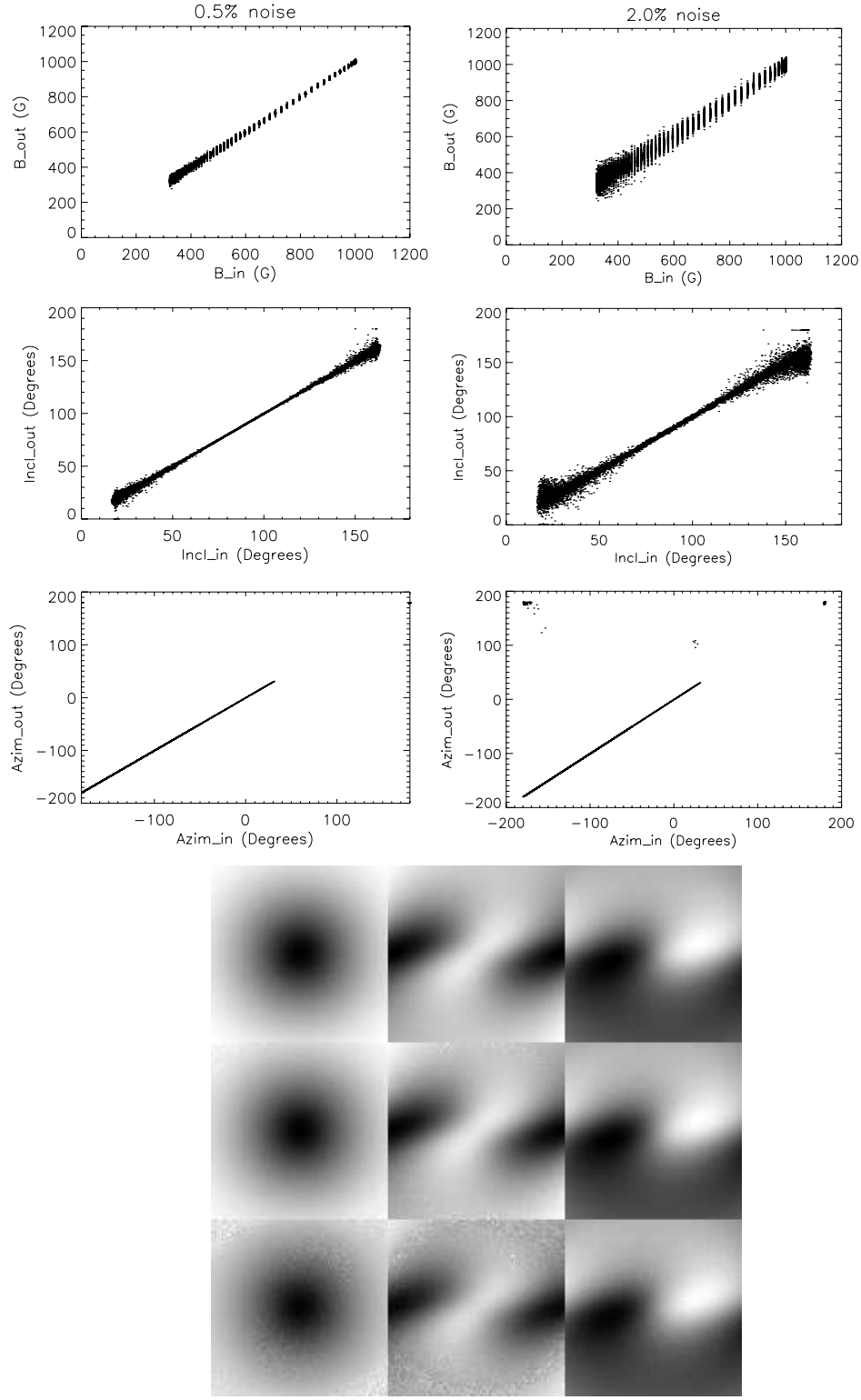

Figure 3. Scatter plot (upper panel) between the field strength, inclination and azimuth before and after inversion with 0.5% (first column) and 2.0% (second column) noises in the profiles. The lower panel shows the images of vector fields B_x, B_y, and B_z before (first row) and after inversion with 0.5% (second row) and 2% (third row) noises in the profiles.

Thus, magnetic energy of an active region can be calculated simply by substituting the derived vector field components into the surface integral of Equation (16) (Low 1982, 1985, 1989). Magnetic field should be solenoidal and force-free as is the case for our analytical field. So the energy integral is independent of choice of the origin.

If all the above conditions are satisfied then the remaining source of uncertainty in the magnetic energy estimation is the errors in the vector field measurements themselves. So, before the virial theorem can be meaningfully applied to the Sun, it is necessary first to understand how the errors in the vector field measurements produce errors in the calculated magnetic energies.

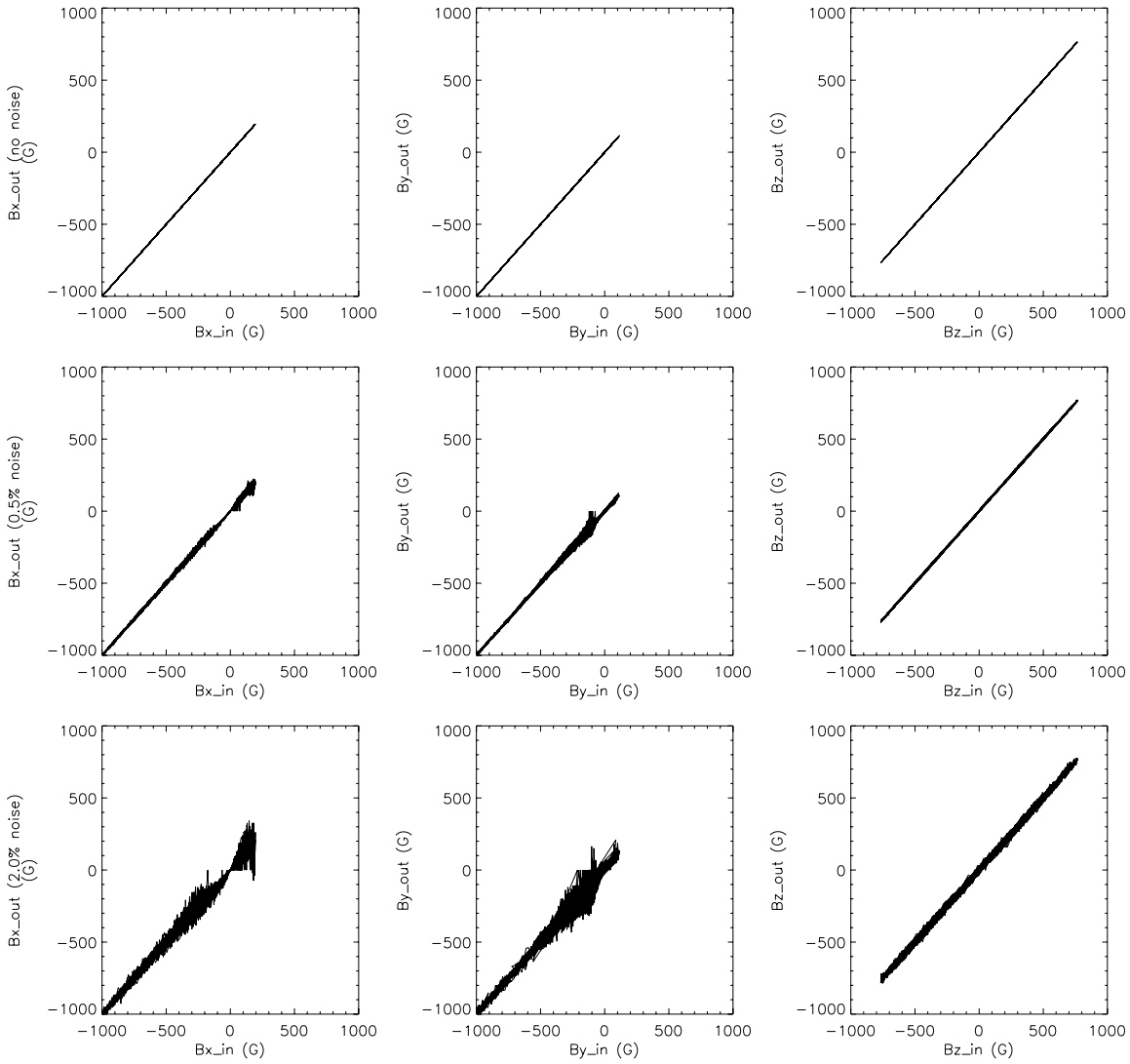

Figure 4. Scatter plot between B_x, B_y, and B_z before and after inversion without noise (first row) and with adding noise in the profiles: second row with 0.5% noise and third row with 2.0% noise (of I_c) in the polarimetric profiles.

Earlier, the efforts were made to estimate the errors (Gary et al. 1987; Klimchuk et al. 1992) for magnetographs like Marshall Space Flight Center (MSFC) magnetograph. Gary et al. (1987) constructed a potential field from MSFC data and computed its virial magnetic energy. Then, they modified the vector field components by introducing random errors in B_x, B_y, and B_z and recomputed the energy. They found the two energies differ by 11%. Klimchuk et al. (1992) approached the problem differently. They introduced errors in the polarization measurements from which the field is derived instead of introducing errors to magnetic fields directly. This way they were able to approximate reality, more closely and were able to include certain type of errors such as cross talk which were beyond the scope of the treatment by Gary et al. (1987). They found that the energy uncertainties are likely to exceed 20% for the observations made with the vector magnetographs present at that time (e.g., MSFC).

Here, our approach is very similar to that of Klimchuk et al. (1992) except that we consider full Stokes profile measurements to derive the magnetic fields like in the most of the recent vector magnetographs, e.g., *Hinode* (SOT/SP), SVM-USO etc. as mentioned earlier. We begin with an analytical field, determine polarization signal as explained in earlier parts, introduce the random noise of certain known levels (0.5% and 2.0% of I_c) in the polarization profiles, infer an "observed" magnetic field after doing the inversion of the noisy profiles, compute an "observed" magnetic energy from the "observed" field and then compare this energy with the energy of the "true" magnetic field. The percentage error is calculated from the following expression:

$$\frac{\triangle E_m}{E_m}(\%) = \frac{E_m^* - E_m}{E_m} \times 100, \tag{17}$$

where E_m^* is the "observed" energy and E_m is the "true" energy. All the above processes have been described in detail in Section 4.

Figure 6 shows the uncertainty estimated in the calculation of magnetic energy in two cases when error in the polarimetric profiles is 0.5% and 2.0% of I_c. Needless to say, we first checked the procedure by calculating the magnetic energy from the vector fields derived from inverted results with no noise in the profiles. We found the same energy as calculated from the initial analytical fields.

We can see that the magnetic energy can be calculated with a very good accuracy when less noise is present in the polarization as is observed in the modern telescopes like *Hinode* (SOT/SP) for which very small (of the order of 10^{-3} of I_c) noise is expected

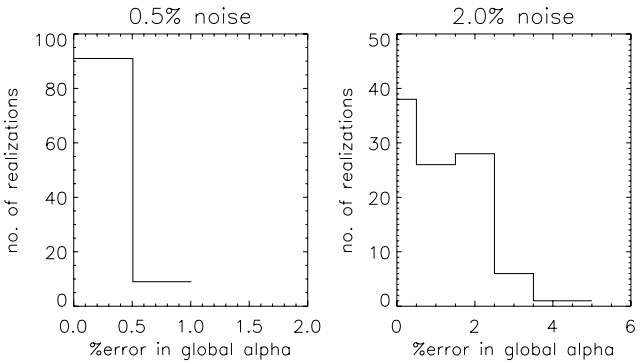

Figure 5. Histogram of the percentage error in calculation of α_g with 0.5% and 2.0% noise (of I_c) in polarimetric profiles, respectively.

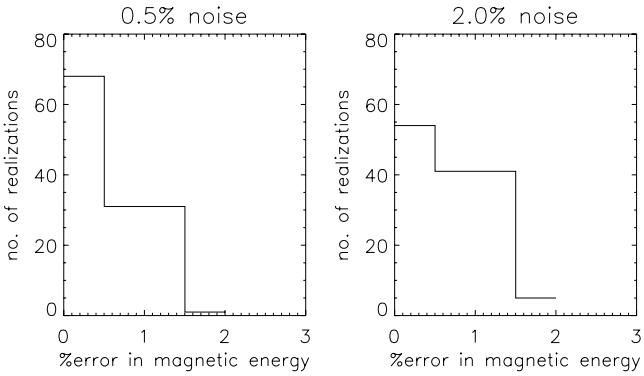

Figure 6. Histogram of the percentage error in calculation of magnetic energy when 0.5% and 2.0% noise (of I_c) is present in polarimetric profiles, respectively.

in profiles. We find that a mean of 0.5% and maximum up to 2% error is possible in the calculation of magnetic energy with such data. So, the magnetic energy calculated from the *Hinode* data will be very accurate provided the force-free field condition is satisfied.

The error in the determination of magnetic energy increases for larger levels of noise. In the case of high noise in profiles (e.g., 2.0% of I_c) the energy estimation is very much vulnerable to the inaccuracies of the field values. We replaced the inverted value of the field parameters with the analytical value wherever the inverted values deviated by more than 50% of the "true" values. We then get the result shown in the right panel. We can see that the error is very small even in this case. The mean value of error is ∼0.7%.

7. DISCUSSION AND CONCLUSIONS

We have discussed the direct method of estimating α_g from vector magnetograms using the second moment of minimization. The higher-order moments also hold promise for generating an index for predicting the flare productivity in active regions.

The global value of twist of an active region can be measured with very good accuracy by calculating α_g. Accurate value of twist can be obtained even if one polarity of a bipole is observed.

The magnetic energy calculation is very accurate as seen from our results. Very less error (approximately 0.5%) is seen in magnetic energy with 0.5% noise in the profiles. Thus, we conclude that the magnetic energy can be estimated with very good accuracy using the data obtained from modern telescopes like *Hinode* (SOT/SP). This gives us the means to look for magnetic energy changes released in weak C-class flares which release radiant energy of the order of 10^{30} erg (see Appendix C), thereby improving the statistics.

These energy estimates are however subject to the condition that the photospheric magnetic field is force-free, a condition which is not always met with. We must then obtain the energy estimates using vector magnetograms observed at higher atmospheric layers where the magnetic field is force-free (Metcalf et al. 1995).

The 180° azimuthal ambiguity (AA) is another source of error for determining parameters like α_g and magnetic free energy in real sunspot observations. The smaller the polarimetric noise, the smaller is the uncertainty in azimuth determination, thereby allowing us to extend the range of the acute angle method used in our analysis. On the other hand it is difficult to predict the level of uncertainty produced by AA. Influence of AA is felt more at highly sheared regions which will anyway deviate from the global alpha value. Thus, avoiding such pixels will improve determination of α_g. Magnetic energy calculation at such pixels could be done by comparing energy estimates obtained by "flipping" the azimuths and choosing the mean of the smallest and the largest estimate of the energy. Here we assume that half the number of pixels has the true azimuth. This is the best one can do for a problem that really has no theoretical solution allowed by the Zeeman effect (but see also, Metcalf et al. 2006 and references therein). Observational techniques such as the use of chromospheric chirality (López Ariste et al. 2006; Martin et al. 2008; Tiwari et al. 2008) or the use of magnetograms observed from different viewing angles could perhaps resolve the AA.

Patches of both signs of alpha are sometimes present in a single sunspot (Pevtsov et al. 1994; Hagino & Sakurai 2004). In those cases the physical meaning of α_g becomes unclear. Efforts are needed to understand the origin of such complex variation of α in a sunspot. Real sunspots show filamentary structures. If this structure is accompanied by local variations of α, then does the global α result from correlations in the local α values? Or, are the small scale variations due to a turbulent cascade from the large scale features? The answers to these questions are beyond the scope of our present study. Modeling sunspots with such complex fine structures is a great challenge. However, we plan to address the question of fine structure of twists in real sunspots observed from HINODE (SOT/SP), in our forthcoming study.

For the present, we demonstrate that the global twist present in an active region can be accurately measured without ambiguity in its sign. Furthermore, the high accuracy of magnetic energy estimation that can be obtained using data from modern instruments will improve the probability for detecting the flare related changes in the magnetic energy of active regions.

We thank Professor E. N. Parker for discussion leading to our understanding the physical meaning of the α parameter during his visit to Udaipur Solar Observatory in November 2007. We also thank him for looking at an earlier draft of the manuscript and for making valuable comments to improve it. One of us (Jayant Joshi) acknowledges financial support under ISRO/CAWSES–India programme. We thank Dr. A. Lagg for providing the HELIX code. We are grateful for the valuable suggestions and comments of the referee which have significantly improved the manuscript.

APPENDIX A

PHYSICAL MEANING OF FORCE-FREE PARAMETER α

(Derived from the discussions with Professor Eugene N. Parker during his visit to Udaipur Solar Observatory)

Taking surface integral on both sides of Equation (2), we get

$$\alpha \int dS \cdot \mathbf{B} = \int dS \cdot \nabla \times \mathbf{B} = \oint dl \cdot \mathbf{B} \text{ (from Stokes theorem)} \quad \text{(A1)}$$

or,

$$\alpha = \oint \frac{dl \cdot \mathbf{B}}{\Phi}. \quad \text{(A2)}$$

In the cylindrical coordinate we can write Equation (A2) as

$$\alpha = \frac{2\pi \varpi B_\Phi}{\pi \varpi^2 B_z} = \frac{2B_\phi}{\varpi B_z}, \quad \text{(A3)}$$

where z and ϖ are axial and radial distances from origin, respectively.

The equation of field lines in cylindrical coordinates is given as

$$\frac{B_z}{dz} = \frac{B_\phi}{\varpi d\phi} \quad \text{(A4)}$$

or,

$$\frac{B_\phi}{B_z} = \frac{\varpi d\phi}{dz}. \quad \text{(A5)}$$

Using Equations (A3) and (A5), we get

$$\alpha = 2\frac{d\phi}{dz}. \quad \text{(A6)}$$

From Equation (A6) it is clear that the α gives twice the degree of twist per unit axial length. If we take one complete rotation of flux tube, i.e., $\phi = 2\pi$, and loop length $\lambda \approx 10^9$ m, then

$$\alpha = \frac{2 \times 2\pi}{\lambda} \quad \text{(A7)}$$

comes out of the order of approximately 10^{-8} per meter.

APPENDIX B

CORRELATION BETWEEN SIGN OF MAGNETIC HELICITY AND THAT OF α

Equation (2) can be written as

$$\nabla \times \mathbf{B} = \alpha(\nabla \times \mathbf{A}) = \nabla \times (\alpha \mathbf{A}) \quad \text{(B1)}$$

giving vector potential in terms of scalar potential ϕ as

$$\mathbf{A} = \mathbf{B}\alpha^{-1} + \nabla\phi, \quad \text{(B2)}$$

which is valid only for constant α. Using this relation in Equation (1), we get magnetic helicity as

$$H_m = \int (\mathbf{B}\alpha^{-1} + \nabla\phi) \cdot \mathbf{B} dV = \int B^2 \alpha^{-1} dV + \int (\mathbf{B} \cdot \nabla)\phi dV. \quad \text{(B3)}$$

Second term on the right-hand side of Equation (B3) can be written as

$$\int (\mathbf{B} \cdot \nabla)\phi dV = \int \nabla \cdot (\phi \mathbf{B}) dV = \int (\phi\ \mathbf{B}) \cdot \mathbf{n} dS \quad \text{(B4)}$$

(from Gauss Divergence Theorem) which is equal to zero for a closed volume where magnetic field does not cross the volume boundary ($\mathbf{n} \cdot \mathbf{B} = \mathbf{0}$) provided that ϕ remains finite on the surface. Therefore, we get magnetic helicity in terms of α as

$$H_m = \int B^2 \alpha^{-1} dV, \quad \text{(B5)}$$

which shows that the force-free parameter α has the same sign as that of the magnetic helicity. However, if $\mathbf{n} \cdot \mathbf{B} \neq \mathbf{0}$, then the contribution of the second term in Equation (B3) remains unspecified. Thus, it is not correct to use alpha to determine the sign of magnetic helicity for the half space above the photosphere since $\mathbf{n} \cdot \mathbf{B} \neq \mathbf{0}$ at the photosphere.

APPENDIX C

ESTIMATE OF ENERGY RELEASE IN DIFFERENT CLASSES OF X-RAY FLARES:

With the simplifying assumption that all classes of soft X-ray flares have a typical duration of 16 minutes (Drake 1971), we can see that the energy released in the different classes of flares will be proportional to their peak power. Since X-class flares typically release radiant energy of the order of 10^{32} erg (Emslie et al. 2005), therefore M-class, C-class, B-class, and A-class flares will release radiant energy of the order of respectively 10^{31}, 10^{30}, 10^{29}, and 10^{28} erg.

REFERENCES

Abramenko, V. I., Wang, T., & Yurchishin, V. B. 1996, Sol. Phys., 168, 75
Ai, G.-X., & Hu, Y.-F. 1986, Publ. Beijing Astron. Obs., 8, 1
Ambastha, A., Hagyard, M. J., & West, E. A. 1993, Sol. Phys., 148, 277
Arnaud, J., Mein, P., & Rayrole, J. 1998, in ESA Special Publication 417, Crossroads for European Solar and Heliospheric Physics. Recent Achievements and Future Mission Possibilities, ed. E. R. Priest, F. Moreno-Insertis, & R. A. Harris (ESA-SP 417; Noordwijk: ESA), 213
Bao, S., & Zhang, H. 1998, ApJ, 496, L43
Berger, M. A., & Field, G. B. 1984, J. Fluid Mech., 147, 133
Bernasconi, P. N., Rust, D. M., & Hakim, D. 2005, Sol. Phys., 228, 97
Burnette, A. B., Canfield, R. C., & Pevtsov, A. A. 2004, ApJ, 606, 565
Chandrasekhar, S. 1961, in Hydrodynamic and Hydromagnetic Stability (International Series of Monographs on Physics) (Oxford: Clarendon)
Drake, J. F. 1971, Sol. Phys., 16, 152
Elmore, D. F., et al. 1992, Proc. SPIE, 1746, 22
Elsasser, W. M. 1956, Rev. Mod. Phys., 28, 135
Emslie, A. G., Dennis, B. R., Holman, G. D., & Hudson, H. S. 2005, J. Geophys. Res., 110, A11103
Gary, G. A., Moore, R. L., Hagyard, M. J., & Haisch, B. M. 1987, ApJ, 314, 782
Gosain, S., Venkatakrishnan, P., & Venugopalan, K. 2004, Exp. Astron., 18, 31
Gosain, S., Venkatakrishnan, P., & Venugopalan, K. 2006, J. Astron. Astrophys., 27, 285
Hagino, M., & Sakurai, T. 2004, PASJ, 56, 831
Hagino, M., & Sakurai, T. 2005, PASJ, 57, 481
Hagyard, M. J., Adams, M. L., Smith, J. E., & West, E. A. 2000, Sol. Phys., 191, 309
Hagyard, M. J., Cumings, N. P., West, E. A., & Smith, J. E. 1982, Sol. Phys., 80, 33
Hagyard, M. J., & Pevtsov, A. A. 1999, Sol. Phys., 189, 25
Hagyard, M. J., Stark, B. A., & Venkatakrishnan, P. 1999, Sol. Phys., 184, 133

Hale, G. E. 1925, PASP, 37, 268
Hale, G. E. 1927, Nature, 119, 708
Ichimoto, K., et al. 2008, Sol. Phys., 249, 233
Jones, H. P., Harvey, J. W., Henney, C. J., Hill, F., & Keller, C. U. 2002, in ESA Special Publication 505, SOLMAG 2002. Proceedings of the Magnetic Coupling of the Solar Atmosphere Euroconference, ed. H. Sawaya-Lacoste (Dordrecht: Kluwer), 15
Keller, C. U., Aebersold, F., Egger, U., Povel, H. P., Steiner, P., & Stenflo, J. O. 1992, Tech. Rep. No. 53, LEST Found., Univ. of Oslo
Keller, C. U., Harvey, J. W., & Giampapa, M. S. 2003, Proc. SPIE, 4853, 194
Khomenko, E. V., Shelyag, S., Solanki, S. K., & Vögler, A. 2005, A&A, 442, 1059
Klimchuk, J. A., Canfield, R. C., & Rhoads, J. E. 1992, ApJ, 385, 327
Lagg, A., Woch, J., Krupp, N., & Solanki, S. K. 2004, A&A, 414, 1109
Landolfi, M., & Landi Degl'Innocenti, E. 1982, Sol. Phys., 78, 355
Leka, K. D., Canfield, R. C., McClymont, A. N., & van Driel-Gesztelyi, L. 1996, ApJ, 462, 547
Lites, B. W., & Skumanich, A. 1985, in NASA Marshall Space Flight Center Measurements of Solar Vector Magnetic Fields (SEE N85-29869 18-92), 342
Longcope, D. W., Fisher, G. H., & Pevtsov, A. A. 1998, ApJ, 507, 417
López Ariste, A., Aulanier, G., Schmieder, B., & Sainz Dalda, A. 2006, A&A, 456, 725
Low, B. C. 1982, Sol. Phys., 77, 43
Low, B. C. 1985, in NASA Marshall Space Flight Center Measurements of Solar Vector Magnetic Fields (SEE N85-29869 18-92), 49
Low, B. C. 1989, in Geophysical Monograph Series 54, Solor System Plasma Physics, ed. J. H. Jr. Waite, J. L. Burch, & R. L. Moore (Washington, DC: American Geophysical Union), 21
Makita, M., Hamana, S., Nishi, K., Shimizu, M., & Koyano, H. 1985, PASJ, 37, 561
Martin, S. F., Bilimoria, R., & Tracadas, P. W. 1994, in Solar Surface Magnetism ed. R. J. Rutten & C. J. Schrijver (Dordrecht: Kluwer), 303
Martin, S. F., Lin, Y., & Engvold, O. 2008, Sol. Phys., 250, 31
Martin, S. F., & McAllister, A. H. 1996, in IAU Colloq. 153, Magnetodynamic Phenomena in the Solar Atmosphere—Prototypes of Stellar Magnetic Activity, ed. Y. Uchida, T. Kosugi, & H. S. Hudson (Dordrecht: Kluwer), 497
Metcalf, T. R., Jiao, L., McClymont, A. N., Canfield, R. C., & Uitenbroek, H. 1995, ApJ, 439, 474
Metcalf, T. R., et al. 2006, Sol. Phys., 237, 267
Mickey, D. L. 1985, Sol. Phys., 97, 223
Mickey, D. L., Canfield, R. C., Labonte, B. J., Leka, K. D., Waterson, M. F., & Weber, H. M. 1996, Sol. Phys., 168, 229
Molodensky, M. M. 1974, Sol. Phys., 39, 393
Parker, E. N. 1979, Cosmical Magnetic Fields: Their Origin and Their Activity (Oxford/New York: Clarendon Press/Oxford Univ. Press)
Pevtsov, A. A., Balasubramaniam, K. S., & Rogers, J. W. 2003, ApJ, 595, 500
Pevtsov, A. A., Canfield, R. C., & Latushko, S. M. 2001, ApJ, 549, L261
Pevtsov, A. A., Canfield, R. C., & Metcalf, T. R. 1994, ApJ, 425, L117
Pevtsov, A. A., Canfield, R. C., & Metcalf, T. R. 1995, ApJ, 440, L109
Pevtsov, A. A., & Longcope, D. W. 2001, in ASP Conf. Ser. 236, Advanced Solar Polarimetry—Theory, Observation, and Instrumentation, ed. M. Sigwarth (San Francisco, CA: ASP), 423
Pevtsov, A. A., & Longcope, D. W. 2007, in ASP Conf. Ser. 369, New Solar Physics with Solar-B Mission, ed. K. Shibata, S. Nagata, & T. Sakurai (San Francisco, CA: ASP), 99
Povel, H. 1995, Opt. Eng., 34, 1870
Rachkowsky, D. N. 1967, Izv. Krymsk. Astrofiz. Obs., 37, 56
Richardson, R. S. 1941, ApJ, 93, 24
Rust, D. M. 1994, Geophys. Res. Lett., 21, 241
Rust, D. M., & Kumar, A. 1996, ApJ, 464, L199
Sakurai, T., et al. 1995, PASJ, 47, 81
S'anchez Almeida, J. 1998, in ASP Conf. Ser. 155, Three-Dimensional Structure of Solar Active Regions ed. C. E. Alissandrakis & B. Schmieder (San Francisco, CA: ASP), 54
Sankarasubramanian, K., et al. 2004, Proc. SPIE, 5171, 207
Sankarasubramanian, K., et al. 2006, in ASP Conf. Ser. 358, Solar Polarization 4, ed. R. Casini & B. W. Lites (San Francisco, CA: ASP), 201
Schmidt, W., Beck, C., Kentischer, T., Elmore, D., & Lites, B. 2003, Astron. Nachr., 324, 300
Seehafer, N. 1990, Sol. Phys., 125, 219
Skumanich, A., & Lites, B. W. 1987, ApJ, 322, 473
Socas-Navarro, H. 2001, in ASP Conf. Ser. 236, Advanced Solar Polarimetry – Theory, Observation, and Instrumentation, ed. M. Sigwarth (San Francisco, CA: ASP), 487
Solanki, S. K. 1989, A&A, 224, 225
Staude, J., Hofmann, A., & Bachmann, G. 1991, in 11 National Solar Observatory/Sacramento Peak Summer Workshop: Solar polarimetry, 49–58, 49
Stenflo, J. O. 1996, Nature, 382, 588
Stenflo, J. O., & Keller, C. U. 1997, A&A, 321, 927
Stepanov, V. E., & Severny, A. B. 1962, Izv. Krymsk. Astrofiz. Obs., 28, 166
Tiwari, S. K., Joshi, J., Gosain, S., & Venkatakrishnan, P. 2008, in Proc. Astrophys. and Space Science, Turbulence, Dynamos, Accretion Disks, Pulsars and Collective Plasma Processes, ed. S. S. Hasan, R. T. Gangadhara, & V. Krishan (Dordrecht: Springer), 329
Tsuneta, S., et al. 2008, Sol. Phys., 249, 167
Unno, W. 1956, PASJ, 8, 108
Venkatakrishnan, P., & Gary, G. A. 1989, Sol. Phys., 120, 235
Wang, J., Shi, Z., Wang, H., & Lue, Y. 1996, ApJ, 456, 861
West, E. A., & Hagyard, M. J. 1983, Sol. Phys., 88, 51
Wilkinson, L. K., Emslie, G. A., & Gary, G. A. 1989, Sol. Phys., 119, 77

The Astrophysical Journal, 702:L133–L137, 2009 September 10 doi:10.1088/0004-637X/702/2/L133

GLOBAL TWIST OF SUNSPOT MAGNETIC FIELDS OBTAINED FROM HIGH-RESOLUTION VECTOR MAGNETOGRAMS

Sanjiv Kumar Tiwari[1], P. Venkatakrishnan[1], and K. Sankarasubramanian[2]
[1] Udaipur Solar Observatory, Physical Research Laboratory, Dewali, Bari Road, Udaipur-313 001, India; stiwari@prl.res.in, pvk@prl.res.in
[2] Space Astronomy & Instrumentation Division, ISRO Satellite Center, Airport Road, Vimanapura, Bangalore-560017, India; sankark@isac.gov.in
Received 2009 June 24; accepted 2009 July 28; published 2009 August 21

ABSTRACT

The presence of fine structures in sunspot vector magnetic fields has been confirmed from *Hinode* as well as other earlier observations. We studied 43 sunspots based on the data sets taken from ASP/DLSP, *Hinode* (SOT/SP), and SVM (USO). In this Letter, (1) we introduce the concept of signed shear angle (SSA) for sunspots and establish its importance for non-force-free fields. (2) We find that the sign of global α (force-free parameter) is well correlated with that of the global SSA and the photospheric chirality of sunspots. (3) Local α patches of opposite signs are present in the umbra of each sunspot. The amplitude of the spatial variation of local α in the umbra is typically of the order of the global α of the sunspot. (4) We find that the local α is distributed as alternately positive and negative filaments in the penumbra. The amplitude of azimuthal variation of the local α in the penumbra is approximately an order of magnitude larger than that in the umbra. The contributions of the local positive and negative currents and α in the penumbra cancel each other giving almost no contribution for their global values for the whole sunspot. (5) Arc-like structures (partial rings) with a sign opposite to that of the dominant sign of α of the umbral region are seen at the umbral–penumbral boundaries of some sunspots. (6) Most of the sunspots studied belong to the minimum epoch of the 23rd solar cycle and do not follow the so-called hemispheric helicity rule.

Key words: Sun: magnetic fields – Sun: photosphere – sunspots

1. INTRODUCTION

Helical patterns in sunspots and associated features have been observed for a long time (Hale 1925, 1927; Richardson 1941) with a hemispheric preference of their chirality, which is independent of the solar cycle. Since the 1990s, the subject has been intensively revisited and the similar behavior of hemispheric patterns for various solar features has been reported by many researchers (Hagino & Sakurai 2004; Nandy 2006; Bernasconi et al. 2005; Pevtsov & Longcope 2001, 2007 and references therein). However, this hemispheric behavior needs further investigation due to some inconsistencies reported for different phases of a solar cycle and also for data sets obtained from different magnetographs (Hagino & Sakurai 2005; Pevtsov et al. 2008).

For a force-free field, the global twist per unit axial length is given by the force-free parameter α (see Appendix A of Tiwari et al. 2009a). Some recent studies (Tiwari et al. 2008, 2009b; S. K. Tiwari et al. (2009, in preparation) have shown that the global α of an active region bears the same sign as its associated features/structures observed at chromospheric and coronal heights. The chromospheric and coronal sign of twist is inferred from the topological chirality sign of the observed features. This leads us to believe that some form of the photospheric global twist exists on the scale of sunspots. However, the structures in the sunspot fields revealed by modern vector magnetographs with high spatial and spectral resolution compels us to make a careful revaluation of global α and its physical meaning.

Since the photospheric field is not force-free (Metcalf et al. 1995), we need an alternative measure of the twist other than α. We introduce the concept of the signed shear angle (SSA) for sunspot magnetic fields in this Letter and show how the SSA is directly related to vertical current (J_z) and α, irrespective of the force-free nature of the sunspot fields.

The presence of oppositely directed currents in a single unipolar sunspot was first shown by Severnyi (1965). For a detailed investigation of local α distribution in three sunspots using 46 vector magnetograms, see Pevtsov et al. (1994). Recently, Su et al. (2009) reported an interesting pattern of fine structures in the α distribution within one active region (AR) using *Hinode* data with higher resolution. We present a comprehensive study of 43 sunspots with high resolution and establish the contribution of such fine structures to the global twist. For this purpose we will rely on J_z and α values.

The helicity hemispheric rule or, more precisely, twist hemispheric rule is claimed to be established by many researchers (Seehafer 1990; Pevtsov et al. 1995; Abramenko et al. 1996; Bao & Zhang 1998; Longcope et al. 1998; Hagino & Sakurai 2005) and has recently been a matter of some debate (Hagino & Sakurai 2005; Pevtsov et al. 2008). A model developed by Choudhuri et al. (2004) predicts deviation from the twist hemispheric rule in the beginning of the solar cycle. However, some observers claim that this deviation from the hemispheric rule may be present in different phases of different solar cycles (Pevtsov et al. 2008). We have studied 43 ARs (as shown in Table 1) mostly observed during the declining phase of solar cycle 23. None but five follow the twist hemispheric rule.

In the following section (Section 2), we discuss the data sets used. Section 3 describes the analysis and results obtained. Finally, in Section 4 we present our conclusions.

2. DATA SETS USED

We have used the vector magnetograms obtained from the Solar Optical Telescope/Spectro-polarimeter (SOT/SP: Tsuneta et al. 2008; Suematsu et al. 2008; Ichimoto et al. 2008) onboard *Hinode* (Kosugi et al. 2007) and the Advanced Stokes Polarimeter (ASP; Elmore et al. 1992) as well as the Diffraction Limited Spectro-polarimeter (DLSP; Sankarasubramanian et al. 2004, 2006) of the Dunn Solar Telescope (DST). A standard and well-established calibration procedure was adopted for ASP/DLSP data. The procedure for obtaining the vector fields

Table 1
List of the Active Regions Studied

AR No. (NOAA)	Date of Observation	Global Alpha (α_g:/meter)	Shear Angle (SSA: deg)	Position	Hemispheric Helicity Rule
10972	2007 Oct 7	-2.331×10^{-8}	−1.085	S05W20(t)	No
10971	2007 Sep 29	3.053×10^{-8}	3.214	N03W07	No
10970	2007 Sep 5	-2.001×10^{-8}	−0.308	S07W58(t)	No
10969	2007 Aug 29	-3.424×10^{-8}	−4.488	S05W33(t)	No
10966	2007 Aug 9	-2.539×10^{-8}	−3.595	S06E07	No
10963(−)	2007 Jul 12	-2.459×10^{-8}	−4.636	S06E14(t)	No
10963(+)	2007 Jul 12	-3.440×10^{-8}	−4.495	S06E14(t)	No
10961	2007 Jul 2	-5.119×10^{-8}	−4.973	S10W16(t)	No
10960	2007 Jun 7	3.027×10^{-8}	4.486	S07W03	Yes
10956(−)	2007 May 18	9.642×10^{-8}	11.595	N02E07	No
10956(+)	2007 May 18	6.458×10^{-8}	5.352	N02E07	No
10955	2007 May 13	-6.737×10^{-8}	−1.887	S09W35(t)	No
10953	2007 Apr 29	-6.673×10^{-9}	−3.071	S10E22(t)	No
10944	2007 Mar 3	-2.084×10^{-8}	−4.635	S05W30(t)	No
10941	2007 Feb 6	-2.745×10^{-8}	−3.069	S07W36(t)	No
10940	2007 Feb 1	-1.948×10^{-8}	−4.726	S04W05	No
10939(−)	2007 Jan 23	-3.033×10^{-8}	−5.105	S04W57(t)	No
10939(+)	2007 Jan 23	-8.289×10^{-9}	−0.869	S04W57(t)	No
10935	2007 Jan 9	-2.412×10^{-8}	−3.414	S07W30(t)	No
10933	2007 Jan 5	-1.119×10^{-9}	−2.423	S04W01	No
10930(−)	2006 Dec 12	-3.519×10^{-8}	−6.676	S05W21(t)	No
10930(+)	2006 Dec 12	-1.624×10^{-7}	−18.067	S05W21(t)	No
10926	2006 Dec 3	-7.049×10^{-9}	−1.538	S09W32(t)	No
10923	2006 Nov 16	1.090×10^{-9}	0.350	S05W30(t)	Yes
10921	2006 Nov 6	-3.318×10^{-7}	−14.054	S08W38(t)	No
10841	2005 Dec 28	1.114×10^{-7}	9.383	N12E20(t)	No
10838	2005 Dec 22	2.294×10^{-7}	14.757	N17E20(t)	No
10808(−)	2005 Sep 13	1.017×10^{-7}	8.015	S11E17(t)	Yes
10808(+)	2005 Sep 13	1.225×10^{-7}	1.020	S11E17(t)	Yes
10804	2005 Aug 26	-4.977×10^{-8}	−5.237	N11W02	Yes
10803	2005 Aug 26	2.559×10^{-7}	6.151	N12E53(t)	No
10800	2005 Aug 26	1.331×10^{-7}	3.967	N17W49(t)	No
10782	2005 Jul 2	-3.626×10^{-7}	−10.230	S17W18(t)	No
10781	2005 Jul 4	1.027×10^{-7}	7.786	N13W03	No
10780	2005 Jun 24	-6.357×10^{-8}	−0.806	S08W28(t)	No
10752	2005 Apr 17	9.960×10^{-8}	8.365	N02W00	No
10330	2003 Apr 9	3.988×10^{-8}	11.031	N07W04	No
09601	2001 Sep 3	1.367×10^{-8}	2.178	N14W06(t)	No
09596	2001 Aug 30	2.125×10^{-7}	9.297	N21E15(t)	No
09591(−)	2001 Aug 30	-2.359×10^{-7}	−6.111	S18W36(t)	No
09591(+)	2001 Aug 30	-1.839×10^{-7}	−2.226	S18W36(t)	No
09590	2001 Aug 26	-3.148×10^{-7}	−2.069	S29W01(t)	No
09585	2001 Aug 24	5.310×10^{-8}	1.730	N14W30(t)	No

(t) : *transformed*

Note. The global α value, the SSA, and other details of the sunspots are given.

from the ASP/DLSP data is described elsewhere (Elmore et al. 1992; Sankarasubramanian et al. 2004, 2006).

The *Hinode* (SOT/SP) data have been calibrated by the standard "sp_prep" routine available in the Solar-Soft packages. The prepared polarization spectra have been inverted to obtain vector magnetic field components using an Unno–Rachkowsky (Unno 1956; Rachkowsky 1967) inversion under the assumption of a Milne–Eddington (ME) atmosphere (Landolfi & Landi Degl'Innocenti 1982; Skumanich & Lites 1987). The 180° azimuthal ambiguity in the data sets are removed by using an acute angle method (Harvey 1969; Sakurai et al. 1985; Cuperman et al. 1992). All the data sets used have high spatial sampling. For example, ASP ∼0.3 arcsec pixel^{-1}, DLSP ∼0.1 arcsec pixel^{-1}, and *Hinode* (SOT/SP) ∼0.3 arcsec pixel^{-1}. However, a few observations are seeing limited to about an arcsec.

To minimize noise, pixels having transverse (B_t) and longitudinal magnetic field (B_z) greater than a certain level are only analyzed. A quiet-Sun region is selected for each sunspot and 1σ deviations in the three vector field components B_x, B_y, and B_z are evaluated separately. The resultant deviations in B_x and B_y are then taken as the 1σ noise level for transverse field components. Only those pixels where longitudinal and transverse fields are simultaneously greater than twice the above mentioned noise levels are analyzed.

The data sets with their observation details are given in Table 1. The data sets observed from 2001 August to 2005 April are obtained with the ASP and those observed from 2005 June to 2005 December are from the DLSP. Two vector magnetograms observed on 2007 January 9 and 2007 February 6 from the Solar Vector Magnetograph at the Udaipur Solar Observatory

(SVM-USO: Gosain et al. 2004, 2006), and reported in Tiwari et al. (2008), also have been included to improve the statistics. All the other data sets obtained since 2006 November onward are taken from *Hinode* (SOT/SP).

3. DATA ANALYSIS AND RESULTS

We have used the following formula to compute the local α values

$$\alpha = \frac{(\nabla \times \mathbf{B})_z}{B_z}. \quad (1)$$

The global α value of the active regions is estimated from the following formula as described in Tiwari et al. (2009a):

$$\alpha_g = \frac{\sum \left(\frac{\partial B_y}{\partial x} - \frac{\partial B_x}{\partial y} \right) B_z}{\sum B_z^2}. \quad (2)$$

This estimate was shown to be not seriously affected by the polarimetric noise (Tiwari et al. 2009a). Moreover, since α_g is weighted by strong field values (Hagino & Sakurai 2004) and not affected by singularities at polarity inversion lines (Tiwari et al. 2009a), this parameter is more accurate than a simple average of local α.

Hagyard et al. (1984) introduced the shear angle $\Delta\Phi = \Phi_{\rm obs} - \Phi_{\rm pot}$, where $\Phi_{\rm obs}$ and $\Phi_{\rm pot}$ are the azimuthal angles of the observed and potential fields, respectively. The amplitude of this angle was studied at the polarity inversion lines to investigate the flare related changes (Hagyard et al. 1990; Ambastha et al. 1993; Hagyard et al. 1999). To emphasize the sign of shear angle we wish to introduce the SSA for the sunspots as follows: we choose an initial reference azimuth for a current-free field (obtained from observed line-of-sight field). Then we move to the observed field azimuth from the reference azimuth through an acute angle. If this rotation is counter-clockwise, then we assign a positive sign for the SSA. A negative sign is given for clockwise rotation. This sign convention will be consistent with the sense of azimuthal field produced by a vertical current. This sign convention is also consistent with the sense of chirality (for details, see Appendix A). The potential field has been computed using the method of Sakurai (1989). The mean of the SSA obtained for a whole sunspot is taken as the global value of the SSA for that sunspot.

The force-free parameter α involves three dimensions since it basically represents the rate of change of rotation per unit axial length. The SSA is the rotational deviation of the projection of the field onto the photosphere from that of a reference current-free field. The α parameter is a gradient of angle per unit length, while the SSA is just an angle. We therefore cannot expect a strong correlation between the amplitudes of both the quantities, the SSA and the α parameter. But we do find a good correlation between their signs as evident from Table 1.

The SSA provides the sign of twist irrespective of whether the photospheric magnetic field is force-free or not. Table 1 shows that the sign of α is the same as the sign of SSA. Thus, we conclude that even if the photosphere is non force-free, the sign of global α will empirically give the sign of global SSA and therefore the sign of global twist (chirality) of the sunspots.

To avoid any kind of projection effect we have transformed the data sets to the disk center (Venkatakrishnan & Gary 1989) if the observed sunspot is equal to more than 10° away from the disk center. In some active regions both the polarities are compact enough to be studied separately. We have treated each pole of those active regions as an individual sunspot and this is denoted in Table 1 after the NOAA no. of sunspots by plus or minus sign.

Two examples of the local α distribution for the data sets obtained from *Hinode* (SOT/SP) are shown in Figure 1. The positive/negative contours are shown in red/blue colors. The local α patches are seen in the umbra and filamentary distribution of α is observed in the penumbral region. We find that the inclination angles oscillate between ∼30° and 80° when we go along the azimuthal direction in the filamentary penumbral structures. This is consistent with the interlocking-comb penumbral structure (Ichimoto et al. 2007) of the penumbral magnetic fields. The vertical current J_z has two components, viz. $-\frac{1}{r}\frac{\partial B_r}{\partial \phi}$ and $\frac{1}{r}\frac{\partial (r B_\phi)}{\partial r}$. If we approximate the observed transverse field (B_t) to be mostly radial ($B_t \sim B_r$) then we can interpret the azimuthal variation of J_z to result from the term $-\frac{1}{r}\frac{\partial B_r}{\partial \phi}$. This term is not expected to contribute to global twist. However, $\frac{1}{r}\frac{\partial (r B_\phi)}{\partial r}$ could be an important contributor to the global twist. A detailed investigation of this interesting possibility is deferred to another paper. For the present, we obtain positive and negative values of current side by side in the penumbra. Because the α parameter depends on the current, this oscillation in the filamentary structure across the penumbral filaments is expected for the α values too.

The distribution of vertical current and local α in the penumbra show higher values than that in the umbral regions. An arc and a straight line, selected respectively in the penumbra and umbra of AR NOAA 10933, have been over plotted as shown in the left panel of Figure 1. The corresponding values of vertical current and α along the arc and the line are shown in Figures 2(a) and (b), respectively. We can see that both the positive and negative vertical current as well as α are equally distributed in the penumbra along the azimuthal direction. This gives a negligible contribution to the global current and global α values, thereby indicating that the contribution of $-\frac{1}{r}\frac{\partial (B_r)}{\partial \phi}$ is indeed small. We have selected an arc rather than the complete circle because many times sunspots are not circular and therefore selecting a proper penumbral region is not possible by a full circle. Similar arcs have been selected in the other sunspots and all the time it is seen that both the positive and the negative vertical current as well as α are distributed equally in the penumbra giving negligible contribution to their global values. While current and α variations are correlated for positive B_z, they will be anti-correlated for negative B_z.

Figure 2(b) shows a typical profile of spatial variations of current and α across the umbra (along the line) in the AR NOAA 10933 shown in the left panel of Figure 1. We see that the amplitude of variation of α in the umbra is smaller than that in the penumbra by approximately an order of the magnitude and is of the same order as that of the global α value of the whole sunspot. The variation of J_z in the umbra is of the same order as the penumbral J_z variation. The mean umbral J_z is much larger than the mean penumbral J_z.

In the right panel of Figure 1 an arc-like structure (partial ring) with a bunch of red contours (positive α) can be observed. This is opposite to that of the dominant negative global α of the sunspot. Such partial rings with opposite signs of the global value are observed in 10 of the sunspots from our sample. In the rest of the sunspots mixed current and α are present in the umbra with one dominant sign and no such specific structures are seen at the umbral–penumbral boundaries.

A few sunspots in our data sets studied are small and have no penumbra. Some ASP data do not show fine structures in the penumbra due to lack of spatial resolution. We have included

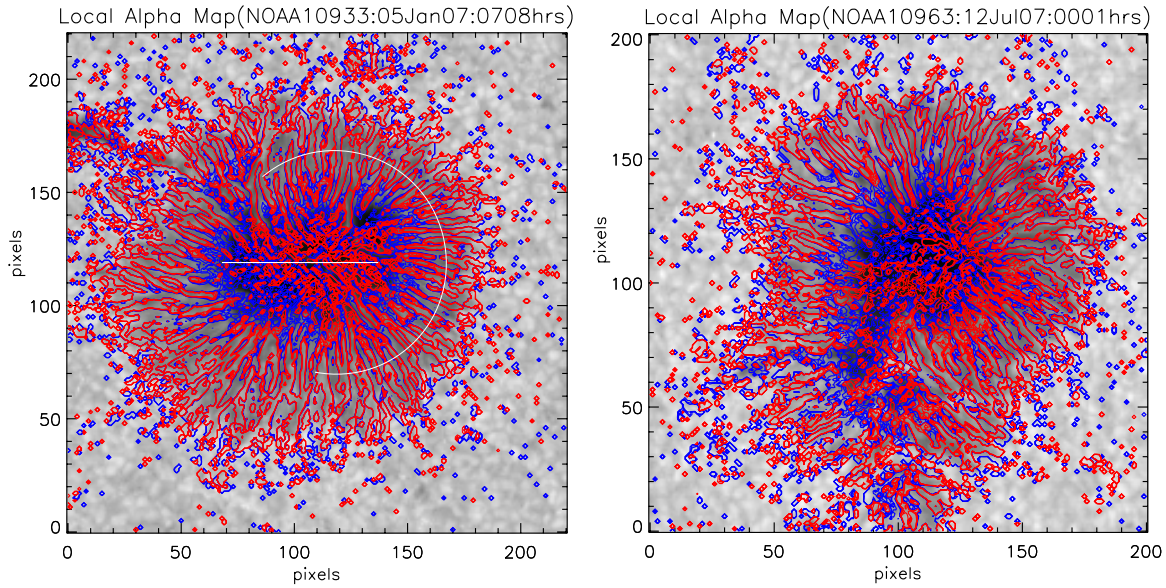

Figure 1. Two examples of local α distribution observed in *Hinode* (SOT/SP) data. The background is the continuum image. Red and blue contours represent positive and negative values of α, respectively. The contour levels are $\pm 1 \times 10^{-8}\ m^{-1}$, $\pm 5 \times 10^{-8}\ m^{-1}$, and $\pm 10 \times 10^{-8}\ m^{-1}$. The values of vertical current and α along the arc shown in the penumbra of the image in the left panel are plotted in Figure 2(a) and those along the straight line in the umbra are plotted in Figure 2(b).

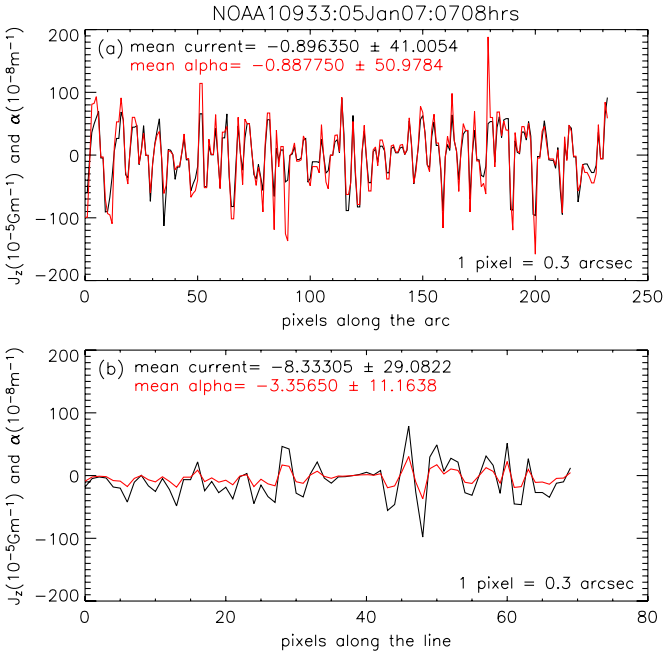

Figure 2. Plots of vertical current and α values along (a) the arc and (b) the straight line shown in the penumbra and umbra of AR NOAA 10933 (the left panel of Figure 1) respectively. Black and red colors represent the current and α values, respectively. The mean values of both the vertical current and the α values with their 1σ standard deviations in the arc and the line are printed on the plots in their respective colors.

these active regions in our study to look at the hemispheric behavior of the global twist.

Most of the data sets we studied are observed during the declining minimum phase of solar cycle 23. All except five of the sunspots observed do not follow the twist hemispheric rule.

4. DISCUSSION AND CONCLUSIONS

We have introduced the concept of SSA for sunspots and further find that the SSA and the global α value of sunspots have the same sign. Thus, α gives the same sign as the SSA and therefore the same sign of the photospheric chirality of the sunspots, irrespective of the force-freeness of the sunspot fields. As can be observed from Table 1, the magnitudes of SSA and α_g are not well correlated. This lack of correlation could be due to a variety of reasons: (1) departure from the force-free nature, (2) even for the force-free fields, α is the gradient of twist variation whereas the SSA is purely an angle. The missing link is the scale length of variation of twist. The magnitude of the global SSA, therefore, holds promise for characterizing global twist of the sunspot magnetic fields, irrespective of its force-free nature.

Patches of vertical current and α with opposite signs are present in the umbra of each sunspot studied. Since opposite currents repel, the existence of a dominant current may be a useful binding force for the umbra (cf. Parker 1979). This will be examined in detail in further studies of evolution of twist in decaying sunspots. One sign of α dominates in the umbra which is also seen to be the sign of the global α of the sunspot. Similarly, the magnitude of the global α is of the same order as the amplitude of the local α in the umbra.

The filamentary structures of vertical current and local α are observed in the penumbra of the sunspots and are, as discussed above, due to oscillatory behavior in the inclination values and therefore gradients of the transverse field in the azimuthal direction. We find that the contributions of both positive and negative values of vertical current and α to their global values cancel each other in the penumbra of the sunspot. Thus the penumbral fine structures provide a negligible contribution to the global α and current values of sunspots. The mutual repulsion of opposite currents also seems to balance out in the azimuthal direction. It is to be seen whether disruption of this balance leads to sunspot rotation and change in global twist. At any rate, the observed balancing of the filamentary currents in the azimuthal direction may be an important contribution to the force-free nature of the sunspot fields. The amplitude of α variation is approximately an order of magnitude smaller in the umbral regions than that in the penumbral regions and is of the order of the global α of the whole sunspot.

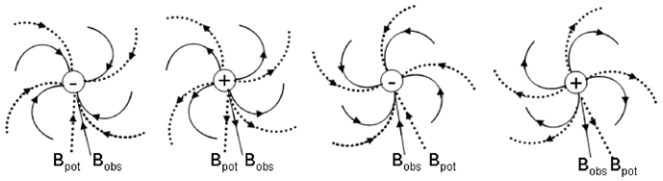

Figure 3. Diagrams of circular unipolar spots with positive and negative chirality are shown with the directions of the observed transverse field (B_{obs}) and potential transverse field (B_{pot}). Solid and dashed lines represent observed and potential fields, respectively. In this cartoon, the B_{obs} is tangential to the solid curved lines, while B_{pot} is tangential to the dashed curved lines which have lesser curvature than the solid lines. The first two cases bear positive chirality and the latter two negative chirality. The plus and minus signs in the central circular region represents the positive and negative polarity, respectively. For details, see the text.

Partial rings with opposite signs to that of dominant sign of umbral α are observed at sunspot umbral–penumbral boundaries in 10 out of 43 sunspots studied. However, even in these few cases, the rings are never complete in any sunspot.

Most of the ARs observed do not follow the twist hemispheric rule. This issue of the hemispheric rule needs to be reinvestigated over a longer period as well as with improved data.

Some researchers have tried to predict flare activity from local distribution of α as well as global α values of sunspots (Nandy 2008; Hahn et al. 2005 and references therein). Nandy (2008) concluded from a study of AR 6982 that the global twist present in a sunspot does not influence the flaring activity. It is, rather, governed by the spatial distribution and evolution of twisted substructures present in the sunspot. This conclusion indeed needs more study. We plan to address, in our forthcoming study, the question of relation between flaring activity and the role of global as well as the local twist present in a large number of sunspots.

For the present, we demonstrate that the sign of the SSA provides the sign of the photospheric chirality irrespective of its force-free nature. The sign of the global α of a sunspot is determined by the dominant sign of umbral α values without much contribution from the penumbral α values.

We thank the referee for very useful comments and suggestions. *Hinode* is a Japanese mission developed and launched by ISAS/JAXA, collaborating with NAOJ as a domestic partner, NASA and STFC (UK) as international partners. Scientific operation of the *Hinode* mission is conducted by the *Hinode* science team organized at ISAS/JAXA. This team mainly consists of scientists from institutes in the partner countries. Support for the post-launch operation is provided by JAXA and NAOJ (Japan), STFC (U.K.), NASA (U.S.A.), ESA, and NSC (Norway). National Solar Observatory is Operated by the Association of Universities for Research in Astronomy (AURA) Inc., under cooperative agreement with the National Science Foundation.

APPENDIX

RELATION BETWEEN THE SIGN OF SSA AND THE SENSE OF CHIRALITY

The definition of the SSA is introduced in Section 3. Figure 3 shows four structures, the first two having positive chirality and the next two having negative chirality. The sign of B_{pot} and B_{obs} point inward for negative B_z and outward for positive B_z. The rotation from B_{pot} to B_{obs} through an acute angle is counterclockwise for cases of positive chirality and clockwise for negative chirality. This is consistent with positive and negative SSA, respectively, by definition. Thus, the sign of SSA will bear the same sign of the chirality.

REFERENCES

Abramenko, V. I., Wang, T., & Yurchishin, V. B. 1996, Sol. Phys., 168, 75
Ambastha, A., Hagyard, M. J., & West, E. A. 1993, Sol. Phys., 148, 277
Bao, S., & Zhang, H. 1998, ApJ, 496, L43
Bernasconi, P. N., Rust, D. M., & Hakim, D. 2005, Sol. Phys., 228, 97
Choudhuri, A. R., Chatterjee, P., & Nandy, D. 2004, ApJ, 615, L57
Cuperman, S., Li, J., & Semel, M. 1992, A&A, 265, 296
Elmore, D. F., et al. 1992, Proc. SPIE 1746, 22
Gosain, S., Venkatakrishnan, P., & Venugopalan, K. 2004, Exp. Astron., 18, 31
Gosain, S., Venkatakrishnan, P., & Venugopalan, K. 2006, J. Astrophys. Astron., 27, 285
Hagino, M., & Sakurai, T. 2004, PASJ, 56, 831
Hagino, M., & Sakurai, T. 2005, PASJ, 57, 481
Hagyard, M. J., Stark, B. A., & Venkatakrishnan, P. 1999, Sol. Phys., 184, 133
Hagyard, M. J., Teuber, D., West, E. A., & Smith, J. B. 1984, Sol. Phys., 91, 115
Hagyard, M. J., Venkatakrishnan, P., & Smith, J. B., Jr. 1990, ApJS, 73, 159
Hahn, M., Gaard, S., Jibben, P., Canfield, R. C., & Nandy, D. 2005, ApJ, 629, 1135
Hale, G. E. 1925, PASP, 37, 268
Hale, G. E. 1927, Nature, 119, 708
Harvey, J. W. 1969, PhD thesis, AA (Univ. Colorado at Boulder)
Ichimoto, K., et al. 2007, PASJ, 59, 593
Ichimoto, K., et al. 2008, Sol. Phys., 249, 233
Kosugi, T., et al. 2007, Sol. Phys., 243, 3
Landolfi, M., & Landi Degl'Innocenti, E. 1982, Sol. Phys., 78, 355
Longcope, D. W., Fisher, G. H., & Pevtsov, A. A. 1998, ApJ, 507, 417
Metcalf, T. R., Jiao, L., McClymont, A. N., Canfield, R. C., & Uitenbroek, H. 1995, ApJ, 439, 474
Nandy, D. 2006, J. Geophys. Res. (Space Phys.), 111, 12
Nandy, D. 2008, in ASP Conf. Ser. 383, Subsurface and Atmospheric Influences on Solar Activity, ed. R. Howe, R. W. Komm, K. S. Balasubramaniam, & G. J. D. Petrie (San Francisco, CA: ASP), 201
Parker, E. N. 1979, Cosmical magnetic fields: Their Origin and Their Activity (Oxford: Clarendon), 1979, 151
Pevtsov, A. A., Canfield, R. C., & Metcalf, T. R. 1994, ApJ, 425, L117
Pevtsov, A. A., Canfield, R. C., & Metcalf, T. R. 1995, ApJ, 440, L109
Pevtsov, A. A., Canfield, R. C., Sakurai, T., & Hagino, M. 2008, ApJ, 677, 719
Pevtsov, A. A., & Longcope, D. W. 2001, in ASP Conf. Ser. 236, Advanced Solar Polarimetry—Theory, Observation, and Instrumentation, ed. M. Sigwarth (San Francisco, CA: ASP), 423
Pevtsov, A. A., & Longcope, D. W. 2007, in ASP Conf. Ser. 369, New Solar Physics with Solar-B Mission, ed. K. Shibata, S. Nagata, & T. Sakurai (San Francisco, CA: ASP), 99
Rachkowsky, D. N. 1967, Izv. Krymsk. Astrofiz. Obs., 37, 56
Richardson, R. S. 1941, ApJ, 93, 24
Sakurai, T. 1989, Space Sci. Rev., 51, 11
Sakurai, T., Makita, M., & Shibasaki, K. 1985, MPA Rep., No., 212, 312
Sankarasubramanian, K., et al. 2004, Proc. SPIE 5171, 207
Sankarasubramanian, K., et al. 2006, in ASP Conf. Ser. 358, ed. R. Casini & B. W. Lites (San Francisco, CA: ASP), 201
Seehafer, N. 1990, Sol. Phys., 125, 219
Severnyi, A. B. 1965, Izv. Krymsk. Astrofiz. Obs., 33, 34
Skumanich, A., & Lites, B. W. 1987, ApJ, 322, 473
Su, J. T., Sakurai, T., Suematsu, Y., Hagino, M., & Liu, Y. 2009, ApJ, 697, L103
Suematsu, Y., et al. 2008, Sol. Phys., 249, 197
Tiwari, S. K., Joshi, J., Gosain, S., & Venkatakrishnan, P. 2008, in Astrophysics and Space Science Proc., ed. S. S. Hasan, R. T. Gangadhara, & V. Krishan (Dordrecht: Springer), 329
Tiwari, S. K., Venkatakrishnan, P., Gosain, S., & Joshi, J. 2009a, ApJ, 700, 199
Tiwari, S. K., Venkatakrishnan, P., & Sankarasubramanian, K. 2009b, in Astrophysics and Space Science Proc., ed. S. S. Hasan & R. J. Rutten (Dordrecht: Springer), in press (arXiv:0904.4353)
Tsuneta, S., et al. 2008, Sol. Phys., 249, 167
Unno, W. 1956, PASJ, 8, 108
Venkatakrishnan, P., & Gary, G. A. 1989, Sol. Phys., 120, 235

The Astrophysical Journal, 706:L114–L119, 2009 November 20 doi:10.1088/0004-637X/706/1/L114

ON THE ABSENCE OF PHOTOSPHERIC NET CURRENTS IN VECTOR MAGNETOGRAMS OF SUNSPOTS OBTAINED FROM *HINODE* (SOLAR OPTICAL TELESCOPE/SPECTRO-POLARIMETER)

P. Venkatakrishnan and Sanjiv Kumar Tiwari
Udaipur Solar Observatory, Physical Research Laboratory, Dewali, Bari Road, Udaipur-313 001, India; pvk@prl.res.in, stiwari@prl.res.in
Received 2009 August 31; accepted 2009 October 19; published 2009 November 2

ABSTRACT

Various theoretical and observational results have been reported regarding the presence/absence of net electric currents in the sunspots. The limited spatial resolution of the earlier observations perhaps obscured the conclusions. We have analyzed 12 sunspots observed from *Hinode* (Solar Optical Telescope/Spectro-polarimeter) to clarify the issue. The azimuthal and radial components of magnetic fields and currents have been derived. The azimuthal component of the magnetic field of sunspots is found to vary in sign with azimuth. The radial component of the field also varies in magnitude with azimuth. While the latter pattern is a confirmation of the interlocking combed structure of penumbral filaments, the former pattern shows that the penumbra is made up of a "curly interlocking combed" magnetic field. The azimuthally averaged azimuthal component is seen to decline much faster than $1/\varpi$ in the penumbra, after an initial increase in the umbra, for all the spots studied. This confirms the confinement of magnetic fields and absence of a net current for sunspots as postulated by Parker. The existence of a global twist for a sunspot even in the absence of a net current is consistent with a fibril-bundle structure of the sunspot magnetic fields.

Key words: Sun: magnetic fields – Sun: photosphere – sunspots

1. INTRODUCTION

Sunspots have shown evidence for twist even from the time of Hale (1925, 1927) who postulated the hemispheric rule for the chirality of chromospheric whirls. This was later confirmed with a larger data set by Richardson (1941). Evidence for photospheric chirality could be seen in early continuum images of sunspots, obtained with exceptional image quality. Later, photospheric vector magnetograms showed global twist inferred from the non-vanishing averages of the force-free parameter (Pevtsov et al. 1994; Hagino & Sakurai 2004; Nandy 2006, and references therein). The non-force-free nature of photospheric magnetic field in the sunspots prompted Tiwari et al. (2009b) to propose the signed shear angle (SSA) as a more robust measure of the global twist of the sunspot magnetic field.

Although, the sign of SSA matches well with the sign of the global alpha parameter, the magnitudes are not so well correlated. The physical significance of a globally averaged α parameter rests heavily on the existence of a net current in the photospheric sunspot magnetic field. One way of arriving at a global α is by taking the ratio of total vertical current to the total flux (integral method). This value was found to agree with the values obtained by other methods (Hagino & Sakurai 2004).

For a monolithic sunspot magnetic field, the global twist and net current are expected to be well correlated by Ampere's law. However, the existence of a net current is ruled out theoretically for fibril bundles as well as for monolithic fields with azimuthal field decreasing faster than $1/\varpi$, where ϖ is the radial distance from the spot center (Parker 1996). Several attempts to resolve this problem using vector magnetograms have not been very conclusive so far (Wilkinson et al. 1992; Leka et al. 1996; Wheatland 2000).

A resolution of this problem can be used to disentangle the relation between global twist and the global α parameter. Also, the resolution is needed to evaluate the so-called hemispheric helicity rule seen in the global α parameter calculated from photospheric vector magnetograms (Pevtsov et al. 1994, 1995; Hagino & Sakurai 2004; Nandy 2006). The availability of high-resolution vector magnetograms from *Hinode* (Solar Optical Telescope/Spectro-polarimeter (SOT/SP)) gives us the best opportunity so far to address this problem. The effect of polarimetric noise is expected to be negligible in the estimation of magnetic parameters (Tiwari et al. 2009a) from these data.

In this Letter, we obtain an expression for the net current using a generalization of the expression obtained by Parker (1996). We then proceed to measure this current from several vector magnetograms of nearly circular sunspots. We finally discuss the results and present our conclusions.

2. EXPRESSION FOR NET CURRENT

Following Parker (1996), we consider a long straight flux bundle surrounded by a region of field-free plasma. We use the words "field free" in the empirical sense that there is no large-scale coherent and unipolar magnetic field surrounding the flux bundle. Also, we include the case where the bundle can be replaced by a monolithic field. Parker (1996) assumed azimuthal symmetry as well as zero radial component B_r, of the magnetic field. For realistic sunspot fields, we need to relax both these assumptions.

The vertical component of the electric current density consists of two terms, viz., $-\frac{1}{\mu_0 r}\frac{\partial B_r}{\partial \psi}$ and $\frac{1}{\mu_0 r}\frac{\partial (r B_\psi)}{\partial r}$. We will call the first term as the "pleat current density," j_p and the second term as the "twist current density," j_t. The net current I_z within a distance ϖ from the center is then given by

$$I_z(\varpi) = \int_0^{2\pi} d\psi \int_0^{\varpi} r dr (j_p + j_t). \quad (1)$$

The ψ integral over j_p vanishes, while the second term yields

$$I_z(\varpi) = \frac{\varpi}{\mu_0} \int d\psi B_\psi(\varpi, \psi) \quad (2)$$

which gives the net current within a circular region of radius ϖ.

3. THE DATA SETS AND ANALYSIS

We have analyzed the vector magnetograms obtained from SOT/SP (Tsuneta et al. 2008; Shimizu et al. 2008; Suematsu

Table 1
List of the Active Regions Studied

AR No. (NOAA)	Date of Observation	Slope δ	Shear Angle (SSA; deg)	Twist Angle ($\tan^{-1}(B_\psi/B_r)$; deg)	Position	Hemispheric Helicity Rule
10969	2007 Aug 29	7.514	−4.488	−4.009	S05W33(t)	No
10966	2007 Aug 7	4.349	−5.120	−7.028	S06E20(t)	No
10963(−)	2007 Jul 12	4.366	−5.123	41.873[a]	S06E14(t)	No
10963(+)	2007 Jul 12	4.210	−4.495	−5.112	S06E14(t)	No
10961	2007 Jul 2	4.976	−4.973	29.451[a]	S10W16(t)	No
10960	2007 Jun 7	3.267	3.182	−24.012[a]	S07W03	Yes
10953	2007 Apr 29	8.249	−3.382	7.200[a]	S10E22(t)	No
10944	2007 Mar 3	2.407	−4.635	−5.130	S05W30(t)	No
10940	2007 Feb 1	2.281	−4.726	−7.950	S04W05	No
10933	2007 Jan 5	9.584	−2.283	−2.689	S04W01	No
10926	2006 Dec 3	2.750	−1.538	6.001[a]	S09W32(t)	No
10923	2006 Nov 10	3.175	0.785	−9.010[a]	S05W30(t)	Yes

Notes. The power index δ: the slope of decrease of B_ψ value, the twist angle, the signed shear angle (SSA), and other details of the sunspots are given. (t): transformed.
[a] Twist angle for irregular sunspots does not fit to a cylindrical assumption and therefore gives incorrect values.

et al. 2008; Ichimoto et al. 2008) onboard *Hinode* (Kosugi et al. 2007). The calibration of data sets have been performed using the standard "sp_prep" routine developed by B. Lites and available in the Solar-Soft package. The prepared polarization spectra have been inverted to obtain vector magnetic field components using an Unno–Rachkowsky (Unno 1956; Rachkowsky 1967) inversion under the assumption of Milne–Eddington (ME) atmosphere (Landolfi & Landi Degl'Innocenti 1982; Skumanich & Lites 1987). We have used the inversion code "Stokesfit.pro" which has been kindly made available by T. R. Metcalf as a part of the Solar-Soft package. We have used the newest version of this code which returns true field strengths along with the filling factor. The azimuth determination has inherent 180° ambiguity due to insensitivity of Zeeman effect to orientation of the transverse fields. Numerous techniques have been developed and applied to resolve this problem, but not even one guarantees a complete resolution. The 180° azimuthal ambiguity in our data sets is removed by using acute angle method (Harvey 1969; Sakurai et al. 1985; Cuperman et al. 1992).

In order to minimize the noise, pixels with transverse (B_t) and longitudinal magnetic field (B_z) greater than a certain level are only analyzed. A quiet-Sun region is selected for each sunspot and 1σ standard deviations in the three vector field components B_x, B_y, and B_z are evaluated separately. The resultant standard deviations of B_x and B_y are then taken as the 1σ noise level for transverse field components. Only those pixels where longitudinal and transverse fields are simultaneously greater than twice the above mentioned noise levels are analyzed. The data sets with their observation details are given in Table 1. We have treated each polarity as an individual sunspot whenever both the polarities are observed and compact enough to be studied. We have studied only those spots where the polarity inversion lines are well separated from the edge of the sunspot.

The results of the inversions yield the three magnetic parameters, viz., the field strength B, the inclination to the line of sight γ, and the azimuth ϕ. These parameters are used to obtain the three components of magnetic field in Cartesian geometry as

$$B_z = B\cos\gamma, \tag{3}$$

$$B_y = B\sin\gamma\sin\phi, \tag{4}$$

$$B_x = B\sin\gamma\cos\phi. \tag{5}$$

This vector field is transformed to heliographic coordinates (Venkatakrishnan & Gary 1989) for the spots observed at viewing angle more than 10°. The transverse vector is then expressed in cylindrical geometry as

$$B_r = \frac{1}{r}(x B_x + y B_y), \tag{6}$$

$$B_\psi = \frac{1}{r}(-y B_x + x B_y). \tag{7}$$

The azimuthal field B_ψ is then used in Equation (2) for obtaining the value for the total vertical current within a radius ϖ.

We have computed "twist angle" for all the sunspots using B_ψ and B_r as shown in Table 1. The error in "twist" measurement is simply the error in azimuth measurement. Using the weak field approximation, we can find the azimuth ψ from $\tan 2\psi = U/Q$. From this, we can estimate the error in ψ as equal to the percentage error in linear polarization measurements. Thus, a 1% error in polarimetry means that the error in ψ equals 0.01 radians or 0.57 deg. We have performed Monte Carlo simulations of the effect of noise on the inversions which we plan to present in a more detailed paper. We have verified that the error in ψ is consistent with the value estimated from the weak field approximation.

We can see in the Table 1 that the twist angles for regular sunspots match well with the global SSA as expected, whereas they do not match for irregular sunspots.

4. THE RESULTS

Figure 1 shows an example of the maps of twist current, pleat current, B_ψ, and B_r for a sunspot NOAA AR 10933, which is nearly circular. Figure 2(a) shows plots of B_ψ and B_r along with the different concentric circles around spot center. In Figure 2(b), the spatial variations of both B_ψ and B_r are clearly seen. This variation is corresponding to a typical circle selected in the penumbra. The B_r variation in the penumbra is a manifestation of the interlocking combed structure (Ichimoto et al. 2007; Tiwari et al. 2009b). The B_ψ variation in the penumbra shows that not only is there an interlocking combed structure, but these structures are curled as well. In other words, we may describe the penumbral field as possessing a "curly interlocking combed" structure. This feature of the deviation

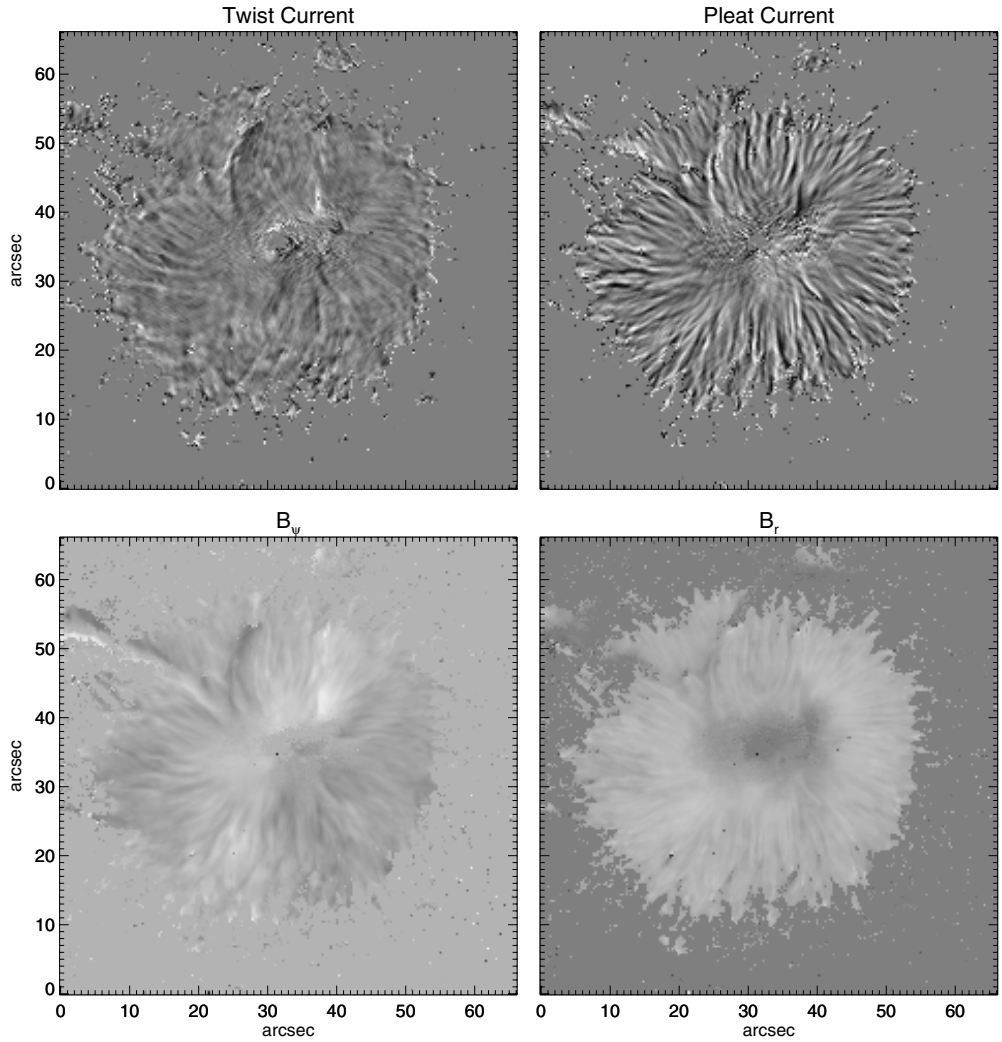

Figure 1. Examples of the two components of the vertical electric current density, namely, the "twist" and the "pleat" current densities (j_t and j_p) observed in NOAA AR 10933 are shown in the upper panel. The lower panel shows the azimuthal and radial component of the magnetic field (B_ψ and B_r).

of the vector field azimuths from a radial direction was also seen by Mathew et al. (2003) in the magnetic field of a sunspot belonging to NOAA AR 8706, using the infrared Fe I line pair at 1.56 μm.

The azimuthal averages $\langle B_\psi \rangle$ and $\langle B_r \rangle$ were obtained at different values of ϖ. Figure 2(c) shows the plots of $\langle B_\psi \rangle$ and $\langle B_r \rangle$ as a function of ϖ. The circles corresponding to the selected radii are shown in the upper panel of the same figure. The azimuth-averaged $\langle B_r \rangle$ drops rapidly to a very low value at the edge of the sunspot. This is a clear evidence for the existence of a canopy where the field lines lift up above the line forming region. Figure 3 shows the plot of log $\langle B_\psi \rangle$ as a function of log ϖ. The slope δ of the declining portion of this plot is 9.584, which shows that field varies faster than $1/\varpi$. This can be construed as evidence for the neutralization of the net current. The δ for other sunspots have also been computed and are given in Table 1.

The map of vertical current density j_z for the same sunspot is shown with intensity scale in the left panel of Figure 4. The values are expressed in giga amperes per square meter (GA m^{-2}). We can see that the distribution of j_z is dominated by high amplitude fluctuations on small scale as also reported in Tiwari et al. (2009b). It is therefore difficult to make out any systematic behavior of the sign of j_z as a function of ϖ.

The right panel of the same figure shows the total current within a radius ϖ as a function of ϖ. As expected from the trend in Figure 3, the total current shows evidence for a rapid decline after reaching a maximum. Similar trends were seen in other sunspots. We have also plotted in right panel of Figure 4, the net current as calculated by the derivative method (viz., summation of current densities calculated as the local curl of B). We do see a trend of neutralization, although the effect is less pronounced because of the larger noise present in the derivative method. We can also infer from the right panel of Figure 4 that the increments of net vertical current flowing through annular portions of the sunspot do show a reversal in sign.

Table 1 shows the summary of results for all the sunspots analyzed. Along with the power-law index δ of B_ψ decrease, we have also shown the average deviation of the azimuth from the radial direction ("twist angle"), as well as the SSA. The average deviation of the azimuth is well correlated with the SSA for nearly circular sunspots, but is not correlated with SSA for more irregularly shaped sunspots. Thus, SSA is a more general measure of the global twist of sunspots, irrespective of their shape.

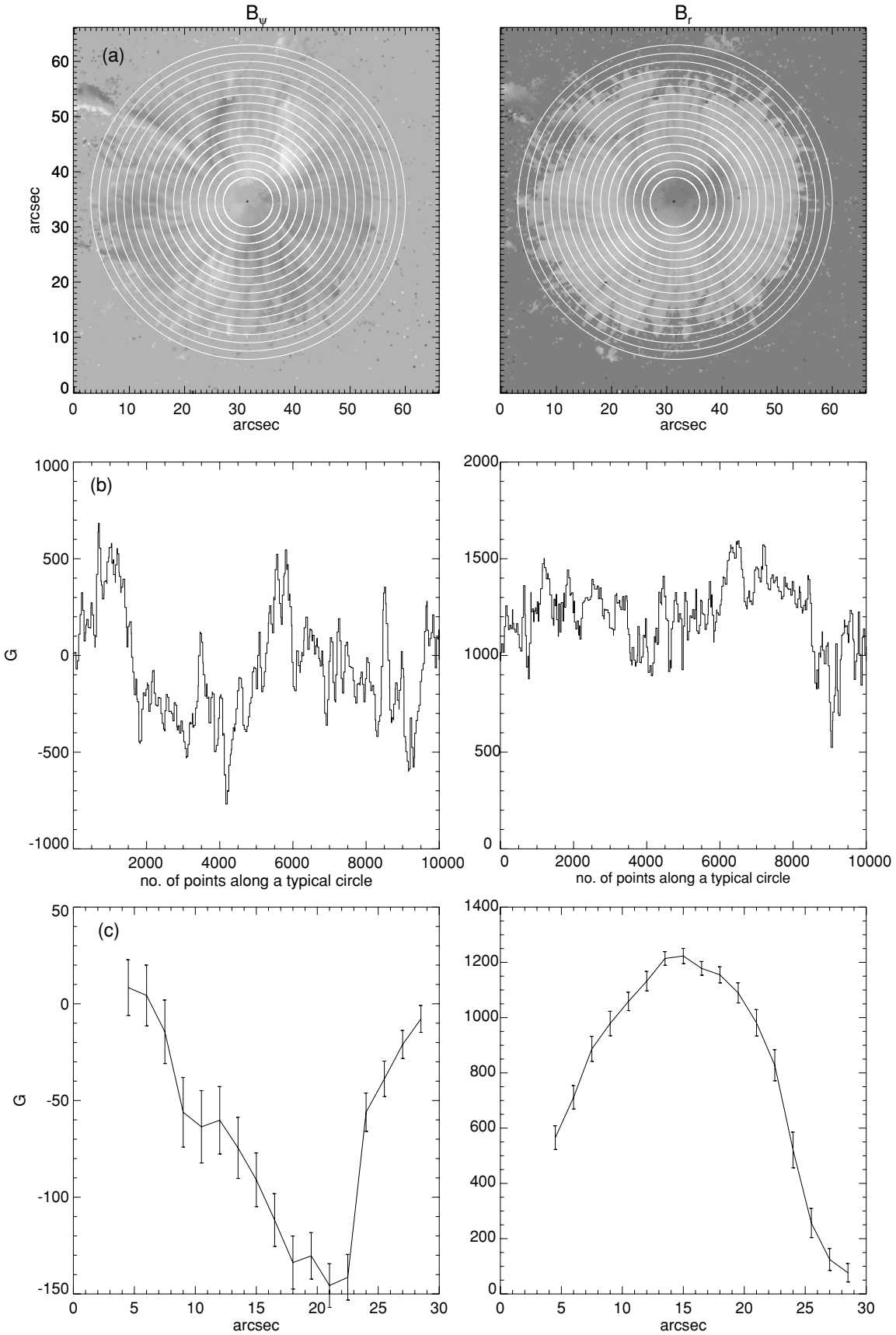

Figure 2. (a) Same image as the lower panel of Figure 1 but with concentric circles over plotted on them. (b) Plots of B_ψ and B_r along the periphery of a typical circle (45th pixel away from center) selected in the sunspot. (c) The mean B_ψ and mean B_r with $\frac{1}{16}$ and $\frac{1}{8}$ of their variations, respectively, along radial direction with different ϖ have been plotted.

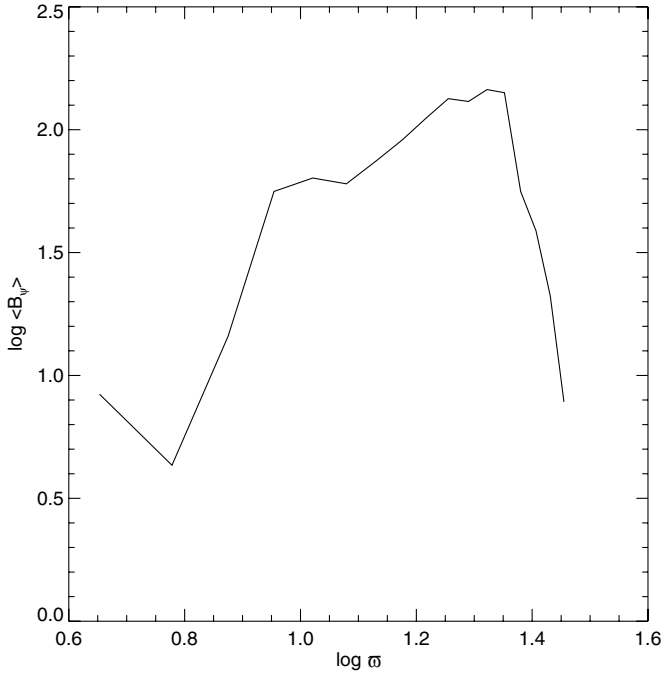

Figure 3. Variation of log $\langle B_\psi \rangle$ with log ϖ. The slope of the declining portion of plot has been calculated as a simple power-law index δ for each sunspot and has been given in Table 1.

5. DISCUSSION AND CONCLUSIONS

It is well known for astrophysical plasmas that the plasma distorts the magnetic field and the curl of this distorted field produces a current by Ampere's law (Parker 1979, Chapt. 2). Parker's (1996) expectation of net zero current in a sunspot was chiefly motivated by the concept of a fibril structure for the sunspot field. However, he also did not rule out the possibility of vanishing net current for a monolithic field where the azimuthal component of the vector field in a cylindrical geometry declines faster than $1/\varpi$. While it is difficult to detect fibrils using the Zeeman effect notwithstanding the superior resolution of SOT on *Hinode*, the stability and accuracy of the measurements have allowed us to detect the faster than $1/\varpi$ decline of the azimuthal component of the magnetic field, which in turn can be construed as evidence for the confinement of the sunspot field by the external plasma. The resulting pattern of curl **B** appears as a drop in net current at the sunspot boundary.

If this lack of net current turns out to be a general feature of sunspot magnetic fields in the photosphere, then measurement of helicity from a global average of the force-free parameter becomes suspect. On the other hand, sunspots are evidently twisted at photospheric levels, as seen from the non-vanishing average twist angle as well as the SSA (Table 1). Although the existence of a global twist in the absence of a net current is possible for a monolithic sunspot field (Baty 2000; Archontis et al. 2004; Fan & Gibson 2004; Aulanier et al. 2005), a fibril model of the sunspot field can accommodate a global twist even without a net current (Parker 1996).

The spatial pattern of current density in a sunspot (e.g., left panel of Figure 4) is really a manifestation of the deformation of the magnetic field ($\nabla \times \mathbf{B}$) by the forces applied by the plasma. The Lorentz force exerted by the field on the plasma produces an equal and opposite force by the plasma, thereby confining the field. Thus, our analysis actually shows the pattern of the forces exerted by the plasma on the field. The sharp decline of the azimuthal field with radial distance thus shows the confinement of the sunspot magnetic field by the radial gradient of the plasma pressure.

Theoretical understanding of the penumbral fine structure has improved considerably in recent times (Thomas et al. 2002; Weiss et al. 2004). The onset of a convective instability

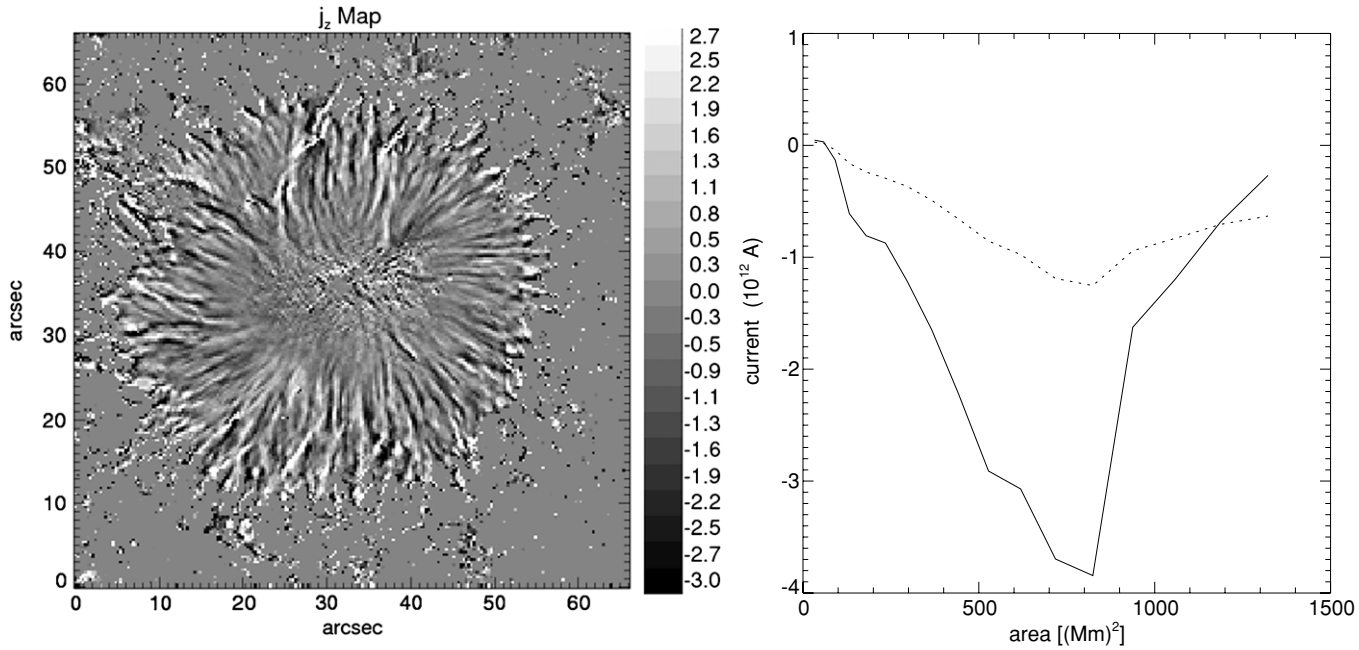

Figure 4. Left panel: the map of vertical current density j_z in NOAA AR 10933 is shown with intensity scale. The values are expressed in giga amperes per square meter (GA m^{-2}). Right panel: the net current variation with increasing area has been shown. The solid line shows the results of the calculations from the Equation (2). Also shown, by a dashed line, are the results from the derivative method. We can see the net current reduces very fast after a peak and almost vanishes for complete sunspot. On the other hand, the net current computed from the derivative method shows a shallow behavior.

for magnetic field inclination exceeding a critical value was proposed by Tildesley (2003) and Hurlburt et al. (2002). A bifurcation in the onset (Rucklidge et al. 1995) could explain other features like hysteresis in the appearance of penumbra as a function of sunspot size. Numerical simulation of magneto-convection also steadily improved (Heinemann et al. 2007; Rempel et al. 2009b), culminating in very realistic production of penumbral field structure (Rempel et al. 2009a). It is possible, owing to the random and stochastic nature of convective structures, that no net twist in the simulated spot field would be produced by convection for negligible Coriolis force. If so, it would be very interesting to simulate magneto-convection in a twisted sunspot field. In this case, would the resulting fine structure mimic the observed "curly interlocking combed" structure of the penumbral magnetic field? If not, we must look elsewhere for explaining the "curly interlocking combed" structure. A twisted fibril bundle would then be a solution. Recent examples of filamentary penumbral structures based on such cluster models (Solanki & Montavon 1993; Spruit & Scharmer 2006; Scharmer & Spruit 2006) have also been proposed.

Parker (1996) also mentions the possibility of net currents in the corona, continuing down to the height where the first cleaving takes place. It would therefore be imperative to look for net currents at higher reaches of the solar atmosphere. This is very important because several theories of flares (Melrose 1995) and coronal mass ejection triggers (Forbes & Isenberg 1991; Kliem & Török 2006) rely heavily on the existence of net currents in the corona above the sunspots.

Future large ground-based telescopes equipped with adaptive optics and multispectral line capabilities would go a long way in addressing these issues. In the meantime, direct measurement of the global twist of sunspots using parameters like the SSA should serve as proxies for estimating the net currents of active regions in the corona. The SSA will also be a better parameter to base a fresh look at the hemispheric rule in photospheric chirality.

We thank Professor Eugene N. Parker for very instructive comments on an early version of the manuscript. His comments on the interpretation of currents in astrophysical plasmas have been particularly useful. The remarks of an anonymous referee have enhanced the clarity of the presentation and improved the understanding of the results. The contributions of the late Professor Metcalf to the inversion software package are also acknowledged. *Hinode* is a Japanese mission developed and launched by ISAS/JAXA, collaborating with NAOJ as a domestic partner, NASA and STFC (UK) as international partners. Scientific operation of the *Hinode* mission is conducted by the *Hinode* science team organized at ISAS/JAXA. This team mainly consists of scientists from institutes in the partner countries. Support for the post-launch operation is provided by JAXA and NAOJ (Japan), STFC (U.K.), NASA (U.S.A.), ESA, and NSC (Norway).

REFERENCES

Archontis, V., Moreno Insertis, F., Galsgaard, K., Hood, A., & O'Shea, E. 2004, A&A, 426, 1047
Aulanier, G., Démoulin, P., & Grappin, R. 2005, A&A, 430, 1067
Baty, H. 2000, A&A, 360, 345
Cuperman, S., Li, J., & Semel, M. 1992, A&A, 265, 296
Fan, Y., & Gibson, S. E. 2004, ApJ, 609, 1123
Forbes, T. G., & Isenberg, P. A. 1991, ApJ, 373, 294
Hagino, M., & Sakurai, T. 2004, PASJ, 56, 831
Hale, G. E. 1925, PASP, 37, 268
Hale, G. E. 1927, Nature, 119, 708
Harvey, J. W. 1969, PhD thesis, Univ. Colorado at Boulder
Heinemann, T., Nordlund, Å., Scharmer, G. B., & Spruit, H. C. 2007, ApJ, 669, 1390
Hurlburt, N. E., Alexander, D., & Rucklidge, A. M. 2002, ApJ, 577, 993
Ichimoto, K., et al. 2007, PASJ, 59, 593
Ichimoto, K., et al. 2008, Sol. Phys., 249, 233
Kliem, B., & Török, T. 2006, Phys. Rev. Lett., 96, 255002
Kosugi, T., et al. 2007, Sol. Phys., 243, 3
Landolfi, M., & Landi Degl'Innocenti, E. 1982, Sol. Phys., 78, 355
Leka, K. D., Canfield, R. C., McClymont, A. N., & van Driel-Gesztelyi, L. 1996, ApJ, 462, 547
Mathew, S. K., et al. 2003, A&A, 410, 695
Melrose, D. B. 1995, ApJ, 451, 391
Nandy, D. 2006, J. Geophys. Res. (Space Phys.), 111, 12
Parker, E. N. 1979, Cosmical Magnetic Fields: Their Origin and their Activity (Oxford/New York: Clarendon/Oxford Univ. Press)
Parker, E. N. 1996, ApJ, 471, 485
Pevtsov, A. A., Canfield, R. C., & Metcalf, T. R. 1994, ApJ, 425, L117
Pevtsov, A. A., Canfield, R. C., & Metcalf, T. R. 1995, ApJ, 440, L109
Rachkowsky, D. N. 1967, Izv. Krymsk. Astrofiz. Obs., 37, 56
Rempel, M., Schüssler, M., Cameron, R. H., & Knölker, M. 2009a, Science, 325, 171
Rempel, M., Schüssler, M., & Knölker, M. 2009b, ApJ, 691, 640
Richardson, R. S. 1941, ApJ, 93, 24
Rucklidge, A. M., Schmidt, H. U., & Weiss, N. O. 1995, MNRAS, 273, 491
Sakurai, T., Makita, M., & Shibasaki, K. 1985, MPA Rep. 212 (Garching: MPA), 312
Scharmer, G. B., & Spruit, H. C. 2006, A&A, 460, 605
Shimizu, T., et al. 2008, Sol. Phys., 249, 221
Skumanich, A., & Lites, B. W. 1987, ApJ, 322, 473
Solanki, S. K., & Montavon, C. A. P. 1993, A&A, 275, 283
Spruit, H. C., & Scharmer, G. B. 2006, A&A, 447, 343
Suematsu, Y., et al. 2008, Sol. Phys., 249, 197
Thomas, J. H., Weiss, N. O., Tobias, S. M., & Brummell, N. H. 2002, Nature, 420, 390
Tildesley, M. J. 2003, MNRAS, 338, 497
Tiwari, S. K., Venkatakrishnan, P., Gosain, S., & Joshi, J. 2009a, ApJ, 700, 199
Tiwari, S. K., Venkatakrishnan, P., & Sankarasubramanian, K. 2009b, ApJ, 702, L133
Tsuneta, S., et al. 2008, Sol. Phys., 249, 167
Unno, W. 1956, PASJ, 8, 108
Venkatakrishnan, P., & Gary, G. A. 1989, Sol. Phys., 120, 235
Weiss, N. O., Thomas, J. H., Brummell, N. H., & Tobias, S. M. 2004, ApJ, 600, 1073
Wheatland, M. S. 2000, ApJ, 532, 616
Wilkinson, L. K., Emslie, A. G., & Gary, G. A. 1992, ApJ, 392, L39